



HAL
open science

Time alignment of the electromagnetic and hadronic calorimeters, reconstruction of the $B \rightarrow D^- \rho(770)^+$, $B_s \rightarrow D_s^- \rho(770)^+$ and $B_s \rightarrow D_s^- K^{*+}(892)$ decay channels with the LHCb detector

Y. Amhis

► **To cite this version:**

Y. Amhis. Time alignment of the electromagnetic and hadronic calorimeters, reconstruction of the $B \rightarrow D^- \rho(770)^+$, $B_s \rightarrow D_s^- \rho(770)^+$ and $B_s \rightarrow D_s^- K^{*+}(892)$ decay channels with the LHCb detector. High Energy Physics - Experiment [hep-ex]. Université Paris Sud - Paris XI, 2009. English. NNT: . tel-00425102

HAL Id: tel-00425102

<https://theses.hal.science/tel-00425102>

Submitted on 20 Oct 2009

HAL is a multi-disciplinary open access archive for the deposit and dissemination of scientific research documents, whether they are published or not. The documents may come from teaching and research institutions in France or abroad, or from public or private research centers.

L'archive ouverte pluridisciplinaire **HAL**, est destinée au dépôt et à la diffusion de documents scientifiques de niveau recherche, publiés ou non, émanant des établissements d'enseignement et de recherche français ou étrangers, des laboratoires publics ou privés.

LAL 09-93
Juillet 2009

THÈSE

présentée le 2 juillet 2009 par

Yasmine Amhis

pour obtenir le grade de
Docteur en sciences de l'Université Paris XI Orsay

**Time alignment of the electromagnetic and
hadronic calorimeters, reconstruction of the
 $B \rightarrow D^- \rho(770)^+$, $B_s \rightarrow D_s^- \rho(770)^+$ and
 $B_s \rightarrow D_s^- K^{*+}(892)$ decay channels with the
LHCb detector**

soutenue devant la commission d'examen composée de:

M.	Jacques	Lefrançois	Invité
Mme	Marie-Noëlle	Minard	Rapporteur
M.	Olivier	Pène	
Mme	Marie-Hélène	Schune	Directrice de thèse
Mme	Isabelle	Wingerter-Seez	Rapporteur
M.	Guy	Wormser	Président
M.	Fabian	Zomer	

Contents

1	Theoretical overview	5
1.1	Symmetries in physical laws	5
1.2	The Standard Model	6
1.3	From quarks to hadrons	10
1.4	The CKM matrix	11
1.5	The Unitarity Triangle	13
1.6	Constraining the Unitarity Triangle	16
1.6.1	Existing measurements	16
1.6.2	ϕ_s , beyond the Standard Model	20
1.6.3	$\phi_s + \gamma$	20
1.6.4	γ extraction under U-spin symmetry	21
1.7	$B_s^0 \rightarrow D_s^- \rho(770)^+$ and $B_s^0 \rightarrow D_s^- K(892)^{*+}$ branching ratio estimation	22
1.7.1	Low energy effective Hamiltonian	22
1.7.2	Factorization of hadronic matrix elements	25
1.7.3	Branching ratio estimation	26
2	The LHCb detector	28
2.1	The Large Hadron Collider	28
2.2	LHCb	31
2.3	VELO	33
2.4	Magnet	35
2.5	Tracking system	35
2.6	RICH counters	37
2.7	Calorimeters	38
2.8	Muons	39
2.9	Trigger system	39
2.9.1	Level 0 trigger	39
2.9.2	High Level Trigger	40

2.10	Online system and data acquisition	41
2.11	LHCb software	42
2.11.1	Event simulation and reconstruction	43
2.11.2	GRID computing	44
3	Calorimeters	46
3.1	General detector structure	48
3.2	Electronics overview	48
3.3	Sub detectors	50
3.3.1	SPD/PS	50
3.3.2	ECAL	51
3.3.3	HCAL	52
3.4	Electronics of the ECAL/HCAL	53
3.4.1	The analog part(Pulse shaping)	53
3.4.2	The digital part	56
3.4.3	The calorimeter readout card(CROC)	57
3.5	The calorimeter Level-0 system	57
3.6	Monitoring and high voltage system	58
4	Time alignment procedure	62
4.1	Source of time misalignment	62
4.2	Methodology	63
4.3	Monte Carlo study	65
4.3.1	Implementation of the time in the simulation	66
4.3.2	Retrieving the shape of the integrated signal	66
4.3.3	Building an asymmetry	68
4.3.4	R_j extraction from the calibration distribution	68
4.3.5	Impact of the particles' properties on the time mis- alignment	70
4.3.6	Improving the amount of aligned cells	72
4.4	Minimum bias events in the ECAL	74
4.4.1	Time alignment with minimum bias in the standard conditions	74
4.4.2	Time alignment with minimum bias events with the magnetic field off	77
4.4.3	PilotRun conditions	79
4.5	Time alignment with minimum bias events in the HCAL in the pilot run conditions	81

4.6	Scan of the integrated signal	84
4.7	Conclusion	94
5	Time alignment with cosmics data	95
5.1	Detection of cosmics at LHCb	95
5.2	Setup for cosmics acquisition	98
5.3	Cosmics reconstruction	100
5.4	Internal time alignment	110
5.5	Relative time alignment between the ECAL and the HCAL . .	113
5.6	Behaviour of the time correlation between the ECAL and the HCAL	120
5.7	Sensitivity to the the signal shape	123
5.8	Time alignment with other sub detectors	126
	5.8.1 PreShower	126
	5.8.2 Outer Tracker	130
	5.8.3 Muon chambers	130
5.9	Conclusion	131
6	Time alignment with the first beam data	134
6.1	A new variable: the Kernel	135
6.2	Zoology of recorded beam one events in the HCAL	136
6.3	Time structure of the single events	140
6.4	Conclusion	143
7	Reconstruction of the $B \rightarrow D^- \rho(770)^+$, $B_s \rightarrow D_s^- \rho(770)^+$ and $B_s \rightarrow D_s^- K^{*+}(892)$ decay channels	145
7.1	Monte Carlo samples	146
7.2	Computation of the numbers of signal and background events	148
7.3	Preselection	150
	7.3.1 Neutral pions, pions, kaons selection	150
	7.3.2 $\rho(770)$, $K^*(892)$ selection	153
	7.3.3 D , D_s selection	154
7.4	B^0, B_s^0 selection	155
7.5	$B^0 \rightarrow D^- \rho(770)^+$ selection	160
	7.5.1 Fisher coefficients computation	161
	7.5.2 $\frac{S}{\sqrt{S+B}}$ optimization	163
	7.5.3 Signal and background estimation	163
7.6	$B_s^0 \rightarrow D_s^- \rho(770)^+$ and $B_s^0 \rightarrow D_s^- K^{*+}(892)$ selection	165
	7.6.1 Fisher coefficients computation	166

7.6.2	$\frac{S}{\sqrt{S+B}}$ optimization	167
7.6.3	Exploring the D_s^- properties	173
7.6.4	Signal and background estimation for $B_s \rightarrow D_s^- \rho(770)^+$ 179	
7.6.5	Signal and background estimation for $B_s \rightarrow D_s^- K^{*+}$ (892)	180
7.7	Conclusion	184
7.8	What can we do with 200 pb ⁻¹ of data	184

Introduction

LHCb (Large Hadron Collider beauty) est l'une des quatre expériences auprès du Large Hadron Collider (LHC) au CERN. Cette expérience est dédiée à l'étude de la violation de CP , des désintégrations rares ainsi qu' à la recherche de nouvelle physique dans le secteur des mésons B . Le LAL a participé à la conception, la construction et à l'installation de l'électronique des calorimètres électromagnétique (ECAL) et hadronique (HCAL) de LHCb. Ces détecteurs sont entre autre utilisés dans le niveau zéro de déclenchement. En vue du démarrage du LHC, il est important de s'assurer du bon fonctionnement du détecteur mais aussi de préparer les analyses pour la physique. Cette thèse s'articule autour de ces deux aspects. Nous montrons dans un premier temps la mise au point d'une méthode d'alignement en temps des calorimètres électromagnétique et hadronique, puis l'application de cette méthode à des données cosmiques et à des données provenant du faisceau du LHC. Dans un second temps, nous montrons le potentiel de LHCb pour reconstruire des canaux hadroniques, contenant un pion neutre dans l'état final.

Après une brève description du Modèle Standard nous décrivons dans le premier chapitre les observables physiques accessibles via les canaux analysés dans cette thèse. Les rapports d'embranchement de certains de ces canaux n'étant pas encore mesurés à ce jour, nous présentons les aspects théoriques permettant d'extrapoler ces rapports d'embranchement à partir de valeurs mesurées dans d'autres canaux.

Après une rapide description de l'accélérateur LHC, une vue d'ensemble du détecteur LHCb est donnée dans le chapitre 2. Nous décrivons chacun des sous-détecteurs, le système de déclenchement et les outils informatiques permettant de reconstruire des événements.

Le troisième chapitre est consacré à la description du calorimètre qui joue un

rôle essentiel dans cette thèse.

Grâce à des simulations Monte Carlo complètes des calorimètres électromagnétique et hadronique nous avons mis au point une procédure pour effectuer l'alignement en temps. Cette partie est détaillée dans le chapitre 4, où nous vérifions les performances de la méthode sous différentes conditions de prise de données, ainsi que le temps nécessaire pour effectuer la calibration avec de vraies données.

Dans le cadre de la préparation à la mise en route des détecteurs, plus d'un million d'événements cosmiques ont été collectés au printemps 2008. Ils ont permis d'une part la vérification de l'alignement en temps interne des calorimètres électromagnétique et hadronique, et d'autre part l'alignement en temps relatif entre ces deux sous-détecteurs. Les traces reconstruites ont été extrapolées vers d'autres sous-détecteurs de LHCb, comme le trajectographe externe (Outer Tracker), le PS/SPD ou les chambres à muons, afin de les aligner en temps par rapport au calorimètre.

Le 10 septembre 2008 le LHC a délivré une heure de faisceau. Un collimateur placé à l'avant du spectromètre a été fermé, conduisant à la production de gerbes hadroniques détectées dans le calorimètre hadronique. Parmi les événements enregistrés, nous avons utilisé ceux de haute multiplicité appelés "splash". Ces événements, synchronisés avec l'horloge du LHC ont permis de vérifier l'alignement en temps global du calorimètre hadronique, qui sera utilisé comme référence pour l'alignement en temps des autres sous-détecteurs. Cette analyse fait l'objet du chapitre 6.

Les modes $B \rightarrow D^- \rho(770)^+$, $B_s \rightarrow D_s^- \rho(770)^+$ et $B_s \rightarrow D_s^- K^{*+}(892)$ ont des topologies très similaires, et comportent tous un pion neutre dans l'état final. Grâce à des simulations Monte Carlo, nous pouvons préparer l'analyse de ces modes de désintégrations. La stratégie employée consiste à favoriser des coupures robustes au niveau de la présélection. Nous avons ensuite utilisé une analyse multi-variables pour sélectionner les événements de signal en maximisant leur signification statistique par rapport au bruit de fond $b\bar{b}$.

Introduction

LHCb (Large Hadron Collider beauty) is one of the four experiments at the Large Hadron Collider (LHC) at CERN. Its aim is to study CP violation, rare decays and to search for new physics in the B sector. The LAL laboratory has actively taken part in the conception, construction and installation of the electronics of the electromagnetic calorimeter (ECAL) and the hadronic calorimeter (HCAL) of LHCb. In preparation for the start of the LHC, it is important to make sure that they function smoothly, as well as to prepare physics analysis. The work presented in this thesis reflects these two aspects. To begin with, we present the development of a method that enables us to ensure the time alignment of the hadronic and electromagnetic calorimeters, and the application of this method both to cosmic and LHC beam data. We will then explain the potential of LHCb for reconstructing hadronic channels with a neutral pion in the final state.

After briefly describing the Standard Model in the first chapter, we describe the physics observables accessible with these channels. The branching fractions of these channels are necessary to establish our physics reach. We explain the theoretical arguments we use to infer those which are not yet known from available measurements.

A brief description of the LHC accelerator is followed by an overview of the LHCb detector in chapter 2. Each of the subdetectors is described, as well as the trigger system and the software tools allowing to reconstruct events. The third chapter is devoted to the description of the calorimeter, which plays a major role in this thesis.

Thanks to complete Monte Carlo simulations of the electromagnetic and hadronic calorimeters, we have developed a procedure to allow us to perform the time alignment. This is detailed in chapter 4 where we also establish the performances of the method under various data conditions, as well as the

number of events necessary to calibrate with real data.

As part of the preparation for the launch of the detectors, more than a million events of cosmic rays were collected in spring 2008. Special Software tools were designed to select and reconstruct interesting events. These cosmics allowed us to check both the internal time alignment of electromagnetic and hadronic calorimeters, and to adjust the relative time alignment between the two subdetectors.

On September 10th 2008, the LHC delivered about one hour beam. The interaction between the beam and the collimator produced hadronic showers, detected in the hadronic calorimeter. We used the high-multiplicity events, referred to as “splash” and synchronized with the LHC clock, to verify the global time alignment of the hadronic calorimeter. This subdetector will be used as a reference for the time alignment of other LHCb subdetectors. This analysis is discussed in chapter 6.

The $B \rightarrow D^- \rho(770)^+$, $B_s \rightarrow D_s^- \rho(770)^+$ and $B_s \rightarrow D_s^- K^{*+}(892)$ modes have very similar topologies. In addition, they all have a neutral pion in their final state. We have analyzed these modes based on Monte Carlo simulations. This will be the starting point of the analysis on real data. The chosen strategy favors robust cuts in the preselection of the events. We have developed a multi-variate analysis which maximises the statistical significance with respect to the $b\bar{b}$ background.

Chapter 1

Theoretical overview

We introduce in this chapter the basic concepts of the Standard Model. We describe the role of the strong interaction through hadronization and weak interaction via the CKM matrix. The branching ratios of some of the decay channels analyzed in this thesis were not measured yet. These branching ratios are estimated in the last section using factorization and measured experimental quantities. In this chapter we will also try to motivate the use of the decay modes studied in Chapter 7.

1.1 Symmetries in physical laws

Symmetries are fundamental in particle physics. They establish the connection between conservation laws and symmetries of nature. According to Noether's theorem [1], there exists an associated conserved quantity, whenever a physical system is invariant under a continuous transformation. For example, the conservation of momentum follows from invariance under translations. For particle physics, discrete symmetries are also relevant. Of particular interest are:

- C : the charge conjugation changing the sign of all additive quantum numbers;
- P : the parity is the operation of reflection which changes \vec{r} into $-\vec{r}$, where \vec{r} is a spatial vector;

- T : the time reversal operator reversing the direction of motion by reflection of the time axis.

These symmetries can be combined. For example the operation CP transforms a particle into its antiparticle and inverts its momentum. There is no experimental evidence that the strong and the electromagnetic interactions violate C , P , or T , while the weak interaction does. CP violation by the weak interaction has been observed for the first time in 1964 [2] studying rare decays in the neutral kaon system and recently further investigated in the B sector [3]. Even though each of these three discrete symmetries is broken in weak interactions, no violation of the CPT symmetry has been observed. This is an exact symmetry in any local Lagrangian field theory [4].

1.2 The Standard Model

The Standard Model describes in a common framework the strong, electromagnetic and weak interactions. It is based on quantum field theory that accommodates both quantum mechanics and special relativity. To date, almost all experimental tests have agreed with its predictions. The particle content of the Standard Model is the following:

- six leptons (and six antileptons), organized in three families;

$$\begin{pmatrix} \nu_e \\ e \end{pmatrix}, \begin{pmatrix} \nu_\mu \\ \mu \end{pmatrix}, \begin{pmatrix} \nu_\tau \\ \tau \end{pmatrix}$$

- six flavors of quarks (and six antiquarks), organized in three generations;

$$\begin{pmatrix} u \\ d \end{pmatrix}, \begin{pmatrix} c \\ s \end{pmatrix}, \begin{pmatrix} t \\ b \end{pmatrix}$$

- a *gauge* boson for the electromagnetic interaction, the photon γ ;
- three *gauge* bosons for the weak interaction: W^+ , W^- and Z^0 ;
- eight *gauge* bosons for the strong interaction, the gluons;
- the Higgs boson, H not yet experimentally observe.

The Standard Model is built on the symmetry group $SU(3)_C \otimes SU(2)_L \otimes U(1)_Y$, where $SU(3)_C$ describes the *color* symmetry of strong interactions, $SU(2)_L$ the *weak isospin* symmetry and $U(1)_Y$ the symmetry under *hypercharge* transformations. The Lagrangian for this theory is the sum of the strong interactions term \mathcal{L}_{QCD} and the term that accounts for electroweak interactions $\mathcal{L}_{EW}(SU(2)_L \otimes U(1)_Y)$. The electroweak term for one fermion generation, of the Lagrangian is:

$$\mathcal{L}_{EW} = i\{ \bar{Q}_L^{int.}(x)\gamma_\mu \mathcal{D}^\mu Q_L^{int.}(x) + \bar{u}_R^{int.}(x)\gamma_\mu \mathcal{D}^\mu u_R^{int.}(x) + \bar{d}_R^{int.}(x)\gamma_\mu \mathcal{D}^\mu d_R^{int.}(x) + \bar{\Psi}_L^{int.}(x)\gamma_\mu \mathcal{D}^\mu \Psi_L^{int.}(x) + \bar{\nu}_R^{int.}(x)\gamma_\mu \mathcal{D}^\mu \nu_R^{int.}(x) + \bar{l}_R^{int.}(x)\gamma_\mu \mathcal{D}^\mu l_R^{int.}(x) \}$$

$$\mathcal{D}^\mu = \partial^\mu + i\frac{g}{2}\tau_j W_j^\mu + 2ig'Y B^\mu \quad (1.1)$$

g and g' are the coupling constants associated to the gauge fields W_j ($j = 1, 2, 3$) and B (related to the isospin $SU(2)_L$ and hypercharge $U(1)_Y$ symmetry groups) and τ_j are the Pauli matrices in the $SU(2)_L$ space. The W^\pm bosons are related to the $W_{1,2}$ components of the W_j gauge field, the photon and the Z^0 to the W_3 component and to the B field through the weak angle θ_W [7]). In more detail, for the charged boson one defines the field:

$$W^{\mu\pm}(x) = \frac{W_1^\mu \mp iW_2^\mu}{\sqrt{2}}$$

and its hermitian conjugate, related to W^+ and W^- respectively. For the neutral bosons one can write:

$$W_3^\mu = \cos\theta_W Z^\mu - \sin\theta_W A^\mu$$

$$B^\mu = -\sin\theta_W Z^\mu + \cos\theta_W A^\mu$$

where $\sin^2\theta_W = 0.2326 \pm 0.0008$, Z^μ is the field associated to the Z^0 and A^μ with the photon. The following relation holds for the weak angle:

$$\frac{g}{\sin\theta_W} = \frac{g'}{\cos\theta_W} = e$$

with e the positron electric charge. The Lagrangian can be split into a free theory and an interaction part: $\mathcal{L}_{EW} = \mathcal{L}_0 + \mathcal{L}_I$. The interaction Lagrangian is composed of a charged current term \mathcal{L}_{CC} and a neutral current term \mathcal{L}_{NC} . The charged current term can be written in terms of the observable boson fields:

$$\mathcal{L}_{CC} = \frac{g}{2\sqrt{2}} (J_\mu^+(x)W^\mu(x) + J_\mu^-(x)W^{\dagger\mu}(x))$$

where:

$$J_\mu^+ = \bar{u}^{int.} \gamma_\mu (1 - \gamma_5) d^{int.} + \bar{c}^{int.} \gamma_\mu (1 - \gamma_5) s^{int.} + \bar{t}^{int.} \gamma_\mu (1 - \gamma_5) b^{int.} + \bar{\nu}_e^{int.} \gamma_\mu (1 - \gamma_5) e^{int.} + \bar{\nu}_\mu^{int.} \gamma_\mu (1 - \gamma_5) \mu^{int.} + \bar{\nu}_\tau^{int.} \gamma_\mu (1 - \gamma_5) \tau^{int.}$$

and the neutral current one:

$$\mathcal{L}_{NC} = e J_\mu^{em}(x) A^\mu(x) + \frac{g_W}{2 \cos \theta_W} J_\mu^0(x) Z^{0\mu}(x)$$

where

$$\begin{aligned} J_\mu^{em} &= \sum_f Q_f \bar{f} \gamma_\mu f \\ J_\mu^0 &= \sum_f \bar{f} \gamma_\mu (v_f - a_f \gamma_5) f \\ v_f &= \tau_3^f - 2Q_f \sin^2 \theta_W \quad a_f = \tau_3^f \end{aligned}$$

Q_f is the electric charge, the index f runs over all the flavors. Experimentally the W^+ , W^- and Z^0 bosons have been observed to have non zero masses. These masses are explained in the theory thanks to the presence of the Higgs field and the spontaneous symmetry breaking mechanism. The Higgs field is an isospin doublet of complex scalar fields:

$$\Phi = \begin{pmatrix} \phi_+ \\ \phi_0 \end{pmatrix} \quad \tilde{\Phi} = i \cdot \tau_2 \cdot \Phi = \begin{pmatrix} \phi_0^* \\ \phi_- \end{pmatrix}$$

The Lagrangian for the Higgs field is written as follows:

$$\mathcal{D}^\mu \Phi^\dagger \mathcal{D}_\mu \Phi - \mu^2 \Phi^\dagger \Phi - \lambda (\Phi^\dagger \Phi)^2$$

where the covariant derivative is defined in Equation: 1.1. The Higgs field potential ($V(\Phi) = -\mu^2 \Phi^\dagger \Phi - \lambda (\Phi^\dagger \Phi)^2$) has a relative maximum at $\Phi(x) = 0$ and reaches an absolute minimum for all the points belonging to the circle $\Phi(x) = \sqrt{\frac{-\mu^2}{2\lambda}}$. This means that the state of minimum energy, the vacuum state, is not unique but is degenerate. The choice of one of the infinite possible vacuum states implies the spontaneous symmetry breaking, in which some symmetries of the Lagrangian are lost and some of the massless particles acquire a non zero mass. With the spontaneous breaking, the symmetry group $SU(2)_L \otimes U(1)_Y$ is reduced to $U(1)_Q$ (with Q the electric charge)

and the three gauge bosons (W^+ , W^- and Z^0) acquire a mass (the photon, related to the electric charge conservation, remains massless). The choice of the minimum energy state is operated by assigning a non zero expectation value for the Higgs field in the vacuum state. A usual choice is:

$$\langle 0|\Phi|0\rangle = \begin{pmatrix} 0 \\ \frac{v}{\sqrt{2}} \end{pmatrix}$$

with $v = \sqrt{\frac{-\mu^2}{2\lambda}}$. The mass terms for the W^\pm and Z^0 bosons arise from the kinetic term and the masses have the values $M_W = \frac{vg}{2}$ and $M_Z = \frac{vg}{2\cos\theta_W}$. Lepton and quark mass arise from the Yukawa coupling terms of the leptons and quarks with the Higgs field:

$$\begin{aligned} \mathcal{L}_M = & Y_{ij}^d \bar{Q}_{L_i}^{int.} \Phi d_{R_j}^{int.} + Y_{ij}^u \bar{Q}_{L_i}^{int.} \tilde{\Phi} u_{R_j}^{int.} + \\ & Y_{ij}^l \bar{L}_{L_i}^{int.} \Phi l_{R_j}^{int.} + h.c. \end{aligned}$$

Writing explicitly the Φ field, one obtains for the quarks:

$$\mathcal{L}_M = M_{ij}^d \bar{d}_{L_j}^{int.} d_{R_i}^{int.} + M_{ij}^u \bar{u}_j^{int.} u_{R_i}^{int.} + h.c.$$

where

$$M_{ij}^{u,d} = \frac{Y_{ij}^{u,d} \cdot v}{\sqrt{2}}$$

is the quark mass matrix. It can be shown that the conservation of the symmetry CP is described by the matrix M being real. Any complex term would on the other hand transform under CP into its complex conjugate, hence producing CP violation. Generally speaking, the M matrix is not diagonal in the weak interaction eigenstates basis (that we have used up to now), since the weak interaction eigenstates are not also mass eigenstates. One can always pass to the mass eigenstates basis simply by diagonalizing the M matrix; this can be done with a pair of unitary matrices, V_L and V_R :

$$\mathcal{M}^{u,d} = V_L^{u,d} M^{u,d} V_R^{u,d}$$

with \mathcal{M}^f diagonal ($f = u, d$). These unitary matrices change the interaction eigenstates into mass eigenstates.

$$\begin{aligned} d_{L_i} &= (V_L^d)_{ij} d_{L_j}^{int.} \quad ; \quad d_{R_i} = (V_R^d)_{ij} d_{R_j}^{int.} \\ u_{L_i} &= (V_L^u)_{ij} u_{L_j}^{int.} \quad ; \quad u_{R_i} = (V_R^u)_{ij} u_{R_j}^{int.} \end{aligned}$$

In the mass eigenstates basis, the Lagrangian mass term is diagonal and the electroweak charged current term becomes:

$$\mathcal{L}_{CC} = i\frac{g}{2}\bar{u}_{L_i}\gamma^\mu(V_{L_{ik}}^u V_{L_{kj}}^{d\dagger})d_{L_j}\tau_a W_\mu^a.$$

$V = V_{L_{ik}}^u V_{L_{kj}}^{d\dagger}$ being a 3×3 matrix. It can always be parametrized with three Euler angles (real parameters) and six phases (complex parameters). Five of these six phases disappear under transformations that redefine the phase of the quark fields in the quark mass eigenstate basis and leave the diagonal mass matrix unchanged. One of the six phases is irreducible. The presence of this phase accounts for the CP violation in the Standard Model. The choice of operating in the quark mass eigenstates basis has hence moved the CP violation description from the mass sector to the electroweak Lagrangian sector, where it is described by the quark mixing matrix $V = V_{L_{ik}}^u V_{L_{kj}}^{d\dagger}$. This matrix, is the generalization of the Cabibbo mechanism to the three quark generations case, which is known as CKM matrix (from Cabibbo, Kobayashi and Maskawa) [8] is discussed in the next section.

1.3 From quarks to hadrons

In pp collisions, all kind of quarks are produced. In particular b quarks can hadronize into beauty mesons (B^0, B^+, B_s^0, \dots) via the strong interaction and decay through the weak interaction. We describe in this section, how B mesons productions and decays are governed by these two interactions. paragraphThe strong interaction The strong interaction plays an important role for the LHCb experiment since it is responsible for the production of the B hadrons we are studying. The strong interaction is first responsible for the $b\bar{b}$ pair production in gluon fusion (see Figure: 1.1). In a second stage the b

b hadron	Fraction at Z [%]	Combined with $p\bar{p}$
B^+, B^0	40.2 ± 0.9	39.9 ± 1.1
B_s^0	10.5 ± 0.9	11.1 ± 1.2
b baryons	9.1 ± 1.5	9.2 ± 1.9

Table 1.1: Fraction of b hadrons species in $Z \rightarrow b\bar{b}$ decay and in $p\bar{p}$ at $\sqrt{s} = 1.8$ TeV [59].

and \bar{b} quark hadronize into B hadrons. This hadronization also takes place

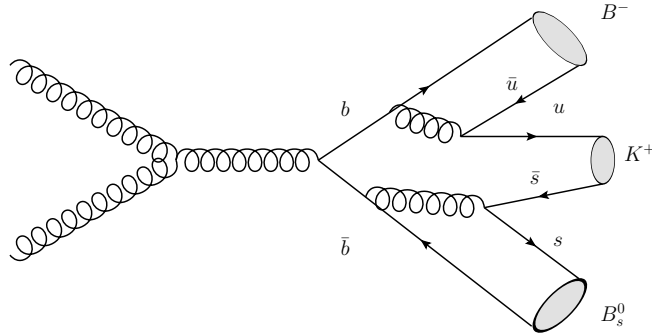


Figure 1.1: Feynman diagram representing the production of a $b\bar{b}$ pair via gluon fusion, followed by the hadronization of the produced quarks into mesons.

due to the strong interaction (see Figure: 1.1). The fractions of b quarks hadronizing into the various B hadrons were measured at LEP and Tevatron (see Table: 1.1). To determine experimentally the b -hadron fractions produced in $p\bar{p}$ collisions and in the Z resonance decay, two constraints are used: $f_u = f_d$ assuming isospin invariance, and $f_u + f_d + f_s + f_{\text{baryon}} = 1$ where, f_u, f_d, f_s and f_{baryon} are the fractions of B^+, B^0, B_s^0 and b baryons, respectively. The B_c production is neglected in the previous equation, as the B_c fraction, f_c , is expected to be very small $\sim 0.2\%$ [5]. Until demonstrated otherwise, these fractions are assumed to be equal at all high-energy colliders.

The weak interaction B mesons decay through the weak interaction. As it was shown previously, the various couplings are given by the CKM matrix elements.

1.4 The CKM matrix

The CKM matrix, the unitary matrix that relates the weak interaction eigenstates to the mass eigenstates, can be written as:

$$V_{CKM} = \begin{pmatrix} V_{ud} & V_{us} & V_{ub} \\ V_{cd} & V_{cs} & V_{cb} \\ V_{td} & V_{ts} & V_{tb} \end{pmatrix}$$

where $V_{q_1 q_2}$ is the coupling associated with the transition $q_2 \rightarrow q_1$. Many parametrizations exist in the literature, the most used are the *standard parametrization* [13], and a generalization of the *Wolfenstein parametrization* [14] as presented in [15]. In the standard parametrization, also used by the Particle Data Group [59], the CKM matrix is written as:

$$V_{CKM} = \begin{pmatrix} c_{12}c_{13} & s_{12}c_{13} & s_{13}e^{-i\delta} \\ -s_{12}c_{23} - c_{12}s_{23}s_{13}e^{i\delta} & c_{12}c_{23} - s_{12}s_{23}s_{13}e^{i\delta} & s_{23}c_{13} \\ s_{12}s_{23} - c_{12}c_{23}s_{13}e^{i\delta} & -s_{23}c_{12} - s_{12}c_{23}s_{13}e^{i\delta} & c_{23}c_{13} \end{pmatrix}$$

where $c_{ij} = \cos \theta_{ij}$ and $s_{ij} = \sin \theta_{ij}$ with θ_{ij} the mixing angles between the different families and δ is the \mathcal{CP} violating phase. Because s_{13} and s_{23} are small and of the order of $O(10^{-3})$ and $O(10^{-2})$ respectively, the standard choice for the four independent parameters is:

$$s_{12} = |V_{us}| \ , \ s_{13} \sim |V_{ub}| \ , \ s_{23} \sim |V_{cb}| \ \text{and} \ \delta.$$

Starting from the consideration that the mixing angles are small, the Wolfenstein parametrization [14] emphasizes a hierarchy in the magnitudes of the V_{CKM} elements: the ones on the diagonal are of order 1, and the others become smaller the further they are from the diagonal. In the Wolfenstein parametrization, the matrix elements are the result of an expansion in terms of a small parameter $\lambda = |V_{us}| \sim 0.22$. The four independent parameters are in this case:

$$\lambda \ , \ A \ , \ \rho \ \text{and} \ \eta$$

where η is related to the \mathcal{CP} violating phase and the matrix is written:

$$V_{CKM} = \begin{pmatrix} 1 - \frac{\lambda^2}{2} & \lambda & A\lambda^3(\rho - i\eta) \\ -\lambda & 1 - \frac{\lambda^2}{2} & A\lambda^2 \\ A\lambda^3(1 - \rho - i\eta) & -A\lambda^2 & 1 \end{pmatrix} + O(\lambda^4) \quad (1.2)$$

If we define:

$$s_{12} = \lambda \ , \ s_{23} = A\lambda^2 \ , \ s_{13}e^{i\delta} = A\lambda^3(\rho - i\eta) \quad (1.3)$$

then, to all orders in λ

$$\rho = \frac{s_{13}}{s_{12}s_{23}} \cos \delta \ , \ \eta = \frac{s_{13}}{s_{12}s_{23}} \sin \delta$$

and the CKM matrix, as a function of (λ, A, ρ, η) , satisfies the unitarity condition exactly. Substituting the expressions given in Equation: 1.3 into

the standard parametrization one obtains the CKM parameters as Taylor expansions with terms of order $O(\lambda^4)$ and higher orders. With respect to the Wolfenstein parametrization, given in Equation: 1.2, the corrections to diagonal elements and to V_{ts} are of order $O(\lambda^4)$, corrections to V_{cd} and V_{td} are of order $O(\lambda^5)$, while additional terms to V_{us} and V_{cb} only appear at the orders $O(\lambda^7)$ and $O(\lambda^8)$ and the expression for V_{ub} stay unchanged. The main corrections to the imaginary parts are $\Delta V_{cd} = -iA^2\lambda^5\eta$ and $\Delta V_{ts} = -iA\lambda^4\eta$. Thanks to the use of the variables:

$$\bar{\rho} = \rho\left(1 - \frac{\lambda^2}{2}\right) \quad , \quad \bar{\eta} = \eta\left(1 - \frac{\lambda^2}{2}\right)$$

the orders $O(\lambda^5)$ can be included in the expression of V_{td}

$$V_{td} = A\lambda^3(1 - \bar{\rho} - i\bar{\eta})$$

and the CKM matrix can be expressed as:

$$V_{CKM} = \begin{pmatrix} 1 - \frac{\lambda^2}{2} - \frac{\lambda^4}{8} & \lambda & A\lambda^3(\bar{\rho} - i\bar{\eta}) \\ -\lambda + \frac{A^2\lambda^5}{2}(1 - 2(\bar{\rho} + i\bar{\eta})) & 1 - \frac{\lambda^2}{2} - \lambda^4(1/8 + A^2/2) & A\lambda^2 \\ A\lambda^3(1 - \bar{\rho} - i\bar{\eta}) & -A\lambda^2 + \frac{1}{2}A\lambda^4 + A\lambda^4(\bar{\rho} + i\bar{\eta}) & 1 - \frac{A^2\lambda^4}{2} \end{pmatrix} + O(\lambda^6).$$

1.5 The Unitarity Triangle

The unitarity of the V_{CKM} matrix,

$$V_{CKM}V_{CKM}^\dagger = V_{CKM}^\dagger V_{CKM} = \mathbf{1},$$

implies several relations between its elements:

$$\sum_{i=1}^3 V_{ij}V_{ik}^* = \delta_{jk}$$

The six independent vanishing relations are listed Table: 1.2. Each one of these relations can be represented as a triangle in the $(\bar{\rho}, \bar{\eta})$ plane, where the ones obtained by product of neighboring rows or columns are nearly degenerate. The areas of all these triangles are equal to half of the Jarlskog invariant J , which is a phase convention measurement of CP violation, defined by:

$$\Im\{V_{ij}V_{kl}V_{il}^*V_{kj}^*\} = J \sum_{m,n=1}^3 \epsilon_{ikm}\epsilon_{jln}$$

Relations	Order in λ
$V_{ud}^* V_{us} + V_{cd}^* V_{cs} + V_{td}^* V_{ts} = 0$	$\lambda, \lambda, \lambda^5$
$V_{ub}^* V_{ud} + V_{cb}^* V_{cd} + V_{tb}^* V_{td} = 0$	$\lambda^3, \lambda^3, \lambda^3$
$V_{us}^* V_{ub} + V_{cs}^* V_{cb} + V_{ts}^* V_{tb} = 0$	$\lambda^4, \lambda^2, \lambda^2$
$V_{ud} V_{cd}^* + V_{us} V_{cs}^* + V_{ub} V_{cb}^* = 0$	$\lambda, \lambda, \lambda^5$
$V_{td} V_{ud}^* + V_{ts} V_{us}^* + V_{tb} V_{ub}^* = 0$	$\lambda^3, \lambda^3, \lambda^3$
$V_{cd} V_{td}^* + V_{cs} V_{ts}^* + V_{cb} V_{tb}^* = 0$	$\lambda^4, \lambda^2, \lambda^2$

Table 1.2: Relations between the CKM elements V_{ij} and their order in λ .

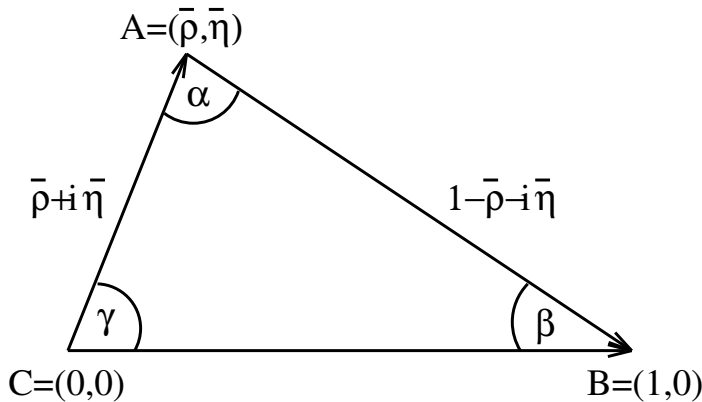


Figure 1.2: Unitarity Triangle(bd), represented in the $(\bar{\rho}, \bar{\eta})$ plane

where ϵ_{abc} is the antisymmetric tensor. The presence of a non-zero CKM phase, and hence of CP violation, requires $J \neq 0$.

Within the six relations, we choose the second one, $V_{ub}^* V_{ud} + V_{cb}^* V_{cd} + V_{tb}^* V_{td} = 0$, whose elements can be determined by B physics measurements. This triangle is particularly attractive from the experimental point of view, since its sides are of order λ^3 . Dividing all the terms of the relation by $|V_{cb}^* V_{cd}|$, one obtains:

$$\frac{V_{ub}^* V_{ud}}{|V_{cb}^* V_{cd}|} + 1 + \frac{V_{tb}^* V_{td}}{|V_{cb}^* V_{cd}|} = 0$$

which is represented by the triangle of Figure 1.2. The imaginary coordinate of the apex is $\bar{\eta}$, the presence of CP violation, i.e. $\bar{\eta} \neq 0$, is described by the area of the triangle being non-zero. The sides of the triangle can be expressed

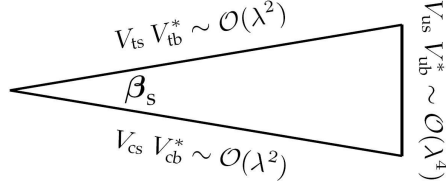


Figure 1.3: Unitarity triangle(bs)

in terms of $\bar{\rho}$ and $\bar{\eta}$:

$$\begin{aligned}\overline{AC} &= R_b = \frac{|V_{ub}^* V_{ud}|}{|V_{cb}^* V_{cd}|} = \sqrt{\bar{\rho}^2 + \bar{\eta}^2} \\ \overline{AB} &= R_t = \frac{|V_{tb}^* V_{td}|}{|V_{cb}^* V_{cd}|} = \sqrt{(1 - \bar{\rho})^2 + \bar{\eta}^2},\end{aligned}$$

and each angle is the relative phase between two adjacent sides:

$$\begin{aligned}\alpha &= \arg \left[\frac{V_{ub}^* V_{ud}}{V_{tb}^* V_{td}} \right] \\ \beta &= \arg \left[\frac{V_{tb}^* V_{td}}{V_{cb}^* V_{cd}} \right] \\ \gamma &= \arg \left[\frac{V_{cb}^* V_{cd}}{V_{ub}^* V_{ud}} \right].\end{aligned}$$

In the Wolfenstein parametrization the only complex elements, up to terms of order $O(\lambda^5)$, are V_{ub} and V_{td} and the phases γ and β can be directly related to them:

$$V_{td} = |V_{td}|e^{-i\beta} \quad , \quad V_{ub} = |V_{ub}|e^{-i\gamma}.$$

The angles of the Unitarity Triangle, or quantities strictly related to them, are accessible by different experimental techniques. Using the third relation $V_{us}^* V_{ub} + V_{cs}^* V_{cb} + V_{ts}^* V_{tb} = 0$, one can build another Unitarity Triangle (see Figure: 1.3), and define the angle:

$$\beta_s = \arg \left[- \frac{V_{tb}^* V_{ts}}{V_{cs}^* V_{cb}} \right]. \quad (1.4)$$

As it will be shown, LHCb will play a major role in the determination of the angle β_s .

1.6 Constraining the Unitarity Triangle

Various experimental measurements from the LEP, the B -factories and the Tevatron are used to constrain the unitarity triangle. Other observables extracted from the B_s system and not appearing directly on the Unitarity Triangle will be considered too.

1.6.1 Existing measurements

We first list the existing measurements:

- $|V_{ub}|$ and $|V_{cb}|$
 B mesons can decay through the $b \rightarrow c$ and $b \rightarrow u$ transitions. Semi leptonic decays offers a relatively large branching fraction ($\sim 10\%$) and corresponding measurements can be interpreted using well established theoretical framework. The relative rate of charmless over charmed b hadrons semileptonic decays is proportional to the square root of the ration:

$$\frac{|V_{ub}|}{|V_{cb}|} = \frac{\lambda}{1 - \frac{\lambda^2}{2}} \sqrt{\bar{\rho}^2 + \bar{\eta}^2}, \quad (1.5)$$

and it allows to measure the length of the side AC of the UT.

- Δm_d
 In the Standard Model, $B^0 - \bar{B}^0$ oscillations occur via the so called box diagrams. The dominant process is the one where a *top* quark is exchanged. The mass difference between the heavy and the light mesons eigenstates of the $B^0 - \bar{B}^0$ system can be written as follows:

$$\Delta m_d = \frac{G_F^2}{6\pi^2} m_W^2 \eta_b S(x_t) A^2 \lambda^6 [(1 - \bar{\rho})^2 + \bar{\eta}^2] m_{B_d} f_{B_d}^2 \hat{B}_{B_d}, \quad (1.6)$$

where $S(x_t)$ is the Inami-Lim function [6] and $x_t = m_t^2/M_W^2$, m_t is the top quark mass and η_b is the perturbative QCD short-distance NLO correction. The scale for the evaluation of those corrections entering into η_b and the running of the t quark mass have to be defined in a consistent way. The value of $\eta_b = 0.55 \pm 0.01$ has been obtained in [9] and, in order to be consistent, the measured value of the pole top quark mass,

obtained by CDF and D0 collaborations, $m_t = (172.6 \pm 1.4)\text{GeV}/c^2$ [10], has to be corrected downwards by $(7 \pm 1)\text{GeV}/c^2$. The remaining factor, $f_{B_d}^2 \hat{B}_{B_d}$, encodes the information of non-perturbative QCD. The constant f_{B_d} translates the size of the B meson wave function at the origin. The bag factor \hat{B}_{B_d} is also introduced to take into account all possible deviation from vacuum saturation approximation. The values of the non-perturbative QCD parameters f_{B_d} , \hat{B}_{B_d} are obtained from lattice QCD calculations. The measurement of Δm_d gives a constraint on the length of the side AB of the Unitarity Triangle.

- $\Delta m_d/\Delta m_s$

The $B_s^0 - \bar{B}_s^0$ time oscillation frequency, which can be related to the mass difference between the light and heavy mass eigenstates of the $B_s^0 - \bar{B}_s^0$ system, is proportional to the square of the $|V_{ts}|$ element. Neglecting terms of order $O(\lambda^4)$, $|V_{ts}|$ is independent of $\bar{\rho}$ and $\bar{\eta}$. The measurement of Δm_s then give a strong constraint on the non-perturbative QCD parameter $f_{B_s}^2 \hat{B}_{B_s}$. The ratio between the values of the mass difference between the mass eigenstates measured in the B_d and in the B_s systems can be used in the Unitarity Triangle analyzes:

$$\frac{\Delta m_d}{\Delta m_s} = \frac{m_{B_d} f_{B_d}^2 \hat{B}_{B_d}}{m_{B_s} f_{B_s}^2 \hat{B}_{B_s}} \left(\frac{\lambda}{1 - \frac{\lambda^2}{2}} \right)^2 \frac{(1 - \bar{\rho})^2 + \bar{\eta}^2}{\left(1 + \frac{\lambda^2}{1 - \frac{\lambda^2}{2}} \bar{\rho} \right)^2 + \lambda^4 \bar{\eta}^2}. \quad (1.7)$$

Using the ratio $\frac{\Delta m_d}{\Delta m_s}$ instead of Δm_d and Δm_s separately, exploits the fact that $\xi = f_{B_s} \sqrt{\hat{B}_{B_s}}/f_{B_d} \sqrt{\hat{B}_{B_d}}$ is better determined from lattice QCD than the individual quantities entering into its expression. The measurement of the ratio $\frac{\Delta m_d}{\Delta m_s}$ gives a similar type of constraint as Δm_d , on the length of the side AB of the Unitarity triangle.

Despite the fact that the B_s oscillation has already been very precisely measured at the Tevatron, one of the first goals of the LHCb experiment is to study it. Indeed it will be used as a control channel (for tagging, time acceptance, etc...) for other analyses, for example the ϕ_s measurement (see Section: 1.6.2). The golden channel for B_s oscillations measurement is $B_s \rightarrow D_s \pi$. With an integrated luminosity of 2 fb^{-1} (corresponding to one nominal year of data taking) the expected statistical precision on Δm_s is 0.008 ps^{-1} [17]. The current statistical and systematic errors on the measurement of Δm_s at CDF are 0.10

$\text{ps}^{-1}(\text{stat})$ and $0.07 \text{ ps}^{-1}(\text{syst})$ [18]. The decay mode $B_s \rightarrow D_s \rho(770)$ can also be used for the same purpose too (see Chapter 7).

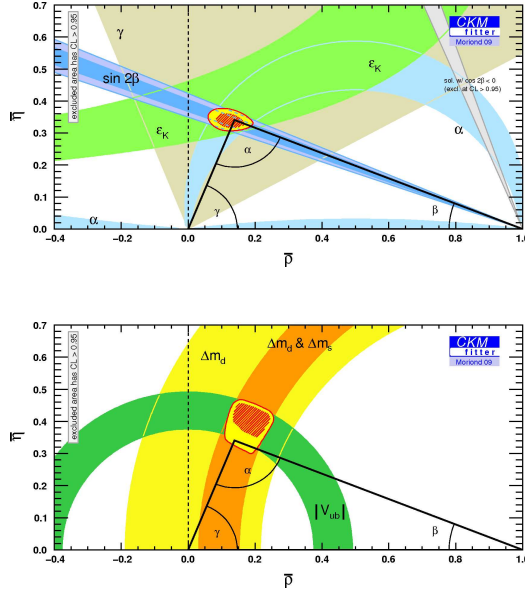


Figure 1.4: Allowed regions for $\bar{\rho} - \bar{\eta}$, or by the measurement of CP violating quantities ($\alpha, \beta, \gamma, \epsilon_K$) (left plot) and as given by the measurements of CP conserving quantities ($\Delta m_s, \Delta m_d, \dots$) (right plot). The closed contours show the 68% and 95% probability regions for the triangle apex, while the colored zones are the 95% probability regions for each individual constraint. The experimental inputs are updated including the most recent results presented at the Moriond 2009 conference [12].

- ϵ_K

Indirect CP violation in the $K^0 - \bar{K}^0$ system is usually expressed in terms of the ϵ_K parameter, which is the fraction of CP -violating component in the mass eigenstates. In the SM, the following equation is:

$$\epsilon_K = C_\epsilon A^2 \lambda^6 \bar{\eta} \times \left[-\eta_1 S(x_c) \left(1 - \frac{\lambda^2}{2} \right) + \eta_2 S(x_t) A^2 \lambda^4 (1 - \bar{\rho}) + \eta_3 S(x_c, x_t) \right] \hat{B}_K \quad (1.8)$$

where $C_\epsilon = \frac{G_F^2 f_K^2 m_K m_W^2}{6\sqrt{2}\pi^2 \Delta m_K}$. $S(x_i)$ and $S(x_i, x_j)$ are the appropriate Inami-Lim functions [6] depending on $x_q = m_q^2/m_W^2$, including the next-to-leading order QCD corrections [9, 11, 16]. An important theoretical uncertainty comes from the non-perturbative QCD bag parameter

\hat{B}_K , that is evaluated from lattice QCD calculations. The constraint brought by the measurement of ϵ_K corresponds to an hyperbola in the $(\bar{\rho}, \bar{\eta})$ plane.

- ***CP* violation measurements in the *B* sector**

The advent of the *B*-factories has allowed the measurement of many observables related to the Unitarity Triangle angles. The studied decays and constrained quantities are briefly listed below:

- $\sin 2\beta$, the first *CP*-violating quantity measured by the *B*-factories, can be determined from the mixing induced *CP* asymmetry in $b \rightarrow c\bar{c}s$ decays. The golden observable is $A_{J/\Psi K^0}$ in $B_d^0 \rightarrow J/\Psi K_S(K_L)$ decays, which has a very small theoretical uncertainty. It is now a precision measurement : $\sin 2\beta = 0.681 \pm 0.025$ [59].
- the angle α is constrained by the study of $B \rightarrow \pi\pi$, $B \rightarrow \rho\rho$ and $B \rightarrow \rho\pi$ decays, the current value is : $\alpha = (88_{-5}^{+6})^\circ$ [59].
- the angle γ , is measured using the interference between $b \rightarrow c\bar{u}s$ and $b \rightarrow u\bar{c}s$ transitions, which occurs in several $B \rightarrow DK$ decays. The present combination obtained by the CKMfitter group [12] is : $\gamma = (77_{-30}^{+27})^\circ$.
- the combination of Unitarity Triangle angles $2\beta + \gamma$, is constrained using $B^0 \rightarrow D\pi$, $B^0 \rightarrow D^*\pi$, $B^0 \rightarrow D\rho$ and $B^0 \rightarrow DK^0\pi$ decays;
- $\cos 2\beta$ can be determined from $B \rightarrow J/\psi K^{*0}(K_S\pi^0)$ and $B^0 \rightarrow D^0\rho^0$ decays. These measurements do not give a very precise measurement of the phase β , but are useful in removing the ambiguity between β and $\pi/2 - \beta$ that remains when only when $\sin 2\beta$ is measured [59].

If these observables were perfectly determined, each of them would be represented by a curve in the $\bar{\rho} - \bar{\eta}$ plane. If particle physics was only explained by the Standard Model, all these curves would intersect in one point, $(\bar{\rho}, \bar{\eta})$ the apex of the Unitarity Triangle. Due to the presence of experimental and theoretical errors on the various constrains used, the region in which the apex of the Unitarity Triangle is located has to be known with a certain probability. The left plot of Figure: 1.4 shows the various constraints from the measured angles (α, β, γ) . The information from *CP* conserving quantities such as, Δm_d and Δm_s , as well as the direct *CP* violation measurements in the kaon sector are shown in right plot of Figure: 1.4.

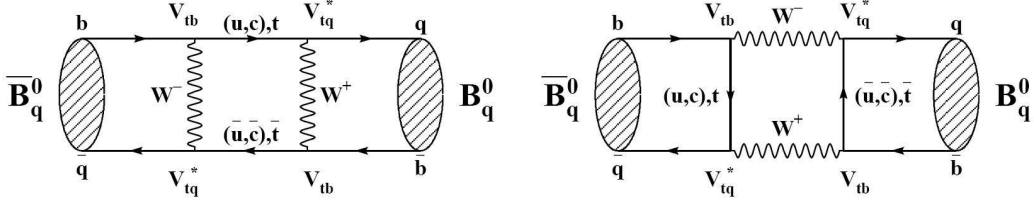


Figure 1.5: Diagrams responsible for the $B_q - \bar{B}_q$ mixing, within the Standard Model ($q = s, d$).

1.6.2 ϕ_s , beyond the Standard Model

Although the Standard Model is very successful, there are reasons to think that it is not more than an effective theory valid at low energies [19]. This would imply the existence of new particles or new couplings at higher energy scales. Besides direct searches, it is possible to look for New Physics measuring weak CP violating phases. CP asymmetries in B decays originate from the interference of amplitudes which have different properties through CP transformation. In the Standard Model the $B_s^0 - \bar{B}_s^0$ mixing phase $\phi_s^{SM} = -2\beta_s$ is predicted to be very small 0.0368 ± 0.0017 rad [20]. Since box diagrams are involved in the process (see Figure: 1.5) it is plausible that particles beyond the Standard Model enter in these box diagrams and affect the ϕ_s value: $\phi_s = \phi_s^{NP} + \phi_s^{SM}$. LHCb will measure ϕ_s by studying the time dependent asymmetry in the $B_s^0 \rightarrow J/\psi\phi$ decay channel.

1.6.3 $\phi_s + \gamma$

When trying to measure the weak phase $2\beta + \gamma$ in various neutral B decays for example, $B \rightarrow D\pi$ and $B \rightarrow D\rho(770)$ an important quantity to be taken into account is $r = \frac{|A(b \rightarrow u)|}{|A(b \rightarrow c)|}$ [21]. The channel dependent parameter r gives the sensitivity to the weak phase γ . If we assume that these decays are dominated by pure tree diagrams (we neglect W -exchange contributions [22]), from the point of view of the strong interaction the two decays (with $b \rightarrow u$ or $b \rightarrow c$) are the same. The ratio r will thus be governed by the the corresponding CKM matrix elements:

$$r \sim \left| \frac{V_{ub}V_{cd}^*}{V_{ud}V_{cb}^*} \right| = 0.02 \quad (1.9)$$

At LHCb, B_s mesons will be produced in very large quantities. The decays of $B_s \rightarrow D_s K$ which will be accessible at LHCb, can be used to measure $\phi_s + \gamma$, the same way $B \rightarrow D\pi$ or $B \rightarrow D\rho(770)$ are used to measure $2\beta + \gamma$. It is important to mention the enhancement of the sensitivity to the weak phase, when going from the neutral B system to the B_s system:

$$r \sim \left| \frac{V_{ub}V_{cs}^*}{V_{us}V_{cb}^*} \right| = 0.4 \quad (1.10)$$

Similarly to what has been said for $B_s \rightarrow D_s\rho(770)$, the decay mode $B_s \rightarrow D_s K^*(892)$ can be used to increase the precision of this measurement (see Chapter: 7).

1.6.4 γ extraction under U-spin symmetry

Unlike α and β , the angle α is now also reasonably well constrained (see Section: 1.6.1) but the angle γ is still only poorly constrained. One way is to measure γ through the interference in decay and mixing using modes such as $B_d \rightarrow D\pi, D\rho(770)$ for $2\beta + \gamma$ and $B_s \rightarrow D_s K, D_s K^*(892)$ for $\phi_s + \gamma$. These measurements suffer for the existence of multiple solutions or ambiguities¹. Reducing these ambiguities, takes to know the strong phases. One possible approach is to relate the $B_s \rightarrow D_s K, D_s K^*(892)$ and $B_d \rightarrow D\pi, D\rho(770)$ modes through the so-called U-spin symmetry [23]. U-spin is a $SU(2)$ subgroup of the flavour $SU(3)$ symmetry. Under this symmetry, the pair of quarks (d, s) is a doublet, the same way the pair (d, u) is a doublet under the isospin symmetry. Using this symmetry, one can make the assumption that for example the strong phases contributing to $B_s \rightarrow D_s K, D_s K^*(892)$ are the same as the one contributing to $B_d \rightarrow D\pi, D\rho(770)$. The combination of the B_d and B_s channels allows a simultaneous determination of the phases δ_q and $\phi_q + \gamma$ from time dependent asymmetries, obtained from decay rates [24]. Results obtained with this method have to take into account the uncertainty due to the fact that U-spin is not an exact symmetry. It is broken due to the mass difference between the d and s quarks. The related systematical uncertainty is estimated to be of the order of 30% [25]. A possible experimental

¹In the formalism used to extract these weak phases using these modes [24], ambiguities appear from the observables : $\cos(\delta_q) \sin(\phi_q + \gamma)$ and $\sin(\delta_q) \cos(\phi_q + \gamma)$. Where, $\phi_q = 2\beta$ for the B_d system, and $\phi_q = \phi_s$ for the B_s system and δ_q with $q = d, s$ are the strong phases.

test is to compare the pion($u\bar{d}$) and the kaon($u\bar{s}$) decay constants, f_π and f_K [59].

1.7 $B_s^0 \rightarrow D_s^- \rho(770)^+$ and $B_s^0 \rightarrow D_s^- K(892)^{*+}$ branching ratio estimation

The branching ratios corresponding to the decay channels $B_s^0 \rightarrow D_s^- \rho(770)^+$ and $B_s^0 \rightarrow D_s^- K(892)^{*+}$ are not measured yet. To compute the expected yields at LHCb we extrapolate their branching ratio from existing measurements. We show in this section the formalism that allow us to do so within the Standard Model. We will first discuss the effective Hamiltonian describing these non leptonic B decays, which we assume are dominated by tree diagrams. Then we show how this amplitude transition can be rewritten in terms of measurable quantities such as form factors and decay constants. Finally we make the numerical extrapolation.

1.7.1 Low energy effective Hamiltonian

Non-leptonic B decays can be mediated by $b \rightarrow q_1 \bar{q}_2 d(s)$ quark-level processes, with $q_1 q_2 \in \{u, d, c, s\}$. There are two kinds of topologies contributing to such decays: tree level and penguins diagrams. According to the final state flavour content, the $b \rightarrow q_1 \bar{q}_2 d(s)$ can be classified as follows:

- $q_1 \neq q_2 \in \{u, c\}$: *only* tree diagrams contribute.
- $q_1 = q_2 \in \{u, c\}$: tree *and* penguins diagrams contribute.
- $q_1 = q_2 \in \{d, s\}$: *only* penguin diagrams contribute.

To analyze non-leptonic B decays theoretically, we use low-energy effective Hamiltonians [26]. There are calculated by means of "Operator Product Expansion" [27]. Transition yield transition matrix elements can thus be written as follows:

$$\langle f | \mathcal{H}_{eff} | i \rangle = \frac{G_F}{\sqrt{2}} \lambda_{CKM} \sum_k C_k(\mu) \langle f | Q_k(\mu) | i \rangle \quad (1.11)$$

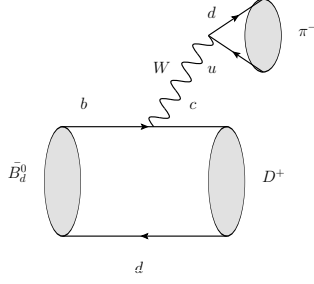


Figure 1.6: Feynman diagram contribution to the tree-level $B_d^0 \rightarrow D^+ \pi^-$ decay.

The technique of the Operator Product Expansion (OPE) allows to separate the short-distance contributions to this transition amplitude from the long-distance one. The short distance contributions are described by perturbative quantities $C_k(\mu)$, the so called "Wilson coefficient functions". The long-distance ones are parametrized by the non perturbative quantities $\langle f | Q_k(\mu) | i \rangle$, known as "hadronic matrix elements". G_F is the Fermi constant, whereas λ_{CKM} is the relevant matrix element from the CKM matrix, μ denotes the appropriate renormalization scale separating the long-distance and the short-distance contributions. Q_k are local operators, they are generated by electroweak and QCD interaction and govern "effectively" the decay in question. The Wilson coefficients $C_k(\mu)$ can be considered as scale-dependent coupling related to the vertices described by Q_k .

To illustrate this formalism, we consider the decay $B_d^0 \rightarrow D^+ \pi^-$ (see the Feynman diagram of Figure: 1.6). This transition originates from a $b \rightarrow c \bar{u} d$ quark-level process, it is a pure "tree" decay. The leading order Feynman diagram at the quark and electroweak level contributing to $B_d^0 \rightarrow D^+ \pi^-$ yields to the following decay amplitude:

$$-\frac{g_2^2}{8} V_{ud}^* V_{cb} [\bar{d}_\alpha \gamma^\nu (1-\gamma_5) u_\alpha] \left[\frac{g_{\mu\nu}}{k^2 - M_W^2} \right] [c_\beta \gamma^\mu (1-\gamma_5) b_\beta]$$

Where, g_2 is the $SU(2)_L$ gauge coupling, and $V_{ud}^* V_{cb}$ the corresponding elements of the CKM matrix. μ and ν are the Lorentz indices, and M_W the mass of the W gauge boson. α, β denote the color indices of the $SU_C(3)$

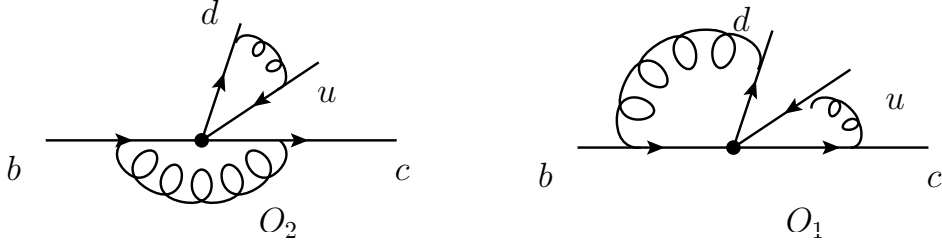


Figure 1.7: Factorizable QCD corrections in the effective theories (left diagram), non-factorizable QCD corrections in the effective theories (right diagram).

gauge group of QCD. Since the four-momentum that is carried by the W satisfies $k^2 \sim m_B^2 \ll M_W^2$, we may write:

$$\frac{g_{\mu\nu}}{k^2 - M_W^2} \rightarrow -\frac{g_{\mu\nu}}{M_W^2} \equiv -\left(\frac{8G_F}{\sqrt{2}g_2^2}\right)g_{\mu\nu} \quad (1.12)$$

This is called "integrating out" the W boson from the theory. The same result can be reached using directly an effective Hamiltonian instead of the full Standard Model Lagrangian:

$$\mathcal{H}_{eff} = \frac{G_F}{\sqrt{2}}V_{ud}^*V_{cb}[\bar{d}_\alpha\gamma_\mu(1-\gamma_5)u_\alpha][\bar{c}_\beta\gamma^\mu(1-\gamma_5)b_\beta] \quad (1.13)$$

$$\mathcal{H}_{eff} = \frac{G_F}{\sqrt{2}}V_{ud}^*V_{cb}(\bar{d}_\alpha u_\alpha)_{V-A}(\bar{c}_\beta b_\beta)_{V-A} \equiv \frac{G_F}{\sqrt{2}}V_{ud}^*V_{cb}O_2 \quad (1.14)$$

Effectively the process $b \rightarrow c\bar{u}d$ is now described by the "current-current" operator O_2 . Up to this point, all QCD corrections were neglected. *Factorizable* QCD corrections are shown in the left diagram of Figure: 1.7 and *non-factorizable* QCD corrections are illustrated in the right diagram of the same figure. The *non-factorizable* QCD corrections generate a second current-current operator, O_1 , through "operator mixing", it is given by:

$$O_1 \equiv [\bar{d}_\alpha\gamma_\mu(1-\gamma_5)u_\beta][\bar{c}_\beta\gamma^\mu(1-\gamma_5)b_\alpha] \quad (1.15)$$

A low-energy effective Hamiltonian of the following structure is obtained:

$$\mathcal{H}_{eff} = \frac{G_F}{\sqrt{2}}V_{ud}^*V_{cb}[C_1(\mu)O_1 + [C_2(\mu)O_2] \quad (1.16)$$

1.7.2 Factorization of hadronic matrix elements

We consider once again the decay $B_d^0 \rightarrow D^+ \pi^-$. To evaluate the transition amplitude, we encounter the hadronic matrix elements of the operators between the $\langle \pi^- D^+ |$ and the final state and the initial state $|B^0\rangle$. Using the $SU(N_c)$ color algebra relation:

$$T_{\alpha\beta}^a T_{\gamma\delta}^a = \frac{1}{2}(\delta_{\alpha\delta}\delta_{\beta\gamma} - \frac{1}{N_C}\delta_{\alpha\beta}\delta_{\gamma\delta}) \quad (1.17)$$

where T are the generators of the $SU(N_C)$ group, and N_C the number of colors, it can be shown that after rewriting O_1 , the effective Hamiltonian is:

$$\begin{aligned} \langle \pi^- D^+ | \mathcal{H}_{eff} | \bar{B}_d^0 \rangle &= \frac{G_F}{\sqrt{2}} V_{ud}^* V_{cb} [a_1 \langle \pi^- D^+ | (\bar{d}_\alpha u_\alpha)_{V-A} (\bar{c}_\beta b_\beta)_{V-A} | \bar{B}_d^0 \rangle \\ &+ 2C_1 \langle \pi^- D^+ | (\bar{d}_\alpha T_{\alpha\beta}^a u_\beta)_{V-A} (\bar{c}_\gamma T_{\gamma\delta}^a b_\delta)_{V-A} | \bar{B}_d^0 \rangle] \end{aligned} \quad (1.18)$$

with:

$$a_1 = C_1/N_C + C_2 \sim 1. \quad (1.19)$$

The quantity a_1 expressed in Equation: 1.19 is a phenomenological "color factor", which governs the "color-allowed" tree level decays as $\bar{B}_d^0 \rightarrow D^+ \pi^-$ [28], where the color indices of the π^- meson and $B_d^0 - D^+$ system run independently from each other in the corresponding leading order. The hadronic matrix elements of Equation: 1.18 can now be *factorized* in terms of a decay constant, describing a π mesons "popping out" from the vacuum, a form factor describing the $B \rightarrow D$ transition and a kinematical term:

$$\begin{aligned} &\langle \pi^- D^+ | (\bar{d}_\alpha u_\alpha)_{V-A} (\bar{c}_\beta b_\beta)_{V-A} | \bar{B}_d^0 \rangle |_{\text{fact}} \\ &= \langle \pi^- | [\bar{d}_\alpha \gamma_\mu (1 - \gamma_5) u_\alpha] | 0 \rangle \langle D^+ | \bar{c}_\beta \gamma^\mu (1 - \gamma_5) b_\beta | \bar{B}_d^0 \rangle \quad (1.20) \\ &= \underbrace{if_\pi}_{\text{Decay constant}} \times \underbrace{F_0^{B \rightarrow D}(M_\pi^2)}_{B \rightarrow D \text{ Form factor}} \times \underbrace{(M_B^2 - M_D^2)}_{\text{Kinematical factor}} \quad (1.21) \end{aligned}$$

$$\langle \pi^- D^+ \bar{B}_d^0 | (\bar{u}_\alpha T_{\alpha\beta}^a)_{V-A} (\bar{c}_\gamma T_{\gamma\delta}^a)_{V-A} | \bar{B}_d^0 \rangle |_{\text{fact}} = 0. \quad (1.22)$$

An intuitive way of explaining the factorization hypothesis is provided by the *color transparency* argument, proposed for the first time by Bjorken [29]. The emitted meson is defined as the one that does not contain the B spectator quark. In the hypothesis that the emitted meson is produced with a large momentum its two quarks (that have opposite color) will have a large momentum along the meson flight direction and a relatively small momentum in the transverse direction. The exchange of soft gluons with other fermionic lines is hence suppressed because the gluon can not discriminate the two quarks inside the mesons that appears as a color singlet. In this assumption, the emitted meson creation can then be considered in first approximation as a stand alone process with respect to the rest of the decay. Factorization uses the fact that the emitted meson is light, for example the π , it is not valid in the case of a heavy emitted meson like the D (for example $B \rightarrow D\bar{D}$ decays). Nonetheless, factorization is useful for making first order approximation as it is the case here.

1.7.3 Branching ratio estimation

When comparing the branching ratios of $\bar{B}_d^0 \rightarrow D^+ \rho(770)^-$ and $\bar{B}_d^0 \rightarrow D^+ \pi^-$ which are equal to $(7.7 \pm 1.3) \times 10^{-3}$ and $(2.68 \pm 0.13) \times 10^{-3}$ respectively [59], it appears that the observed difference is due in large part to the difference in the decay constants of the $\rho(770)$ and the π . Making such measurement as performed by CLEO [33] allows to test the factorization approach in the case of "pure" tree level diagrams:

$$\frac{\Gamma(\bar{B}_d^0 \rightarrow D^+ \rho(770)^-)}{\Gamma(\bar{B}_d^0 \rightarrow D^+ \pi^-)} \sim \left[\frac{f_\rho}{f_\pi} \right]^2 = R \quad (1.23)$$

Where, f_{π^+} is the pion decay constant, this precisely measured quantity is equal to 130.7 ± 0.1 MeV, it can be extracted from the leptonic decay: $\pi^+ \rightarrow \mu^+ \nu_\mu$ [59]. The vector resonance $\rho(770)^+$ decay constant $f_{\rho(770)^+}$ can be measured from $e^+ e^- \rightarrow \rho^0$ decays or τ decay...

Even though $\bar{B}_s^0 \rightarrow D_s^+ \rho(770)^-$ events were observed at CDF, the corresponding branching ratio has not been measured yet. Exchanging the quark spectator d with an s quark, in the $B \rightarrow D$ leading to the $B_s \rightarrow D_s$, is not expected to affect strongly the form factor $F_0^{B \rightarrow D}$ appearing in equation 1.21. Therefore, the difference in the branching ratios of $\bar{B}_s^0 \rightarrow D_s^+ \pi^-$

and $\bar{B}_s^0 \rightarrow D_s^+ \rho(770)^-$ will arise yet again from the difference in the decay constants f_π and $f_{\rho(770)}$. Using these arguments, we extrapolate from the existing measurement of the branching ratio of $\bar{B}_s^0 \rightarrow D_s^+ \pi^-$ equal to $(3.2 \pm 0.9) \times 10^{-3}$, performed at CDF [31], to the branching ratio of $\bar{B}_s^0 \rightarrow D_s^+ \rho(770)^-$ together with their errors and we obtain:

$$\begin{aligned} Br(\bar{B}_s^0 \rightarrow D_s^+ \rho(770)^-) &= R \times Br(\bar{B}_s^0 \rightarrow D_s^+ \pi^-) \\ Br(\bar{B}_s^0 \rightarrow D_s^+ \rho(770)^-) &= (9.2 \pm 3.0) \times 10^{-3}. \end{aligned} \quad (1.24)$$

CDF measured recently the branching fraction $Br(\bar{B}_s^0 \rightarrow D_s^+ K^-)/(\bar{B}_s^0 \rightarrow D_s^+ \pi^-)$ [32]. This value $(0.107 \pm 0.019 \pm 0.008)$ is used to estimate the branching ratio of $\bar{B}_s^0 \rightarrow D_s^+ K(892)^*-$, which has not yet been observed.

$$\begin{aligned} Br(\bar{B}_s^0 \rightarrow D_s^+ K(892)^*-) &= \frac{Br(\bar{B}_s^0 \rightarrow D_s^+ K^-)}{(\bar{B}_s^0 \rightarrow D_s^+ \pi^-)} \times R \times Br(\bar{B}_s^0 \rightarrow D_s^+ \pi^-) \\ Br(\bar{B}_s^0 \rightarrow D_s^+ K(892)^*-) &= \frac{Br(\bar{B}_s^0 \rightarrow D_s^+ K^-)}{(\bar{B}_s^0 \rightarrow D_s^+ \pi^-)} \times Br(\bar{B}_s^0 \rightarrow D_s^+ \rho(770)^-) \\ Br(\bar{B}_s^0 \rightarrow D_s^+ K(892)^*-) &= (0.89 \pm 0.33) \times 10^{-3}. \end{aligned} \quad (1.25)$$

These branching fraction estimates will be used in Chapter 7 to predict the number of signal events for LHCb.

Chapter 2

The LHCb detector



Johann Sebastian Bach - BWV 565
Toccata und fugue in d-Moll

The Large Hadron Collider (LHC) is one of the four large experiments installed on the LHC, at CERN. It is dedicated to study CP violation and rare decays of beauty particles. The LHCb experiment is now fully operational and will start taking data in fall 2009.

2.1 The Large Hadron Collider

The Large Hadron Collider (LHC) is a 27 km circumference, high luminosity proton-proton collider with a nominal center-of-mass energy of $\sqrt{s} = 14$ TeV. A change of technology from LEP to LHC was necessary, since the TeV scale can not be reached using e^+e^- circular colliders, due to high energy loss via synchrotron radiation. A proton collider is thus preferred although the hadronic background environment makes the experiment more difficult. The 27 km tunnel that housed the LEP accelerator and its injection scheme is reused. The accelerating complex of the Super Proton Synchrotron (SPS) is used as injector for the LHC. The proton bunches are accelerated in a linear accelerator at the Meyrin site (*Linac*) up to 50 MeV. Then, two circular

CERN Accelerator Complex

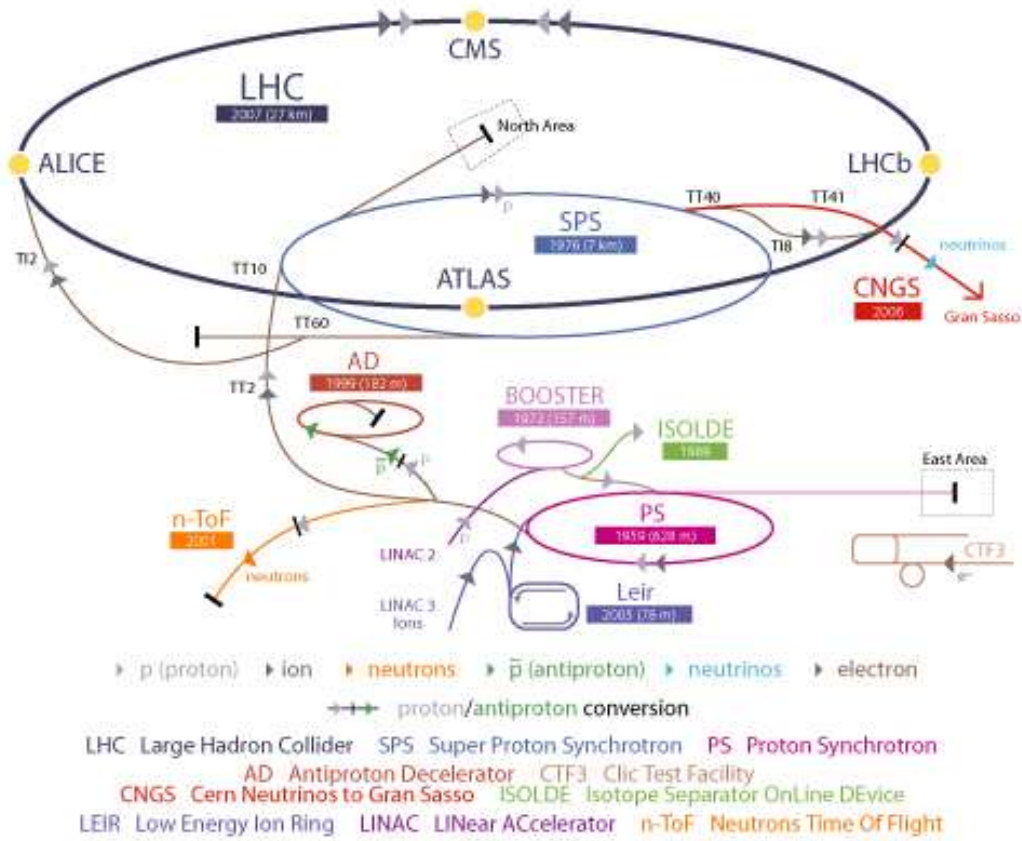


Figure 2.1: The LHC complex with the main experiment [37].

accelerators boost them to 1 GeV in the *Booster* and then to 26 GeV in the Proton Synchrotron (PS) before they enter the SPS, where they reach an energy of 450 GeV and enter the LHC via two tunnels in TI2 and TI8 (see Figure: 2.1). The final energy of 7 TeV is limited by the magnetic field of 8.34 Tesla in the super-conducting magnets.

Luminosity The luminosity at a given interaction point is expressed by:

$$\mathcal{L} = \frac{N_1 N_2 k_b f_\gamma F}{4\pi \beta^* \epsilon} \quad (2.1)$$

where N_1 and N_2 are about $\sim 10^{11}$ are the number of protons per bunch, k_b the number of bunch crossing at the considered interaction point, $f_\gamma = 11.25$

Total	$\sigma_{tot} = 100 \text{ mb}$
Inelastic	$\sigma_{inel} = 5.5 \text{ mb}$
$c\bar{c}$	$\sigma_{c\bar{c}} = 3.5 \text{ mb}$
$b\bar{b}$	$\sigma_{b\bar{b}} = 500 \mu\text{b}$

Table 2.1: Assumed cross sections [35] at $\sqrt{s} = 14 \text{ TeV}$.

kHz the revolution frequency and $\gamma = E_p/m_p$. The emittance $\epsilon = 3.75\mu \text{ mrad}$ measures the compactness of the beam and the betatron function $\beta^*=0.5 \text{ m}$ measures the ability of the magnets to focus the beam at the interaction point. Finally, F is a factor which takes into account the crossing angle of the two beams. An important number for the design of the electronics of all the LHC experiments is the bunch crossing frequency $k_b f = 40 \text{ MHz}$. This defines the basic clock cycle of the front-end electronics. The maximal luminosity at the LHC is $\mathcal{L} = 10^{34} \text{ cm}^{-2} \text{ s}^{-1}$ which will be accessible for ATLAS and CMS. For reasons to be explained below, the LHCb experiment will run at about $\mathcal{L}=2 \times 10^{32} \text{ cm}^{-2} \text{ s}^{-1}$.

pp interactions The relevant cross section for the LHC are given in Table: 2.1. The inelastic cross-section σ_{inel} is extrapolated from the UA1, CDF and D0 experiments [34], they are affected by large uncertainties. The total inelastic cross section σ_{inel} defines the average number of interactions per bunch crossing:

$$\langle N \rangle = \frac{\mathcal{L} \sigma_{inel}}{k_b f} \quad (2.2)$$

The average number of inelastic pp interactions ("primary vertices") is thus ~ 17 at ATLAS and CMS at nominal luminosity and 0.37 at LHCb (see Figure: 2.2). This value is chosen to avoid having several pp interactions in the same events. At this luminosity there are interactions in 30 % of the bunch crossing and the effective interaction rate is about 12 MHz.

The $b\bar{b}$ cross section maybe between 175 μb and 950 μb depending on the value of badly known parameters [34]. The value of 500 μb is a mean value assumed for the $b\bar{b}$ production at the LHC experiments. The dominant $b\bar{b}$ production mechanism in pp collisions is the fusion of two or more gluons radiated from the constituent quarks of the protons. This leads to an approximately flat distribution in rapidity, $\eta = -\ln \tan(\theta/2)$, and hence an angular distribution peaked at low polar angles. The direction of the two

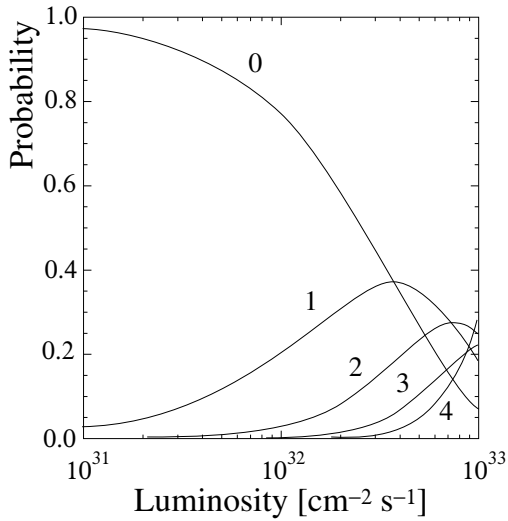


Figure 2.2: Probabilities for having a number of inelastic pp interactions at as a function of the luminosity

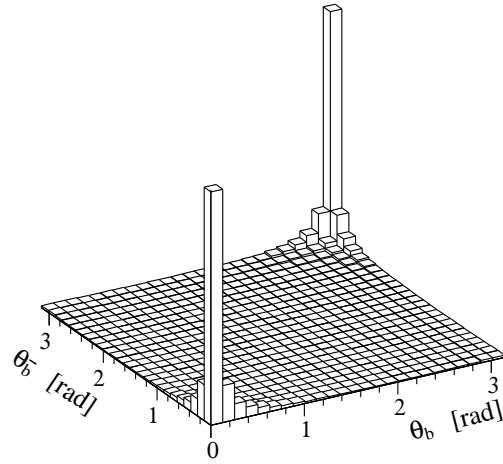


Figure 2.3: Polar angles of b and \bar{b} hadrons calculated by PYTHIA.

hadrons is very correlated at the LHC. The Figure: 2.3 shows the polar angles θ of the two b hadrons. The two peaks corresponds to the $b\bar{b}$ pairs flying in either direction of the beam axis. Consequently a dedicated b experiment should cover low polar angles.

2.2 LHCb

The LHCb detector is a forward single arm spectrometer, it is housed at the interaction region IP8. The angular coverage is 10-300 mrad in the horizontal plane and 10-250 mrad in the vertical plane. Equivalently, the acceptance corresponds to a range in pseudo-rapidity of $1.9 < \eta < 4.9$, the dimension of the detector are approximatively of $(x = \pm 6\text{m}) \times (y = \pm 5\text{m}) \times (z = 20\text{m})$. As shown if Figure: 2.4, the LHCb detector is composed of several subdetectors, listed here from the left (upstream) to right (downstream):

- VERTex LOcator (VELO),
- First Ring Imaging Cherenkov counter (RICH1),
- Trigger Tracker (TT),

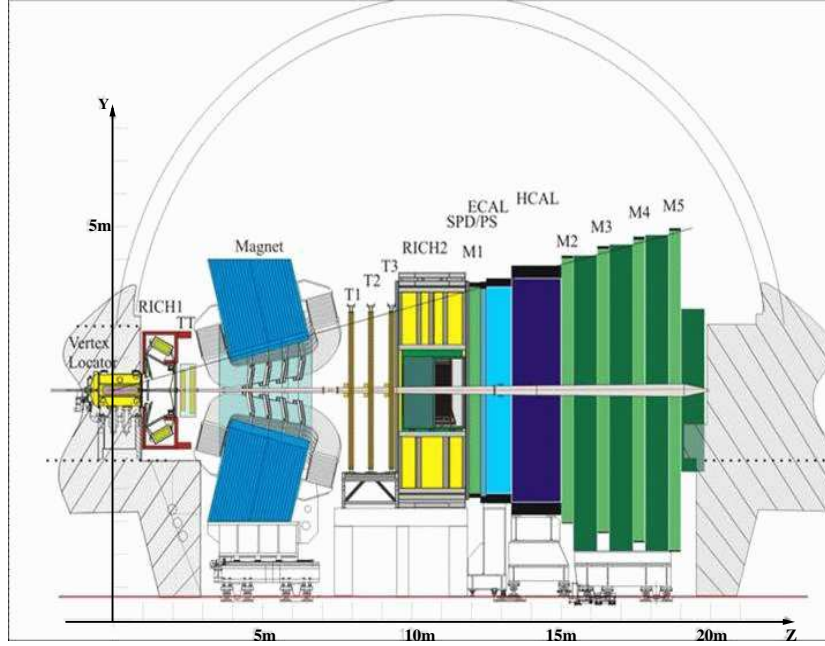


Figure 2.4: The LHCb detector

- Magnet,
- Tracking stations (T1, T2, T3), consisting of an inner part, the Inner Tracker (IT), an outer part and the Outer Tracker(OT);
- Second Ring Imaging Cherenkov counter (RICH2);
- First muon station (M1);
- Scintillating Pad/PreShower detector (SPS/PS);
- Electromagnetic calorimeter(ECAL);
- Hadronic calorimeter(HCAL);
- Remaining muon stations (M2,M3, M4, M5).

Their respective roles will be detailed in the following sections. The beam pipe crosses the whole detector setup except the VELO which is enclosed in a vacuum vessel connected to the beam pipe (see Figure: 2.5). The sub-detectors can be categorized into tracking devices, used to determine the track trajectories and vertices, and particle identification(PID) detectors, used to identify the various particles:

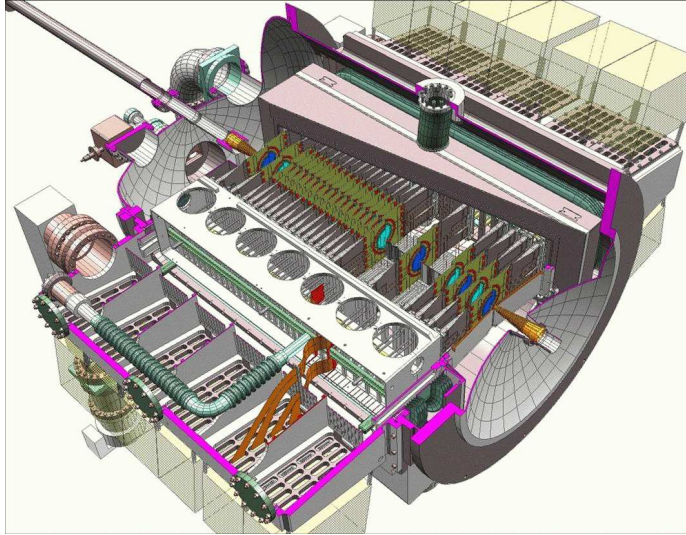


Figure 2.5: The VELO sub detector, showing the vacuum vessel containing the sensors in the center, and readout electronics on either side of the beam line.

- **Tracking:** VELO, TT, Magnet, IT, OT, muon chambers.
- **PID:** RICH1, RICH2, ECAL, HCAL, muon chambers.

2.3 VELO

The role of the VERTex LOcator is to provide precise measurements of the charged particles close to the interaction region [42]. These measurements are used to reconstruct primary vertices and decay vertices. The VELO provides information on backward tracks used together with forward tracks to identify primary vertices. The forward VELO tracks determine the direction of charged particles to be later matched to the track segment found in the other tracking stations. An accurate measurement of track parameters is required to determine the time of flight of long-lived particles in B mesons. The VELO uses silicon strip sensors placed very close to the beam (8mm), perpendicular to the beam direction. The whole system is contained inside a vacuum vessel with a Roman pot system to be able to move away from the beam the two detectors halves during the beam injection, and to avoid radiation damage. The VELO sensors are placed in a secondary vacuum

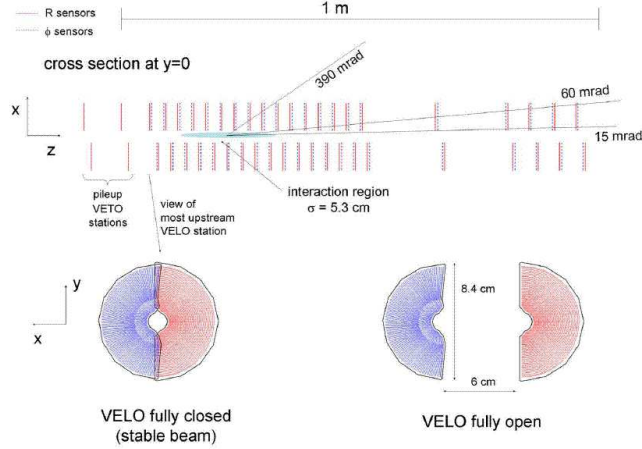


Figure 2.6: Cross section in (x, z) plane of the VELO silicon sensors at $y = 0$, with the detector in the fully closed positions. The front face of the first modules is also illustrated in both the closed and the open positions. The two pile-up veto stations are located upstream of the VELO sensors.

separated by a thin aluminum corrugated foil. This so-called RF foil acts as a radio frequency (RF) shield and protects the electronics from electromagnetic pickup from the LHC beams. The VELO consists on 21 stations spread along the beam line each with two different types of silicon sensors: one measures the radial r coordinate with circular strips centered around the beam axis and the second one measures the azimuthal ϕ coordinate with radial strips. The half-disc sensors, shown in Figure: 2.6 are arranged in pairs mounted on the side of the beam pipe.

2.4 Magnet

The spectrometer's dipole is located near the interaction region. The momentum of the tracks is determined from their curvature in the magnetic field, which has a bending power characterized by the total integrated field $\int Bdl \sim 4\text{mT}$. The main component of the field is oriented along the vertical y axis; it is shown as a function of the z coordinate in Figure: 2.7, where the area of the curve represents the integrated field for B_y . The magnet's bending power enables precise measurements of the momentum. For instance, a momentum resolution of $\delta p/p \sim 0.4\%$ is achieved for high-momentum long tracks with $p \sim 40 \text{ GeV}/c$ [41]. The polarity of the magnet can be reversed in

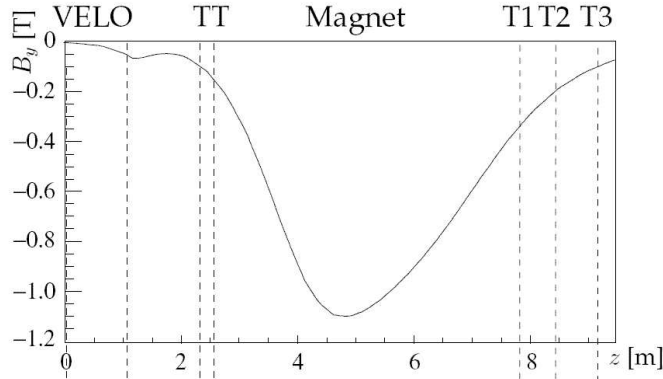


Figure 2.7: The main component of the magnetic field strength B_y , along the z axis.

order to study the systematics induced by possible left-right asymmetries in the detector. This had motivated the choice of a warm magnet rather than superconducting one.

2.5 Tracking system

The trigger tracker(TT) is located downstream of the RICH1 and in front of the entrance of the magnet, at ~ 2.5 m from the interaction region. The deflection of tracks induced by the residual magnetic field in TT can then be used to roughly estimate the momentum of particles. This is sufficient to determine the momentum with 10-40 % accuracy without the use of the other tracking stations T. TT consists of four detection layers grouped in two stations of two layers each, TTa and TTb separated by 27 cm. The layout of one of the detection layers is illustrated in Figure: 2.8. The readout strips are arranged in stereo views to allow the spatial reconstruction, with a vertical orientation to precisely measure the position in the horizontal bending-plane. The first and the fourth layers have vertical strips (X layers, 0 degrees with the y axis) whereas the second and the third have strips rotated by a stereo angle of -5 degrees (U layer) and +5 degrees (V later) respectively ¹. The main purpose of the tracking stations (T1, T2, T3), situated right after

¹The stereo angle is defined here as the angle between the strip's direction and the y axis, in the $x - y$ plane. The angle is *positive* when rotating from the positive x axis to the positive y axis in the transverse plane.

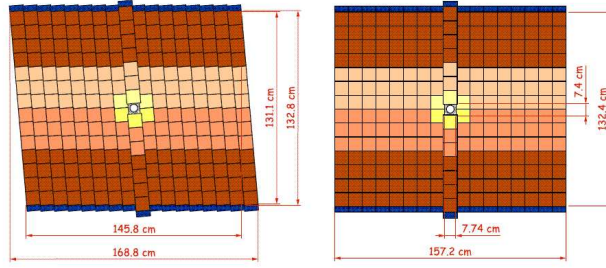


Figure 2.8: Layout of the third TT detection layer. The different readout sectors along a silicon ladder are indicated by different colors.

the magnet, is to provide the different clusters to be used in the reconstruction of long charged tracks in order to measure their momentum. Moreover, the T stations have to provide the direction of the tracks to be used for the reconstruction of the Cherenkov rings. The T measurements are also used as seeds for the reconstruction on the calorimeters and the muon chambers. Each T station consists of two parts: the Inner Tracker(IT) and the Outer Tracker (OT) [43], [44]. This separation is the result of the variation in particle density as a function of polar angles, making it necessary to use two detectors with different granularity. The track multiplicity is expected to be higher at small, angles thus requiring the use of silicon micro-strip sensors. This is the technology used for the IT. At larger polar angles and away from the beam, the particle density will be moderate. This region will be covered by the OT using gas drift chambers, where the choice of the detector is based on the optimization of the cost and spatial resolution.

Inner Tracker The Inner Tracker(IT) covers the inner most region of the T stations which is a cross-shaped area around the beam pipe. An IT station contains four boxes with four layers each. Similarly to the TT station, the layers are arranged in X-U-V-X stereo views with silicon sensors. The area covered by the IT is approximately 120 cm in width and 40 cm in height.

Outer Tracker The Outer Tracker (OT) covers the rest of the area of the T stations, outside of the IT acceptance. As for the IT, the configuration of the detection layers is two stereo layers embraced between the external X layers. The detection layers are made of straw tubes filled with a gas mixture containing 75 % of Ar, 15 % of CF_4 and 10 of % $C0_2$. This composition was

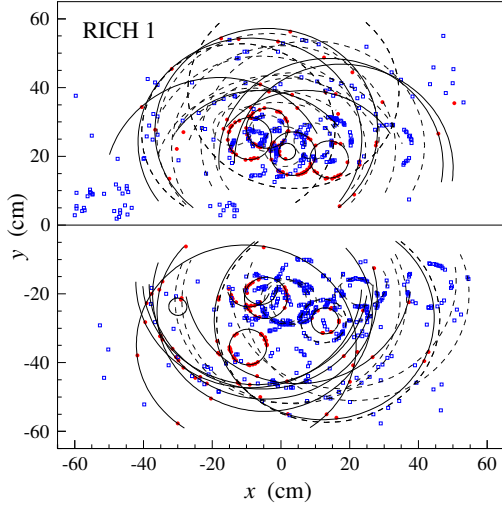


Figure 2.9: A typical LHCb event as seen by RICH 1. Fitted rings are superimposed over the HPD hits, with solid lines for long tracks and dashed lines for other track types.

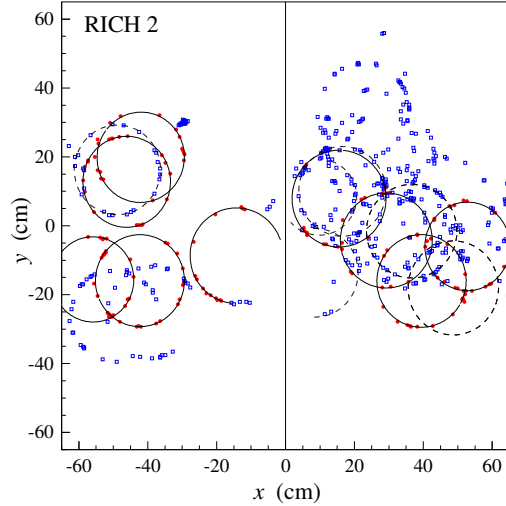


Figure 2.10: A typical LHCb event as seen by RICH 2. Fitted rings are superimposed over the HPD hits, with solid lines for long tracks and dashed lines for other track types.

determined to get a total drift time (or a total signal collection time) well below the maximum 50 ns.

2.6 RICH counters

The Ring Imaging Cherenkov counters (RICH) provide particle identification [39]. This information is required in b -physics analysis for the separation of the decay channels with the same topology, such as $B_q \rightarrow D_q h$ ($q = d, s$ and $h = \pi, K$). Moreover good $\pi - K$ separation is needed for the flavor tagging. The particle identification by the RICH counters must cover the largest momentum spectrum. Two RICH detectors are used at LHCb: the RICH1 located between the VELO and TT, and the RICH2 which is situated between the T stations and the calorimeters. RICH1 identifies particles with the a momentum range between 1 GeV/c and 60 GeV/c and RICH2 provides identification up to 150 GeV/c. The RICH detectors use the Cherenkov effect: when a charged particle goes through a medium with a speed greater than the speed of light in the medium, then an electromagnetic radiation is emitted. By measuring the angle θ_C between the Cherenkov light and

the direction of the particle, one can determine the particle velocity β and thus determine its mass when the momentum is known. The Cherenkov angle θ_C satisfies $\cos\theta_C = \frac{1}{n\beta}$, where n is the refraction index of the radiator medium. In order to observe the Cherenkov light, the condition $n\beta \geq 1$ must be satisfied. The different radiators are then chosen depending on the desired momentum coverage. For instance, for the large momentum range a small refractive index will be used. The radiators used for the RICH1 are silica aerogel ($n = 1.03$) and C_4F_{10} ($n = 1.0014$). For the RICH2 the radiator is CF_4 ($n = 1.0005$). In the RICH detectors mirrors project the light cones as rings onto a plane of photon detectors (Hybrid Photon Detectors, HPDs), where the radius of each ring gives a measurement of the corresponding Cherenkov angle θ_C . A global likelihood analysis is performed to fit at best the rings on the observed patterns, and thus to assign to each track probabilities associated with each mass hypothesis. A typical event in RICH1 and RICH2 is show in Figures: 2.9, 2.10.

2.7 Calorimeters

The calorimetry system identifies photons, electrons and hadrons and measures their position and energy, which are used as input to the Level-0 trigger. A complete description of the performances and the electronics of this system is given in the calorimeters chapter.

2.8 Muons

Muons are the only charged particle likely to cross the calorimeters. They are thus identified by a dedicated muon system, placed behind the calorimeters (M2, M3, M4, M5) with the exception of the M1 station which is located before the SPD [45]. The muon detectors play an important role in the trigger. In the off-line reconstruction the muon system is used to identify muons, starting from the track found in the T stations and extrapolating them to the muon stations to confirm the muon hypothesis. The muon stations are equipped with multi-wire proportional chambers (MWPC), divided in four regions with different pad granularity. The muon shield consists of the calorimeters and four layers of 80 cm thick iron walls.

2.9 Trigger system

The bunch frequency at the LHCb is 40 MHz. For a nominal luminosity at LHCb of $2 \times 10^{32} \text{ cm}^{-2}\text{s}^{-1}$, the bunch crossing with visible pp interactions are expected to contain a rate of about 100 kHz of $b\bar{b}$ pairs [40]. However about only 15 % of these events will include at least one B meson with all the decay products in the LHCb acceptance. The purpose of the trigger system is to reduce from the LHC crossing rate down to 2 kHz. This system is divided in a hardware part, namely the L0, and a software one, the High Level Trigger (HLT).

2.9.1 Level 0 trigger

Because B mesons have a large mass their decay products will often have large transverse momentum (p_t) and transverse energy (E_t). Therefore the L0 uses:

- the highest E_t hadron, electron and photon clusters in the calorimeters (see details in Calorimeters chapter);
- the two highest p_t muons in the muon chambers.

In addition a pile-up veto in the VELO estimates the number of primary pp interactions in each bunch crossing. The calorimeter system computes the total observed energy and an estimation of the expected number of tracks using the multiplicity in the SPD. A Level-0 Decision unit (L0DU) collects all the information and derives the final Level-0 decision for each bunch crossing. It allows for overlapping of several trigger conditions and for pre-scaling.

2.9.2 High Level Trigger

The High Level Trigger (HLT) is a C++ application that runs in a dedicated online farm (Event Filter Farm). The farm contains between 1000 and 2000 nodes. The aim is to reduce the L0 output from 1 MHz down to 2 kHz which will be written to tape. The HLT has two stages, HLT1 and HLT2. In Figure: 2.11 we shows the "alleys" that compose the HLT1, they run in parallel and confirm the decision from the L0-Trigger. The HLT2 is a

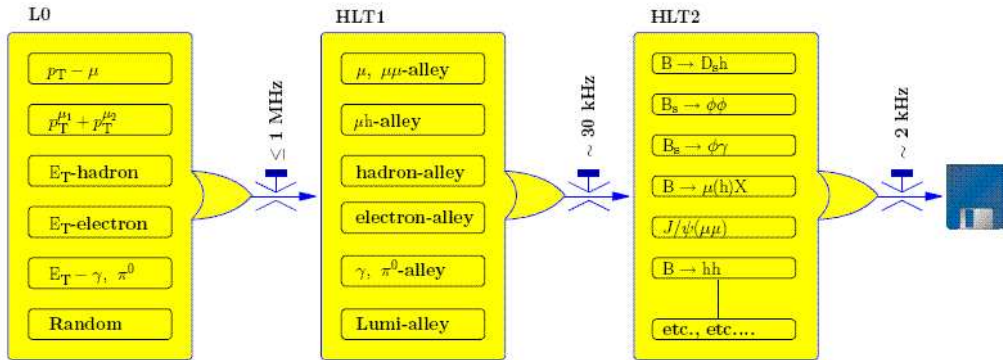


Figure 2.11: Architecture of the LHCb trigger

combination of inclusive trigger algorithms with a partial B reconstruction and exclusive trigger which aim to fully reconstruct the B in their final states. Prior to the final selections, a set of tracks is selected with very loose cuts on their momentum and impact parameter to make composite particles such as $K^* \rightarrow K\pi$. Cuts on the invariant mass or the pointing of the B momentum towards the primary vertex are applied on the B candidates. The resulting reduction rate imposed by the data writing on disk is 2 kHz.

2.10 Online system and data acquisition

We describe in this section the data path between the various sub detectors and the final storage [47]. The online system ensures that the data transfer from all the front-end cards to the permanent storage system. It is essential to keep record of all the conditions under which the data were taken (the Condition Data Base). The online system ensures that all the detectors channels are properly synchronized with the LHC clock. The LHCb online system consists in three components:

- the data acquisition (DAQ) system (see Figure: 2.12),
- the Timing and Fast Control (TFC),
- the Experiment Control System (ECS).

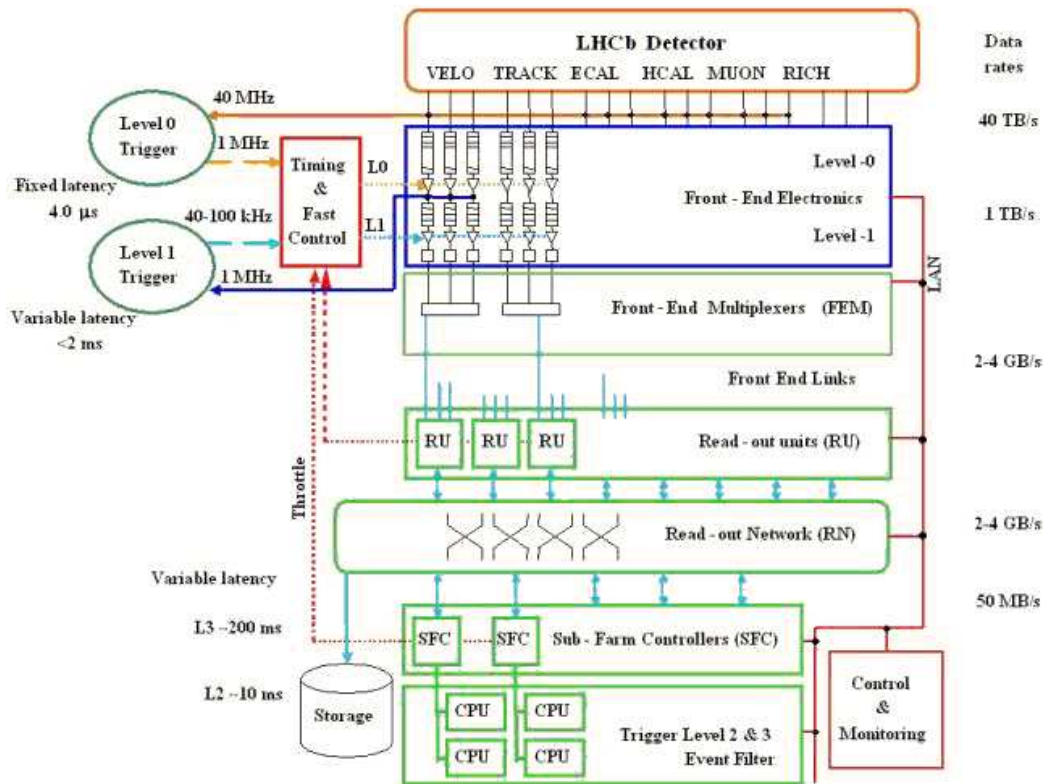


Figure 2.12: The LHCb DAQ system architecture.

Data acquisition For L0 accepted events, the readout supervisor (ODIN card) transmits the information to the detector's front-end cards. The cards being usually installed close to the detectors, the signal are sent through optical or analog format to the TELL1s located in the barracks behind a shielding wall in order to be protected from radiation damages. Besides the RICH all the sub detectors have the same TELL1. Nevertheless the implemented algorithms in the TELL1 are specific to each sub detector. They allow processing such as zero suppression or data compression. Afterward the data are sent in IP-packet to a given node of the farm via an Ethernet link.

TFC The TFC system distributes the beam-synchronous clock, the L0 trigger and the various synchronous resets and fast control commands. The Readout Supervisor synchronizes trigger decisions and beam-synchronous commands to the LHC clock and orbit signal provided by the LHC. It allows as well to produce a variety of other "triggers" used for the sub-detector calibration and tests. Depending on the trigger type the transmitted data banks, contain an identifier of the event, the time and the source of trigger.

ECS The Experimental Control System works in parallel of all the operations described previously. This system ensures the control of the various components of the sub-detectors for example the high voltage system of the calorimeters. The Serial Protocol for ECS (SPECS) provides a high-speed 10 Mb/s access to the front-end card electronics.

2.11 LHCb software

All results in this thesis have been obtained using PYTHIA [61] generated Monte Carlo data, processed by the full LHCb detector simulation. This software is important not only for designing analysis before the detector is switched on, but will also be used to help in detector calibration and the analysis. The LHCb software is documented online [48].

2.11.1 Event simulation and reconstruction

The simulation of events at the LHC consists of five phases: event generation, detector response simulation, digitization, event reconstruction, and event selection and analysis, which are outlined in turn.

- **Event generation** : The LHCb Monte Carlo events are generated using PYTHIA and EvtGen [62]. PYTHIA simulates the production of $b\bar{b}$ pairs in pp collisions through the processes of gluon fusion, gluon splitting and flavor excitation. The EvtGen package then decays the resulting B mesons from a table of predetermined decay channels and rates.
- **Detector response simulation**: Once an event has been generated, it is necessary to simulate the path of the particles through the detector and their interactions with it. The package GEANT 4 [63] is used for this purpose, controlled through the LHCb simulation program Gauss. The LHCb detector is simulated in detail, including:
 - **Passive materials** In which secondary interactions can occur. Such as supports, frames, shielding elements, and the LHC beam pipe.
 - **The LHCb magnet** is simulated using a field map measured on the magnet which will be used in the running detector;
 - **The spill over** of particles from one event into another, is simulated. The probability of neighbouring bunch crossings producing particles is calculated from the instantaneous luminosity;
 - **Individual subdetectors** are fully simulated. For example, effects such as noise, are included in the simulation;
- **Digitization**: The digitization reproduces the response of the detector and the readout electronics once an event has been generated. This includes simulating the propagation of electrical signals through the detector, the response of the readout hardware to these signals, and the analog to digital conversions performed in the readout modules and L0 trigger boards. The digitization is performed using the package Boole. Boole produces digitized data in the same format as that which will be produced by the LHCb hardware on real data.

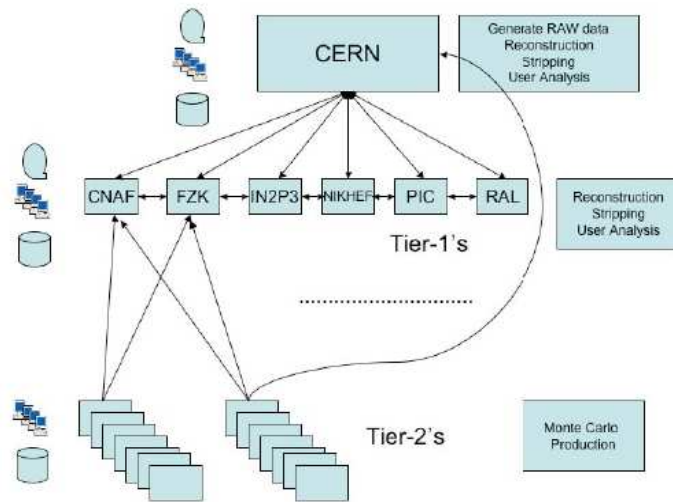


Figure 2.13: LHCb computing model

- **Reconstruction:** The LHCb reconstruction software called Brunel creates tracks, RICH Cherenkov rings and clusters out of the digitized output provided by Boole. Brunel was used to reconstruct the data in this thesis, it contains the full pattern recognition and tracking software which will be used to reconstruct data taken during LHCb running.
- **Analysis:** The reconstructed information output by Brunel are the inputs to the LHCb analysis package called DaVinci, which uses them to reconstruct the B mesons in a decay mode of interest.
- **Online Monitoring** Various packages allow to monitor the data on-line, in particular Orwell which is the dedicated package for the calorimeters. It provides event displays and plenty of control histograms.

2.11.2 GRID computing

The amount of data collected and processed by the LHC detectors will far exceed any previous high energy physics experiment, and this fact has necessitated the development of new computing strategies, in particular the GRID distributed computing model. The GRID distributed computing project has been developed to meet the above demands, and the GRID based LHCb computer model is detailed in [46]. A schematic of the model can be seen in

JobID	Status	MinorStatus	ApplicationStatus	Site	JobName	LastJobData [UTC]	LastSigOfLife [UTC]	SubmissionTime [UTC]	Owner
2083986	Done	Execution Complete	diraccliManuy (D...	LCO-CERN.ch	[venga_Dev]_LC...	2008-05-09 13:03	2008-05-09 13:03	2008-05-09 12:59	growen
802457	Completed	Application Finished	Gauss v591 step 1	LCO-CNAF-T2.4	0000145_000691	2008-12-04 04:59	2008-12-04 04:59	2008-12-03 08:45	growen
902009	Completed	Application Finished	Gauss v591 step 1	LCO-CNAF-T2.4	0000145_000698	2008-12-03 20:26	2008-12-03 20:26	2008-12-03 08:36	growen
901846	Completed	Application Finished	Gauss v591 step 1	LCO-CNAF-T2.4	0000145_000678	2008-12-03 23:30	2008-12-03 23:30	2008-12-03 08:33	growen
901753	Completed	Application Finished	Gauss v591 step 1	LCO-CNAF-T2.4	0000145_000671	2008-12-03 23:31	2008-12-03 23:31	2008-12-03 08:32	growen
901748	Completed	Application Finished	Gauss v591 step 1	LCO-CNAF-T2.4	0000145_000676	2008-12-04 04:59	2008-12-04 04:59	2008-12-03 08:31	growen
901389	Completed	Application Finished	Gauss v591 step 1	LCO-CNAF-T2.4	0000145_000674	2008-12-03 20:26	2008-12-03 20:26	2008-12-03 08:24	growen
901364	Completed	Application Finished	Gauss v591 step 1	LCO-CNAF-T2.4	0000145_000672	2008-12-03 23:37	2008-12-03 23:37	2008-12-03 08:24	growen
901315	Completed	Application Finished	Gauss v591 step 1	LCO-CNAF-T2.4	0000145_000675	2008-12-03 23:48	2008-12-03 23:48	2008-12-03 08:23	growen
901301	Completed	Application Finished	Gauss v591 step 1	LCO-CNAF-T2.4	0000145_000673	2008-12-03 23:31	2008-12-03 23:31	2008-12-03 08:23	growen
901295	Completed	Application Finished	Gauss v591 step 1	LCO-CNAF-T2.4	0000145_000677	2008-12-03 20:19	2008-12-03 20:19	2008-12-03 08:23	growen
901179	Completed	Application Finished	Gauss v591 step 1	LCO-CNAF-T2.4	0000145_000672	2008-12-03 20:26	2008-12-03 20:26	2008-12-03 08:21	growen
901092	Completed	Application Finished	Gauss v591 step 1	LCO-CNAF-T2.4	0000145_000671	2008-12-04 03:47	2008-12-04 03:47	2008-12-03 08:19	growen
900918	Completed	Application Finished	Gauss v591 step 1	LCO-CNAF-T2.4	0000145_000692	2008-12-04 03:45	2008-12-04 03:45	2008-12-03 08:15	growen
900893	Completed	Application Finished	Gauss v591 step 1	LCO-CNAF-T2.4	0000145_000695	2008-12-03 23:30	2008-12-03 23:30	2008-12-03 08:15	growen
900883	Completed	Application Finished	Gauss v591 step 1	LCO-CNAF-T2.4	0000145_000694	2008-12-03 23:32	2008-12-03 23:32	2008-12-03 08:15	growen
900890	Completed	Application Finished	Gauss v591 step 1	LCO-CNAF-T2.4	0000145_000699	2008-12-03 23:31	2008-12-03 23:31	2008-12-03 08:15	growen
900825	Completed	Application Finished	Gauss v591 step 1	LCO-Legnano.4	0000145_000698	2008-12-03 23:32	2008-12-03 23:32	2008-12-03 08:14	growen
900725	Completed	Uploading Output S...	Gauss v591 step 1	LCO-Legnano.4	0000145_000681	2008-12-04 00:00	2008-12-04 00:00	2008-12-03 08:12	growen
900717	Completed	Application Finished	Gauss v591 step 1	LCO-Legnano.4	0000145_000688	2008-12-03 23:36	2008-12-03 23:36	2008-12-03 08:12	growen
900698	Completed	Application Finished	Gauss v591 step 1	LCO-Legnano.4	0000145_000691	2008-12-03 23:48	2008-12-03 23:48	2008-12-03 08:11	growen

Figure 2.14: Grid monitoring web page

Figure 2.13. The GRID serves two functions: to quickly distribute raw data from the LHC to processing centers around the world, and to dynamically allocate computing resources as data processing jobs are initiated. Raw data will be produced at CERN and distributed among the Tier-1 computing centers, where they will be reconstructed and “stripped” into a smaller data set ready for physics analysis. Raw data will be stored at CERN, with another copy distributed across the other Tier-1 centers, while each year’s stripped data will be distributed across all Tier-1 centers to balance the analysis load. Jobs are submitted to the GRID as a whole, and are allocated to whatever processing center has spare capacity at that time, in a manner transparent to the user. The Tier-2 centers serve primarily for Monte Carlo production, although they are expected to provide modest disk storage capacity and may also be used to run certain analysis jobs.

Grid shifts During my thesis, I was a member of the LHCb production team. The job of the shifter is to ensure that the available CPU and storage resources are used efficiently using the monitoring web page (see Figure: 2.14). It is fundamental to check as well, that the Monte Carlo productions and the real data reconstruction in a near future are well progressing. As it is to detect problematic sites.

Chapter 3

Calorimeters

PRÉLUDE



Johann Sebastien Bach - BWV 1007
Cello Solo Suite 1

In this chapter, we first describe the four parts the calorimeter system is made of. Then we focus on the electronics of the ECAL and the HCAL, the LED and high voltage systems as well as the calorimeter Level-0 trigger, emphasizing the relevant aspects for this thesis. The calorimeter system identifies photons, electrons and hadrons and measures their position and energy. These information are collected and sent to the data acquisition and used to reconstruct particle momentum as an input to the Level 0-trigger. The detector composition is a compromise between a small number of read-out channels and a low occupancy with a satisfactory energy and position resolution. Four sub detectors compose the calorimeter system, the Scintillator Pad Detector (SPD), the PreShower (PS), the Electromagnetic (ECAL) and Hadronic (HCAL) calorimeters see Figure: 3.1.

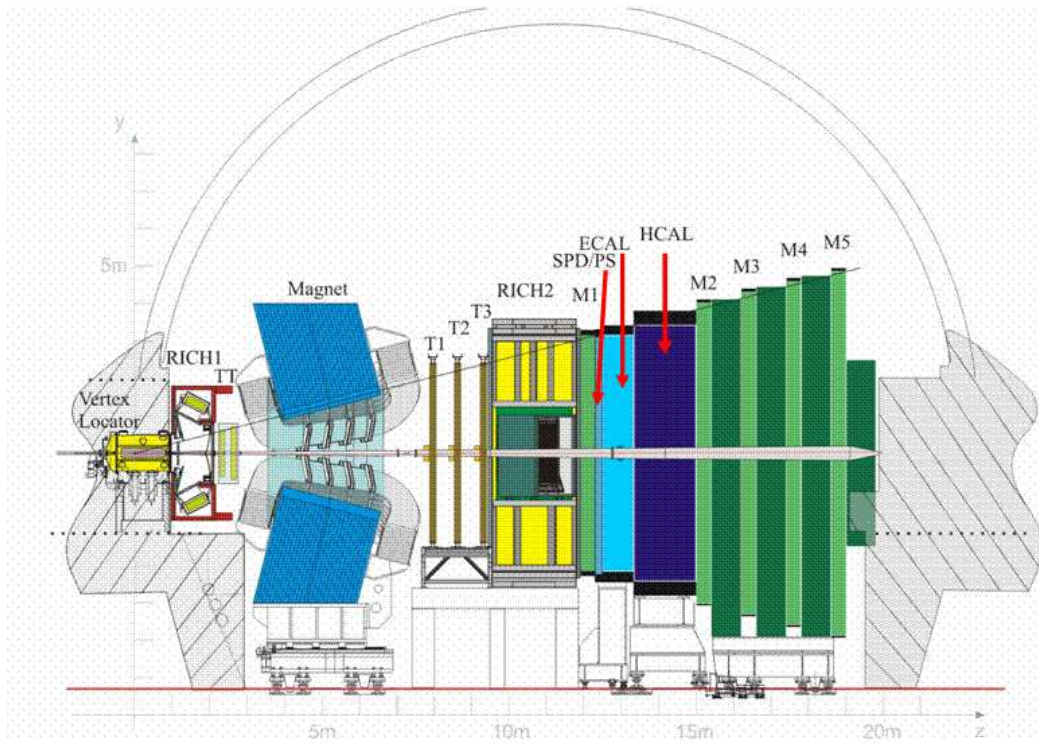


Figure 3.1: View of the LHCb detector

3.1 General detector structure

All four calorimeter elements follow the same basic principle: the scintillation light is transmitted to a Photo-Multiplier (PMT) by wavelength-shifting (WLS) fibers. The single WLS fibers for the SPD/PS cells are connected to clear fibers and read out using multi anode photomultiplier tubes (MAPMT), while the fiber bunches of the ECAL and the HCAL modules require individual phototubes. The gain in the ECAL and HCAL phototubes is set in proportion to their distance from the beam pipe in order to have a constant E^T scale. This is not the case for the SPD/PS system as the photomultipliers are grouped by 64. The HCAL tubes operate at higher gain with respect to the ECAL tubes, since the delivered light for a given energy by the HCAL module is 30 times smaller than by the ECAL. This is due mainly to the fact that, the ratio of the energy loss in the scintillator and the absorber is higher in the ECAL than in the HCAL. The ECAL and the HCAL are structured in a sandwich of absorber and scintillators. For the ECAL a shashlik technology is used, the modules are illustrated in Figure: 3.2. The HCAL is an assembly of Tilecal modules made of iron and scintillators.

3.2 Electronics overview

The main requirement that should be fulfilled by the electronics is imposed by the L0 trigger: the electronics need to be able to cope as fast as possible with the data rate. The HCAL and the ECAL phototubes are housed directly on the detector modules. The signal are shaped directly on the back of the photomultiplier for the SPD/PS and after 12 m and 16 m of cables for the ECAL and the HCAL respectively. The digitization is done in the front end cards hosted in the crates. The crates are positioned on top of the detectors, the triggers circuits are hosted in the same cards. At the LHC the bunch crossing rate is 40 MHz, therefore the data are sampled at the same rate. They are stored in a digital pipeline until the L0 trigger decision is taken. An additional requirement is to reduce the tails of signal associated to the bunch crossing preceding the one being sampled (these tails are known as spill-over). For both electromagnetic and hadronic calorimeters this is done by a suitable signal treatment within 25 ns. Because of the fluctuation of the shape of the SPD/PS signals a longer possible integration time is required.

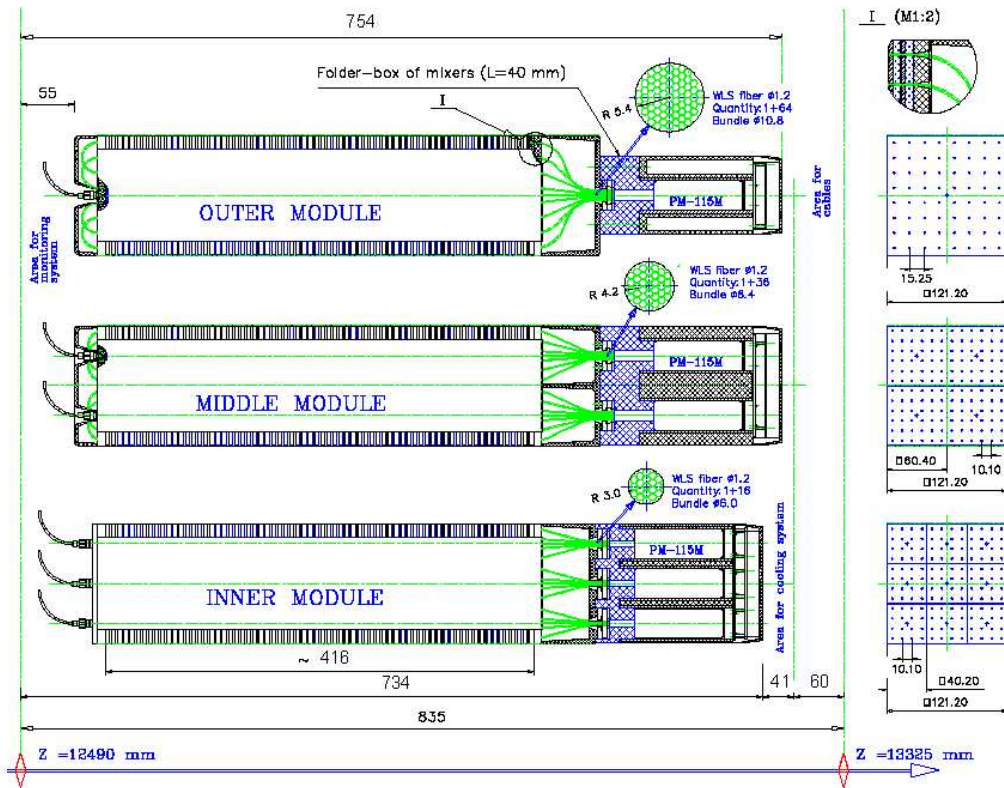


Figure 3.2: The electromagnetic calorimeter modules for the inner, middle and the outer sections.

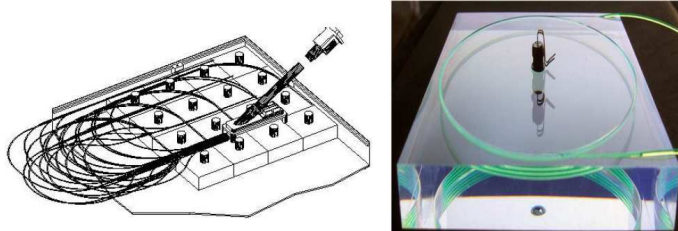


Figure 3.3: Cells of the PreShower

3.3 Sub detectors

We describe in this section in more detail the functioning of each sub detector composing the calorimetry system.

3.3.1 SPD/PS

The SPD/PS uses a scintillator pad readout by WLS fibers that are coupled to the MAPMT through clear plastic fibers. For economic reasons and space reduction the readout is done by 64 channel MAPMT. The SPD/PS detector is composed by a 15 mm thick lead converter leading to $2.5 X_0$ sandwiched between two planes of rectangular scintillator of high granularity with a total of 12032 channels. The inner, middle and outer dimension cells are respectively: 4×4 , 6×6 and 12×12 cm² see Figure: 3.3. The electron/pion separation performance of the PS prototype was measured in test beams using electrons and pions between 10 and 50 GeV/c momtum. The measurements show that with a threshold of 4 MIPs corresponding to about 100 ADC counts, pion rejection factors of 99.6%, 99.6% and 99.7% with electron retentions of 91%, 92% and 97% are achived for 10, 20 and 50 GeV/c particle momentum respectively [51]. To respect the projectivity structure the cells of the SPD are about 0.45% smaller than the PS ones. The separation of photons and charged particles is done in the SPD, the photons are not expected to deposit energy in the SPD nevertheless, some backscattering from the lead can cause a residual production. Of course, photons which have converted in pair in the apparatus before the calorimeter are identified as charged particles. These processes of photon conversion occurring in the material before the SPD constitute the dominant source of background. For 20 to 50 GeV photons, the misidentification probability due to back scattering

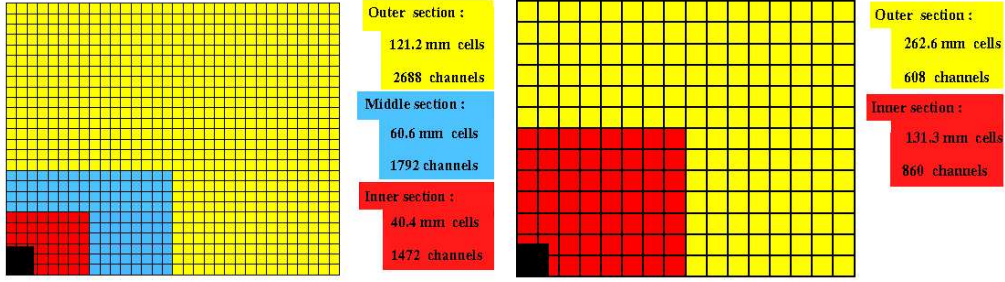


Figure 3.4: Lateral segmentation of the SPD/PS and the ECAL(left) and the HCAL(right). One quarter of the detector front face is shown. In the left figure the cell dimensions are given for the ECAL.

is: $0.8 \pm 0.3\%$ [50].

3.3.2 ECAL

In order to optimize the energy resolution in the ECAL, the thickness must be such that the whole showers produced by high energetic photons are contained. The segmentation in the transverse plane is shown in Figure: 3.4 since the hit density is a steep function around the beam pipe, the size of the squared cells in inner, middle and outer region are respectively: 4.04 cm, 6.06 cm and 12.12 cm respectively. The ECAL is 25 radiation lengths thick, the Moliere radius of the stack is 3.5 cm. In order to improve the light collection efficiency the fibers are looped such that each traverses the module twice. The uniformity in the ECAL response was studied during test beams. Only a few percent of scintillation light is registered by the phototubes after capture and re-emission in the WLS fibers. Two sources of the lateral non-uniformity in the light collection efficiency were determined, namely the imperfect reflection from the edges and a dependence on the emission point of the scintillating light with respect to the fibers. The energy resolution of the ECAL modules had been determined using dedicated test beams. The following parametrization is used:

$$\frac{\sigma_E}{E} = \frac{a}{\sqrt{E}} \oplus b \oplus \frac{c}{E} \text{ where, } E \text{ is given in GeV,}$$

where a , b and c stand for the stochastic, the constant and the noise terms respectively. Depending on the test beam conditions the following results

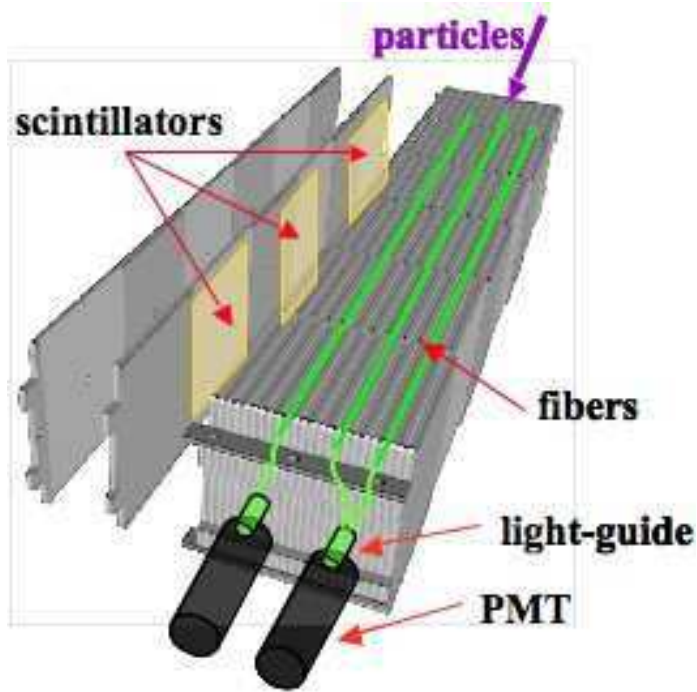


Figure 3.5: HCAL module

were obtained, for the stochastic and the constant terms are:
 $8.5\% < a < 9.5\%$ and $b \sim 0.8\%$. The term c varies with the position of the cells, $c = \frac{0.003}{\theta}$

3.3.3 HCAL

A special characteristic of the sampling structure of the hadronic calorimeter is the orientation of the scintillating tiles which are parallel to the beam axis. In the lateral direction tiles are interspaced with 1 cm of iron, while in the longitudinal direction the length of the tiles and iron spacers corresponds to the hadron interaction length Λ_I in steel. Like in the ECAL the light is collected by WLS fibers running along the detector towards the back side where the photomultiplier tubes are installed. The HCAL is segmented transversely (see Figure: 3.4) into squared cells of size 131.3 mm for the inner part of 262.6 mm in the outer region. The measured resolution is:

$$\frac{\sigma_E}{E} = \frac{80\%}{\sqrt{E}} \oplus 5\% \text{ where } E \text{ is given in GeV} \quad (3.1)$$

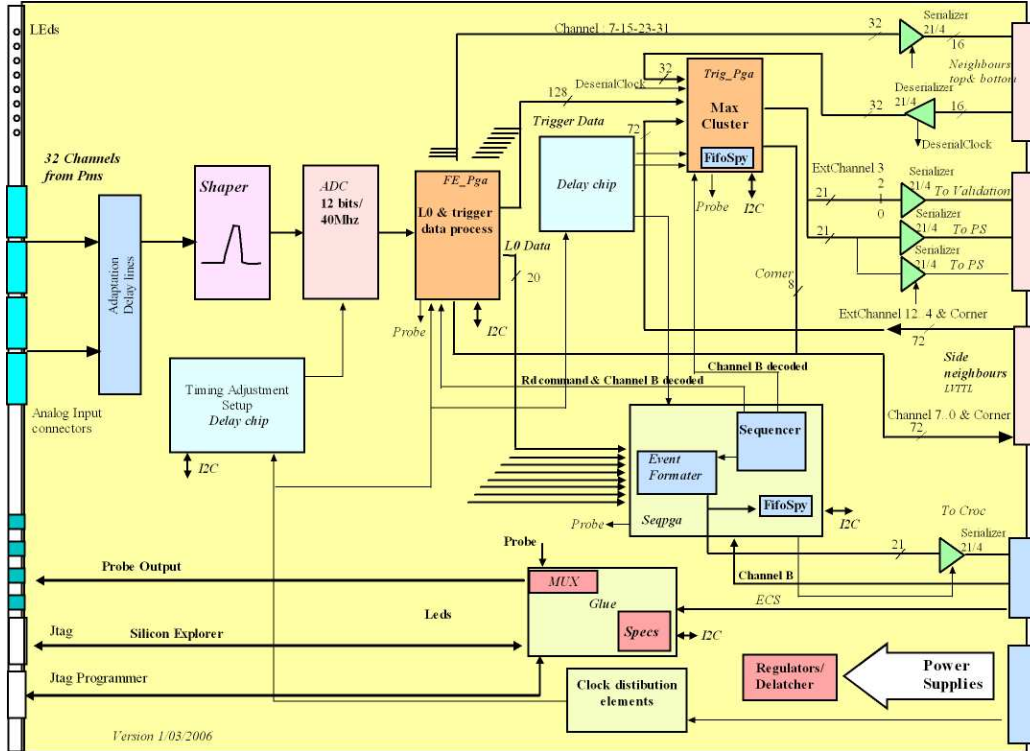


Figure 3.6: Schematics of the prototype of the front-end board (FEB).

3.4 Electronics of the ECAL/HCAL

The input signals coming from the ECAL and the HCAL are very similar, this had motivated the usage of common electronics for both systems. Each card (see Figure: 3.6) is connected to 32 channels of the ECAL and of the HCAL. The data are digitized in the front-end cards and sent to the trigger validation card. The data are also stored in a pipeline of the front-end cards, and then sent via the backplane to the calorimeter read-out card, called the CROC. We will describe in this section in more details the structure of the electronic of the ECAL and the HCAL. When describing each card we will focus of the components related to the time alignment procedure.

3.4.1 The analog part(Pulse shaping)

In order to avoid the spill-over, the PTM pulses are shaped by removing the pulse tails in such a way that they are entirely contained in a 25 ns

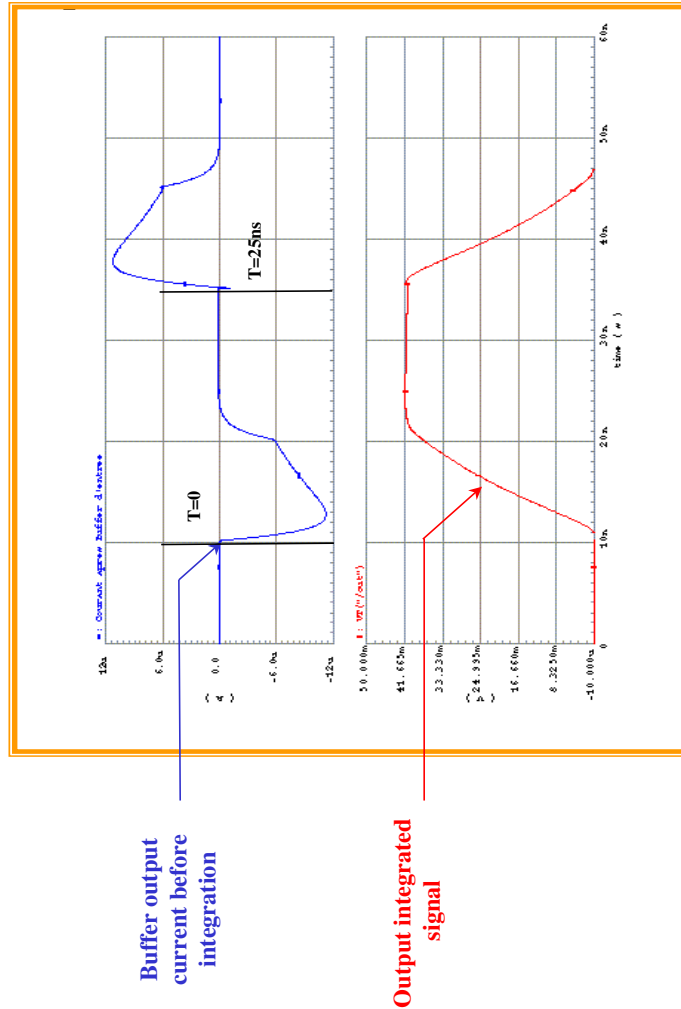


Figure 3.7: Simulated input and output pulses of the integrator.

time window. The pulses are shortened by a "clipping" line. This consists in a cable for the HCAL and a delay chip for the ECAL (due to the lack of space). Since the number of photoelectrons fluctuate, the shaped pulse is expected to fluctuate as well. Nevertheless, in the ECAL the number of produced photoelectrons is about 3000 per GeV, therefore the fluctuations will be small. The pulses are sent along ~ 10 m of coaxial cables to the front-end cards located in the crates on top of the detectors. A component called, a pole-zero is placed after the integrator to compensate the distortion of the pulse shape in the cables. The first element of the card is a front-end chip which contains a buffer and an integrator. After 25 ns delay the same

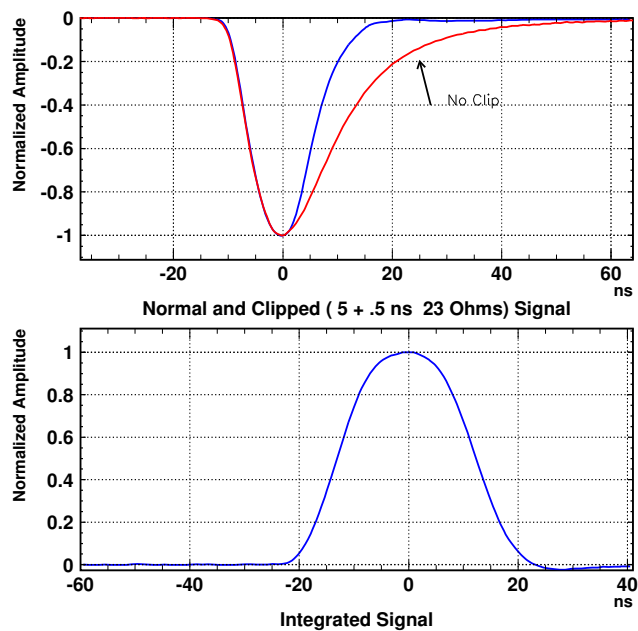


Figure 3.8: 80 GeV HCAL signals obtained during 2002 test beams. The upper figure shows the PM signal before (red) and after the clipping (purple) in both cases the signal is not integrated. The lower one shows the same signal at the output of the integrator.

pulse is subtracted in the buffer amplifier in order to discharge the integrator; this is obtained by using a delay line. To help in the understanding of the system one can see in Figure: 3.7 its response when a fast generated pulse is sent as an input. In top illustration in Figure: 3.8 we show an average 80 GeV photomultiplier HCAL pulse before and after clipping, and after the integration in the bottom. This curve is obtained by means of the average over 1000 measurements on a digital scope. Using the card prototype, it was shown that the contribution of the tail in the next sampling is about 2%, with an extra fluctuation of 1%. The impact of this spill-over is negligible compared to the intrinsic energy resolution the ECAL.

3.4.2 The digital part

The pulses from the amplifier integrator are sent to 12-bit ADCs. Within 1 % the pulses are flat after integration over ± 2 ns around the maximum. A source of time misalignment is introduced by the different delays in the photomultipliers, this is compensated by adjusting the clock of each ADC by a delay chip to an accuracy of 1ns. These chips have a 25 ns range and 1 ns steps. They allow to adjust the 40 MHz clock received by the crate controllers. The digitized output of the ADCs are resynchronized to a common clock per card in a register at the input of the next chip. After integration, the pulses can also have pedestal variations caused by low frequency noise. This is corrected by means of a *digital differentiation*, which consists in subtracting the digitization in the previous sample (25 ns) before. This subtraction also defines the effective integration time of the amplifier and therefore limits the integrated thermal noise from the buffer amplifier. To decrease the possibility of subtracting a signal in an eventual preceding sample, the subtracted quantity corresponds to the smallest of the two preceding measurements. Even at the highest occupancy (about 5%), the probability of subtracting a significant signal is reduced to less than 0.25%. The FPGA placed after each ADC are composed in four blocks:

- As described previously the first block processes the input ADC data;
- The second block produces the trigger data;
- In the third block during the latency and until the L0-Yes the data are stored in a derandomizer, then they are sent in four successive groups

to the SEQ-PGA;

- In order to check the functioning of the cards, it is possible to inject test values instead of the ADC values and this is done in the last block.

Three other PGA are used in the board:

- The Trig-PGA computes the total transverse energy board and the information of the 2×2 cluster of cells with the highest transverse energy;
- The SEQ-PGA serializes the 32 channels of the FEB and sends them to the board controller the CROC. It also sends the L0 trigger signal and control signals linked to the trigger called the *channel B* to the FE-PGAs;
- The Glue-PGA is an interface between the Experiment Control System and the other PGAs of the board. It allows to read and write constant parameters for example those needed to adjust the delay chip values (which will be computed after the time alignment fine tuning procedure).

3.4.3 The calorimeter readout card(CROC)

The CROC collects the front-end L0 data of the calorimeter crates and sends via optical fibers to the LHCb DAQ system (the TELL1 boards described in the next paragraph). Each crate has a unique CROC card which provides the clock, trigger signals, *channel B*, as well as slow control to all the boards of the crate. A TTCrx mezzanine mounted on the CROC boards receives by a fiber the 40 MHz clock from the LHC, the L0 trigger signal and the *channel B* signals. These signals are sent through the backplane to all the boards in the crate.

3.5 The calorimeter Level-0 system

The general structure of the LHCb trigger was discussed in Chapter 2. In this section we will focus on the calorimeter Level-0. A zone of 2×2 cells is used, as it is large enough to contain most of the energy and small enough to

avoid the overlap of various particles. To minimize the number of candidates to be processed, only the highest E_t candidate is kept provided by a three step selection:

- a first selection of the highest E_t is done in the front-end card in the ECAL and the HCAL. Each card handles 32 channels, and the highest E^T sum over the 32 sums of the 2×2 cells is selected.
- the validation card merges the ECAL with the PreShower and SPD information given by the PreShower front-end cards. The identification of the electromagnetic type of the candidate is done (electron, gamma or π^0). Only the candidate with the highest transverse energy is sent to the next step. The validation card also adds the energy deposit in the ECAL to the corresponding hadron candidates. There is one candidate of each type per half crate. Similar cards in the PS crates compute the SPD multiplicity.
- the selection card selects the candidate with the highest transverse energy for each type and produces a measurement of the sum of the highest hadron candidate of each half crate in the HCAL and the total SPD multiplicity.

The selected candidates are sent to the Level-0 Decision Unit via a mezzanine with a 1-channel high speed optical link. Both inputs and outputs of the Selection Boards are sent to the data acquisition system via two high speed optical links connected to the TELL1 boards.

3.6 Monitoring and high voltage system

Using the LHCb's ECS system it is possible to control both the high voltage and the light intensity of the LED as they share the same control board.

The high voltage system The photomultipliers(PMT) bases were chosen to be Crockfot-Walton(CW) for the LHCb calorimeters. We list the quality requirements:

- Individual and precise gain adjustment;

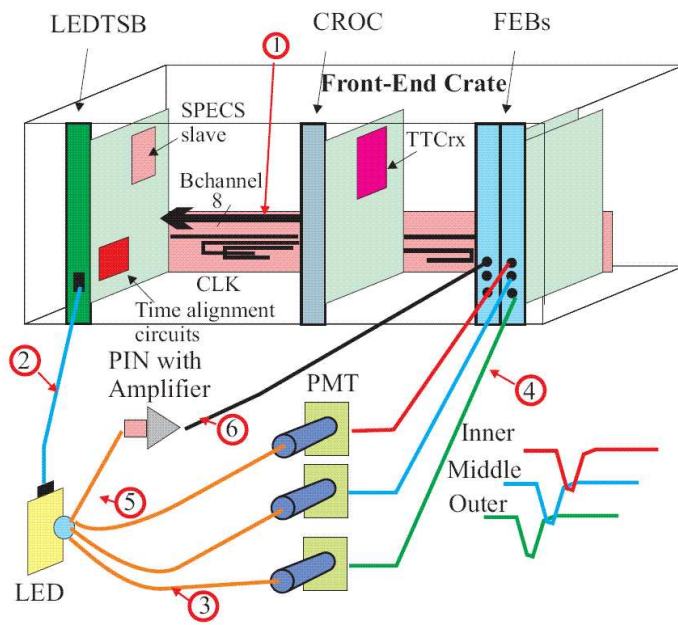


Figure 3.9: A sketch of the LED monitoring of the calorimeter, (1) FE crate backplane over which the monitoring trigger is request is transmitted,(2) LED trigger pulse cable, (3) clear fibre to cell, (4) PMT signal cable, (5) clear fibre to PIN diode, (6) PIN signal cable.

- Effective operation at high rate;
- Low dissipation;
- Low voltage cabling and connectors to reduce to total cost.

As the PMTs are installed directly on the detector, they should sustain radiations, which is expected to be as high as 1 Mrad for 10 years of LHCb operations for the readout of the inner modules.

The LED monitoring system The LED monitoring system is dedicated to control the stability of the four sub detectors of the calorimetry during the operations. Each cell of the four subdetectors is illuminated by a LED. They are triggered by LED drivers while their intensity is controlled by the so called HV-LED-DAC boards. Multichannel LED trigger signal boards (LEDSTB) perform the overall control and adjust the timing. The LED monitoring sequence is initiated by the readout supervisor (RS) upon request and transmitted to the LEDTBs via the CROCs and the front-end crate backplane. The LEDTSBs are located in the front-end crates on the calorimeter platforms and each controls 64 LED drivers. The following set of requirements should be fulfilled by this system:

- High long term and temperature stability;
- The LEDs should have small pulses duration and small dispersion of their amplitudes;
- A variable pulse repetition rate and a variable number of photons in each flash.

The monitoring system has to provide a gain control for all the phototubes with an accuracy better than 1 %. For each LED monitoring sequence a subset of each subdetectors is illuminated. A given group of channels is fired at a rate of 20-30 Hz, resulting in a overall monitoring rate of 1kHz. For each trigger from 3% up to 5% of the channels contain data. These data are read out and sent in a dedicated node of the farm, called the calibration farm. Using these data, histograms are accumulated over a ten minutes period which is enough to detect a gain variation of 1%. If the gain of a given channel is drifting an alarm is generated. Depending on the type

of alarm the run can be stopped or the suitable high voltage correction is then computed and applied using the slow control system. Besides helping to detect disfunctioning cells and bad cable connections, the LED system allow a first relative timing of the cells as explained in Chapter 3.

Chapter 4

Time alignment procedure



Paul Dukas
L'Apprenti sorcier, Scherzo symphonique *fa mineur*

One of the first tasks for the LHCb calorimeter group, is to perform the time alignment of all the channels of both the electromagnetic and the hadronic calorimeters with the first data. Dedicated runs called Time Alignment Event (TAE) runs allow to record several consecutives events each 25 ns. The central sample is called **Current**, it is the one which is kept in standard runs. **Prev1** and **Next1** correspond to the samples recorded respectively 25 ns before and 25 ns after the central one. Using Monte Carlo simulated events with this structure, we have developped a method which allows to perform a precise time alignment. The aim of the simulation is to find a way to compute for each cell of both the electromagnetic and hadronic calorimeters a correction to recover from every potential time misalignment.

4.1 Source of time misalignment

For the calorimeter, various sources of time misalignment should be taken into account and corrected before beam data taking, for example:

- The length of the cables, connecting the ECAL and HCAL photomultiplier to the front-end cards sitting in the racks, can vary by about 20 cm from one cable to the other. Assuming that in these cables the signal propagates at a speed of 5 ns/m, a variation of ~ 1 ns from the average is to be expected for some channels;
- A second source of time misalignment is due to variation of the applied high voltage from one photomultiplier to the other, the way the high voltage affects the timing is computed in Section: 5.4;
- In each crate a clock is sent through fibers causing time misalignment lower than 1 ns.
- Finally, one should take into account the flight distance of the particles detected in the calorimeter.

The aim of the time alignment procedure is to find a way to correct for all these sources of time misalignment for both the electromagnetic and the hadronic calorimeter.

4.2 Methodology

The time alignment fine tuning of all the cells of the ECAL and the HCAL can be done in the following way. The LEDs pulses are short and contained in the 25 ns time window. They are used to perform the very first time alignment (one makes sure that the pulses are contained in the central sample). With this system we make the assumption that all the channels are aligned with a precision better than 5 ns for the ECAL, and better than 2 ns for the HCAL. For the HCAL, all the LEDs fibers have the same length, therefore the precision of time alignment is better. In the following the time misalignment will be noted Δt . It is the parameter we want to determine.

How to find the maximum of the integrated signal The signal of a photomultiplier which collects the light from an ECAL or HCAL module is entirely contained in a 25 ns time window. The distribution of Figure: 4.1 corresponds to the integrated signal of a photomultiplier after the clipping as explained in Section: 3.4.1. The integrated signal plateau is about 2 ns

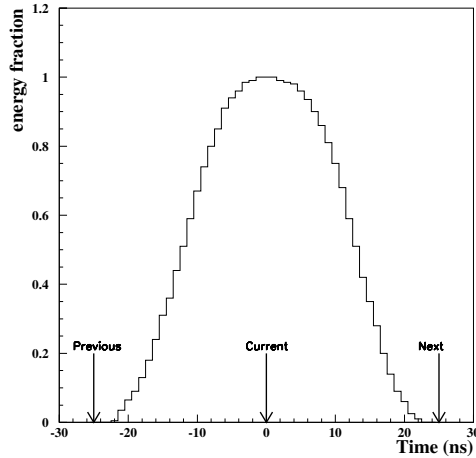


Figure 4.1: Distribution of the fraction of the total energy deposit as a function of time, obtained on test beam data.

large, within 1%. For example if we apply a 1 ns or 2 ns time misalignment 99 % of the energy deposit will remain in the central sample and the rest will be in the **Next1** sample. It would be possible to try to find the maximum of the integrated signal by performing a scan around this region. But, the fluctuation of the number of collected photoelectrons in the photomultiplier causes a fluctuation of the signal shape itself. Therefore the accuracy of this method is not very good.

One could consider the following alternative, instead of exploring the top of the signal one could use the mid-height. We have generated two sets of data, in each case we introduce a time misalignment of respectively +12 ns and +13 ns, where we compare the energy deposits in the central sample with the one in the following sample (**Next1**).

For the dataset with $\Delta t = 12$ ns we have: $A = \frac{E(\text{Current}) - E(\text{Next1})}{E(\text{Current})} = 30\%$.

For a dataset with $\Delta t = 13$ ns we have $A = 4\%$. Around the mid-height of the integrated distribution in Figure: 4.1, we have an important sensitivity to any source of time misalignment, as A varies from 30% down to 4% when we make a 1 ns step. It is this very fact, that introduced the idea of trying to find the maximum of the integrated signal by exploring the mid-height region instead of the actual maximum. For a single channel the procedure is the following:

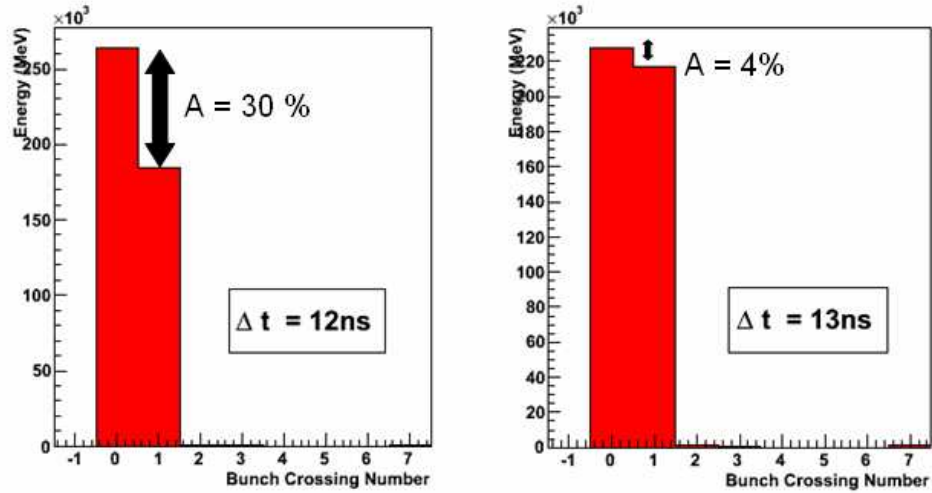


Figure 4.2: Fraction of the energy deposits, in the ECAL when applying a time misalignment of 12 ns (left plot) and 13 ns (right plot) as a function of the bunch crossing number.

- Some data are taken with the “standard” time alignment conditions, *i.e* where the signal is sampled around its maximum while the energy stored for the **Prev1**, **Current** and **Next1** samples is recorded.
- The time is then shifted with +13 ns and some data is taken recording the energy stored in the **Prev1**, **Current** and **Next1** samples.
- An asymmetry R_j , defined in Equation: 4.1, is computed for each cell;
- Using a calibration distribution of R_j , we determine Δt ;
- Knowing the variation of R_j with respect to Δt , we determine the time misalignment.

4.3 Monte Carlo study

In order to test the procedure, we have applied it to simulated data.

4.3.1 Implementation of the time in the simulation

We have used the package Gauss [46] to generate ParticleGun and minimum bias events and the package Boole [46] for the digitization. The distribution in Figure: 4.1 is the integrated signal of a photomultiplier. It was obtained during the calorimeter test beams in 2001 and is implemented in the simulation. This distribution handles the timing in the simulation. It provides the fraction of the energy left in the **Current** sample when a time misalignment is introduced.

4.3.2 Retrieving the shape of the integrated signal

In order to validate the code in the ECAL, we have generated and digitized ParticleGun events. These events are electrons with a momentum of 100 GeV, coming from interaction point and pointing to a given cell of the ECAL. To make this test 51 ParticleGun files are used. In each file we have added a correction that introduces a constant misalignment in all the cells. This correction is called Δt and varies between -25 ns and 25ns with a 1 ns step. In each file we collect the value of the energy deposit for this particular cell and normalize it to the highest value, hence the one generated with $\Delta t = 0$ ns. The top left distribution of Figure: 4.3 shows the superposition of the input in the Monte Carlo simulation and the output of the digitization for a given cell of the inner ECAL. We observe that the shape of the input distribution is conserved, but there is a shift of 1.47 ns. If we remove this shift, we see in the top right distribution that we have a good agreement. We performed this exercise for a cell in both the middle and the outer region and we observe the same behaviour. This is partly due to the definition of the $\Delta t = 0$ ns in the Monte Carlo simulation [52], it is taken to be at $Z_{\text{Shower Max}} = 11$ cm in an ECAL module and not the very front.

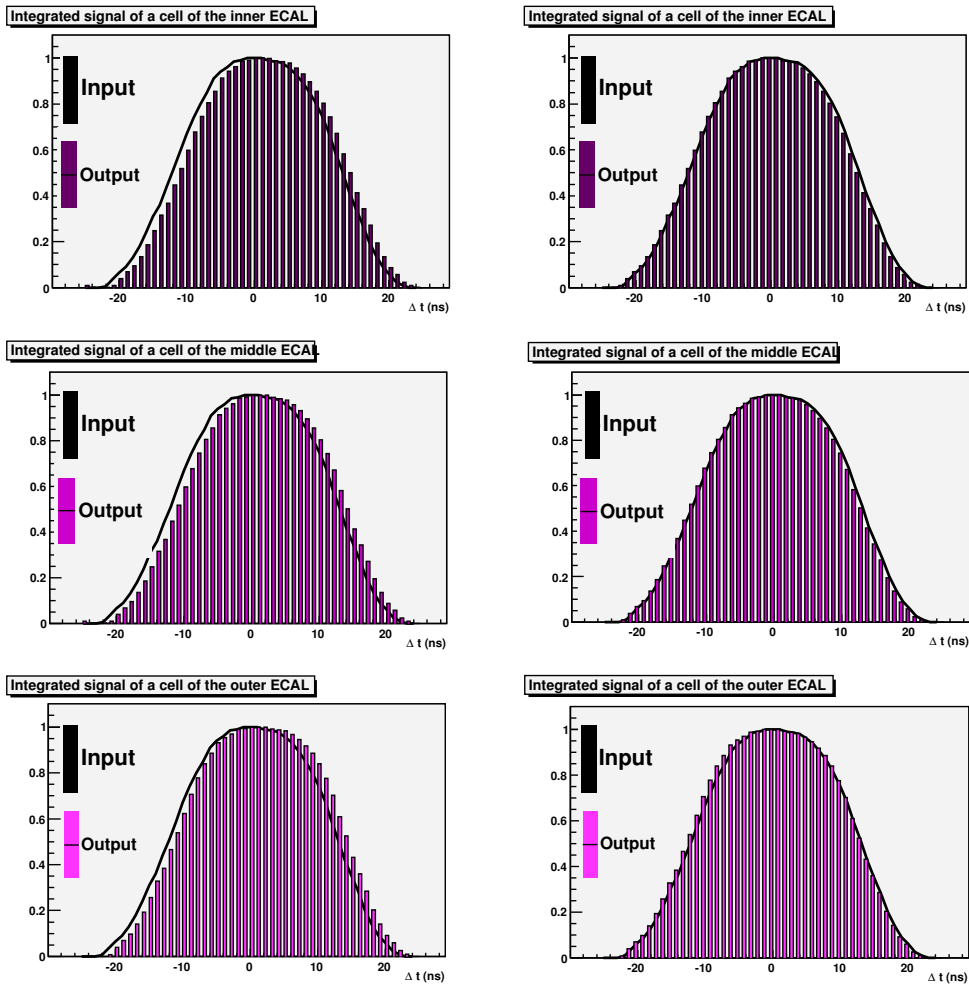


Figure 4.3: Distribution of the fraction of the total energy as a function of the time for a given cell of the inner ECAL (top distributions), middle ECAL(middle distributions) and outer ECAL (bottom distributions). The input distribution refers to the test beam distribution and the output is the distribution obtained after the digitization

4.3.3 Building an asymmetry

For each cell we can write down, the following asymmetry ¹:

$$R_j = \sum_{i=0}^{N_{events}} \frac{E_{ij}(\mathbf{Current}) - E_{ij}(\mathbf{Next1})}{E_{ij}(\mathbf{Current}) + E_{ij}(\mathbf{Next1})} \text{ for an ECAL cell } j \quad (4.1)$$

4.3.4 R_j extraction from the calibration distribution

For each value of the time misalignment Δt , we can plot the computed asymmetry for a given cell, using the same ParticleGun events.

Error on the asymmetry In order to compute the error on the mean value of the asymmetry R_j , we have plotted for each value of Δt the distribution of r_j defined in Equation: 4.2 for a given cell using the ParticleGun events. For a particular cell of the middle ECAL we have obtained the distributions of Figure: 4.4.

$$r_{ij} = \frac{E_{ij}(\mathbf{Current}) - E_{ij}(\mathbf{Next1})}{E_{ij}(\mathbf{Current}) + E_{ij}(\mathbf{Next1})} \quad (4.2)$$

We define the error on R_j as:

$$\sigma_{R_j(\Delta t)} = \frac{rms[r_j(\Delta t)]}{\sqrt{N_{events}}} \quad (4.3)$$

where j is the cell number and i is the event number. We show in Figure: 4.5 the variation of the asymmetry R_j with Δt for a middle ECAL cell . The region $\Delta t \in [11\text{ns}, 18\text{ns}]$ being approximatively linear, a simple line defined as following is used:

$$R = \alpha \times \Delta t + \beta. \quad (4.4)$$

A fit to the data gives $\alpha = (-0.147 \pm 0.001), (-0.147 \pm 0.003), (-0.147 \pm 0.0008)$ and $\beta = (2.026 \pm 0.001), (2.025 \pm 0.005), (2.031 \pm 0.001)$ for an inner, middle and outer cell respectively. Now we have a relation between the R_j s, that we can measure and Δt , that we want to set in delays chips of the front

¹One could have built a similar asymmetry between the **Current** and the **Prev1** containers and used it the same way.

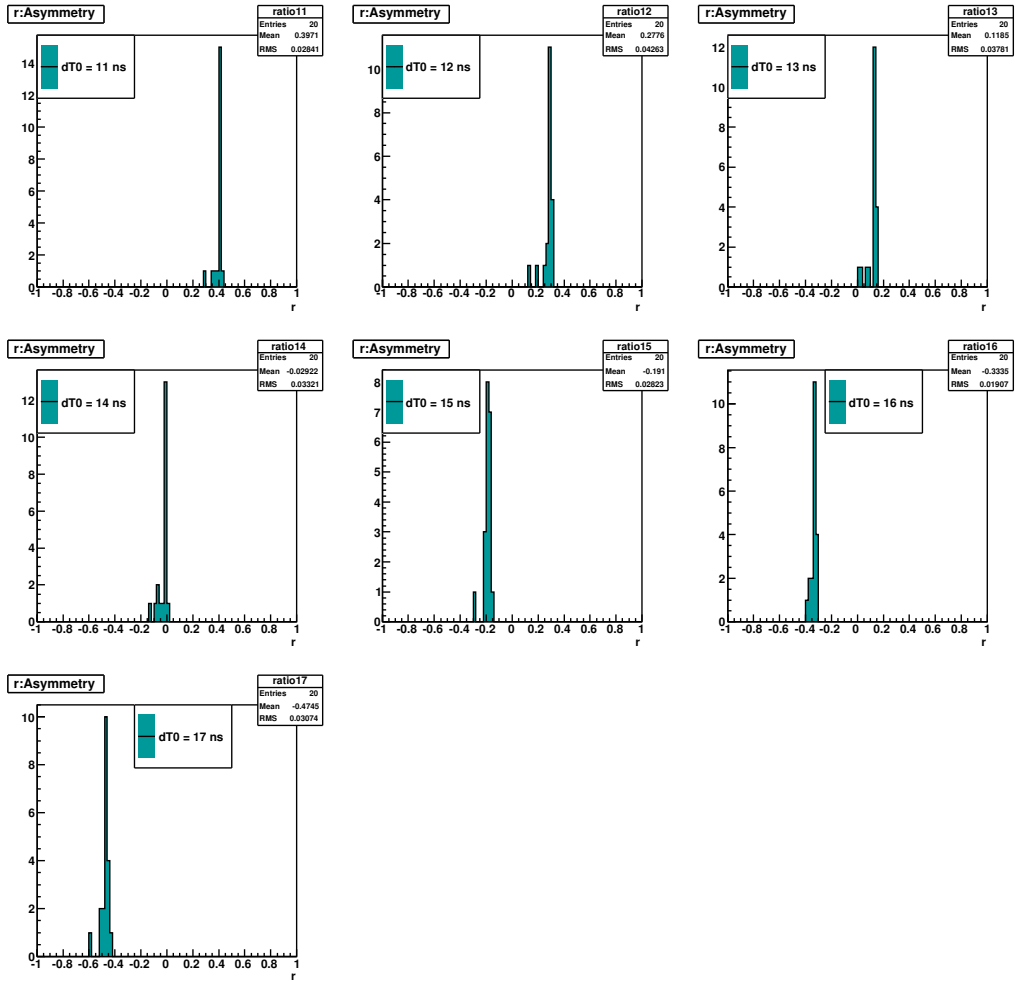


Figure 4.4: r_{ij} distributions for a particular cell of the middle ECAL, the different plots correspond events generated with a different value of Δt as indicated on each plot.

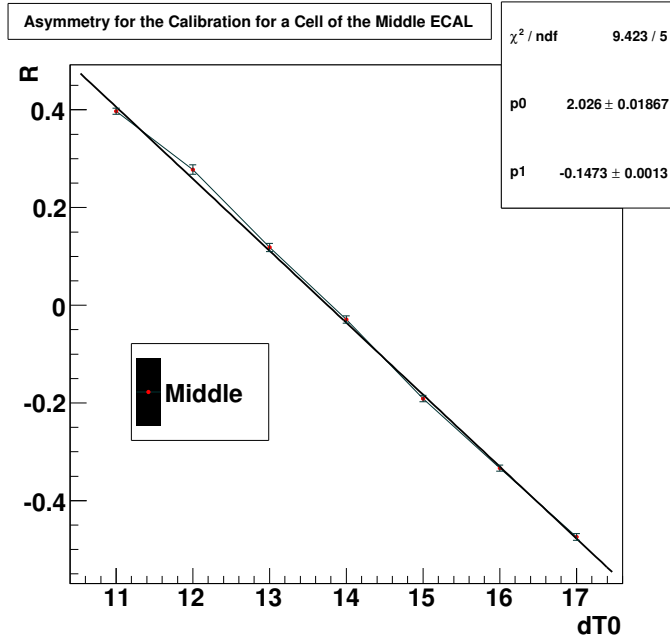


Figure 4.5: Calibration distribution for a particular cell of the middle ECAL.

end cards for ECAL and HCAL.

The aim we want to achieve is to be able to align the cell, with a precision better than 0.5 ns. We will thus call “good cells” the ones for which:

$$0.05 < R_j < 0.20 \quad (4.5)$$

where 0.05 corresponds to $\Delta t = 13.5$ ns and 0.20 to $\Delta t = 12.5$ ns.

4.3.5 Impact of the particles’ properties on the time misalignment

We have shown above what are the expected nominal values for the asymmetry in the ECAL for each value of Δt . When using high energy electrons to obtain the calibration distribution for the ECAL we avoid all possible sources of time misalignment. We categorize in the following the potential sources of time misalignment:

Impact of the magnetic field To understand the effect of the magnetic field on the time alignment, we compare the path D_1 of a particle travelling

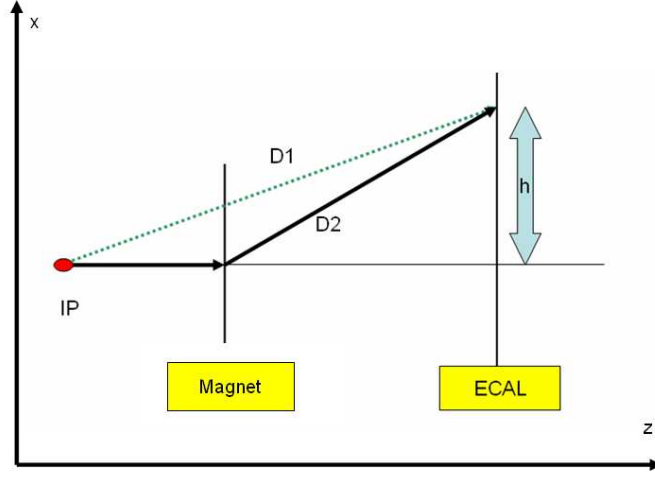


Figure 4.6: Illustration of the difference in path between two particles produced at the interaction point and pointing to the same cell.

at the speed of light and of one with a momentum of 4 GeV for example, coming from the interaction point and pointing to a cell of the outer ECAL. We take $\theta = 300$ mrad (corresponding to a distance h , (see Figure: 4.6) with the magnetic field off to the one of an electron (with 4 GeV momentum, and path D_2) that would be bent by the magnetic field and interacting in the same cell as illustrated in Figure: 4.6. This is computed using the following equation:

$$\theta = 0.3 \frac{BL}{p(\text{GeV})} \text{ with: } BL = 4 \text{ T.m.} \quad (4.6)$$

We call D_2 the path of this particle form the interaction point to the cell with $\theta = 300$ mrad.

$$D_1 = \sqrt{z_{ECAL}^2 + h^2} \text{ and } D_2 = z_{magnet} + \sqrt{(z_{ECAL} - z_{magnet})^2 + h^2} \quad (4.7)$$

$$\delta T_{1-2} = \frac{D_1 - D_2}{c} = 0.4 \text{ ns} \quad (4.8)$$

The time difference (δT_{1-2}) between the two paths is 0.4 ns.

Impact of the non-ultrarelativistic particles We consider as an example of a non-ultrarelativistic particle a charged pion with a momentum of

500 MeV. It will have a value of β_4 given by:

$$E^2 = p^2 + m^2 = 0.519 \text{ GeV} \quad (4.9)$$

therefore,

$$\text{hence: } \beta_4 = 0.96 \quad (4.10)$$

We consider that this particle will point to a cell with $\theta = 300$ mrad and will have a path D_4 . The time difference (δT_{3-4}) between a particle with $\beta_3 = 1$, with a path D_3 , and our charged pion in the absence of the magnetic field, is given by:

$$\delta T_{3-4} = \frac{D_3}{\beta_3 c} - \frac{D_4}{\beta_4 c} = 1.7 \text{ ns.} \quad (4.11)$$

Behavior of the charged pions in the ECAL In the ECAL, the electromagnetic showers initiated by photons or electrons start systematically at the beginning of the module, while the beginning of the shower produced by a charged pion in the ECAL fluctuates [52]. In the ECAL the nuclear interaction length is $\Lambda_I = 1.1$ [49]. Therefore around 67% of the charged pions will interact in the ECAL. To illustrate this fact, we have used two samples of ParticleGun event (generated with a 13 ns time misalignment): electrons and pions with a momentum of 100 GeV pointing to a given cell of the outer ECAL, at $\theta = 230$ mrad. In Figure: 4.7 we plot the energy in the **Current** sample versus the energy in the **Next1** container for both samples. The width of the distribution for the pions is wider. To quantify this effect we compute the asymmetry in both cases for this cell. For the electrons $\langle R_j \rangle = 0.12$ while for the pions $\langle R_j \rangle = 0.05$ which corresponds using the calibration distribution of Figure: 4.5, to a value of $\Delta t = 13.5$ ns while for the electrons we have $\Delta t = 13$ ns.

4.3.6 Improving the amount of aligned cells

There are two possible ways to discard some of the sources of time misalignment:

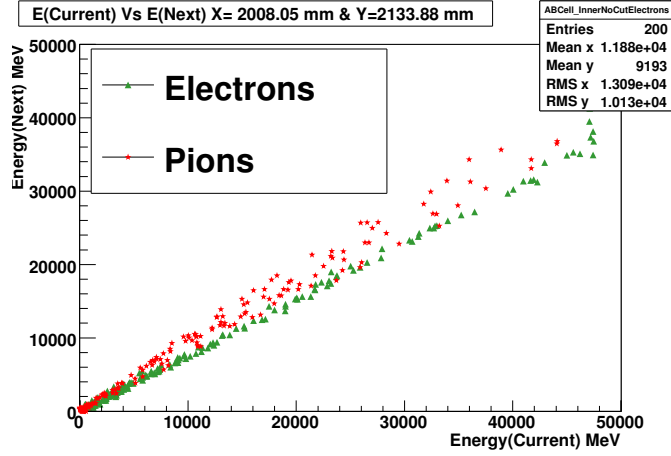


Figure 4.7: Energy(**Current**) Vs Energy(**Next1**) for ParticleGun events, electrons and pions, in a cell of the outer ECAL. These events are generated with a time misalignment of 13 ns.

Applying cuts When dealing with minimum bias events, we have applied the following cut:

$$E_{ij}^T(\mathbf{Current}) + E_{ij}^T(\mathbf{Next1}) > 300 \text{ MeV} \quad (4.12)$$

This eliminates small energy deposits which are badly measured and also removes the particles with a small β as well as the particles with long trajectories (see the top left distribution of Figure: 4.8 where no cuts are applied and the middle left distribution of the same figure, where the cut of Equation: 4.12 is applied).

Iterative method For a given amount of recorded data it is possible to increase the rate of aligned cells using an iterative method. First we compute R_j for each cell and determine a criteria for an event by event selection. For each cell j :

$$|R_j - r_{ji}| < 20 \times (rms(R_{Inner})) \quad (4.13)$$

We have used in this method $rms(R_{Inner})$ as a reference, since we can show (see Section: 4.4.1) that all the cells of the inner ECAL could be aligned in the standard conditions for minimum bias events with a precision better than 0.5 ns. This method allows to reject the events which are far from the slope of the distribution of the energy in the **Current** versus the energy in

the **Next1** (see the bottom distributions of Figure: 4.8 where this method is applied). We have chosen here as an example a cell of the outer ECAL, since we expect the impact of the sources of the time misalignment to be most noticeable in the outer ECAL region.

4.4 Minimum bias events in the ECAL

In order to study a realistic case we have generated misaligned (with $\Delta t = 13\text{ns}$) minimum bias events to test the proposed method in 3 different conditions:

- v200601: These are the standard conditions. The energy of the proton beams is 7 TeV and the magnetic field is on. We have generated 53 k events;
- Pilot run: The proton beams energy is 450 GeV, the magnetic field is off. We have generated 58 k events;
- v200601-BOff: The proton beam energy is 7 TeV and the magnetic field is off. We have generated 55 k events.

4.4.1 Time alignment with minimum bias in the standard conditions

In the standard conditions we obtain for the asymmetry the distributions shown in Figure: 4.9. We require for all the cells:

$$E_{ij}^T(\mathbf{Current}) + E_{ij}^T(\mathbf{Next1}) > 300 \text{ MeV}. \quad (4.14)$$

All the cells of the inner ECAL and almost all the cells of the middle ECAL. The satisfy the criteria given in Equation: 4.5. This is not the case for 53% of the outer ECAL cells. The effect of the magnetic field is mostly observed around the region of the $x = 0$ axis in Figure: 4.11. After one iteration, the amount of “good cells” in the outer region rises from 47% to 62%.

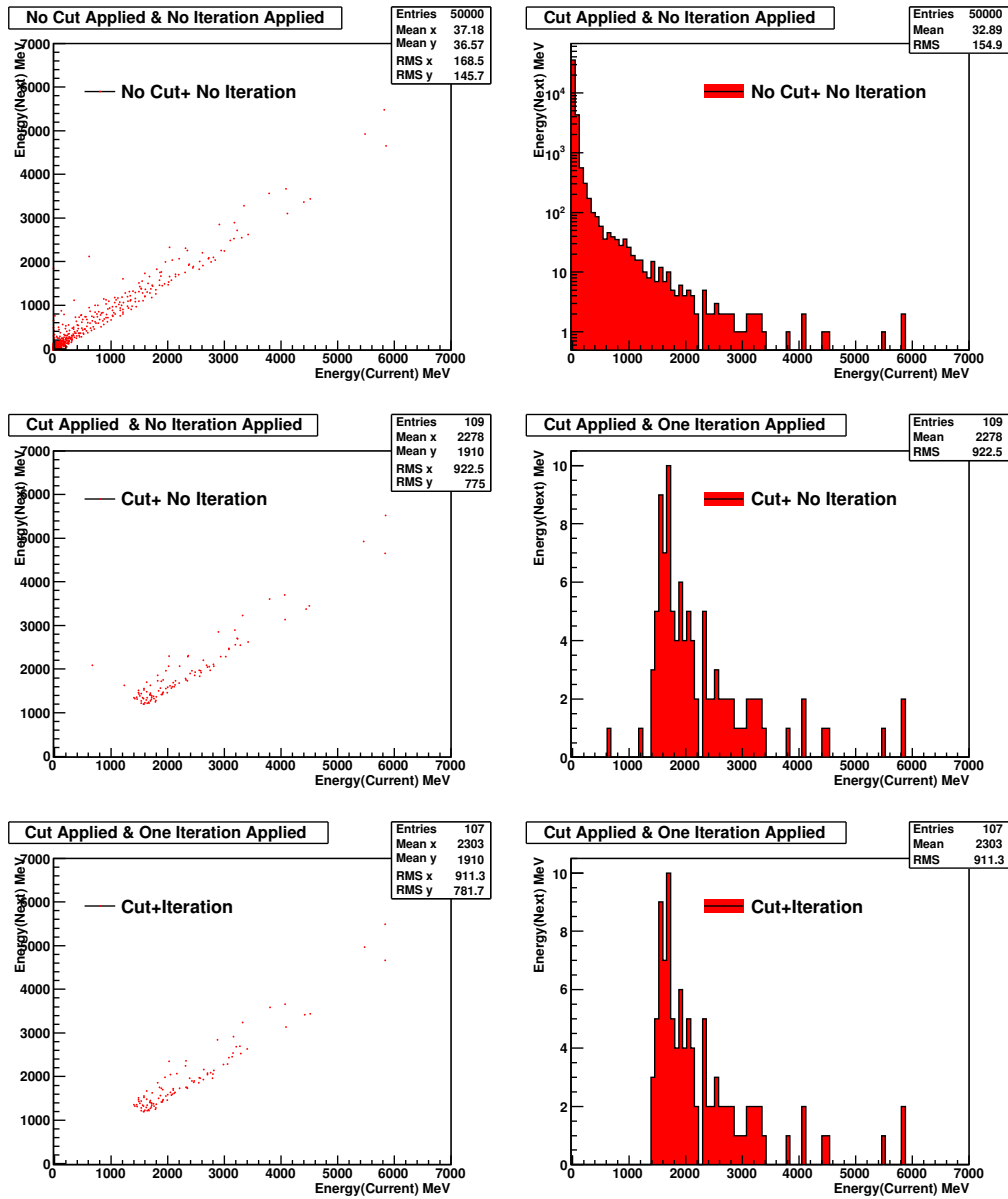


Figure 4.8: Energy(**Current**) Vs Energy(**Next1**) for minimum bias events for a cell of the outer ECAL in the standard conditions with the magnetic field off (left distributions), Energy(**Current**) distribution with minimum bias events for a cell of the outer ECAL in the standard conditions with the magnetic field off (right distributions)

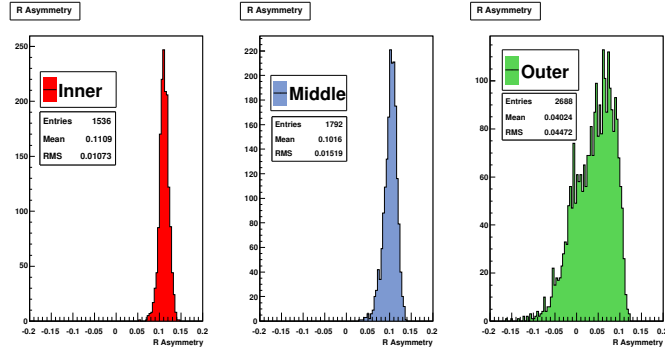


Figure 4.9: R_j asymmetry in the ECAL, standard conditions without iteration (with the magnetic field on).

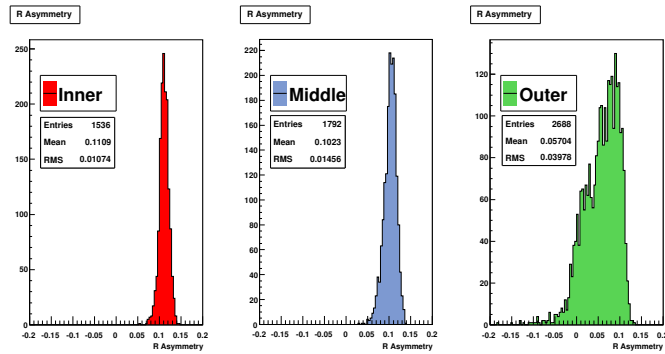


Figure 4.10: R_j asymmetry in the ECAL, standard conditions after one iteration (with the magnetic field on).

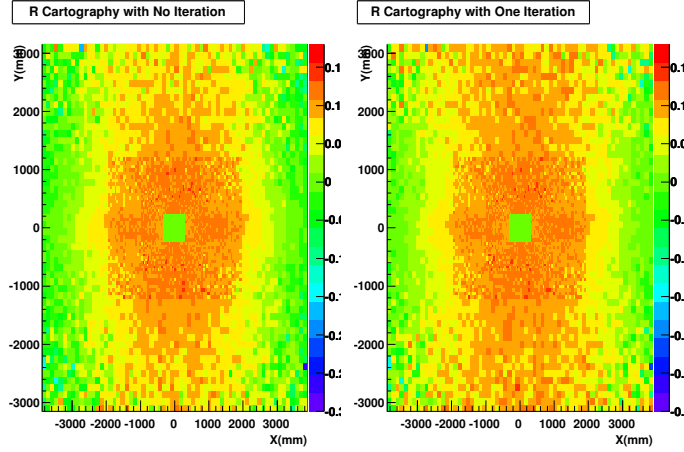


Figure 4.11: R_j cartography in the ECAL, without (left map) and with (right map) an iteration in the standard conditions (with the magnetic field on).

Area	Num. of Iter.	$\langle R \rangle$	$rms(R)$	Good cells
Inner	0	0.110	0.010	100%
Inner	1	0.010	0.010	100 %
Middle	0	0.101	0.015	99 %
Middle	1	0.102	0.014	100%
Outer	0	0.040	0.045	47 %
Outer	1	0.057	0.041	62 %

Table 4.1: Summary table for the ECAL time alignment in the standard conditions.

4.4.2 Time alignment with minimum bias events with the magnetic field off

We have seen the impact of the magnetic field in the standard conditions. With the magnetic field off in these conditions, we no longer have the contribution of the particles with long trajectories. This can be seen in Figure: 4.14 where the distribution of R_j is symmetric in ϕ . In the Table: 4.2 we note that all the cells of the inner and middle ECAL satisfy the condition given in equation: 4.5. After one iteration only 16% of the outer ECAL cells are still not aligned with a precision better than 0.5 ns.

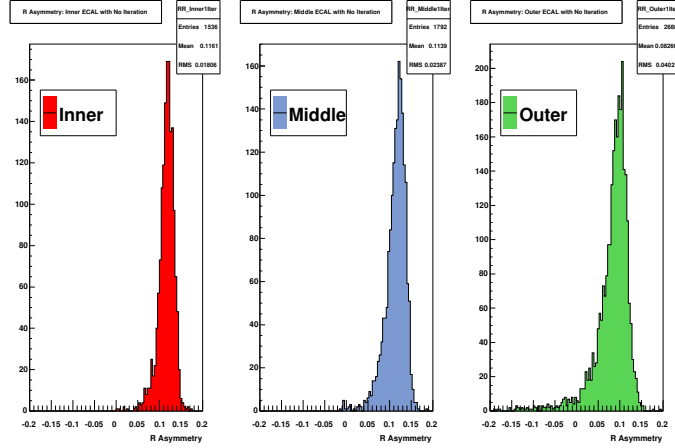


Figure 4.12: R_j asymmetry in the ECAL in the standard conditions, with the magnetic field off and without iteration.

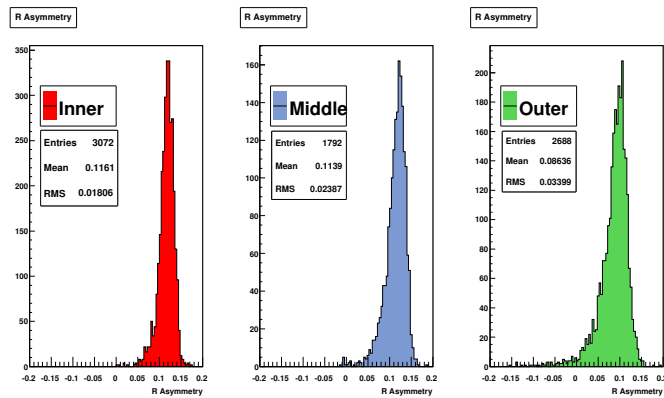


Figure 4.13: R_j asymmetry in the ECAL in the standard conditions, with the magnetic field off and after one iteration.

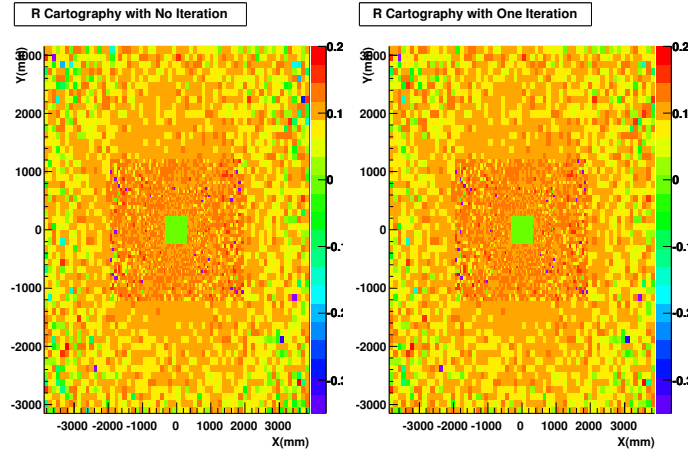


Figure 4.14: R_j cartography in the ECAL, without (left map) and with (right map) an iteration with the magnetic field off.

Area	Num of Iter.	$\langle R \rangle$	$rms(R)$	Good Cells
Inner	0	0.116	0.018	99 %
Inner	1	0.116	0.018	100%
Middle	0	0.113	0.023	99%
Middle	1	0.113	0.023	100%
Outer	0	0.082	0.040	75%
Outer	1	0.086	0.033	84%

Table 4.2: Summary table for the ECAL in time alignment the v200601-BOff conditions.

4.4.3 PilotRun conditions

At the beginning of the data taking, LHCb could run in the so called pilot run conditions, with 450 GeV proton beams. Therefore it is worth studying the behavior of the calorimeters in these conditions. We can see in Table: 4.3 that the rate of 'good' cells drops in the inner and middle ECAL when applying the same cuts as in the standard conditions in Table: 4.1. This is due to the fact that the multiplicity of the events in the pilot run conditions is much lower compared to the standard one. We illustrate this fact on Figure: 4.15 to illustrate this fact where we plot the energy in the **Current** sample versus the energy in the **Next1** sample, for the same cell, located in the inner ECAL in both conditions, using the same statistics.

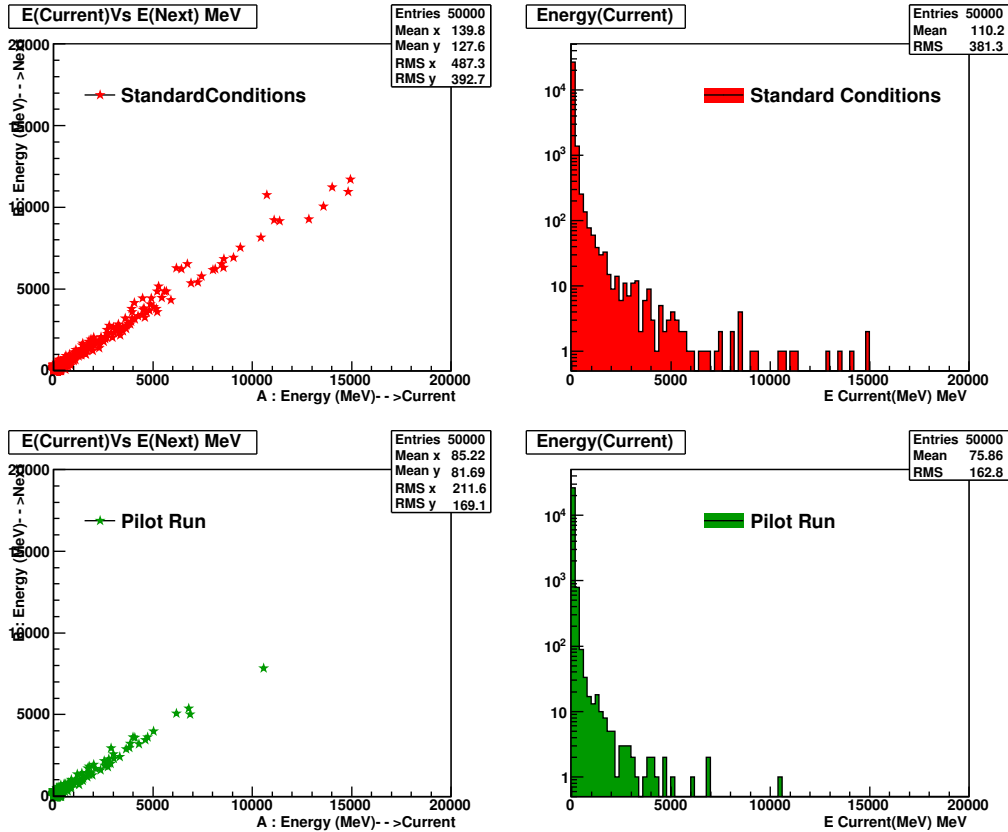


Figure 4.15: Energy(**Current**) Vs Energy(**Next1**) for a cell of the inner ECAL in the pilot run conditions and the standard conditions using 50k events respectively (left), energy spectrum in the **Current** in the pilot run and standard conditions (right).

Despite the low multiplicity, the amount of aligned cells in the outer ECAL is better: 71% after one iteration. This is due to the absence of magnetic field (which has the biggest impact on the outer region of the ECAL).

Understanding the frontier In Figure: 4.16 sharing the R_j cartography in the pilot run conditions, we notice a discontinuity of R_j at the frontier between the middle and the outer ECAL, where the occupancy in the cells is similar (this effect is present in the three conditions, but is most noticeable in the pilot run conditions). In order to understand this effect, we build a 'fake' middle ECAL.

Area	Numb. of Iter.	$E^T >$	$\langle R \rangle$	rms(R)	Good Cells
Inner	0	100 MeV	0.111	0.01	100%
Inner	1	100 MeV	0.111	0.01	100%
Inner	0	300 MeV	0.117	0.029	93%
Inner	1	300 MeV	0.117	0.029	93 %
Middle	0	100 MeV	0.091	0.023	95%
Middle	1	100 MeV	0.094	0.019	97%
Middle	0	300 MeV	0.109	0.037	89 %
Middle	1	300 MeV	0.10	0.037	89%
Outer	0	100 MeV	0.006	0.05	23%
Outer	1	100 MeV	0.043	0.034	48%
Outer	0	300 MeV	0.058	0.062	65%
Outer	1	300 MeV	0.081	0.047	71%

Table 4.3: Summary table for the ECAL time alignment in the pilot run conditions.

Instead of summing up the energy event by event in each cell, we consider blocks of 2 by 2 cells for the middle region in order to mimic the size of the outer cells. We are then left with 448 'fake' middle ECAL cells. In Figure: 4.17 we plot the R_j asymmetry in the 'fake' middle ECAL and in the outer ECAL in the pilot run conditions requiring:

$$E_{ij}^T(\mathbf{Current}) + E_{ij}^T(\mathbf{Next1}) > 300 \text{ MeV}. \quad (4.15)$$

The behavior of R_j in this artificial geometry is smoother and we no longer see the discontinuity around the frontier between the middle ECAL and the outer ECAL. Thus, this frontier was only due to the difference in the size of the cells.

4.5 Time alignment with minimum bias events in the HCAL in the pilot run conditions

We have used the same procedure for the hadronic calorimeter as for the electromagnetic one. We simulated ParticleGun events (Pions with a momentum of 100 GeV, coming for the interaction point and pointing to a given cell of

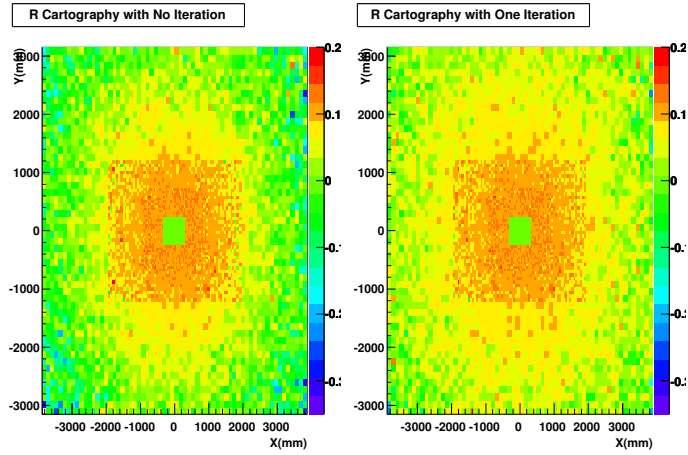


Figure 4.16: R_j cartography in the ECAL in the pilot run conditions.

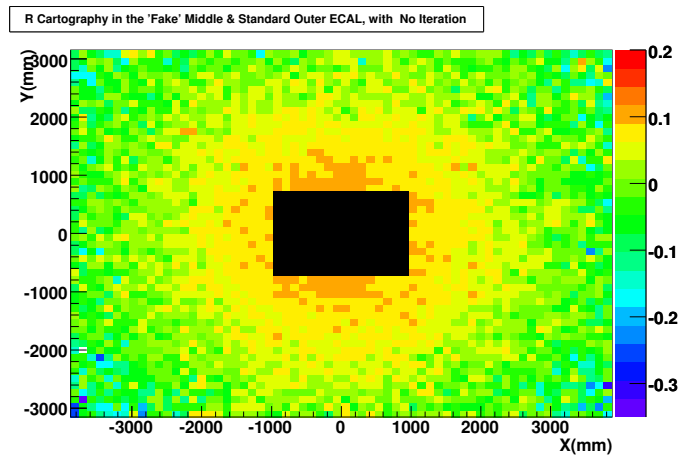


Figure 4.17: R_j cartography in the 'fake' middle ECAL and the outer ECAL in the pilot run conditions.

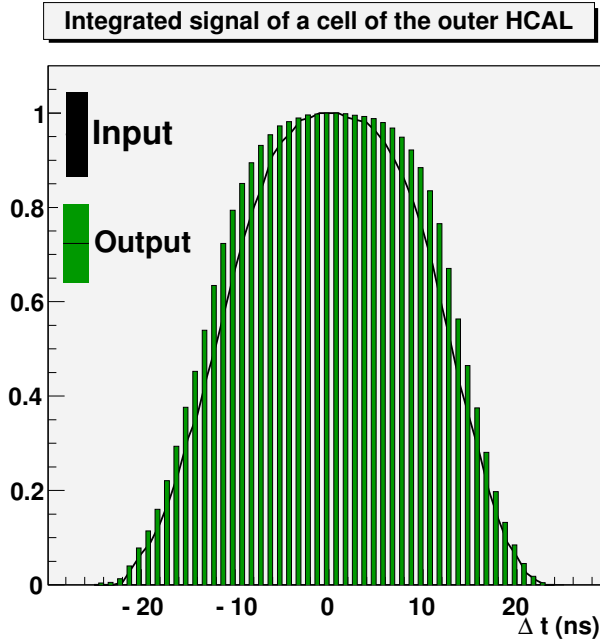


Figure 4.18: Distribution of the fraction of the total energy as a function of time, for a given cell of the outer HCAL.

the HCAL). The distribution of Figure: 4.18 is the integrated signal for a particular cell of the outer HCAL and Figure: 4.19 is its calibration distribution. This distribution is fitted with a simple straight line :

$$R_j = \alpha \times \Delta t + \beta \quad (4.16)$$

where, $\alpha = (-0.142 \pm 0.002)$ and $\beta = (1.895 \pm 0.031)$. We used again the method presented in Section: 4.3.4 to compute the errors on the mean value of the R_j asymmetry. To categorize a cell of the HCAL as a 'good' cell we have used the following criterium:

$$-0.02 < R_j < 0.12 \quad (4.17)$$

where, -0.02 corresponds to $\Delta t = 13.5$ ns and 0.12 to $\Delta t = 12.5$ ns. We have 57k generated minimum bias events in the pilot run conditions, with an initial constant misalignment of 13 ns. We require for each cell to have:

$$E_{ij}^T(\mathbf{Current}) + E_{ij}^T(\mathbf{Next1}) > 300 \text{ MeV} \quad (4.18)$$

In the summary Table: 4.5 we see that only 4% of the cells are not aligned, therefore it is not necessary to apply the iteration procedure. With an equivalent amount of data, generated in the ECAL and the HCAL in the same

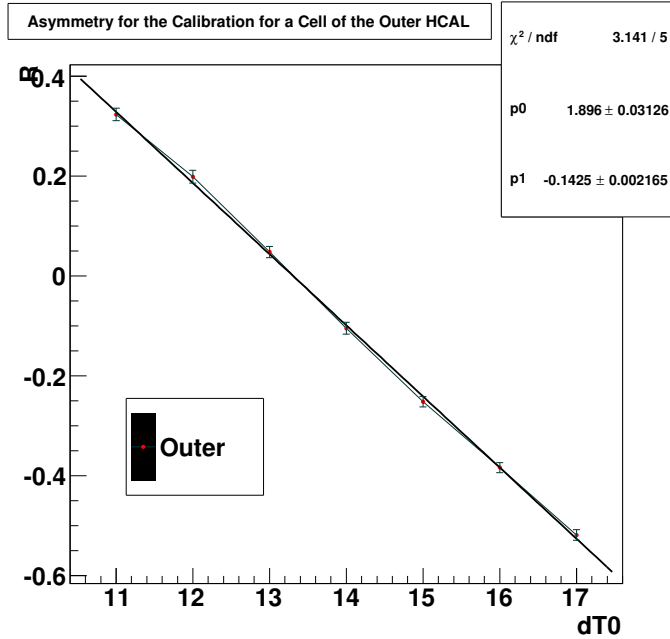


Figure 4.19: Calibration curve for a given cell of the outer HCAL.

PilotRun conditions the reached time alignment is better in the HCAL than the ECAL. Due to the fact that the HCAL cells are larger than the ECAL cells, with the same statistics and in the same conditions the reached precision of time alignment in the HCAL is better than in the ECAL.

Area	Num. of Iter.	$\langle R \rangle$	$rms(R)$	Good cells
Inner	0	-0.0004	0.04	99 %
Outer	0	-0.07	0.06	93%

Table 4.4: Summary table for the HCAL time alignment in the pilot run conditions.

4.6 Scan of the integrated signal

As we showed in this chapter the key ingredient to compute the time misalignment with the asymmetry method is the knowledge of the shape of the integrated signal. We anticipate from the time alignment with the cosmic events, that *in situ* the timing computation is biased. Therefore using data

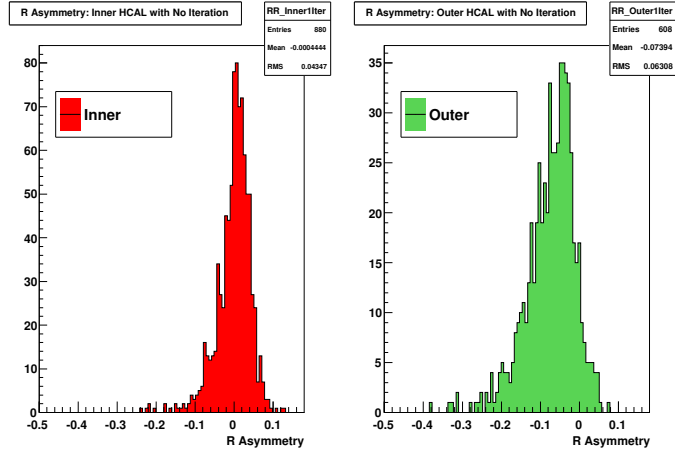


Figure 4.20: R_j asymmetry in the HCAL in the pilot run conditions without iteration.

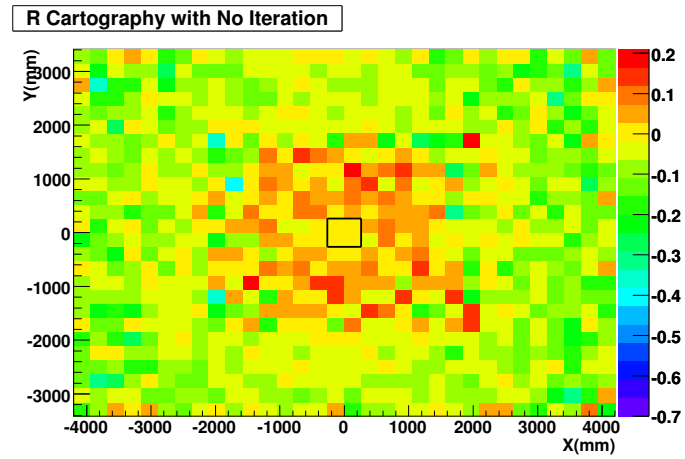


Figure 4.21: Cartography of R_j in the HCAL in the pilot run conditions without iteration.

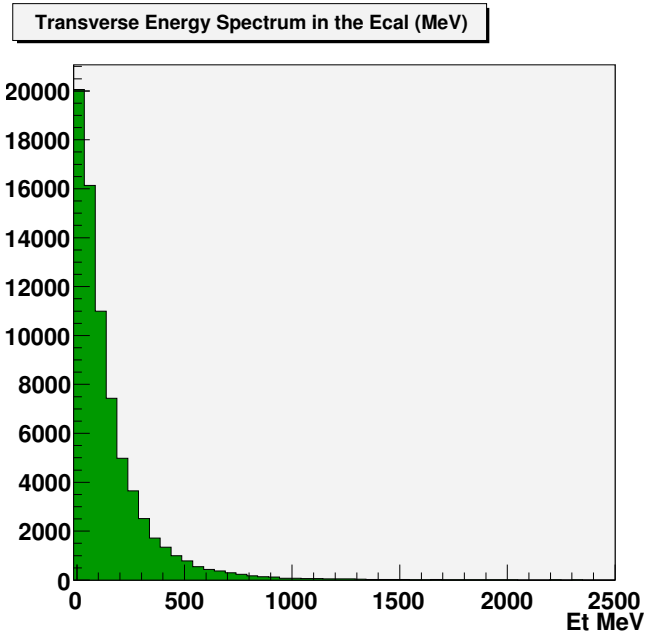


Figure 4.22: Distribution of the transverse energy (MeV) in the ECAL.

from the proton-proton collisions delivered by the LHC, we will scan the shape of the integrated signal. A possible scenario would be the following. We vary the sampling time in the ECAL from -25 ns to $+25$ ns using a 1 ns step. The HCAL sampling time will be set to the standard conditions since it will be used in the minimum bias L0 trigger, the PreShower sampling time is kept in the standard configuration too since it will be used to select cells of interest in the ECAL. At each step we collect a given amount of data. For that purpose we use a Monte Carlo simulation to evaluate what are appropriate sets of cuts to use, as well as the necessary amount of data to reach the needed precision. Given the exponential shape of the transverse energy in the ECAL (see Figure: 4.22) the mean value of this distribution would be directly correlated with a cut on this distribution. To avoid this bias, we require to have enough energy in a given PreShower cell and we pick the ECAL cell behind it, since the geometry of this two subdetectors is the same. We give an example of selected cells in both the PreShower and the ECAL in the event display of Figure 4.23. The cuts on the PreShower cells vary from one area to an other to take into account the fact that the multiplicity decreases from the inner region to the outer one. These cuts must be high enough to remove a large part of the low energy contributions (see

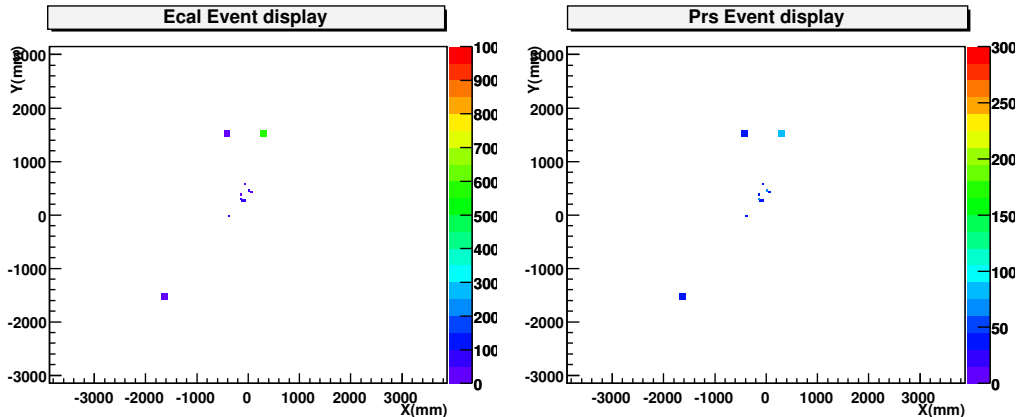


Figure 4.23: PreShower event display (left) and ECAL event display (right)

the pedestal distribution in Figure 4.24) in the ECAL. On the other hand, the integrated signal is flat within 1% around the plateau, therefore on each point the precision of the mean value of the transverse energy must be below 1%.

In Table: 4.6 we state the list of cuts in each area of the PreShower. We give the mean value of the transverse energy in the ECAL together with the obtained precision on the value $(\frac{\langle E^T \rangle}{\sqrt{N}})$, where N is the number of selected cells) for two sets of data, one generated with a time misalignment $\Delta t = 0$ ns corresponding to the top of the integrated signal and a second where $\Delta t = 12$ ns, corresponding to the mid-height of the integrated signal in the ECAL. The set of cuts which satisfy all of our requirement are $E(Prs) > 100, 60, 45$ MeV in the inner, middle and outer areas respectively. The Figure: 4.25 displays the distributions of the energy in the PreShower and the transverse energy in the ECAL for this set of cuts for data with $\Delta t = 12$ ns. In both cases we display the content of the **Current** sample. The distributions of Figure 4.26 show the transverse energy of the same events in the **Prev1** and **Next1** samples. As expected, we observe in the **Prev1** sample a peak around 0 MeV. The mean value of the transverse energy of the selected cells in the **Next1** sample represents 30% of what we have in the **Current** sample. As the simulations are time consuming (~ 12 hours for 500 events) we did not generate events for all the required steps of the scan. Nevertheless, we know that the integrated signal used as an input to the Monte Carlo is symmetric around 0 ns. For example, if we generate data with a time misalignment of 5 ns, the fraction of energy in the **Next1** container would

Area	$E(Prs) >$	$\langle E_t(ECAL(0ns)) \rangle$	$\frac{\sigma_{E^T(ECAL(0ns))}}{\langle E^T(ECAL(0ns)) \rangle}$	$\langle E_t(ECAL(12ns)) \rangle$	$\frac{\sigma_{E(ECAL)^T(12ns)}}{\langle E(ECAL)^T(12ns) \rangle}$	Num cells
Inner	70	211.41	0.38 %	148.78	0.48%	59624
Middle	40	197.22	0.51 %	138.43	0.68%	50041
Outer	30	221.25	0.42 %	155.28	0.57%	77243
Inner	100	272.68	0.51%	191.68	0.53%	27506
Middle	60	279.23	0.68%	197.28	0.72%	20989
Outer	45	303.84	0.57%	214.14	0.60%	33730
Inner	120	312.22	0.62%	219.35	0.65%	17104
Middle	80	364.43	0.89%	259.22	0.96%	9858
Outer	65	415.20	0.84%	296.22	0.89%	13001
Inner	150	366.13	0.82%	259.03	0.84%	8466
Middle	100	449.83	1.15%	326.77	1.25%	4979
Outer	80	498.76	1.09%	362.71	1.16%	6798

Table 4.5: Mean value of the transverse energy in the ECAL in each region in the **Current** sample for various sets of cuts in the PreShower for minimum bias events with $\Delta t = 0$ ns and $\Delta t = 12$ ns

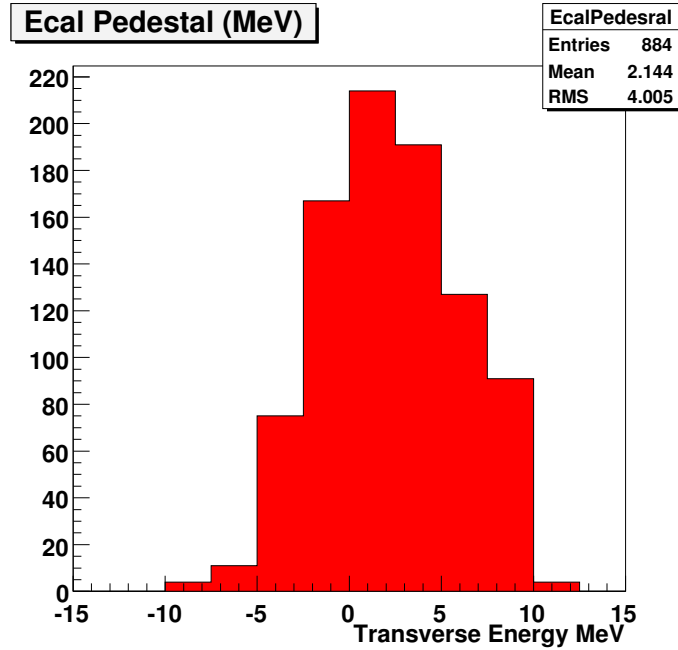


Figure 4.24: Pedestal distribution (E^T in MeV) in the ECAL.

correspond to a set of data generated with a time misalignment of 25 ns - 5 ns = 20 ns. We simulated 50 k events in the pilot run conditions for, $i = -2, 0, 2, 5, 12, 15, 18$ ns. In Table 4.6, we report the mean value of the transverse energy in the three samples of the TAE mode. In each zone the mean value of the transverse energy in the **Current** sample from the data generated with $\Delta t = 0$ ns is used for the normalization:

$$F(i) = \frac{\langle E^T(\mathbf{Current}(i)) \rangle}{\langle E^T(\mathbf{Current}(0ns)) \rangle} \quad (4.19)$$

and compared it for each value of Δt with $F_{theo}(i)$ obtained using ParticleGun events. The most significant deviation we observe is for $\Delta t = 12$ ns, where $F(12ns) - F_{theo}(12ns) = 0.03$, nevertheless this difference is small enough to not confuse this value with the one we would have obtained generating events with $\Delta t = 11$ ns or $\Delta t = 13$ ns. In Figure: 4.27 we display for every area, the integrated signal obtained with ParticleGun events and the computed fraction F for each value of Δt extracted from the minimum bias datasets. To conclude, we found a way to measure without any bias and the with needed precision the integrated signal shape.

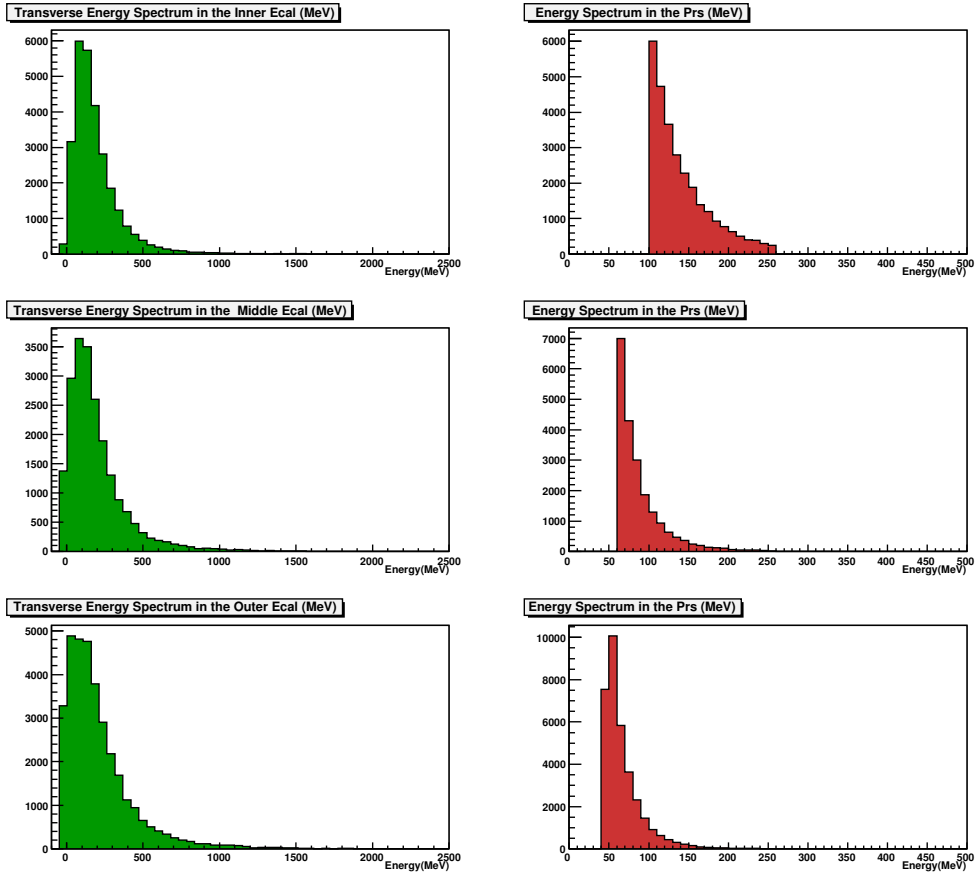


Figure 4.25: Transverse energy (MeV) in the ECAL (left distributions) and energy (MeV) in the PreShower(right distributions) in the **Current** sample, for the inner (top distributions), middle (middle distributions) and outer (bottom distributions) areas. These distributions are obtained with minimum bias events generated with $\Delta t = 12ns$ with the magnetic field off.

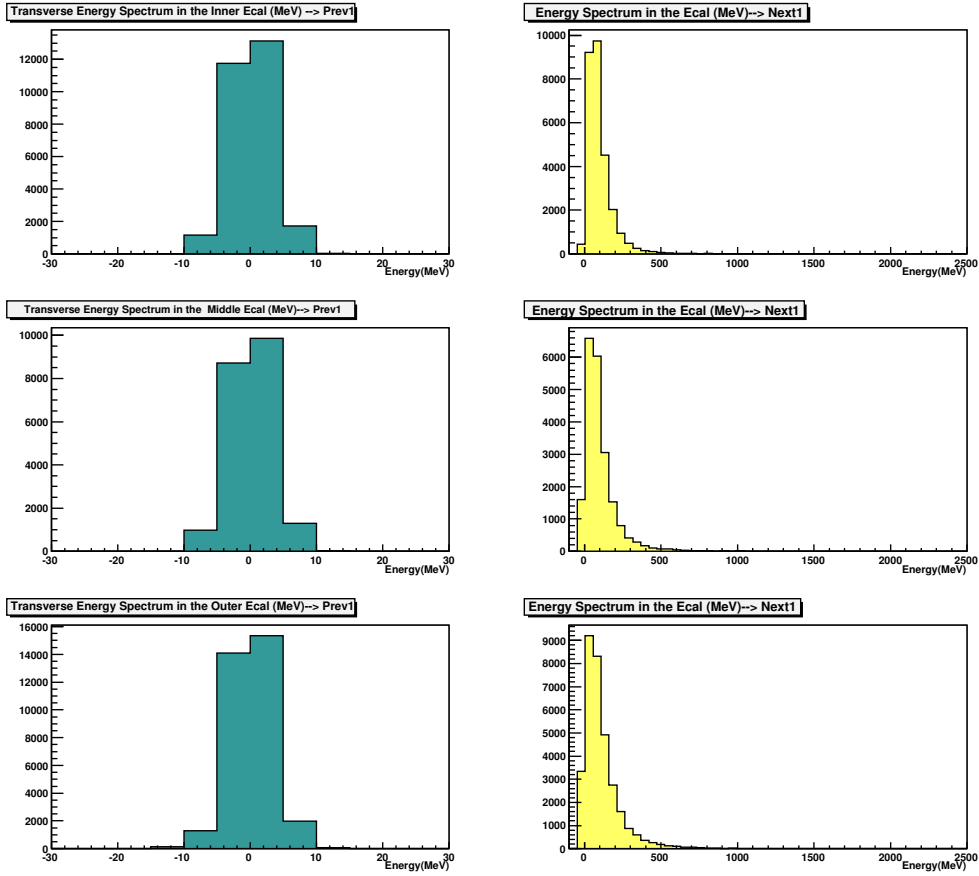


Figure 4.26: Transverse energy (MeV) in the ECAL in the **Prev1** sample(left distributions) and transverse energy (MeV) in the ECAL in the **Next1** sample (right distributions) for the inner (top distributions), middle (middle distributions) and outer (bottom distributions) areas. These distributions are obtained with minimum bias events generated with $\Delta t = 12ns$ with the magnetic field off.

Area(i = timing ns)	$\langle E^T(Current(i)) \rangle$	$\langle E^T(Next1(i)) \rangle$	$\langle E^T(Prev1(i)) \rangle$	$\frac{\langle E^T(Current(i)) \rangle}{\langle E^T(Current(i=0)) \rangle} / F_{Theo}(i)$	$\frac{\langle E^T(Next1(\Delta t(i))) \rangle}{\langle E^T(Current(i=0)) \rangle} / F_{Theo}(i)$	$\frac{\langle E^T(Prev1(\Delta t(i))) \rangle}{\langle E^T(Current(i=0)) \rangle} / F_{Theo}(i)$	Num.cells
I. ($\Delta t = -2$ ns)	267.11 ± 1.37	0.05 ± 0.01	0.06 ± 0.01	$(0.979 \pm 0.007) / 0.980$	0/0	0/0	27888
M. ($\Delta t = -2$ ns)	276.04 ± 1.90	0.03 ± 0.02	0.04 ± 0.01	$(0.989 \pm 0.009) / 0.980$	0/0	0/0	20832
O. ($\Delta t = -2$ ns)	299.89 ± 1.74	0.12 ± 0.02	0.07 ± 0.01	$(0.986 \pm 0.008) / 0.980$	0/0	0/0	33588
I. ($\Delta t = 0$ ns)	272.68 ± 1.40	0 ± 3.25	0 ± 0.45	1/1	0/0	0/0	27506
M. ($\Delta t = 0$ ns)	279.23 ± 1.91	0 ± 3.37	0 ± 0.39	1/1	0/0	0/0	20989
O. ($\Delta t = 0$ ns)	303.84 ± 1.75	0 ± 4.29	0 ± 0.49	1/1	0/0	0/0	33730
I. ($\Delta t = 2$ ns)	273.41 ± 1.39	0.08 ± 0.01	0 ± 0.01	$(1.001 \pm 0.007) / 0.990$	0/0	0/0	27827
M. ($\Delta t = 2$ ns)	280.26 ± 1.93	0.05 ± 0.02	0 ± 0.01	$(1.001 \pm 0.008) / 0.990$	0/0	0/0	20930
O. ($\Delta t = 2$ ns)	304.34 ± 1.76	0.27 ± 0.02	0 ± 0.01	$(1.001 \pm 0.008) / 0.990$	0/0	0/0	33517
I. ($\Delta t = 5$ ns)	267.29 ± 1.37	8.37 ± 0.05	0 ± 0.01	$(0.980 \pm 0.007) / 0.978$	$(0.030 \pm 0.0002) / 0.039$	0/0	27628
M. ($\Delta t = 5$ ns)	275.04 ± 1.88	8.31 ± 0.07	0 ± 0.01	$(0.984 \pm 0.009) / 0.978$	$(0.029 \pm 0.0002) / 0.039$	0/0	20938
O. ($\Delta t = 5$ ns)	298.50 ± 1.72	9.89 ± 0.07	0 ± 0.01	$(0.982 \pm 0.008) / 0.978$	$(0.032 \pm 0.0002) / 0.039$	0/0	33657
I. ($\Delta t = 12$ ns)	191.68 ± 1.02	98.10 ± 0.54	0 ± 0.01	$(0.701 \pm 0.005) / 0.67$	$(0.359 \pm 0.002) / 0.39$	0/0	28141
M. ($\Delta t = 12$ ns)	197.28 ± 1.43	100.56 ± 0.77	0 ± 0.01	$(0.706 \pm 0.007) / 0.67$	$(0.360 \pm 0.003) / 0.39$	0/0	20913
O. ($\Delta t = 12$ ns)	214.14 ± 1.29	111.86 ± 0.70	0 ± 0.01	$(0.704 \pm 0.005) / 0.67$	$(0.368 \pm 0.003) / 0.39$	0/0	33865
I. ($\Delta t = 15$ ns)	119.41 ± 0.64	158.41 ± 0.85	0 ± 0.01	$(0.437 \pm 0.003) / 0.35$	$(0.580 \pm 0.004) / 0.59$	0/0	27912
M. ($\Delta t = 15$ ns)	125.34 ± 0.91	163.67 ± 1.19	0 ± 0.01	$(0.448 \pm 0.002) / 0.35$	$(0.586 \pm 0.004) / 0.59$	0/0	20964
O. ($\Delta t = 15$ ns)	137.31 ± 0.88	182.47 ± 1.13	0 ± 0.01	$(0.451 \pm 0.003) / 0.35$	$(0.600 \pm 0.005) / 0.59$	0/0	33554
I. ($\Delta t = 18$ ns)	58.63 ± 0.31	216.38 ± 1.13	0 ± 0.01	$(0.215 \pm 0.001) / 0.194$	$(0.793 \pm 0.05) / 0.800$	0/0	27835
M. ($\Delta t = 18$ ns)	61.69 ± 0.45	221.98 ± 1.56	0 ± 0.01	$(0.220 \pm 0.002) / 0.194$	$(0.794 \pm 0.07) / 0.800$	0/0	20835
O. ($\Delta t = 18$ ns)	67.32 ± 0.44	245.91 ± 1.46	0 ± 0.01	$(0.221 \pm 0.001) / 0.194$	$(0.809 \pm 0.006) / 0.800$	0/0	33408

Table 4.6: Summary table of the mean value of the transverse energy for various steps of the scan in the **Current**, **Next1** and **Prev1** samples and comparison of the measured fractions $F(i)$ with the theoretical one $F_{theo}(i)$.

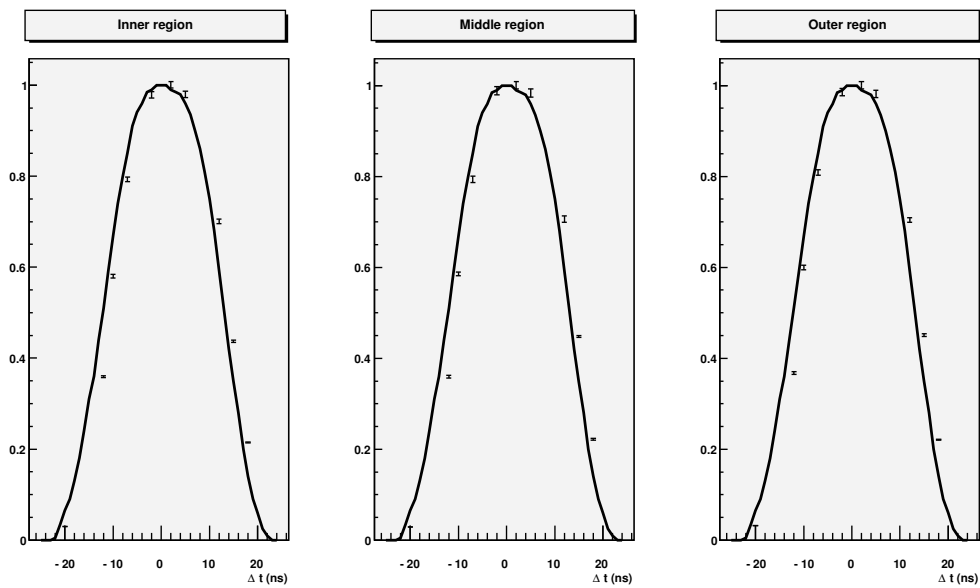


Figure 4.27: Integrated signal($F(i)_{theo}$) obtained with ParticleGun simulated data (plain line), the points correspond to the measured $F(i)$ for each step of the scan (the errors are statistical) for the inner, middle and outer region (from left to right).

4.7 Conclusion

In order to study the time misalignment for the ECAL and HCAL a method for accessing the energy deposits cell by cell on simulated and digitized MonteCarlo data has been implemented in the LHCb software framework. The proposed procedure to achieve the time alignment based on a calibration distribution has been studied separately for the ECAL and the HCAL. In both cases we have shown that the region around the mid-height of the integrated signal distribution was the most sensitive one to the sources time misalignment. For the ECAL the procedure was tested under three conditions. We have seen that in the standard conditions with the magnetic field off, we were able to make a time alignment with a precision better than 0.5 ns for 95% of the cells using 55k minimum bias events. Regarding the HCAL, 96 % of the cells could be aligned under the pilot run conditions with a precision better than 0.5 ns with 57k minimum bias events.

Chapter 5

Time alignment with cosmics data

ALLEMANDE



Johann Sebastien Bach - BWV 1007
Suiten für Violoncello solo Nr.2 d-Moll

Readiness tests started in winter 2008 involving cosmic studies, as the apparatus was able to detect cosmic rays. From the calorimeters point of view, studying cosmics data allowed to test the existence of dead channels, to test *in situ* the calorimeter noise, to fully test the data acquisition from the electronics front end cards up to the writing on disk and to perform offline analysis of this data. In this chapter, we will focus on how cosmics events were reconstructed and selected to be used for the time alignment of the electromagnetic and hadronic calorimeters.

5.1 Detection of cosmics at LHCb

In order to compute the amount of cosmic rays one could expect in the LHCb detector, extrapolations based on studies done for the detectors Aleph, Delphi and L3 were made [53], [54]. Through their passage from the surface to the

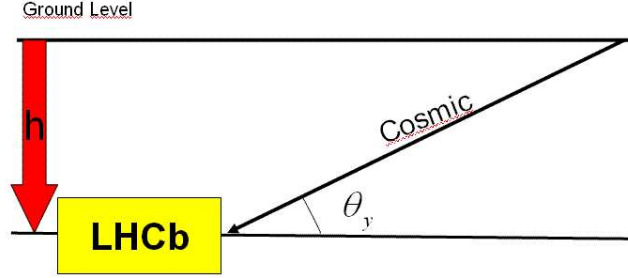


Figure 5.1: Illustration of a cosmic events detected at LHCb.

detector muons are mainly sensitive to energy loss:

$$\frac{dE}{dx} = (0.21\text{GeV} + 4 \times 10^{-4}E(\text{GeV}))/mwe \quad (5.1)$$

where, mwe is the meter water equivalent, which is about $110 \text{ g}\cdot\text{cm}^{-2}$ of rock, the second term corresponds to loss by bremsstrahlung, pair production, the contribution of these effects is estimated to vary between 10% and 20%. The LHCb depth is about 184 mwe , the minimum energy at the surface of a vertical muon which can reach the calorimeter is therefore 43 GeV and for 60 degrees angle the energy at the surface has to be greater than 92 GeV. For muons above $E_{threshold} = 43 \text{ GeV}$ at the surface, the angular distribution is flat. Hence at LHCb, the only angle effect to be considered comes from the $\frac{dE}{dx}$ and the energy spectrum. Hence down to the cavern where LHCb is located (see Figure: 5.1), the energy loss and the energy spectrum of the cosmics will be a function of their direction. It was shown that the muon flux at the surface is about $\frac{0.25}{E^3} \text{ GeV}^{-3}\text{cm}^{-2}\text{s}^{-1}\text{str}^{-1}$ where the coefficient 0.25 can vary down to 0.2 for 300 GeV muons. We have for the integrated flux:

$$F = F(E, \theta_y) = \int_{E=E_{threshold}}^{+\infty} \frac{0.25}{E^3} dE = \frac{0.125}{E_{threshold}^2} \text{GeV}^{-2}\text{cm}^{-2}\text{s}^{-1}\text{str}^{-1} \quad (5.2)$$

To integrate the flux of quasi horizontal muons in 2×2 HCAL modules cluster used in the trigger system, we make the simplifying assumption that we can integrate independently in x and θ_x , and in y and θ_y and that the angle θ_x has no influence on the path through the rock. We call f_x the result of the integral over x and f_y the result of the integration over y . Except for the HCAL edges, muons can produce a 2×2 trigger if they are contained in a module and its right or left neighbours, this defines the angle $\theta_x = \frac{3 \times L_x}{L_z}$

illustrated in the right schema of Figure: 5.2, where $L_x = L_y = 26$ cm and $L_z = 120$ cm correspond to the size of a HCAL outer module. Therefore we can write for the integration of the x part:

$$f_x = \int_{x=0}^{x'=L_x} \int_{\theta'_x=0}^{\theta'_x=\theta_x} dx' d\theta'_{x'} = 26 \times 3 \times \frac{26}{120}. \quad (5.3)$$

We define:

$$l = \frac{h}{\sin\theta_y} \text{ since } \theta_y \text{ is small we have: } l \sim \frac{h}{\theta_y}. \quad (5.4)$$

l and h are illustrated in Figure: 5.1. The energy at the ground level varies with the direction of the cosmic: $\frac{E_{threshold}}{\theta_y} = \frac{43\text{GeV}}{\theta_y}$ and the flux is given by:

$$\frac{0.125}{E_{threshold}^2} \times \theta_y^2 = \frac{0.125}{43^2} \times \theta_y^2 \quad (5.5)$$

where θ_y can vary between 0 and $\frac{2 \times (L_y - y)}{L_z}$ and y can varie between 0 and L_y , as shown in Figure: 5.2. Thus:

$$\begin{aligned} f_y &= \int \int F(E, \theta_{y'}) dy' d\theta_{y'} \\ f_y &= \int \int \frac{0.125}{E_{threshold}^2(\theta_y)} dy' d\theta_{y'} \\ f_y &= 0.125/43^2 \int_{y'=0}^{y'=L_y} \int_{\theta'_{y'}=0}^{\theta'_{y'}=(52-y')/120} \theta_{y'}^2 dy' \end{aligned}$$

Putting all the parts in x and in y parts together, we obtain per HCAL module the following rate for muons fully contained in 2×2 modules, coming in the beam direction:

$$R = f_x \times f_y = 2.4 \times 10^{-4} \text{ muons per second, per module} \quad (5.6)$$

The predicted total rate of these muons in 608 modules is therefore about 0.15 per second. However the trigger threshold that had been set, selected also muons not fully contained in 2×2 modules. Therefore, the trigger rate was a few muons per second. In this computation the trigger selects cosmic events going through the ECAL first. Finally, both kind of cosmics were reconstructed (cosmics going through the ECAL first, or cosmics going through the HCAL first) explaining a factor 2 between the predicted rate and the observed one.

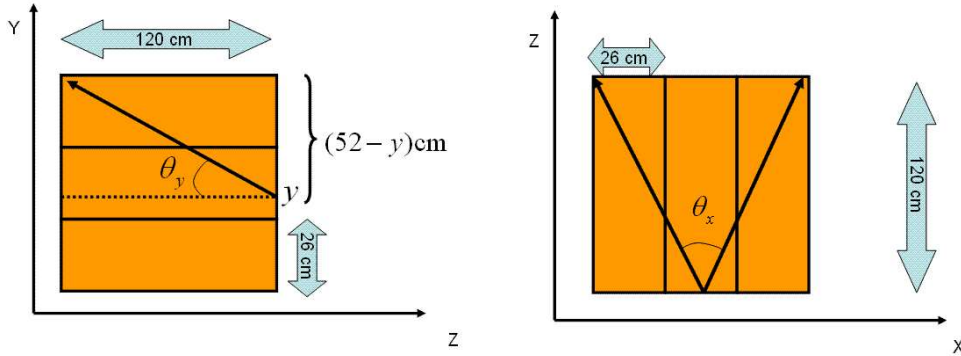


Figure 5.2: Illustration of the angles θ_x and θ_y in the HCAL modules.

5.2 Setup for cosmics acquisition

We describe in this section the properties of cosmic events and what are the necessary settings and requirements to be able to record these data, as well as the encountered limitations.

Cosmics asynchronization The final goal, is to have the calorimeters synchronized with the global LHC clock, itself being synchronized with the 40 MHz LHCb clock. Even though cosmic events are random with respect to the global LHC clock, it is possible using a dedicated trigger setting, to perform a "relative" time alignment of the sub detectors between themselves.

Low statistics LHCb was able to record over a million of cosmic events on tape. Because of the lack of synchronization of the cosmics, this amount of data were not sufficient to perform a cell by cell time alignment of the ECAL and the HCAL. This fine tuning will be performed using beam gas events or particles coming from the proton proton collisions.

Photomultiplier's gain In order to be able to record cosmic events in LHCb, dedicated conditions in terms of photomultiplier gain were used. In the "Physics" conditions *i.e* for the acquisition of data coming from the LHC collisions, the gain of the PMTs are set such that the full scale of the ADC corresponds to a transverse energy of 10 GeV. Thus the gain depends upon

the PMT position and it varies between: 1×10^5 and 4×10^4 for the ECAL and between 2×10^4 and 1.5×10^3 for the HCAL. For cosmic ray data-taking a uniform gain was implemented with 3×10^5 for the ECAL and 2×10^5 in the case of the HCAL. A muon passing fully through the ECAL module generates about 1000 photoelectrons in the PMT, while 200 are produced for the HCAL.

Level-0 trigger requirements The simplest kind of L0 trigger would be to use an "*ECAL only*" or "*HCAL only*" trigger. In practice this means for each sub detector:

- Requiring a 2×2 cluster in the HCAL above a given very low threshold, without adding an ECAL requirement in front of it. This is referred as a "hadron candidate".
- Requiring a 8×4 cluster in the ECAL above a very low threshold, without using a PS/SPD validation. This is referred as a "Local π^0 " candidate.

In situ, it appeared that the noise, due to the presence of cells above threshold and not corresponding to of deposit a cosmic, was high. This affected the acquisition rate, which was too high ~ 100 kHz. Since using the sub-detectors separately in the trigger was giving too high rates, a trigger based on both the ECAL and the HCAL was used. A configuration referred to as *Calo Only*, based on a *coincidence* between a 2×2 cluster in the HCAL and a 2×2 cluster in the ECAL (not necessarily in corresponding cells), triggered mostly on horizontal cosmic and not on noise, giving a rate of 12 Hz. During the commissioning period, other types of triggers, called L0 trigger, configuration Key (L0-TCK) were used. For example:

- a coincidence between two muon chambers;
- a coincidence between the muon chambers and the HCAL or ECAL;
- a SPD multiplicity higher than 10.

Units of energy In the absence of dedicated energy calibration for cosmic events, the energy deposits in the calorimeter, referred to as E, are kept in ADC counts and not the usual MeV or GeV units.

5.3 Cosmics reconstruction

Dedicated algorithms were designed to reconstruct cosmics tracks in the calorimeters. We will first describe the various requirements from the point of view of tracking and timing that need to be fulfilled by an event to be used in the time alignment analysis of the ECAL and HCAL.

Data acquisition settings To be able to perform the time alignment analysis, it is necessary to record data using the dedicated Time Alignment Event (TAE) data format. At LHCb it is possible to record from 3 consecutive events up to 13. In chapter 4 where we discussed the feasibility of the time alignment, we showed that the shape of an integrated signal in the ECAL or the HCAL is contained within ± 25 ns. Therefore we know that starting from any time misaligned configuration the energy deposits of a cosmic can not be "seen" in more than 2 consecutive containers (this argument holds for energy deposits from collision events too). For example, if a cosmic is "seen" in the central (**Current**) container, it can be "seen" as well in the **Next1** (called simply **Next** in the rest of the text) but not in the **Next2**. This is shown in the ECAL event display of Figure: 5.3. Even though the L0 trigger setting is such that most of the recorded events are indeed cosmics, noisy cells remain. A cut called zero suppression is applied on the sum of the energy (in terms of ADC counts) of consecutive containers, we require for each cell:

$$(E(\mathbf{Next1}) + E(\mathbf{Current}) + E(\mathbf{Prev1})) > 100 \text{ for the ECAL} \quad (5.7)$$

$$(E(\mathbf{Next1}) + E(\mathbf{Current}) + E(\mathbf{Prev1})) > 10 \text{ for the HCAL} \quad (5.8)$$

The cut applied for the ECAL is higher than the one in the HCAL, because it was seen during the commissioning that the ECAL photomultiplier bases were more noisy than expected [55]. This issue has been fixed in winter 2008. As explained in Chapter 2, the expected signal for a fully contained muon is 5 times larger in the ECAL than in the HCAL. The ADC spectrum is shown in Figure: 5.4 of cosmics events in the ECAL (left distribution) and in the HCAL (right distribution). To determine if the energy deposits of a cosmic event were shared between the central **Current** and **Prev1** containers or **Current** and **Next1**, as it is illustrated in Figure: 5.5, we sum the ADC counts of the cells after the zero suppression of a pair of samples

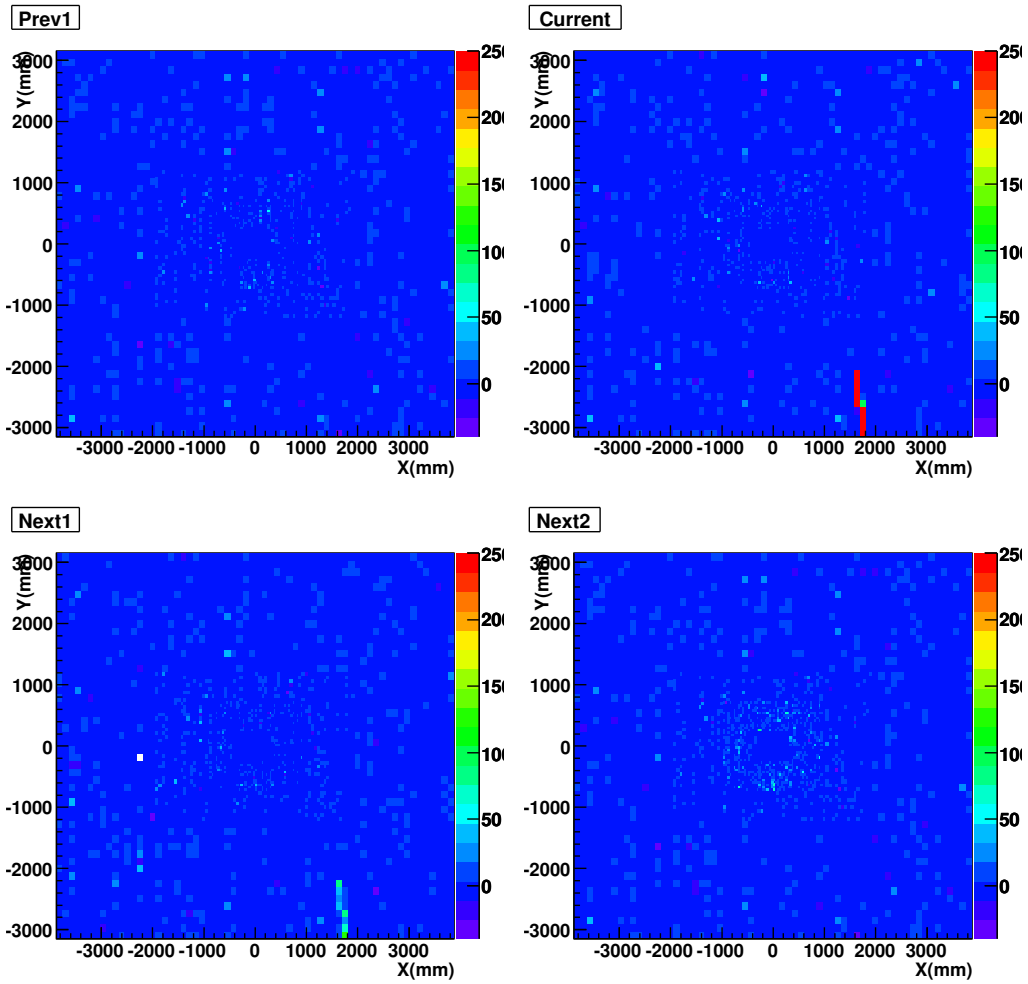


Figure 5.3: Event displays of a "raw" (before applying zero suppression) cosmic event seen in the ECAL in the **Prev1** (top, left), **Current** (top, right), **Next1** (bottom, left) and **Next2** (bottom, right) samples.

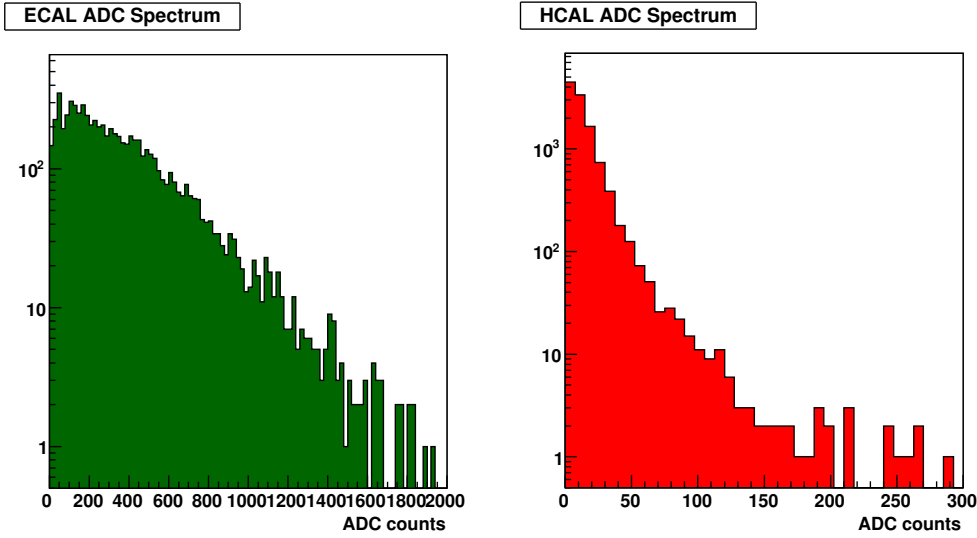


Figure 5.4: ADC spectrum in logarithmic scale of cosmic events in the ECAL (left distribution) and in the HCAL (right distribution).

and compare $(E(\mathbf{Current}) + E(\mathbf{Next1}))$ and $(E(\mathbf{Current}) + E(\mathbf{Prev1}))$. If $(E(\mathbf{Current}) + E(\mathbf{Next1})) > (E(\mathbf{Current}) + E(\mathbf{Prev1}))$ then the energy deposits were shared between the **Current/Next1** sample. The ECAL top event display in Figure: 5.6 shows the same cosmic event as the bottom one of the same figure after applying the zero suppression (to highlight the impact of this cut we display only cells above 0 ADC counts). In each sub detector (ECAL and HCAL) we select also the reference cell with the highest energy deposit (x_0, y_0) .

A two dimensional trajectory In each plane of the ECAL and the HCAL we look for a two dimensional line using the following equation:

$$\phi = \frac{\sum_i \text{atan}(y_i - y_0)/(x_i - x_0)}{\sum_i \omega_i}, \quad (5.9)$$

where, x_i and y_i are the coordinates of each selected cell and E_i its energy, so that $d_i = \sqrt{(x_0 - x_i)^2 + (y_0 - y_i)^2}$ and $\omega_i = E_i/d_i$. Then we compute the average position in x and y of the cosmic cluster in the ECAL and the HCAL shown in Figures: 5.8 and 5.9, requiring at least 2 cells above the zero suppression threshold. In Figure: 5.7, we show the multiplicity (number of cells above the threshold) in the ECAL (left distribution) and in the HCAL

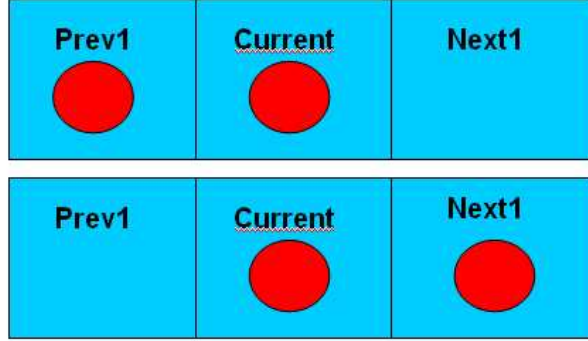


Figure 5.5: Representation of a cosmic event seen in the "**Prev1**" container and in the "**Current**" container (top scheme). Representation of a cosmic event seen in the "**Current**" container and the "**Next1**" container (bottom scheme).

(right distribution). When studying the relative time alignment between the ECAL and the HCAL, the distance between a cluster in the ECAL and a cluster in the HCAL is used as well as the direction of the cosmic. We anticipate the fact that for low multiplicity events, the direction of the cosmic can be badly reconstructed, therefore we apply a cut on the multiplicity of the clusters in each sub-detector. We require to have at least 4 cells in the ECAL and 3 cells in the HCAL. The best two dimensional line assuming it passed through the reference point (x_0, y_0) and the best value of ϕ are the ones that minimize the following χ^2 :

$$\chi^2 = \sum_i \frac{E_i(\phi_i - \phi)^2}{\sigma_i^2} \quad (5.10)$$

$$\sigma = \frac{D}{\sqrt{12}}, \text{ where } D \text{ is the cell size.} \quad (5.11)$$

In Figure: 5.10 we show the ϕ distribution, the peak at $\frac{\pi}{2}$ rad corresponds to the cases where the fit failed.

A three dimensional trajectory We combine the information collected from both ECAL and HCAL clusters and define the angle ϕ using:

$$\phi = \text{atan} \frac{\bar{x}_{ECAL} - \bar{x}_{HCAL}}{\bar{y}_{ECAL} - \bar{y}_{HCAL}} \quad (5.12)$$

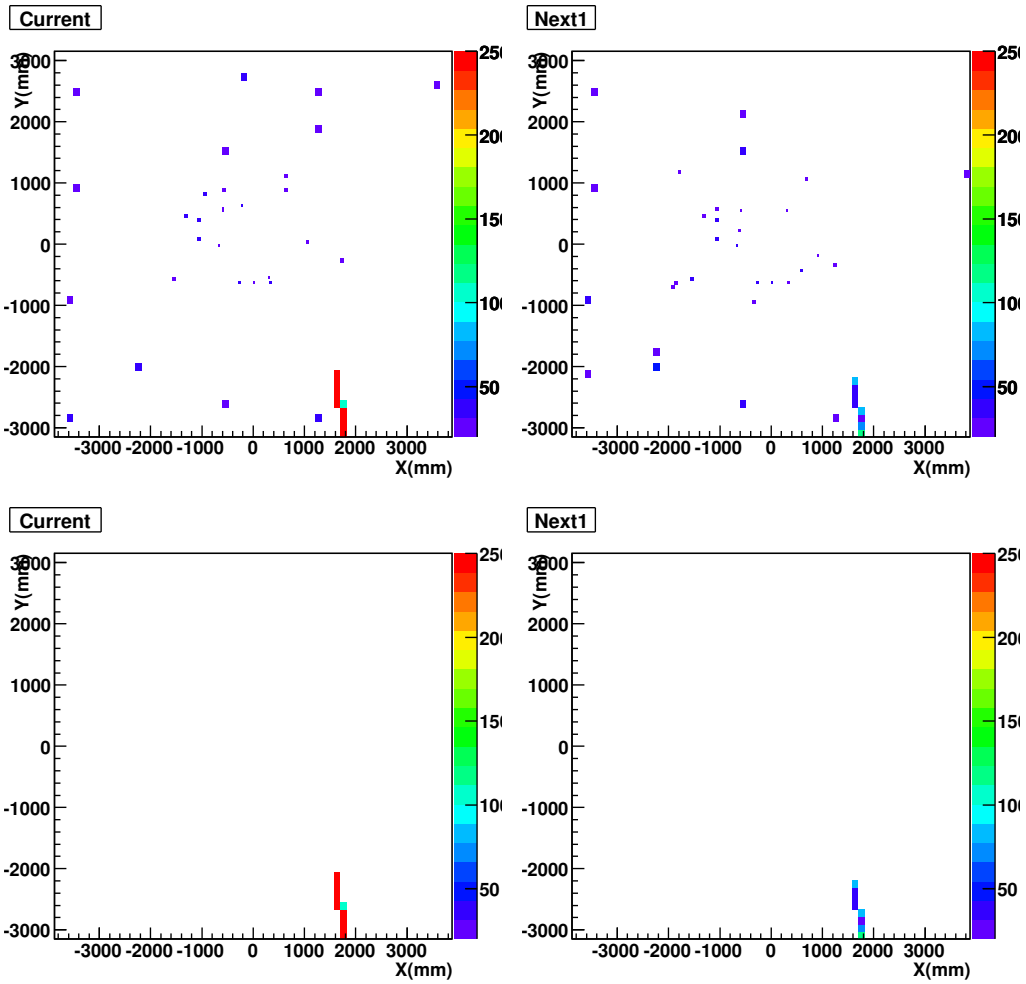


Figure 5.6: Event display of a cosmic in the ECAL before (top) and after (bottom) applying zero suppression seen in both the **Current** and **Next1**.

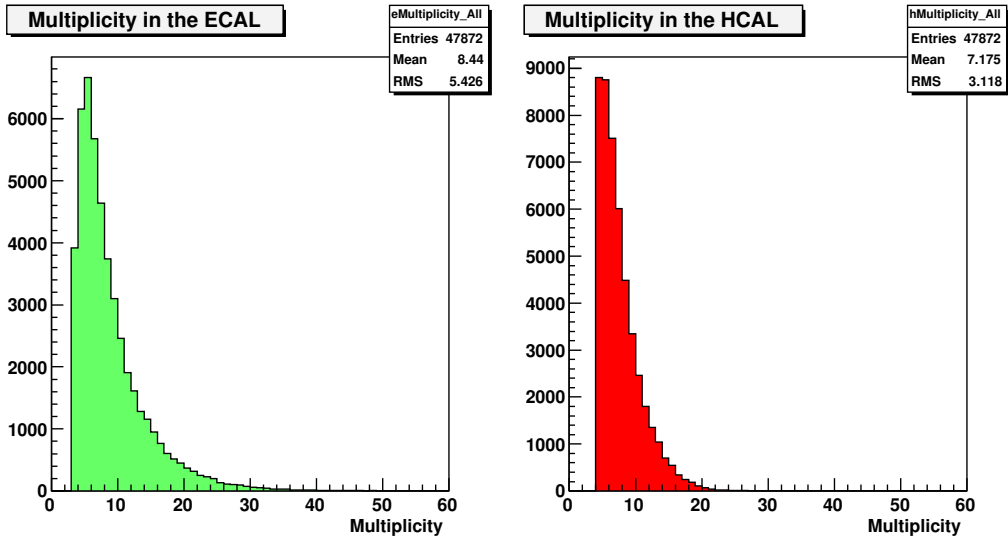


Figure 5.7: Multiplicity (number of cells above threshold) in the ECAL (left distribution) and in the HCAL (right distribution).

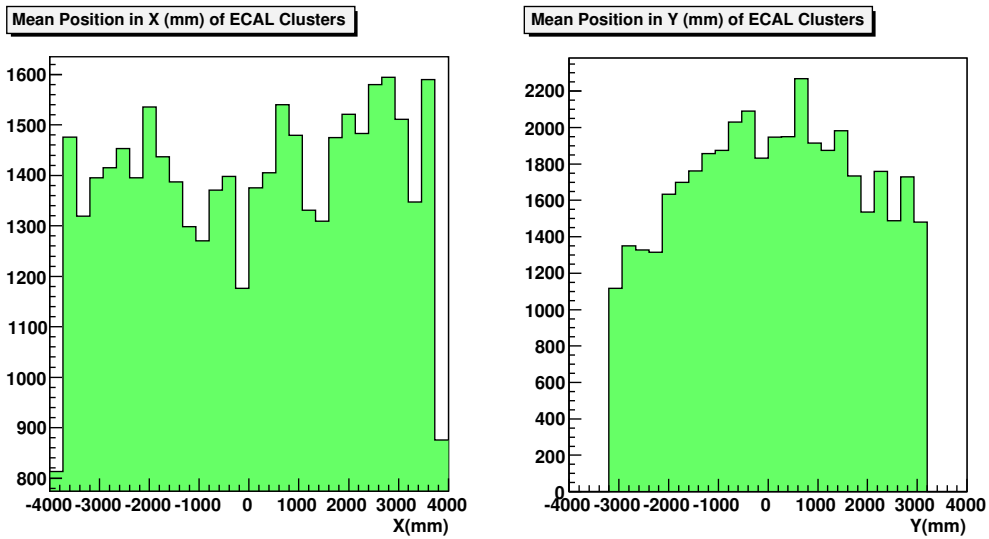


Figure 5.8: X coordinate (left distribution) and Y coordinate (right distribution) of clusters in the ECAL

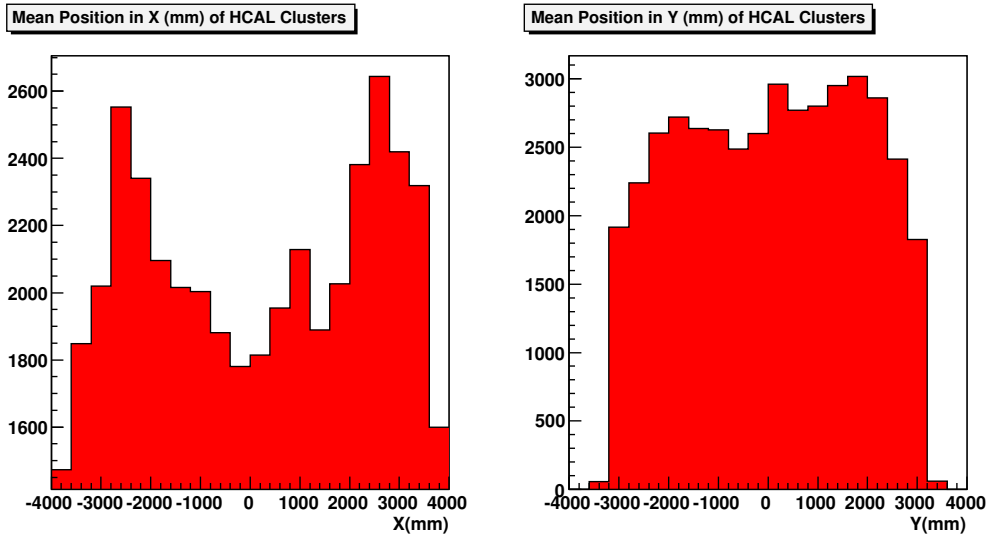


Figure 5.9: X coordinate (left distribution) and Y coordinate (right distribution) of clusters in the HCAL

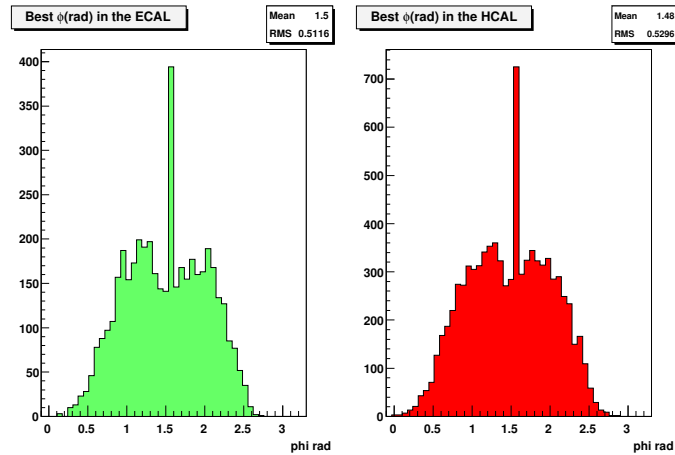


Figure 5.10: ϕ distribution of selected clusters in the ECAL (left distribution) and in the HCAL (right distribution)

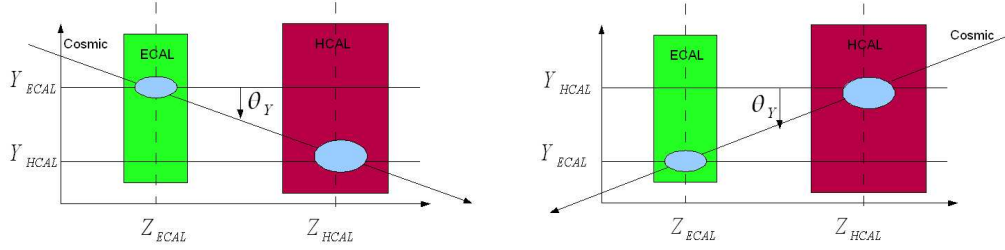


Figure 5.11: Representation of Forward cosmic (left schema) and a Backward cosmic (right schema)

We define two categories of tracks; Forward Tracks, tracks passing the ECAL first (see left illustration of Figure: 5.11) where: $y_{ECAL} > y_{HCAL}$ and Backward Tracks, tracks passing the HCAL first (see right illustration of Figure: 5.11) where $y_{HCAL} > y_{ECAL}$. A track is selected if $\chi^2 < 15$ as shown in Figure: 5.12.

Time information We have shown in Chapter 4 that, using a method based on an "asymmetry" R and a dedicated calibration distribution we were able to convert measurable asymmetries into "time".

One can measure for each selected cell in an ECAL or HCAL cluster the value of the asymmetry and compute the mean value of the asymmetry and the sigma of the asymmetry for each cluster using:

$$\langle R \rangle = \sum_j r_j / N \text{ where } N \text{ is the number of cells in a cluster.} \quad (5.13)$$

In Figure: 5.14 we show the distribution of the asymmetry extracted from the Monte Carlo analysis as a function of time. This distribution is empirically described with the following function:

$$\Delta t = 1.4 - 0.7 \times R^2 + \frac{25}{\pi} \times \arccos\left(\frac{R}{1 + 0.19 * \sqrt{1 - R^2}}\right). \quad (5.14)$$

One can notice the absence of sensitivity for values of $|R| > 0.8$ (see Figure: 5.14). For a track to be used from the point of view of time alignment we require for each of the ECAL and HCAL clusters to have $|R| < 0.8$. Using Equation: 5.3 we compute a mean value for the "time" for a cluster in both the electromagnetic and hadronic calorimeter (see Figure: 5.15). The gap in the middle of these distributions correspond to the requirement $|R| < 0.8$.

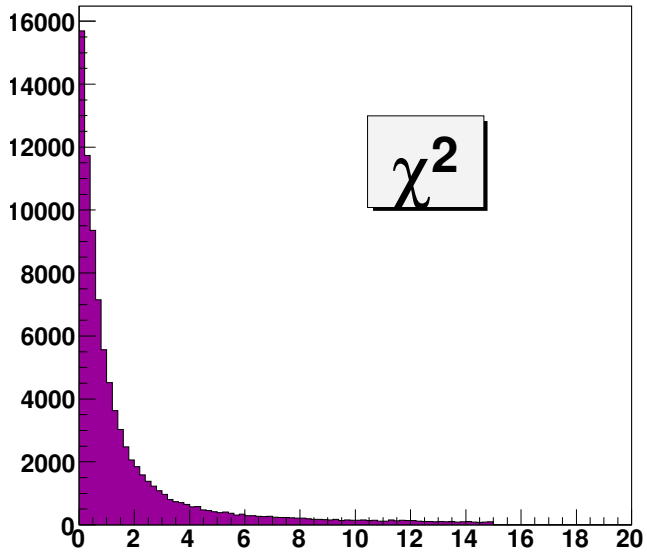


Figure 5.12: χ^2 of selected tracks.

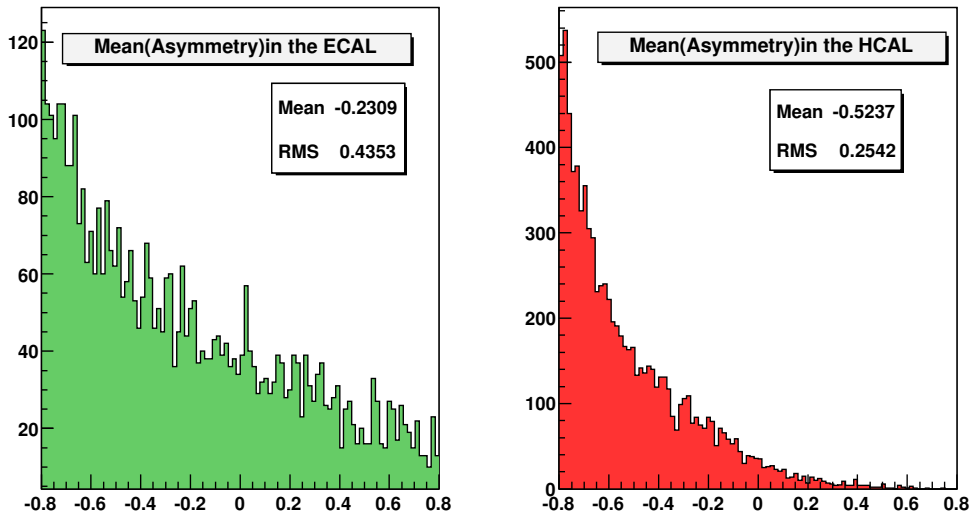


Figure 5.13: Mean value of cell by cell asymmetries in the ECAL (left distribution) and in the HCAL (right distribution).

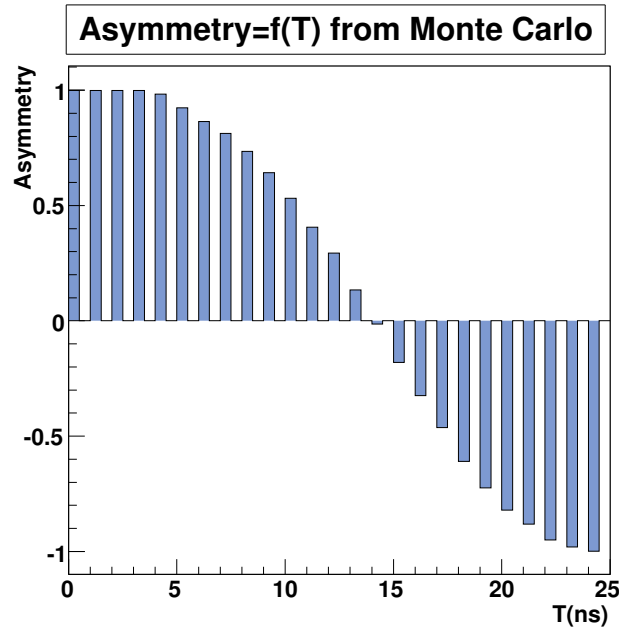


Figure 5.14: The asymmetry as a function of time (from Monte Carlo studies).

The presence of a trigger done by a coincidence in the ECAL and the HCAL in the **Current** sample requires that most energy is present in this particular sample. This biases the asymmetry distribution. In average we observe less clusters with a negative value of time than with positive ones.

Nomenclature Using the timing structure we define:

- **PP Tracks**, tracks with energy deposits shared between the **Current** and **Prev1** containers in the ECAL and between the **Current** and **Prev1** containers in the HCAL;
- **NN Tracks**, tracks with energy deposits shared between the **Current** and **Next1** containers in the ECAL and between the **Current** and **Next1** containers in the HCAL;
- **PN Tracks**, tracks with energy deposits shared between the **Current** and **Prev1** containers in the ECAL and between the **Current** and **Next1** containers in the HCAL;

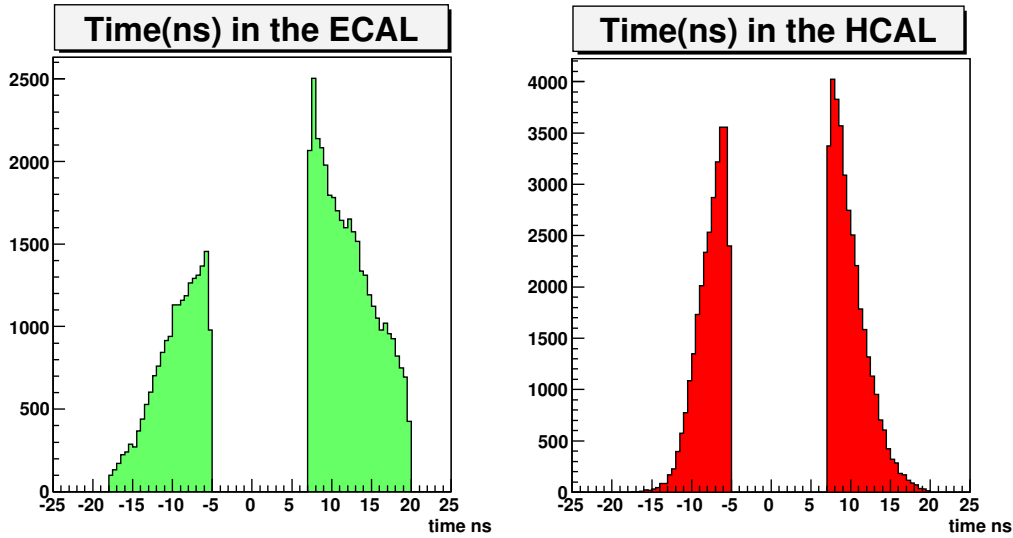


Figure 5.15: Distribution of the time (Δt) of clusters in the ECAL (left distribution) and in the HCAL (right distribution).

- **NP Tracks**, tracks with energy deposits shared between the **Current** and **Next11** containers in the ECAL and between the **Current** and **Prev1** containers in the HCAL.

Track extrapolation All the described track properties are stored in a **Track** object. Since all the cosmics were recorded in the absence of the magnetic field the tracks reconstructed in the calorimeters are extrapolated to other sub-detectors and we propagate the reconstructed "time" information using a linear extrapolator [56]. The propagated time information corresponds to the reconstructed time in the ECAL, if this time could not be reconstructed (for $|R| < 0.8$) the reconstructed time in the HCAL is used.

5.4 Internal time alignment

Since the cable lengths are identical in principal, the ADCs were originally sampled at identical time. However a given PMT gain requires different high voltages. This causes a different transit time in the PMT. To illustrate this fact, we compute in a simple scenario the transit time t of an electron of charge q and mass m in a constant potential V between two planes separated

by a distance s :

$$|\vec{F}| = q \cdot |\vec{E}| \text{ and: } |\vec{F}| = m \cdot |\vec{a}|, \quad (5.15)$$

where, $|\vec{F}|$ is the coulombian force and a is the acceleration of the electron in the electric field $|\vec{E}|$.

$$E = \frac{V}{s} \text{ and : } s = \frac{1}{2} \cdot a \cdot t^2, \quad (5.16)$$

$$t^2 = \frac{2 \cdot V}{a \cdot E} = \frac{2 \cdot q \cdot V}{a \cdot F} = \frac{2 \cdot q \cdot V}{m \cdot a^2}, \quad (5.17)$$

we use :

$$a = \frac{F}{m} \text{ and: } F = \frac{qV}{s} \quad (5.18)$$

and replace it in Equation: 5.4, to finally we obtain:

$$t = \sqrt{\frac{2 \cdot m \cdot s^2}{q \cdot V}}. \quad (5.19)$$

The difference in the signal collection time inside a photomultiplier, follows a square root dependence with the applied high voltage. This difference is estimated to be about 4 ns. Knowing the high voltage¹, the ADC clock could be corrected for this effect.

As the cosmic arrival in the calorimeters is random, a cell by cell fine-tuning of the ECAL and the HCAL is not possible. However using the asymmetry method we can quantify the internal time alignment of the ECAL and the HCAL. For each selected event we compute the *rms* of the cell by cell selected symmetries using:

$$\sigma_R = \sqrt{\sum_i (r_i - \bar{R})^2 / (N - 1)} \quad (5.20)$$

where \bar{R} is the mean value of the asymmetry in a given event, r_i the asymmetry of an individual selected cell and N is the multiplicity of the event.

We use the asymmetry-time conversion of Equation: 5.3 to convert the mean of the *rms* of the cell by cell asymmetries distributions in a typical time fluctuation between the different cells selected in a cosmic event. This neglects the time taken by a cosmic to go from one cell of the ECAL or the HCAL to another cell.

¹The gain is related to the high voltage as $G \sim HV^\alpha$ with $\alpha \sim 6$

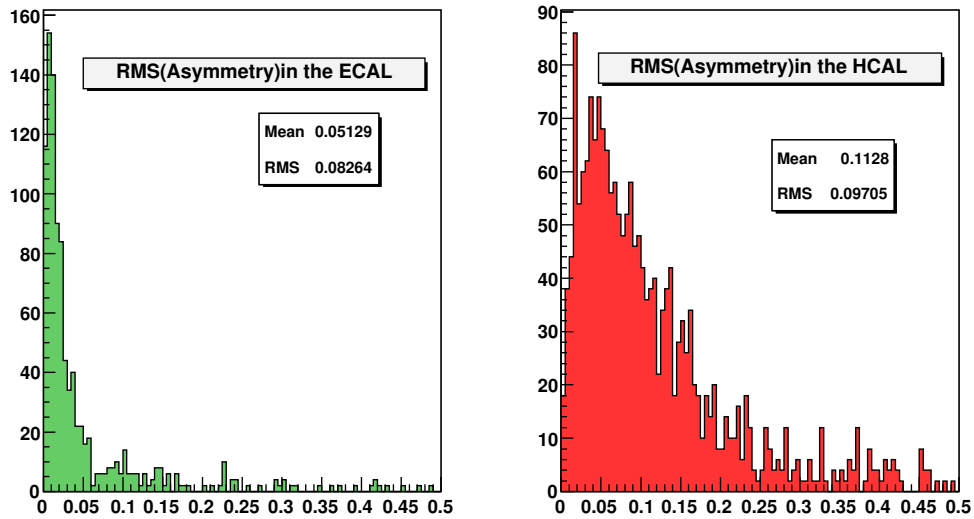


Figure 5.16: *rms* of the cell by cell asymmetries in the ECAL (left distribution) and in the HCAL (right distribution) before applying the high voltage corrections.

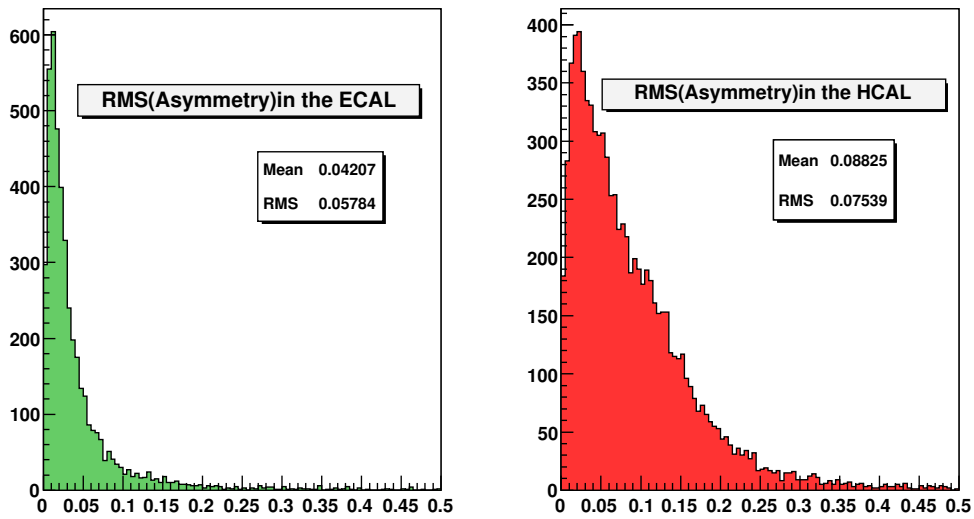


Figure 5.17: *rms* of the cell by cell asymmetries in the ECAL (left distribution) and in the HCAL (right distribution) after applying the high voltage corrections.

Impact of the high voltage corrections Before applying the high voltage corrections (see Figure: 5.16) we obtain after converting the mean value of these distributions in time using 5.3:

- The internal time alignment of the ECAL: 0.34 ns;
- The internal time alignment of the HCAL: 0.75 ns.

After applying the high voltage corrections and using the same conversion (see the distributions of Figure 5.17) we have:

- The internal time alignment of the ECAL: 0.28 ns;
- The internal time alignment of the HCAL: 0.58 ns.

An important conclusion can be reached at this step. After correcting for the fluctuation introduced by the high voltage variations from one cell to the other, the internal time alignment is typically 0.3 ns and 0.6 ns in the ECAL and the HCAL respectively. The fact that the HCAL modules are longer than the ECAL modules explains that the internal time alignment is worse in the HCAL.

5.5 Relative time alignment between the ECAL and the HCAL

In a given run about $\sim 45\%$ of cosmic events fulfill the tracking and the timing selection in the ECAL and HCAL simultaneously. For these selected events, one can compute:

$$SL = \frac{\Delta t_{HCAL} - \Delta t_{ECAL}}{\Delta L}, \quad (5.21)$$

where, Δt_{HCAL} and Δt_{ECAL} are the time measured in each sub-detector using the asymmetry method. ΔL is the distance between a cluster in the ECAL and a cluster in the HCAL. The quantity SL corresponds to the inverse of the speed of cosmic event. As cosmic travel at the speed of light the computed quantity SL should correspond to $SL = 3.3$ ns/m.

Timing setting Ultimately the setting between the various sub-detectors will be such that the time of flight of a particle produced at the interaction point and flying to a given sub detector is taken into account. We will call the "*beam*" setting. For example, a particle will be first seen in the ECAL and then in the HCAL. When taking cosmic data, such a setting is expected to enhance the quantity of forward tracks with respect to the backward tracks, since the trigger required to have the energy in the same sample for both detectors. Nevertheless at the beginning of the commissioning, the setting was such that we were not enhancing one type of cosmic (forward) with respect to other one (backward). This setting will be referred as the "*democratic*" setting in the rest of the text.

Two dimensional visualization It is possible to visualize these various configurations by means of a two dimensional plot built as follows: the y axis of Figure : 5.18 represents $\Delta t_{HCAL} - \Delta t_{ECAL}$ while the X axis represents ΔL for example for **Backward NN Tracks**. A χ^2 is minimized to fit this distribution to a straight line, the fitted parameters are the slope and the offset. On the x axis we can see that all the values of ΔL are above 1.2 m which is expected since this value corresponds to the distance between the middle of the ECAL and the HCAL. Working in the "*democratic*" setting we would expect the offset to be to 0 ns. The following results were obtained using one of the first run taken.

$$\begin{aligned} \text{slope} &= (-2.07 \pm 0.68) \text{ ns/m.} \\ \text{offset} &= (7.40 \pm 2.86) \text{ ns.} \end{aligned}$$

The value of the fitted offset, 7.4 ns is incompatible with what we expected. This shift is due to two different contributions:

- In Section 3.4.3 we showed that the calorimeter readout card (CROC) receives, via an optical fiber a clock from a TTCrx mezzanine, which were found to have by mistake a 3 ns extra shift in the ECAL for this run;
- Besides the coaxial cable length a source of time misalignment was not taken into account, namely the length of the WLS fibers in the HCAL (see Section: 3.1). This correction is estimated to be 4 ns. It was applied to all the TTCrx of the HCAL CROC.

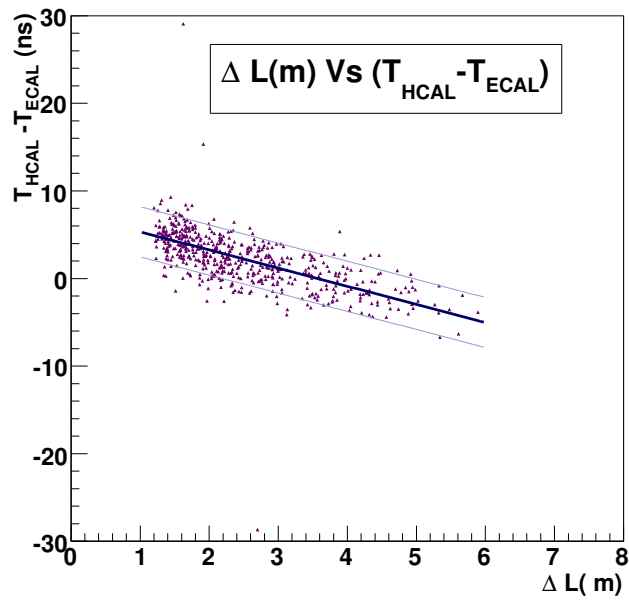


Figure 5.18: ΔL Versus $\Delta t_{HCAL} - \Delta t_{ECAL}$. The fitted straight line is shown in continuous blue. The dashed purple line corresponds to the error on the offset.

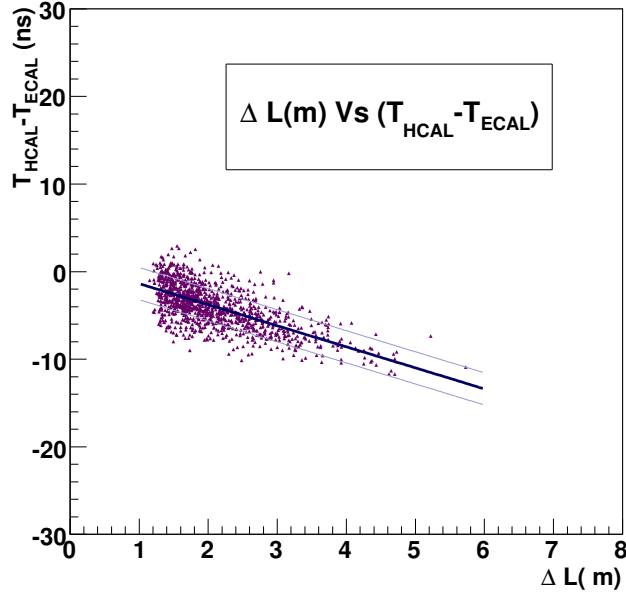


Figure 5.19: ΔL Versus $\Delta t_{HCAL} - \Delta t_{ECAL}$ distribution for **Backward NN** Tracks. The fitted straight line is shown in continuous blue. The dashed purple line corresponds to the error on the offset.

With these corrections we obtained the following values:

$$\begin{aligned} \text{slope} &= (-2.40 \pm 0.38) \text{ ns/m.} \\ \text{offset} &= (1.03 \pm 1.83) \text{ ns.} \end{aligned}$$

The fitted value of the offset is in agreement with our expectation. An important information can be extracted from this two dimensional representation, namely the relative timing between the ECAL and the HCAL. This is given by the value of the error on the offset, see Figure: 5.19. With this particular set of data in these conditions we can conclude that the relative time alignment between ECAL of the cells and the HCAL is around 2 ns.

From the "democratic" setting to the "beam" setting We show in Tables: 5.1 and 5.2 the fit obtained for a run taken in the "democratic" and one taken in the "beam" conditions respectively. In both tables we only

Type	Nb of Events	slope	offset($\Delta L = 0$ m)	offset($\Delta L = 1.5$ m)	σ_{slope}	σ_{offset}
For. NN	1385	2.33	0.00	3.5	0.27	2.05
For. PP	4703	2.25	0.82	4.2	0.19	2.13
Back. NN	6385	-2.29	1.05	-2.38	0.16	2.09
Back. PP	562	-1.82	0.44	-2.30	0.48	-2.30

Table 5.1: Number of selected cosmics, values of the offset and slope per type and category for a run using the "*democratic*" setting.

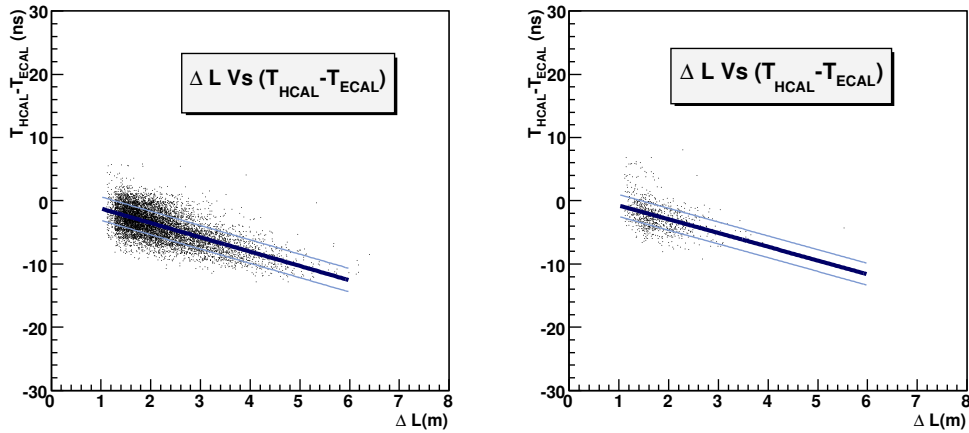


Figure 5.20: ΔL Versus $\Delta t_{HCAL}(T_{HCAL}) - \Delta t_{ECAL}(T_{ECAL})$ distribution for NN and PP backward tracks, in the the "*democratic*" conditions. The fitted straight line is show in countinuous blue. The dashed purple line corresponds to the error on the offset.

show the categories with interesting timing properties, i.e: **Forward NN**, **Forward PP**, **Backward PP** and **Backward NN**.

We notice that in the first case the number of forward events is 6088 while the number of backward events is 6947. After adjusting the setting to be in the *beam* conditions, the number of forward events is 7630 and the number of backward events is 4579.

The fact that the obtained value of the fitted slope marked in Table: 5.2 with a star for **Backward PP** is above 3.3 ns/m, is due to the lack of statistics.

The absolute value of the fitted speed of a cosmic between the ECAL and the HCAL is given by the slope of the two dimensional representation. We observe that the computed value in both runs (before and after applying the

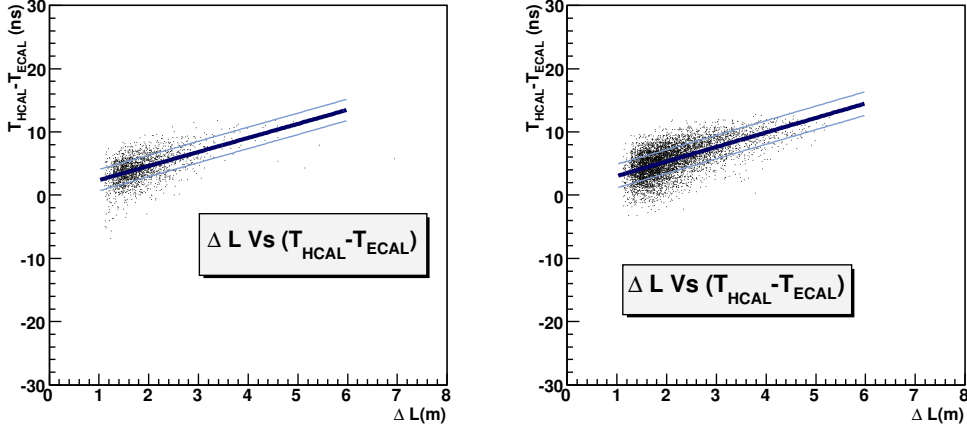


Figure 5.21: ΔL Versus $\Delta t_{HCAL}(T_{HCAL}) - \Delta t_{ECAL}(T_{ECAL})$ distribution for NN and PP forward tracks, in the the "democratic" conditions. The fitted straight line and the dashed line is shown in continuous blue. The dashed purple line corresponds to the error on the offset.

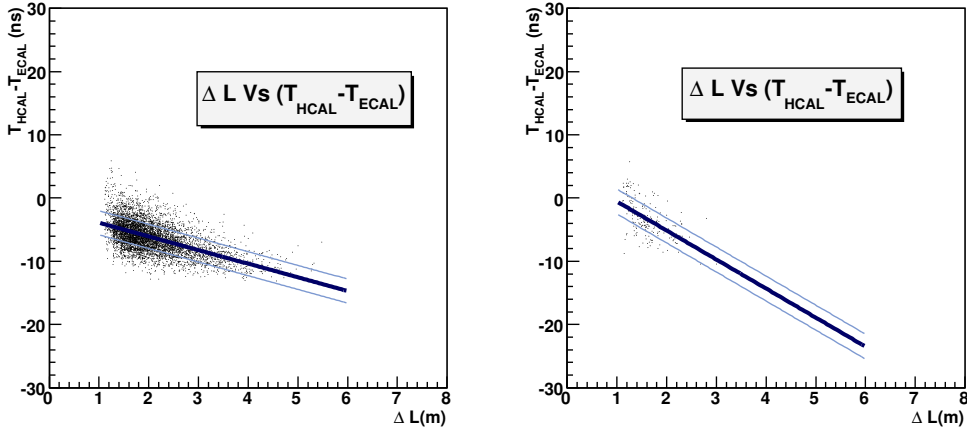


Figure 5.22: ΔL Versus $\Delta t_{HCAL}(T_{HCAL}) - \Delta t_{ECAL}(T_{ECAL})$ distribution for NN and PP backward tracks, in the "beam" conditions. The fitted straight line is shown in continuous blue. The dashed purple line corresponds to the error on the offset.

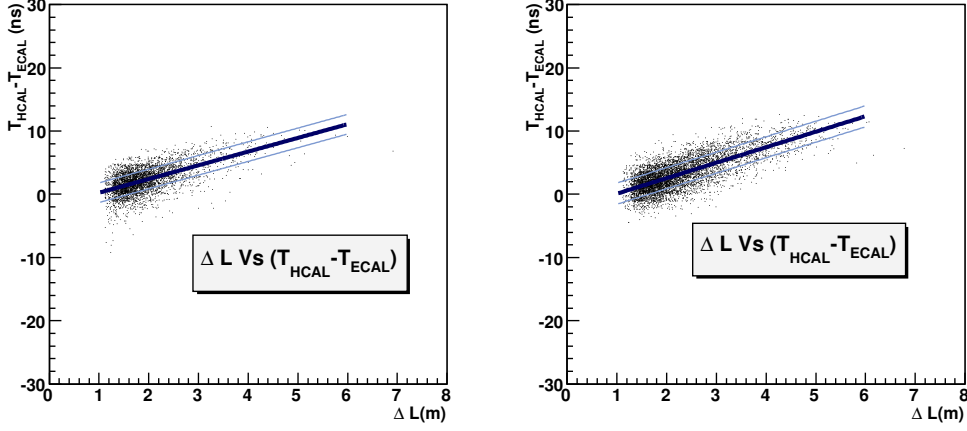


Figure 5.23: ΔL Versus $\Delta t_{HCAL}(T_{HCAL}) - \Delta t_{ECAL}(T_{ECAL})$ distribution for NN and PP backward tracks, in the "beam" conditions. The fitted straight line is shown in continuous blue. The dashed purple line corresponds to the error on the offset .

Type	Nb of Events	slope	offset($\Delta L = 0$ m)	offset($\Delta L = 1.5$ m)	σ_{slope}	σ_{offset}
For. NN	2803	2.24	-2.08	1.28	0.58	1.85
For. PP	4827	2.47	-2.40	1.30	0.80	1.87
Back. NN	4579	-2.10	-1.94	-5.10	0.63	2.19
Back. PP	104	-4.32*	3.59	-2.89	1.45	2.67

Table 5.2: Number of selected cosmics, values of the offset and the slope per type and category for a run using the "beam" setting.

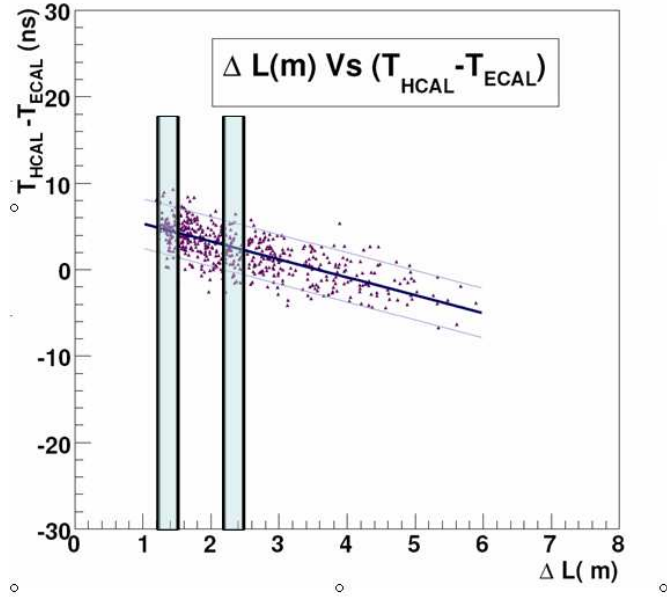


Figure 5.24: Representation of the ΔL slices, on the x axis figures ΔL and on the y axis figures $\Delta t_{HCAL}(T_{HCAL}) - \Delta t_{ECAL}(T_{ECAL})$

TTCrx corrections) is systematically smaller than 3.3 ns/m. To test whether this bias is introduced by the way we select the events we perform a scan in bin of time (see Section: 5.6). Then we test if this bias is due to the way we convert the measured asymmetry into a time information (see Section 5.7).

5.6 Behaviour of the time correlation between the ECAL and the HCAL

As we showed previously, the computed value of the speed of the cosmons between the ECAL and the HCAL never leads to the correct speed of light. This value appears to be systematically under-estimated, even when using various conditions of the L0-trigger. We try in this section to investigate the origin of this bias by refining the event selection and studying the correlation between the time in the ECAL and the time in the HCAL.

We divide a sample of well selected **Forward NN** and **Forward PP** tracks

in two, requiring that the computed distance between the clusters in the ECAL and the HCAL ΔL is contained in two different slices, the first one is given by $[1.2\text{m}, 1.5\text{m}]$ and the second one by $[2.2\text{m}, 2.5\text{m}]$, as illustrated in Figure: 5.24. Since each "event" corresponds to the same cosmic passing through the ECAL and the HCAL (hence they are sampled at the same time) we expect the time in the ECAL to be correlated with the time in the HCAL for each slice of ΔL .

From the point of view of timing an event is selected if it fulfills the timing requirements in each sub detector defined by: $|R| < 0.8$, see top distributions of Figure: 5.25. This cut has been introduced because of the lack of sensitivity in the time measurement for $|R| > 0.8$. It was shown in [57] that events close to the edges of the time distribution introduced by the cut are biased. Further requirements are introduced in the selection to remove these events:

- for the **ForwardNN** tracks we require for both the ECAL and the HCAL to have $\Delta t > 8$ ns, see bottom distributions of Figure: 5.25 ,
- for the **ForwardPP** tracks we require for both the ECAL and the HCAL to have $\Delta t < -6$ ns, see bottom distributions of Figure: 5.25.

The distribution which allows to convert the asymmetry into a value of time is extracted from a Monte Carlo simulation as shown in Chapter 4. We remind that the shape of the integrated signal retrieved after the digitization was shifted by 1.4 ns in the ECAL. This shift was due to the definition of the start of the electromagnetic showers in the ECAL. The cuts applied in this section when refining the track selection are not symmetric, to take into account this shift.

In Figure: 5.26 we show the distributions corresponding to the time in the HCAL as a function of the time in the ECAL in the two slices of ΔL . We minimize a χ^2 to fit both distributions with a straight line:

$$\Delta t_{HCAL} = a_i \times \Delta t_{ECAL} + b_i \text{ where: } i = 1, 2. \quad (5.22)$$

In the first slice of $\Delta L \in [1.2\text{m}, 1.5\text{m}]$ the fitted parameters are: $a_1 = 0.96 \pm 0.026$ and $b_1 = 1.08 \pm 1.68$, while in the second one, $\Delta L \in [2.2\text{m}, 2.5\text{m}]$, $a_2 = 0.94 \pm 0.048$ and $b_2 = 3.02 \pm 1.78$. An important observation we can make here is that, as expected in both slices of ΔL , for both categories of well selected **ForwardNN** and **ForwardPP** tracks, the time in the ECAL

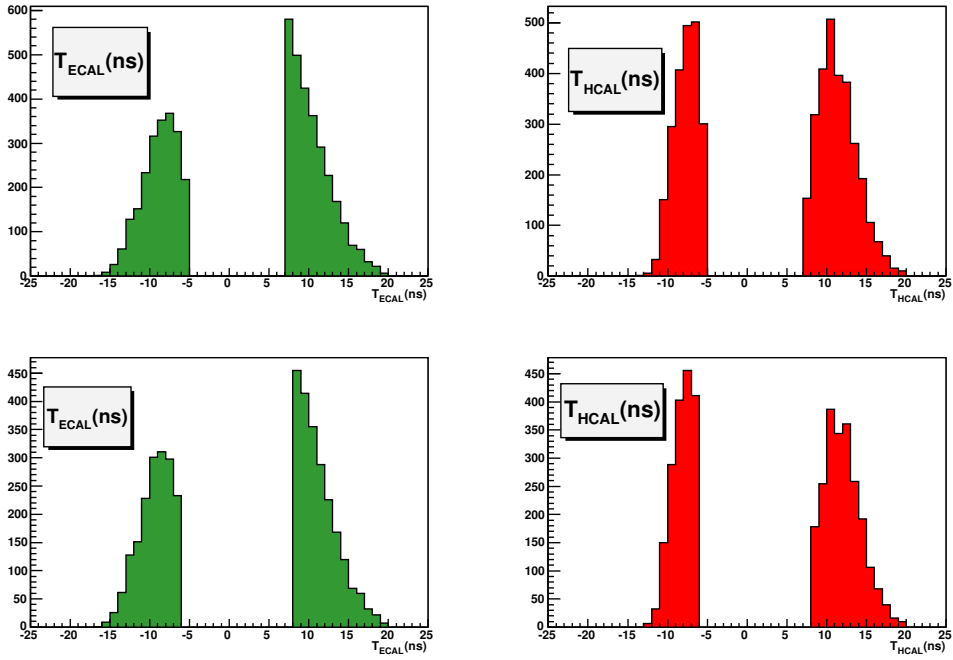


Figure 5.25: Measured time in the ECAL (left distributions) and in the HCAL (right distributions), before (top distributions) and after (bottom distributions) applying cuts.

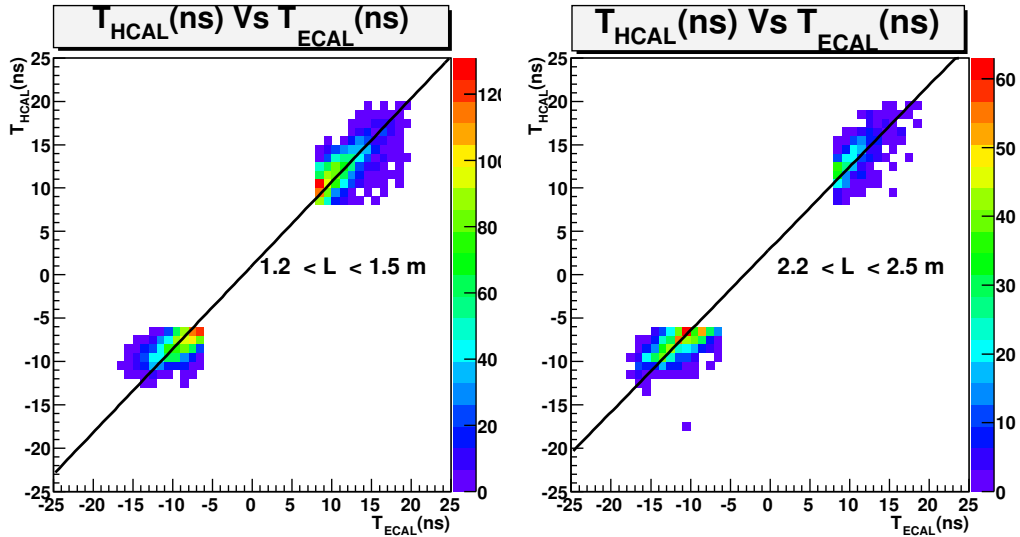


Figure 5.26: Correlation between the measured time in the ECAL and the time measured in the HCAL in two different regions of ΔL .

is indeed correlated with the time in the HCAL since we have $a_i \sim 1$. On the other hand, using the fitted values in each slice, we can compute the speed of the cosmics between the two detectors and we obtain : $SL = 1.94$ ns/m which is still smaller than the expected value (3.3 ns/m).

Therefore we can conclude that, refining the track selection criteria, allowed us to make sure that we are well controlling the time correlations between the ECAL and the HCAL. However, we still do observe a bias in the computed value of the speed of the cosmics between the two detectors. Another origin of this bias is investigated in the next section, through the study of the sensitivity of our method to the external input, namely the shape of the integrated signal.

5.7 Sensitivity to the the signal shape

The distribution that allows to convert a measured asymmetry to a time information for a given cell is extracted from the Monte Carlo (see Chapter: 4). Being limited by the number of recorded cosmics and more importantly by the fact that cosmics events are not synchronized, it is not possible to perform a full scan in time of the integrated signal and test whether *in vivo* the actual shape corresponds to what is present in the simulation. We replace the distribution of Figure: 5.27 with an "fake" one showed in Figure: 5.28. Even though the shape of the "fake" integrated signal is not physical, it allows to test the most extreme case we could expect. We use the same method as in the Monte Carlo simulation. Starting from the "fake" shape we can built an "artificial" asymmetry-time conversion.

Using the standard asymmetry-time conversion for **Forward** NN tracks taken in the "*democratic*" conditions we obtain:

$$\begin{aligned} \text{Slope} &= (-2.4 \pm 0.38) \text{ ns/m.} \\ \text{Offset} &= (1.03 \pm 1.83) \text{ ns.} \end{aligned}$$

for **Backward** NN tracks:

$$\begin{aligned} \text{Slope} &= (1.58 \pm 0.40) \text{ ns/m.} \\ \text{Offset} &= (2.00 \pm 1.71) \text{ ns.} \end{aligned}$$

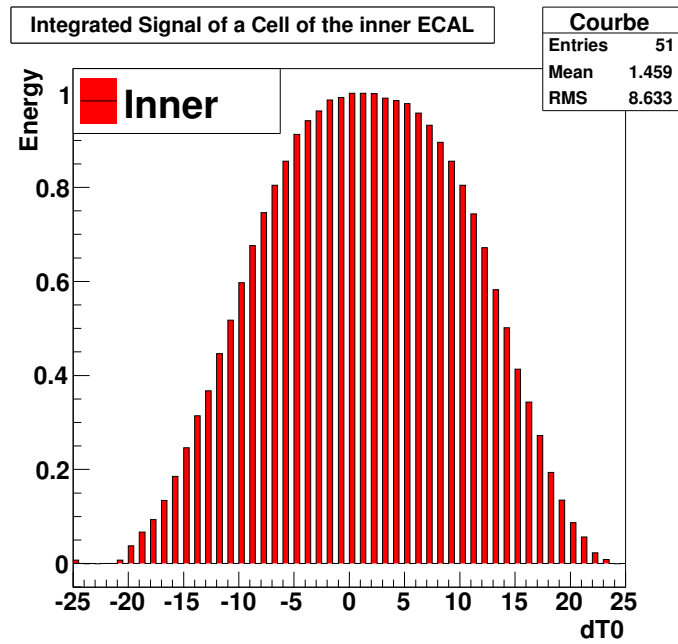


Figure 5.27: Shape on the integrated signal used in the Monte Carlo simulation to produce the asymmetry-time conversion.

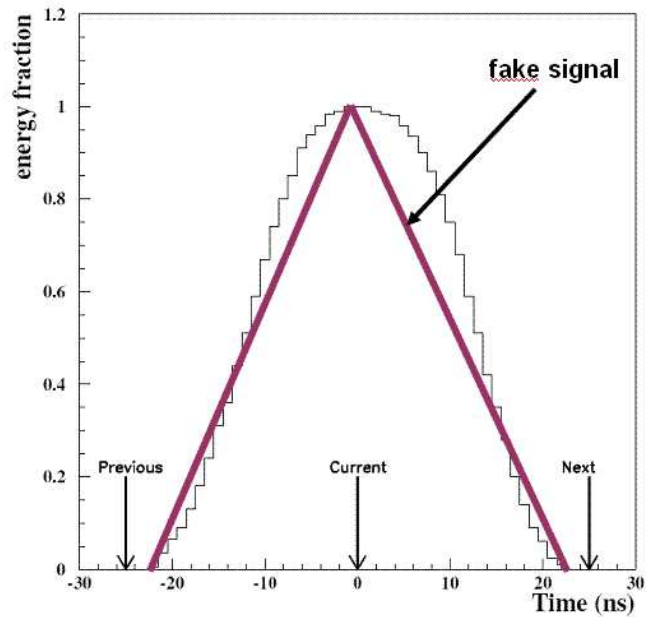


Figure 5.28: Shape of a "fake" integrated signal used to produced to test the asymmetry-time conversion

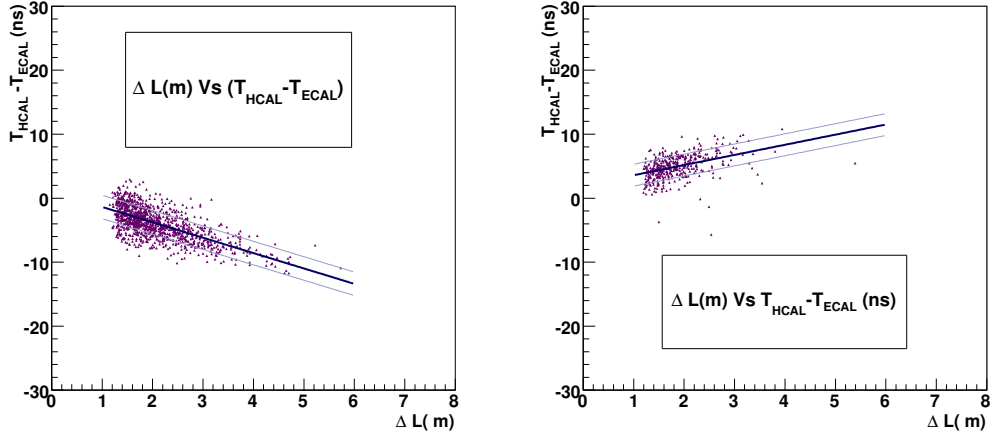


Figure 5.29: ΔL Versus $\Delta t_{HCAL}(T_{HCAL}) - \Delta t_{ECAL}(T_{ECAL})$ distribution for **Backward NN** (left) and **Forward NN** (right) tracks, using the standard asymmetry-time conversion. The fitted straight line is shown in continuous blue. And dashed purple line corresponds to the error on the offset.

The corresponding distributions are shown in Figure: 5.29. Then using the same events we switch from the standard asymmetry-time conversion to the artificial one, for **Forward NN** tracks we have:

$$\begin{aligned} \text{Slope} &= (-4.02 \pm 0.37) \text{ ns/m.} \\ \text{Offset} &= (1.71 \pm 3.25) \text{ ns.} \end{aligned}$$

and for **Backward NN** tracks we obtain:

$$\begin{aligned} \text{Slope} &= (2.72 \pm 0.52) \text{ ns/m} \\ \text{Offset} &= (2.85 \pm 2.90) \text{ ns.} \end{aligned}$$

The corresponding distributions are shown in Figure: 5.30. Even though the fitted value of the slope in one of the cases where we used the "artificial" asymmetry-time conversion reaches a value of $SL > 3.3$ ns/m, from both cases we observe a variation between $\sim 50\%$ of the fitted slope (SL). The observed sensitivity due to a variation of the shape of the integrated signal used as input in the asymmetry method, pushes for a full scan of the integrated signal on beam data.

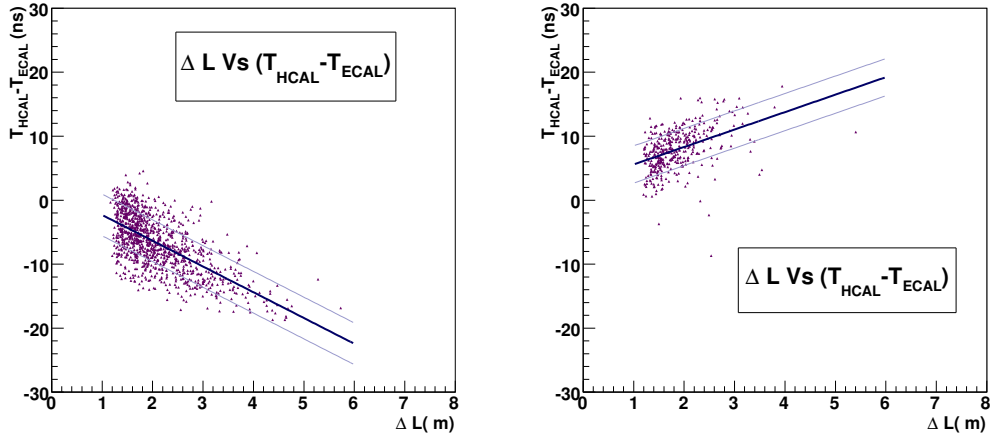


Figure 5.30: ΔL Versus $\Delta t_{HCAL} - \Delta t_{ECAL}$ distribution for backward (left) and forward (right) tracks. using the artificial asymmetry-time conversion. And dashed purple line corresponds to the error on the offset.

5.8 Time alignment with other sub detectors

Using the asymmetry method, to compute the timing in the ECAL and the HCAL. As explained in Section: 5.1 it is possible to store this information in a **Track** object and extrapolate this information to other subdetectors. This exercise was performed for the PreShower, the Outer Tracker and the muon chambers.

5.8.1 PreShower

For reasons developed in Section: 3.3.1, the PreShower readout is performed using a 64 channels MAPMT. For each selected cosmic event the difference between the timing in the ECAL and the PreShower is computed. This allows to fine tune the preliminary corrections (cable length...) that are applied in the readout chain. The distributions of Figure: 5.31, 5.32 and 5.33 show the difference in time between the ECAL and the PreShower for the inner, middle and outer region respectively once these corrections have been applied. From these figures we conclude that the time alignment of all the channels of the Preshower is better than 2 ns.

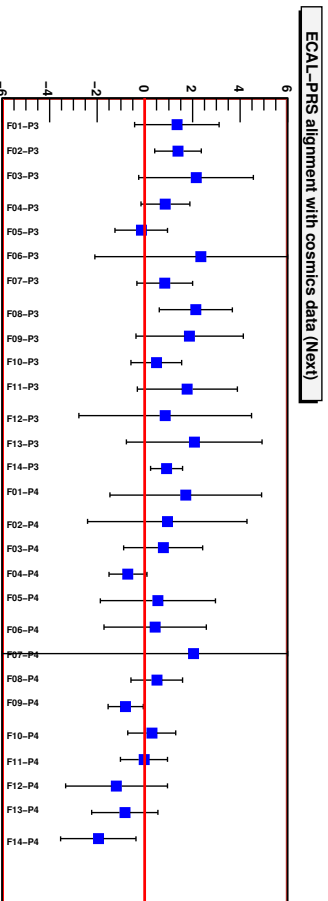
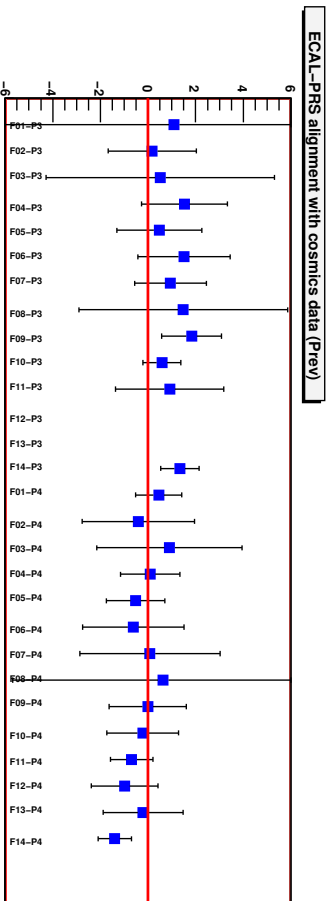


Figure 5.31: Difference between the timing (given in ns) in the ECAL and the PreShower using a **Current/Prev1** or **Current/Next1** asymmetries respectively, in the inner region

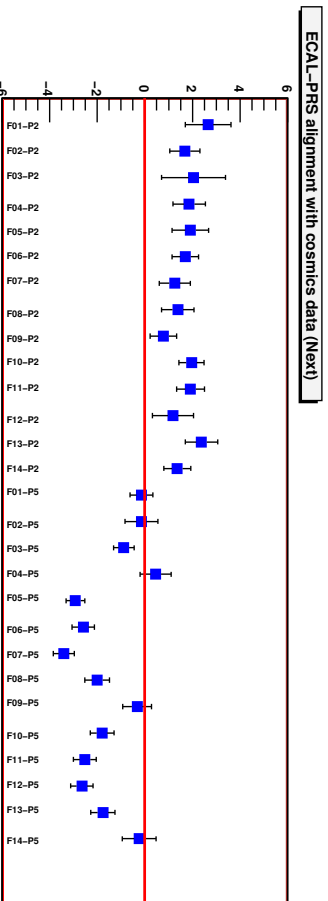
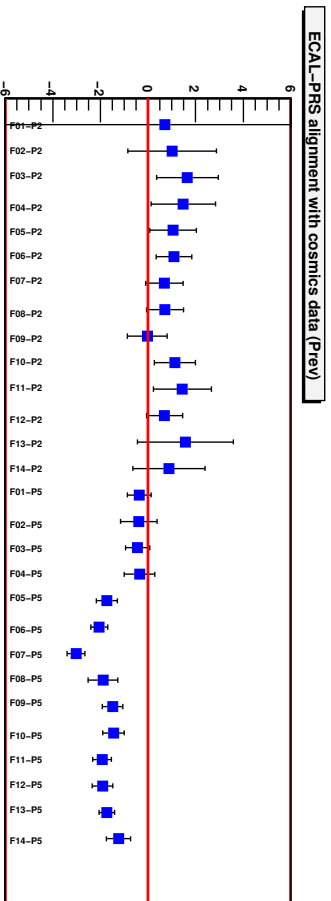


Figure 5.32: Difference between the timing (given in ns) in the ECAL and the PreShower using a **Current/Prev1** or **Current/Next1** asymmetries respectively, in the middle region

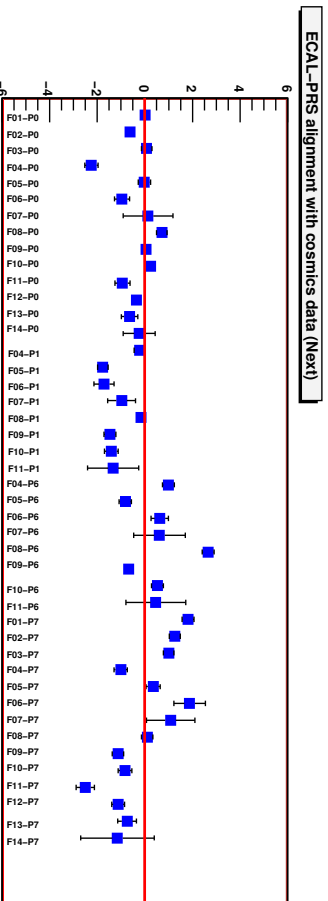
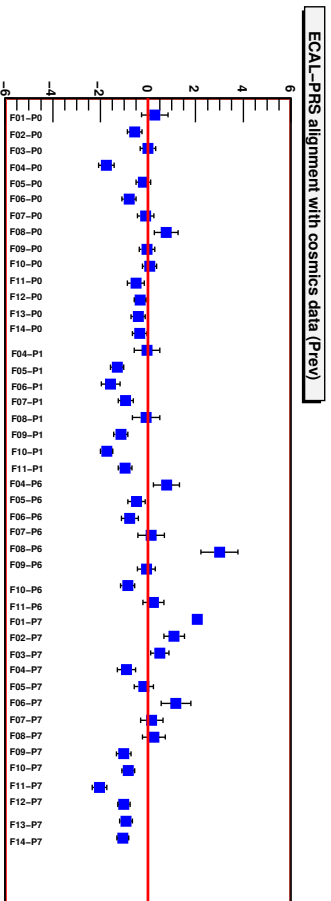


Figure 5.33: Difference between the timing (given in ns) in the ECAL and the PreShower using a **Current/Prev1** or **Current/Next1** asymmetries respectively, in the outer region

5.8.2 Outer Tracker

A "naive" model of the timing in the Outer Tracker based on the knowledge of the timing in the ECAL can be written, for forward tracks (events passing through the OT first) as:

$$T_{TDC} = t_{calo} - t_{tof} + t_{drift} + t_{wire} \quad (5.23)$$

while for backward tracks (events passing through the calorimeter first):

$$T_{TDC} = t_{calo} + t_{tof} + t_{drift} + t_{wire} \quad (5.24)$$

where:

- t_{drift} , is the drift time of ionizing particles in the OT straw tube gas to the wire.
- t_{wire} is the propagation time in the OT wire up to the read out;
- t_{tof} corresponds to the time of flight of the cosmic between the ECAL and the OT;
- t_{calo} is the reconstructed time in the ECAL;
- T_{TDC} the time information in the OT readout is encoded in a dedicated TDC chip.

The horizontal axis of Figure: 5.34 represents the timing in the OT(T_{TDC}) in ns, while the vertical axis represents the timing in the ECAL in ns. As mentioned earlier it is necessary to apply a cut on the asymmetry computed in the calorimeters in order to have a sensitivity to the corresponding time, this explains the gap in the scatter plot of Figure: 5.34. Using this method the relative timing between the ECAL and the Outer Tracker is determined using the mean and spread of the distribution. It was estimated to be better than 3.3 ns.

5.8.3 Muon chambers

As for the Outer Tracker, the muon chambers readout uses a TDC count system to obtain the time in each module in a 25 ns window. Cosmic events

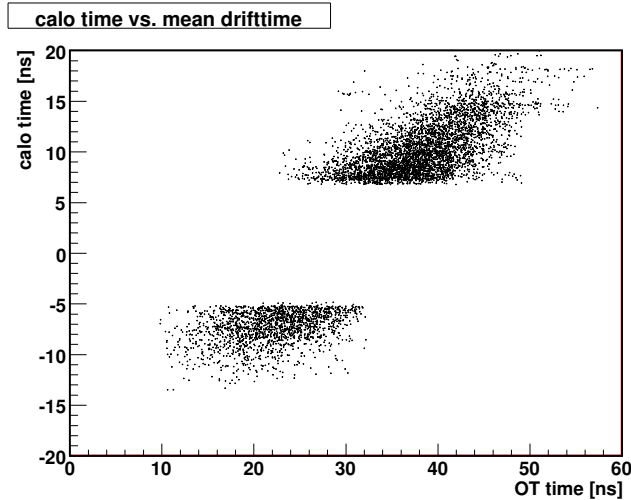


Figure 5.34: Time in the Outer tracker with respect to the time in the calorimeter for forward tracks

were reconstructed in the muon chamber using a simplified reconstruction software (with respect to the standard one used in the offline analysis.) A linear track is fitted between the selected hits in each of the stations. Then a matching is done between the cosmics reconstructed in the muon chambers and those reconstructed in the calorimeter. For these events it is possible to compute the timing difference between the muon chambers (for example M2) given by the TDC counts and the ECAL with respect to the time of flight as shown in Figure: 5.35. The relative timing between the ECAL and M2 is given by the spread of this scattering plot of Figure: 5.35. It is estimated to be ± 10 ns for **Forward NN** tracks. This value is large compared to the relative timing between the ECAL and the HCAL. This can be explained by two facts. The internal timing in the muon station was not performed yet when these cosmics data were taken. Then, the timing between the particle passage and the signal collection is a function of the distance between the wire of the tube and the track. This introduces another source of time misalignment.

5.9 Conclusion

Over a million of cosmics events were recorded at LHCb in 2008, allowing to fully commission the calorimeters, the data acquisition system and the L0-

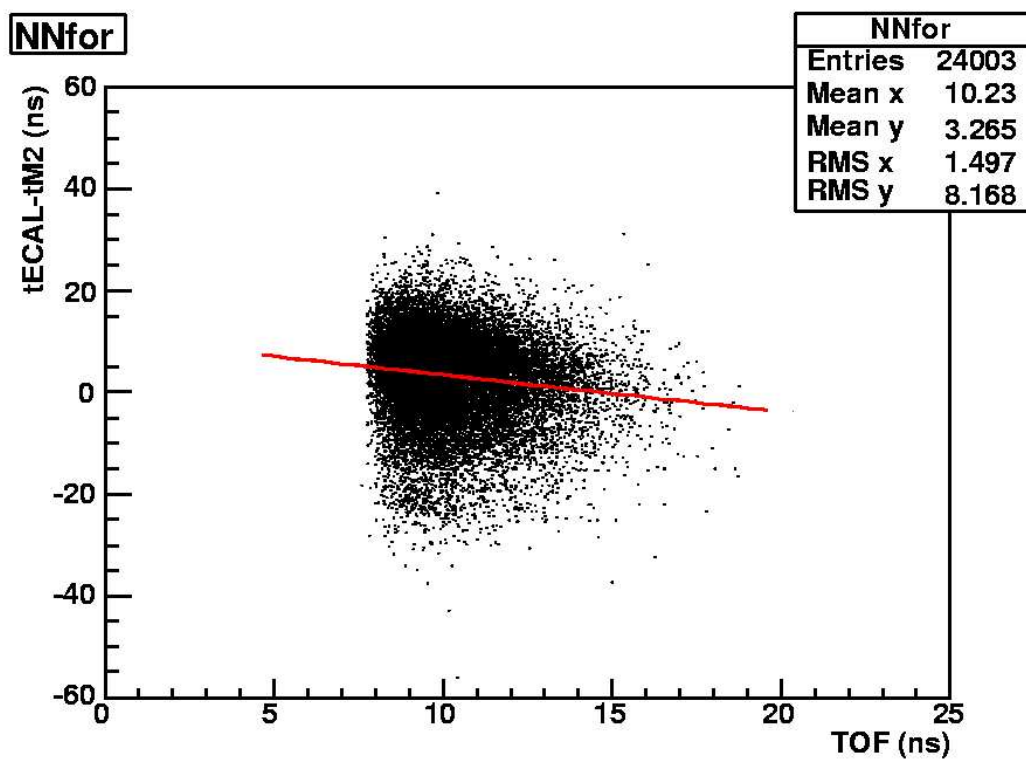


Figure 5.35: Difference in the timing in the ECAL and the timing in M2 as a function of the time of flight of the cosmic between these two sub-detectors.

trigger. More specifically, the asymmetry based method allowing to convert measurable quantities into a *time* information was tested and validated on this data. First of all we have established a set of criteria to have well reconstructed cosmic events in the calorimeters. We were able to control the goodness of the internal time alignment of the ECAL and the HCAL. Using these tracks, various sources of time misalignment between the ECAL and the HCAL were corrected. A limitation of the method was reached, due to the presence of a bias in the computed speed of the cosmic between the electromagnetic and the hadronic calorimeters. A potential origin of this bias was identified and can be recovered using beam data. The time information provided by the calorimeters was extrapolated, using algorithms developed for this purpose, to other sub-detectors (the PS/SPS, the Outer Tracker and the muon stations) and is used as a reliable reference for their time alignment.

Chapter 6

Time alignment with the first beam data



Sir Edward Elgar
Cello Concerto in E minor, Op 85.

On the 10th of September 2008, the LHC delivered some single beam data. LHCb was able to record events, where the direction of the beam is in the forward direction of LHCb (from the Velo up to the muon stations) injected in IP2 (see Figure: 6.1). The beam was circulating from one octant to the other, the current and the intensity (5×10^9 protons per shot each 48 second) were low with respect to the optimal settings. During this short period (about one hour of data taking in the Time Alignment mode) the electromagnetic calorimeter high voltage was off for safety reasons and only the timing of the hadronic calorimeter could be checked.

A dedicated Level-0 trigger setting was based on the information in the muon stations or the combination of the information in the HCAL and SPD multiplicity.

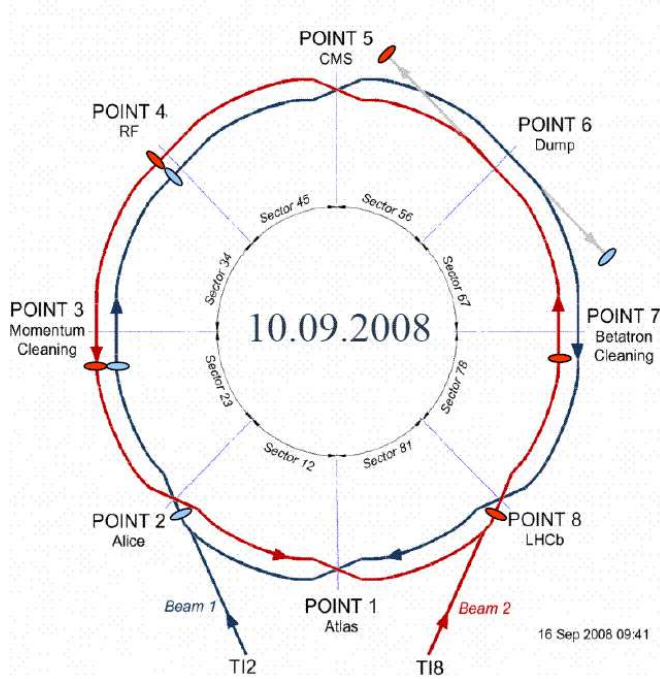


Figure 6.1: Illustration of beam one and beam two at the LHC.

6.1 A new variable: the Kernel

In order to remove noisy cells we require at least 10 ADC counts in each cell of the HCAL. We introduce a new variable called the "Kernel", defined for each cell (j) as following:

$$K_j = \frac{\text{sgn}(E_j(\mathbf{Next1}) - E_j(\mathbf{Prev1})) \times [E_j(\mathbf{Prev1}) + E_j(\mathbf{Next1})]}{[E_j(\mathbf{Prev1}) + E_j(\mathbf{Current}) + E_j(\mathbf{Next1})]} \quad (6.1)$$

By construction the Kernel is expected to vary between -1 and 1. Unlike the asymmetries R_j ($\mathbf{Current}/\mathbf{Next1}$ or $\mathbf{Current}/\mathbf{Prev1}$) the Kernel does not provide a straight forward computation of the time. Nevertheless it allows to estimate in regions where the asymmetries are not sensitive ($|R_j| > 0.8$) how an event is centered in a given sample. For example, for perfectly time aligned events in the HCAL with respect to the global LHCb clock the Kernel distribution is expected to be centered in 0. Negative values of the Kernel correspond to events appearing in the **Current** and **Prev1** while positive values correspond to events appearing in the **Current** and **Next1** samples. This is illustrated in Figure: 6.2 which displays the Kernel distribution of

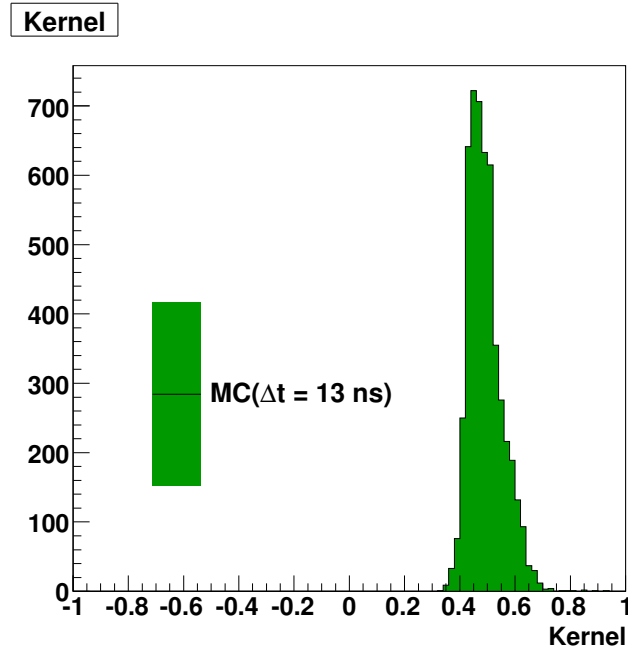


Figure 6.2: Kernel distribution in the HCAL, from Monte Carlo data, generated with $\Delta t = 13$ ns

simulated Monte Carlo minimum bias events in the HCAL where we introduced a time misalignment: $\Delta t = 13$ ns. Of course no new information is provided with respect to the asymmetries, but the Kernel is very convenient for events already roughly centered in the **Current** sample.

6.2 Zoology of recorded beam one events in the HCAL

We observe in the left and middle distributions of Figure: 6.3, two different populations of events: one population centered around 0.1 and a second one centered around 0.9. The protons are shot each 48 seconds, therefore we would have expected to see only one main population. After analyzing these events, we isolated a high multiplicity, not synchronized, event, (see Figure: 6.4).

The distributions of Figure: 6.5 display the Kernel and the asymmetries variables after the removal of this event. The second population (centered at 0.9

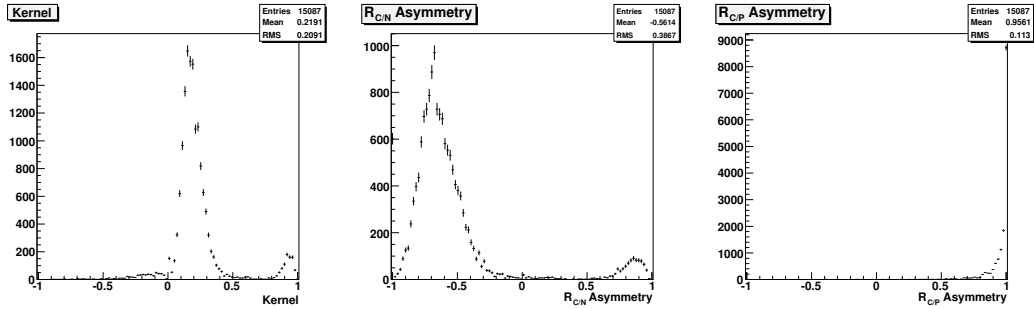


Figure 6.3: Kernel distribution for single beam events in the HCAL(left distribution), **Current/Next1** asymmetry for single beam events in the HCAL (middle), **Current/Prev1** asymmetry for single beam events in the HCAL(right).

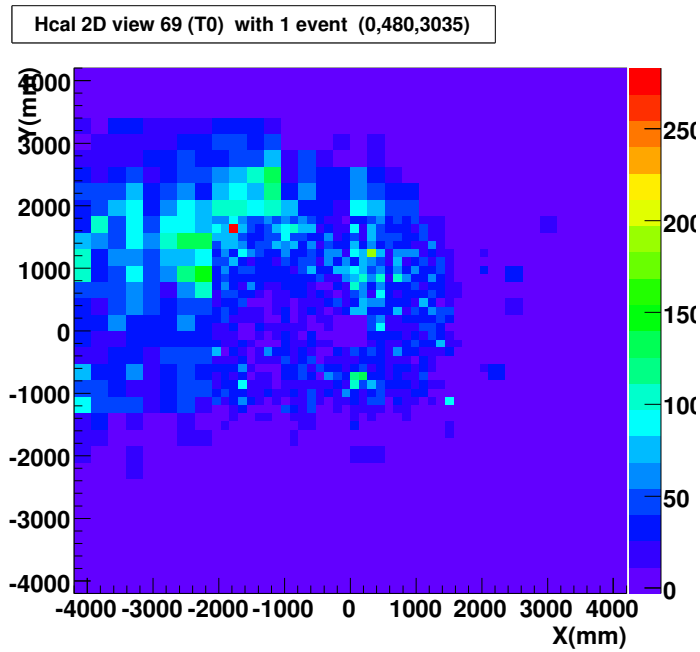


Figure 6.4: Event display of a "splash" event in the HCAL.

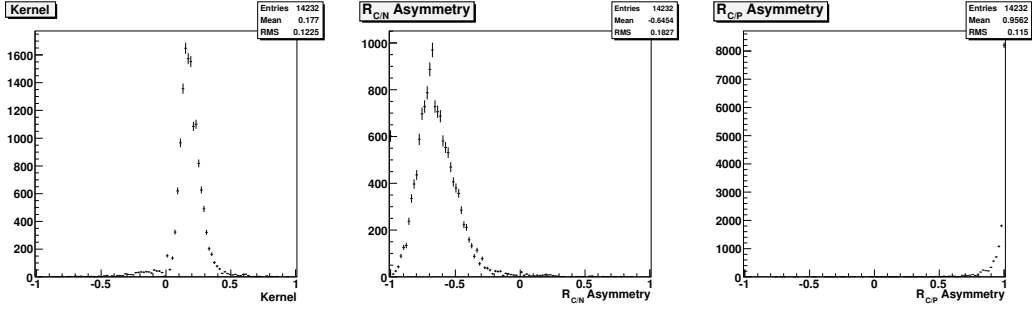


Figure 6.5: **Current/Next1** asymmetry for single beam events in the HCAL (left), **Current/Prev1** asymmetry for single beam events in the HCAL after the removal of the high multiplicity not synchronized splash event.

Category	Number of events	Average multiplicity
splashes	12	1044
beam halo	20	34
cosmics	256	3

Table 6.1: Average multiplicity in each category of single beam events.

for the Kernel has disappeared. We still observe cells for negative value of the Kernel and positive values of the **Current/Next1** asymmetry with a different time structure.

To understand the nature of these events, we use their multiplicity and their ADC spectrum (see distributions in Figure: 6.6). We distinguish three categories of events:

- **Category I:** A collimator placed 30 meters upstream of the LHCb detector, is used to stop the beam, producing hadronic showers (pions and muons). These events, referred to as "splashes", have a multiplicity which is in average higher than 100 in the HCAL. This category of events is the only one which is expected to be fully on time with the LHC clock (see the left event display of Figure: 6.7).
- **Category II:** Events where the multiplicity is smaller than 100 and higher than 10 (see the middle event display of Figure: 6.7). Since the ADC spectrum of these events (see Figure: 6.6) never exceeds 50 ADC counts, they might correspond to beam halo events, which are machine-induced muons travelling along the beam line.

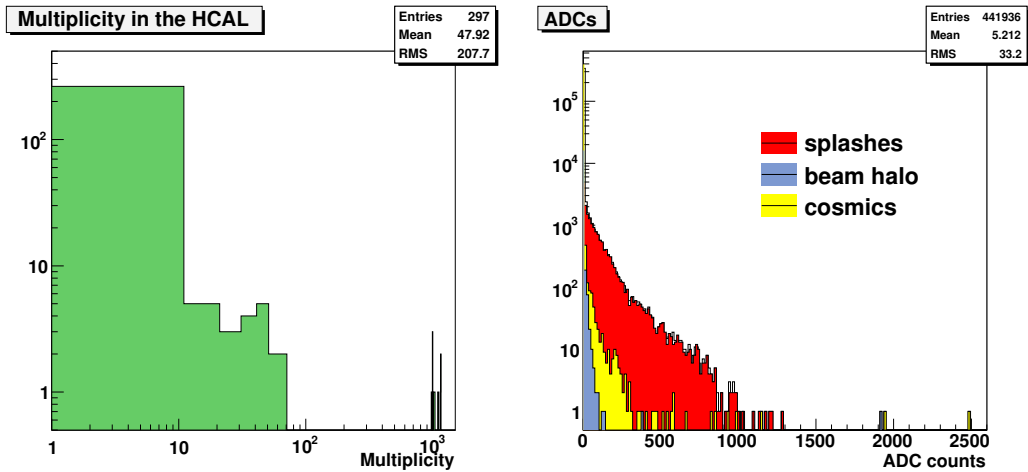


Figure 6.6: Multiplicity in the HCAL, ADC spectrum in the HCAL, the red distribution corresponds to the splashes, the blue one corresponds to the beam halo and the yellow one corresponds to cosmic events.

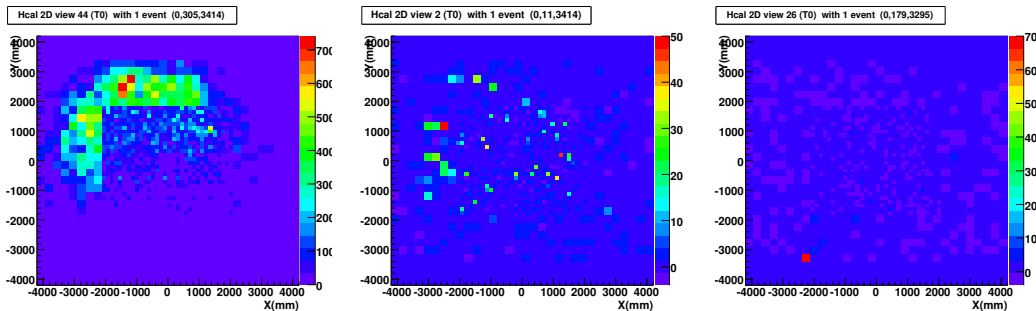


Figure 6.7: Event display (left) of a "splash" event in the HCAL. Event display (middle) of a "beam halo" event in the HCAL. Event display (right) of a "cosmic" event in the HCAL

- **Category III:** During the cosmic runs, we saw that in the HCAL the maximum multiplicity was 10, we define the events with less than 10 cells above the ADC threshold as cosmic events (see the right event display of Figure: 6.7).

We summarize in Table: 6.1 the mean multiplicity per event for splashes(I), beam halo(II) and cosmic(III) events when requiring at least 10 ADC counts in each cell of the HCAL.

6.3 Time structure of the single events

In the previous section we showed how we were able to categorize the events recorded in the HCAL by means of their multiplicity. We now focus on the time structure of each category. The Figure: 6.8 represents the Kernel distribution for splashes, beam halo and cosmic events. The cosmic events are uniformly distributed between -1 and 1. This behaviour is expected, as the cosmic events are not synchronized. On the other hand 98.9% and 92% of selected cells in the splashes and the beam halo events have a positive value of the Kernel, hence in the expected time samples (**Current/Next1**).

In the tables: 6.2, 6.3 and 6.4 we study the evolution of the time related variables namely, the mean value of the Kernel, the **Current/Next1** asymmetry ($R_{C/N}$), the **Current/Prev1** asymmetry ($R_{C/P}$) and their *rms* as well as the number of selected events in each category, with respect to the cut applied on the ADC value of each cell of the HCAL. We note that:

- All beam halo events are removed when applying a 50 ADC cut;
- 88% of cosmics are rejected using this same when requiring 300 ADC counts per cell;
- Even when applying this last very high cut, the mean multiplicity of the splash events is still high enough (~ 100) to obtain a reliable result for the internal time alignment in the HCAL.

ADC Cut	N. of Evt	$\langle R_{C/P} \rangle$	$rms(R_{C/P})$	$\langle R_{C/N} \rangle$	$rms(R_{C/N})$	$\langle K \rangle$	$rms(K)$
10	12	0.938	0.067	-0.641	0.150	0.185	0.082
50	12	0.971	0.021	-0.652	0.120	0.178	0.061
100	12	0.981	0.012	-0.640	0.120	0.182	0.060
300	12	0.99	0.004	-0.545	0.100	0.228	0.053

Table 6.2: Summary table of the asymmetries and the Kernel for splash events.

ADC Cut	N. of Evt	$\langle R_{C/P} \rangle$	$rms(R_{C/P})$	$\langle R_{C/N} \rangle$	$rms(R_{C/N})$	$\langle K \rangle$	$rms(K)$
10	20	0.823	0.199	-0.636	0.234	0.180	0.169
50	0	-	-	-	-	-	-
100	0	-	-	-	-	-	-
300	0	-	-	-	-	-	-

Table 6.3: Summary table of the asymmetries and the Kernel for beam halo events.

ADC Cut	N. of Evt	$\langle R_{C/P} \rangle$	$rms(R_{C/P})$	$\langle R_{C/N} \rangle$	$rms(R_{C/N})$	$\langle K \rangle$	$rms(K)$
10	264	0.657	0.355	-0.726	0.405	0.0374	0.316
50	222	0.692	0.385	-0.709	0.423	0.0491	0.324
100	96	0.703	0.408	-0.708	0.433	0.0485	0.332
300	19	0.858	0.304	-0.836	0.198	0.0258	0.198

Table 6.4: Summary table of the asymmetries and the Kernel for cosmic events.

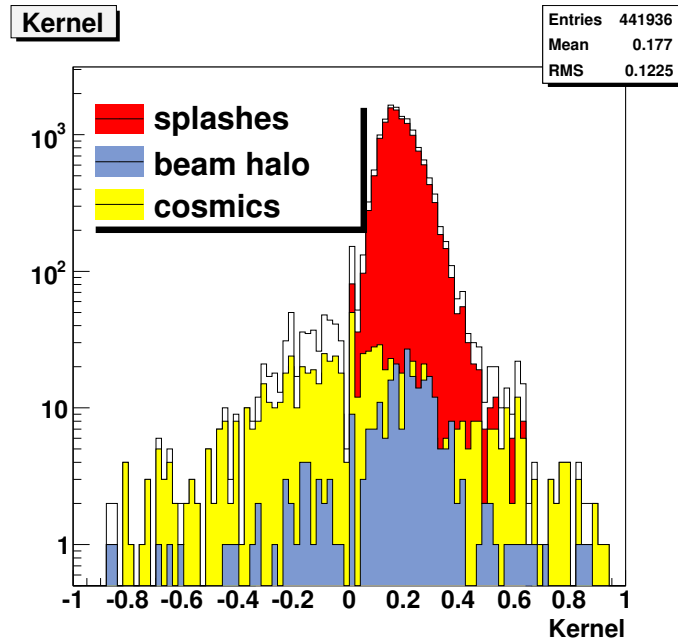


Figure 6.8: Kernel distribution in the HCAL, the red histogram correspond to "splash" events, the blue histogram correspond to "beam halo" events and the yellow histogram correspond to "cosmic events".

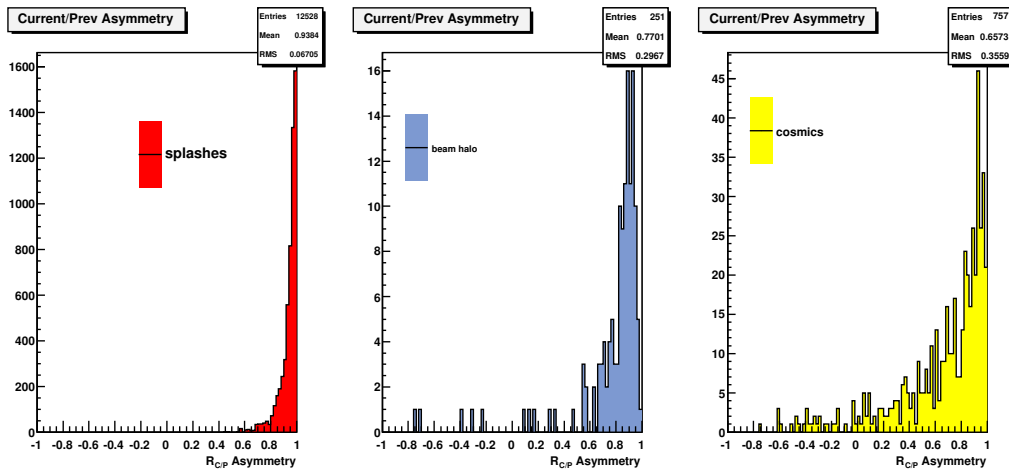


Figure 6.9: Distribution of the **Current/Prev1** asymmetries in the HCAL, the red histogram correspond to "splash" events, the blue histogram correspond to "beam halo" events and the yellow histogram correspond to "cosmic events".

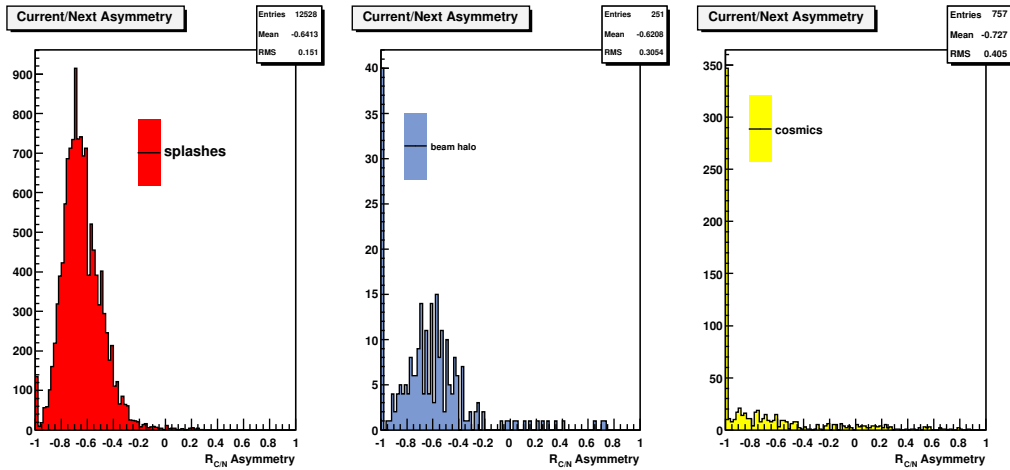


Figure 6.10: Distribution of the **Current/Next1** asymmetries in the HCAL, the red histogram correspond to "splash" events, the blue histogram correspond to "beam halo" events and the yellow histogram correspond to "cosmic events".

6.4 Conclusion

The distribution of Figure: 6.11 shows the most important result of this analysis. To evaluate the internal time alignment in the HCAL, we use the *rms* of the **Current/Next1** distribution when applying a 300 ADC cut. Its value is 1.06 which corresponds using the time-asymmetry conversion extracted from the Monte Carlo to 0.8 ns. From this we can conclude that the hadronic calorimeter is time aligned with respect to the LHC clock with a precision of the order of 0.8 ns. As the hadronic calorimeter provides a precise and reliable measurement of the time alignment with respect to the LHC clock, it will be used as a time reference for all the subdetectors of LHCb.

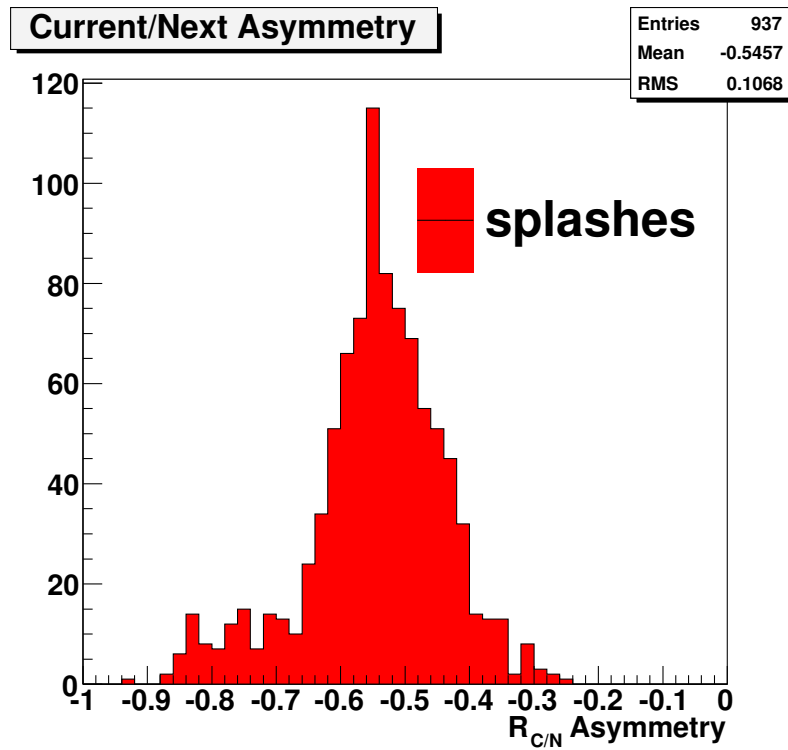


Figure 6.11: Current/Next1 asymmetry distribution in the HCAL, using beam one data.

Chapter 7

Reconstruction of the $B \rightarrow D^- \rho(770)^+$, $B_s \rightarrow D_s^- \rho(770)^+$ and $B_s \rightarrow D_s^- K^{*+}(892)$ decay channels



signal efficiencies while simultaneously rejecting as many background events as possible, keeping in mind the fact that the Monte Carlo is not perfect and thus privileging robust cuts. The event selection is done in two steps. The first one is called preselection, it consists in a set of loose cuts which are applied on both signal and background samples. The second step, called the offline selection, can be based on various methods (cut based method, Fisher discriminant method).

7.1 Monte Carlo samples

Signal data sets Events containing a b hadron of interest within 400 mrad are selected. If an event contains several candidates with the required flavor, one is chosen randomly. For example, if we generate $B_s^0 \rightarrow D_s^- \rho(770)^+$ events and both produced b and \bar{b} quarks hadronize into B_s^0 mesons, one of the two is picked up randomly. The directions of the particles are reversed if the signal hadron is in the backward direction. If the signal hadron does not have the correct flavor, then the hadronization process of PYTHIA [61] is repeated until the interaction contains the required hadron type. Finally the signal candidate is forced to decay using EvtGen [62] according to the decay chain specified in a decay file, and all the underlying particles from the event are decayed. LHCb not being a central detector, generating events in a 4π would just be a waste of processing time. The efficiency of the 400 mrad cut depends on the hadron type and must be taken into account for the yields and background level estimations. The acceptance of the 400 mrad cut is given in the Table: 7.1 for the various samples of the DC06 we have used. The efficiency for the inclusive $b\bar{b}$ sample is higher compared to the signal samples as either one of the two b hadrons can be in the acceptance. The EvtGen package is especially designed to handle b hadron decays. In particular the $B_q - \bar{B}_q$ mixing is simulated with the following parameters:

- B_d : $\Delta m_d = 0.502 \text{ ps}^{-1}$, $\Delta\Gamma = 0$, $\tau_d = 1.536 \times 10^{-12} \text{ s}$;
- B_s : $\Delta m_s = 20 \text{ ps}^{-1}$, $\Delta\Gamma = 0.06852 \text{ ps}^{-1}$, $\tau_s = 1.43 \times 10^{-12} \text{ s}$.

We have used several signal Monte Carlo samples corresponding to the decay modes $B \rightarrow D^- \rho(770)^+$, $B_s \rightarrow D_s^- \rho(770)^+$ and $B_s \rightarrow D_s^- K^{*+}(892)$. The D^-

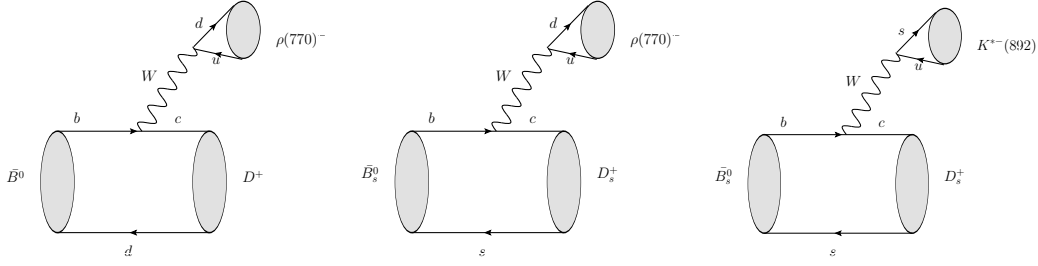


Figure 7.1: Tree level dominant Feynman contribution to $B_d \rightarrow D^- \rho(770)^+$, $B_s \rightarrow D_s^- \rho(770)^+$, $B_s \rightarrow D_s^- K^*(892)^+$ channels.

decays into $K^+ \pi^- \pi^-$, the D_s^- decays into $K^+ K^- \pi^-$, the $\rho(770)^+$ decays into $\pi^+ \pi^0$ and the $K^*(892)^+$ decays into $K^+ \pi^0$. The dominant Feynman graphs for these three channels are shown in Figure: 7.1.

Monte Carlo sample	$A(400 \text{ mrad})$
$B_d \rightarrow D \rho(770)$	0.1641 ± 0.0009
$B_s \rightarrow D_s \rho(770)$	0.1689 ± 0.0010
$B_s \rightarrow D_s K^*(892)$	0.1708 ± 0.0008
Inclusive $b\bar{b}$	0.437 ± 0.1

Table 7.1: Generator-level angular cut efficiencies for the signal channels of interest in DC06. The uncertainties are statistical only.

Background data sets The LHCb trigger is expected to effectively suppress the events not containing b hadrons, therefore the inclusive $b\bar{b}$ events are expected to provide the dominant source of background. During the so called stripping phase, preselection algorithms for all the channels under consideration in LHCb are run in parallel. An event is saved if it is selected by at least one preselection. A given preselection is required to accept at most $\frac{1}{10000}$ of $b\bar{b}$ events, in order to limit the output data size of the stripping.

Minimum bias The minimum bias events are generated with PYTHIA without any requirement on the flavor of the produced particles. Several processes are involved [69]. Examples are: gluon fusion (see left diagram of Figure: 7.2) or quark fusion (see the right diagram of Figure: 7.2). Unlike for the signal or the inclusive $b\bar{b}$ samples, the geometrical cut acceptance is not applied.

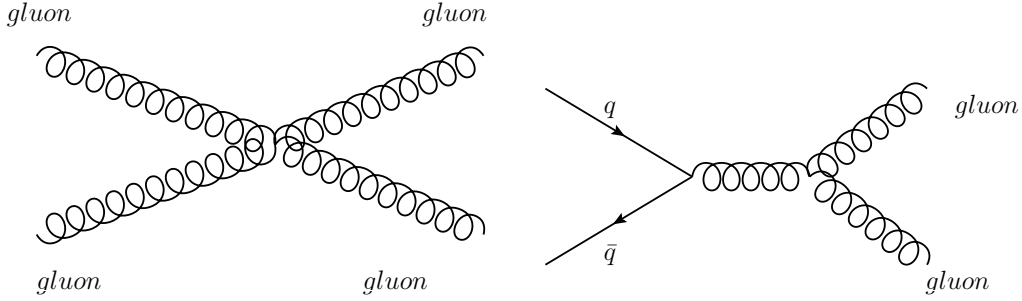


Figure 7.2: Examples of Feynman diagrams for processes included in the minimum bias definition.

7.2 Computation of the numbers of signal and background events

Channels	Branching ratio
$B_d \rightarrow D^- \rho(770)^+$	$(7.7 \pm 1.3) \times 10^{-3}$
$B_s \rightarrow D_s^- \rho(770)^+$	$(9.1 \pm 3) \times 10^{-3}$
$B_s \rightarrow D_s^- K^*(892)^+$	$(0.89 \pm 0.33) \times 10^{-3}$

Table 7.2: Measured or computed branching ratios see Chapter 1, [59].

Channels	Size of the Monte Carlo sample
$B_d \rightarrow D^- \rho(770)^+$	49.5×10^3
$B_s \rightarrow D_s^- \rho(770)^+$	50×10^3
$B_s \rightarrow D_s^- K^*(892)^+$	68.5×10^3
Inclusive unstripped $b\bar{b}$	19.5×10^6
Inclusive stripped $b\bar{b}$	23.2×10^6

Table 7.3: Number of processed Monte Carlo events. It should be noted that the inclusive stripped $b\bar{b}$ sample can be used only for the study of the $B_s \rightarrow D_s^- \rho(770)^+$.

In order to compute the numbers of signal and background events we have used the following assumptions. We have a $b\bar{b}$ cross section of $\sigma_{b\bar{b}} = 500\mu\text{b}$ and the average nominal luminosity of $\mathcal{L} = 2.10^{32} \text{cm}^{-2} \text{s}^{-1}$. The annual number of expected $b\bar{b}$ pairs $N_{b\bar{b}}$ in 4π is thus 10^{12} . The number of signal events produced in 400 mrad is obtained using:

$$N_{sig} = 2 \times N_{b\bar{b}} \times f_{d,s} \times Br_{vis} \times A_{sig}(400 \text{ mrad}).$$

Decay	Branching Fraction
$\rho(770^+) \rightarrow \pi^+\pi^0$	$\sim 100\%$
$K^{*+}(892) \rightarrow K^+\pi^0$	$\frac{1}{3}$

Table 7.4: Branching fraction for $\rho(770^+)$ and $K^{*+}(892)$ [59]

Decay	Branching Fraction
$D^- \rightarrow K^+\pi^-\pi^-$	$9.51 \pm 0.34\%$
$D_s^- \rightarrow K^+K^-\pi^-$	$5.5 \pm 0.2\%$
$D_s^- \rightarrow \phi(1020)(\rightarrow KK)\pi^-$	$2.18 \pm 0.33\%$
$D_s^- \rightarrow K^*(892)(\rightarrow K\pi)K^-$	$2.6 \pm 0.4\%$

Table 7.5: Branching fraction for the D and the D_s [59]

The factor 2 takes into account the production of both b and \bar{b} quark. The production fractions f_d and f_s of $Br(b \rightarrow B_d)$ and $Br(b \rightarrow B_s)$ are taken to be respectively equal to 40% and 10 % [59]. The angular acceptance for the decay channels of interest is given in Table: 7.1. Br_{vis} corresponds to the visible branching ratio of each channel, they are given by:

$$Br_{vis}(B_d \rightarrow D^- \rho(770)^+) = Br(B_d \rightarrow D^- \rho(770)^+) \\ \times Br(D^- \rightarrow K^+\pi^-\pi^-) \times Br(\rho(770)^+ \rightarrow \pi^+\pi^0);$$

$$Br_{vis}(B_s \rightarrow D_s^- \rho(770)^+) = Br(B_s \rightarrow D_s^- \rho(770)^+) \\ \times Br(D_s^- \rightarrow K^+K^-\pi^-) \times Br(\rho(770)^+ \rightarrow \pi^+\pi^0);$$

$$Br_{vis}(B_s \rightarrow D_s^- K^{*+}(892)) = Br(B_s \rightarrow D_s^- \rho(770)^+) \\ \times Br(D_s^- \rightarrow K^+K^-\pi^-) \times Br(K^{*+}(892) \rightarrow K^+\pi^0).$$

The measured branching ratios of the intermediate states are given in Tables: 7.4 and 7.5. The details of the computation of the unmeasured branching ratios corresponding to $B_s \rightarrow D_s^- \rho(770)^+$ and $B_s \rightarrow D_s^- K^{*+}(892)$ channels are given in Chapter 1. The visible branching ratios used for the yield estimations are given in Table: 7.2. We call ϵ_{signal} and $\epsilon_{background}$ the efficiencies of the selections (preselection and offline selection) on signal events and background events respectively. Thus for the annual yield and B/S computations we use for the number of selected signal events:

$$S = 2 \times N_{b\bar{b}} \times f_{d,s} \times Br_{vis} \times A_{sig}(400 \text{ mrad}) \times \epsilon_{signal}.$$

We use for the number of selected background events:

$$B = A_{Bkg}(400 \text{ mrad}) \times 10^{12} \times \epsilon_{background}.$$

7.3 Preselection

Since the topologies of the decay channels of interest are very similar, the preselections are as common as possible. We describe in this section, which criteria are required for all the final state particles (neutral pions, charged pions and the kaons) and on the composite particles (vector resonances $\rho(770)^+$ and $K^*(892)^+$ and the D^- , D_s^- mesons) and finally on the B_d , B_s candidates.

7.3.1 Neutral pions, pions, kaons selection

Neutral pions According to their kinematics, the neutral pions decaying into a pair of photons can be reconstructed either as "resolved" or as "merged" π^0 s. The π^0 invariant mass is given by the following equation:

$$m_{\pi^0} = \sqrt{2E_1E_2(1 - \cos\theta_{12})}, \quad (7.1)$$

where $E_{1,2}$ are the energy of each photon and θ_{12} the angle between the two photons. The mean transverse momentum of the neutral pion from the $B_{d,s}$ decays is about 2 GeV (see Figure: 7.19(b)). Below this value the π^0 s produced at the LHCb interaction point are mostly reconstructed in the calorimeter as a resolved pair of well separated photons.

For each event, all the tracks are extrapolated to the ECAL. A cluster is neutral if none of the tracks are consistent with its position. Quality estimator, χ_{2D}^2 of the cluster-track matching, is required to be greater than unity.

The procedure used to form the resolved π^0 first reconstructs the photon candidates from the list of neutral clusters, then loops over the candidates, pairs them and compares the corresponding invariant masses with the nominal π^0 mass [58]. Among the photons candidates, only those with P_t greater than 200 MeV/c are kept and paired to reconstruct the π^0 within a mass window of 30 MeV.

About 30 % of the reconstructible π^0 from the signal channels lead to a single cluster. Such a configuration, will be referred to as "merged" π^0 which essentially appears for π^0 above 2 GeV of transverse momentum. A procedure

Function	Description
Gaussian	$G(m, \sigma) = \frac{1}{\sqrt{2\pi\sigma}} e^{-\frac{1}{2}\left(\frac{x-m}{\sigma}\right)^2}$
Double Gaussian	$DG(m, \sigma_1, \sigma_2, f) = fG(m, \sigma_1) + (1 - f)G(m, \sigma_2)$
Non relativistic Breit-Wigner	$BW(m, \Gamma) = \frac{1}{(x-M)^2 + \frac{1}{4}\Gamma^2}$

Table 7.6: Description of the functions used to fit the mass distributions.

has been designed to identify a potential pair of photons merged into a single cluster. The algorithm consists in splitting each of the single clusters into two interleaved 3×3 subclusters built around the two main cells of the original cluster. The energy of the common cells is then shared among the two virtual subclusters according to an iterative procedure based on the expected transversal shape of the photon showers. The sharing of the energy depends on the barycenter position of each subcluster that is a function of the energy sharing. The procedure is iterative and fastly converging. Each of the two subclusters for merged π^0 is required to be neutral, using the track matching described above. It is required as well that the invariant mass of the merged photons is compatible with a π^0 mass within 60 MeV. A cut is applied on the minimal distance between the impacts of the two photons in the ECAL front face that is kinematically allowed for a π^0 decay:

$$d_{\gamma\gamma} = 2 \times z_{ECAL} \times \frac{m_{\pi^0}}{E_{\pi^0}} < 1.8 \text{ cell size},$$

where z_{ECAL} is the longitudinal position along the beam axis of the ECAL front face ($z_{ECAL}=12520$ mm). This cut is fully equivalent to an energy cut of 45 GeV, 30 GeV and 15 GeV in the inner, middle and outer ECAL regions, respectively.

Pions Any charged particle track used in the analysis is required to fulfill the set of requirements [67] listed below in order to remove badly measured tracks or secondaries from interaction with matter:

- The particle momentum at its production vertex is larger than 1 GeV/c;
- Three reconstructed clusters in the r sensors of the VELO;
- Three reconstructed clusters in the ϕ detectors of the VELO;
- A reconstructed x and u hit in each of the tracking stations T1-T3;
- It does not interact hadronically before the end of the T stations.

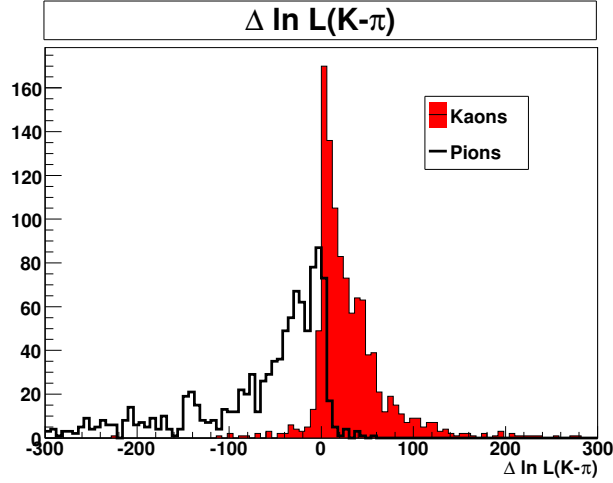


Figure 7.3: $\Delta \ln \mathcal{L}_{K\pi}$ for kaons (plain histogram) and pions (white histogram) from $B_s \rightarrow D_s K^*$ (892) signal events.

Kaons Particle identification is provided by the two RICH detectors, the calorimeter and the Muon detectors. For a hadron particle h one can write a combined likelihood based on the likelihood PID estimators from different subsectors:

$$\mathcal{L}_h = \mathcal{L}^{\text{RICH}}(h) \times \mathcal{L}^{\text{ECAL}}(\text{not } e) \times \mathcal{L}^{\text{Muon}}(\text{not } \mu) \quad (7.2)$$

Because pions are more abundant than kaons in an event, a cut based on the difference between the kaon and the pion hypothesis is used:

$$\Delta \ln \mathcal{L}_{K\pi} = \ln \mathcal{L}(K) - \ln \mathcal{L}(\pi) = \ln \left[\frac{\mathcal{L}(K)}{\mathcal{L}(\pi)} \right] \quad (7.3)$$

This cut is applied to tracks which fulfilled the track requirements. A particle with true type kaon will then tend to have a positive $\Delta \ln \mathcal{L}_{K\pi}$ (see Figure: 7.3). We require for all the kaon candidates: $\Delta \ln \mathcal{L}_{K\pi} > -5$, the efficiency of this $\Delta \ln \mathcal{L}_{K\pi}$ cut is $\sim 91\%$ on kaons, while the pion misidentification rate is 13% . To reduce the combinatorial background, a cut on the momentum P and on the transverse momentum P_t and on the impact parameter significance is applied to all the final state particles. The impact parameter of a track with respect to a vertex is defined as the perpendicular distance between the track and the vertex. The Figure 7.4 shows this graphically in two dimensions. The impact parameter significance is defined as: $\text{IPs} = \text{IP}/\sigma_{\text{IP}}$, where σ_{IP} denotes the uncertainty on the impact parame-

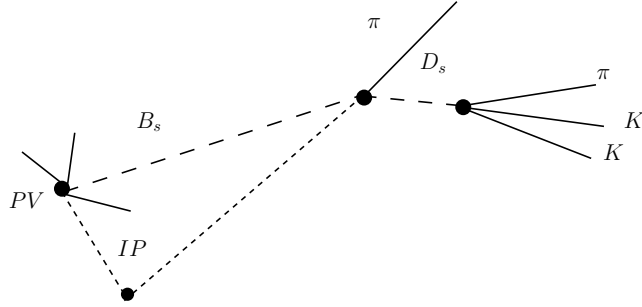


Figure 7.4: 2-dimensional view of the impact parameter of a track with respect to the primary vertex.

ter. Since all the final state particles of interest are produced at a detached vertex, a cut on the IPs is applied for all the charged tracks of the event.

7.3.2 $\rho(770)$, $K^*(892)$ selection

The vector resonances $\rho(770)$, $K^*(892)$ are reconstructed using the following modes: $\rho(770)^+ \rightarrow \pi^+\pi^0$ and $K(892)^{*+} \rightarrow K^+\pi^0$. We do not use the isospin conjugate mode for the $K(892)^{*+}$ decay to $K^0\pi^+$. Even though the branching ratio is larger (2/3), the aim of this study was to check the π^0 reconstruction performances for hadronic B decays.

The charged track from the vector resonance is combined with a π^0 . The branching ratios are listed in Table: 7.4. With only one charged track and a neutral particle no vertexing is done. The resonance mass is defined as the invariant mass of the system (π or K) and π^0 (using the dedicated algorithm ParticleAdder [68]). A symmetric cut is applied on the reconstructed mass (see Figure: 7.5) of the vector resonance around the true nominal Monte Carlo value: $\pm 300 \text{ MeV}/c^2$ for the $\rho(770)^+$ and $\pm 150 \text{ MeV}/c^2$ for the $K^{*+}(892)$. Both mass distributions are fitted with a non relativistic Breit-Wigner function defined in Table: 7.6, convoluted with a simple Gaussian with a fixed sigma ($\sigma = 80 \text{ MeV}/c^2$ for the $\rho(770)^+$ fit and $\sigma = 38 \text{ MeV}/c^2$ for the $K^{*+}(892)$ fit.) to take into account the ECAL resolution. The fitted parameters for

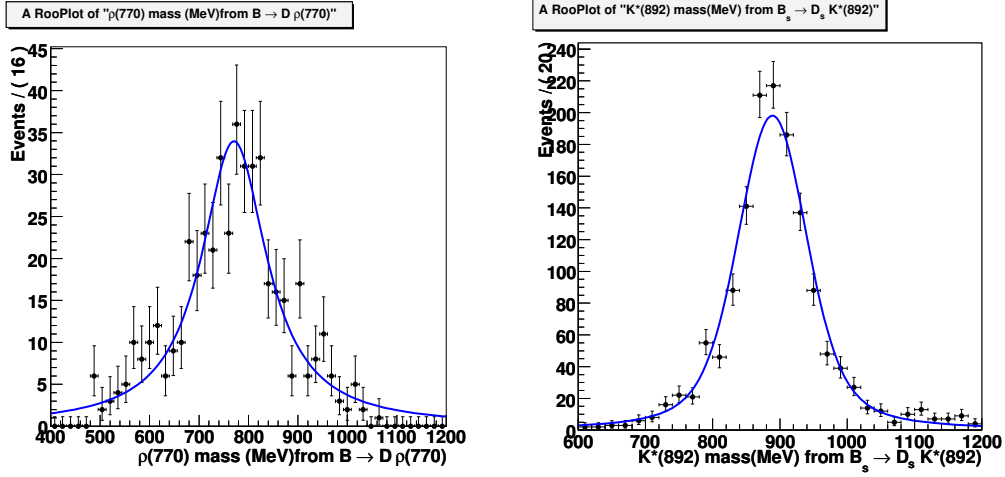


Figure 7.5: $\rho(770)$ invariant mass in $B_d \rightarrow D\rho(770)$ (right), $K(892)^*$ invariant mass in $B_s \rightarrow D_s K(892)^*$ (left).

the $\rho(770)^+$, $K^{*+}(892)$ are given by:

$$m_{\rho(770)} = 769 \pm 4 \text{ MeV}/c^2, \Gamma_{\rho(770)} = 156 \pm 12 \text{ MeV}/c^2, \sigma = 80 \text{ MeV}/c^2,$$

$$m_{K^*(892)} = 888 \pm 2 \text{ MeV}/c^2, \Gamma_{K^*(892)} = 49 \pm 3 \text{ MeV}/c^2.$$

The corresponding distributions are shown in Figure: 7.5.

7.3.3 D, D_s selection

The D and the D_s are reconstructed using the hadronic modes $D^- \rightarrow K^+\pi^-\pi^-$ and $D_s^- \rightarrow K^+K^-\pi^-$. The branching ratios of each mode are given in Table: 7.5. In the preselection, the D_s resonances, $\phi(1020)$ and $K^*(892)$ are not reconstructed explicitly. The charged tracks from the $D_{d,s}$ composite particles are combined by means of a geometrical fit called OfflineVertexFitter [68]. This algorithm is dedicated to secondary vertices fitting, the intermediate resonances for example the $\phi(1020)$ in $D_s^- \rightarrow \phi(1020)\pi^-$ are ignored. The four momentum, the mass, the vertex position, the covariance matrix, and the vertex χ^2 of the mother particle are computed. Like for vector resonance, a symmetric cut of $\pm 15 \text{ MeV}/c^2$ on the reconstructed mass (see Figure: 7.6) around the nominal Monte Carlo mass is applied.

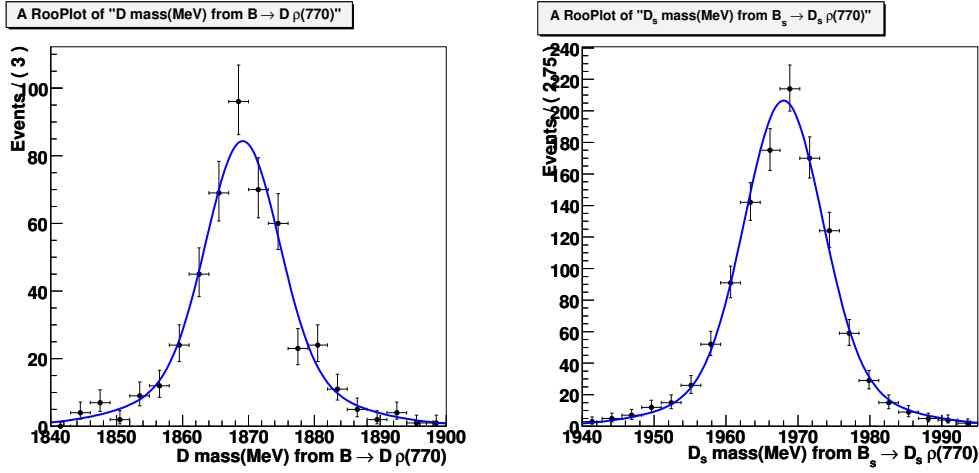


Figure 7.6: D invariant mass in $B_d \rightarrow D\rho(770)$ (right) , D_s invariant mass in $B_s \rightarrow D_s K(892)^*$ (left).

The reconstructed D^- and D_s are fitted with a double Gaussian defined in Table: 7.6:

$$m_D = (1869.1 \pm 0.3) \text{ MeV}/c^2, \sigma_1 = (5.5 \pm 0.2) \text{ MeV}/c^2,$$

$$\sigma_2 = (13 \pm 2) \text{ MeV}/c^2, f = (68.3 \pm 0.1)\%,$$

$$m_{D_s} = (1968.1 \pm 0.3) \text{ MeV}/c^2, \sigma_1 = (5.3 \pm 0.3) \text{ MeV}/c^2,$$

$$\sigma_2 = (13 \pm 1) \text{ MeV}/c^2, f = (75.4 \pm 0.9)\%.$$

7.4 B^0, B_s^0 selection

The $D_{d,s}$ candidate is paired with the charged track from the vector resonance to geometrically fit the vertex of the $B_{d,s}$. The mass of the $B_{d,s}$ candidate is defined as the invariant mass of the $(D_{d,s}(\rho/K^*))$ system. A cut on the quality of the fitted vertex is applied to all the $B_{d,s}$ candidates. Applying geometrical cuts allows to reduce the combinatorial background. The flight

Variables	Cut
$\pi^0 P_t$	$> 0.7 \text{ GeV}$
$\pi^0 P$	$> 2 \text{ GeV}$
πP_t	$> 0.5 \text{ GeV}$
$\pi \text{ IPs}$	> 2
$\rho(770) \text{ Mass window}$	300 MeV
$\rho(770) P_t$	$> 0.3 \text{ GeV}$
$D \text{ Mass window}$	15 MeV
$B_d \text{ Mass window}$	500 MeV
$B_d \text{ Prim. Vertex } \chi^2$	< 10
$B_d \text{ IPs}$	< 5
$B_d \text{ Flight Dist. Sign.}$	> 3
$B_d \cos\theta_B$	> 0.9999
$\epsilon(\text{Signal})$	$(1.63 \pm 0.44) \times 10^{-2}$
$\epsilon(\text{Background})$	$(0.9 \pm 2.2) \times 10^{-4}$

Table 7.7: Preselection cuts for $B_d \rightarrow D^- \rho^+(770)$.

distance FD is defined as the distance between the $B_{d,s}$ decay vertex and the associated primary vertex. A cut is applied on the angle θ_b defined as the angle between the reconstructed $B_{d,s}$ momentum \vec{p} and the direction of flight \vec{F} . The Tables: 7.7, 7.8 and 7.9 summarize all the cuts applied in the preselection.

Starting from the output of these preselections we proceed to an offline selection. There are various techniques to isolate the signal events from the background events. One can use a "cut based" method which is simply a set of cuts. An other approach is to use multi-variables methods, where a set of variables are combined in a single one. The Fisher discriminant is a technique allowing to discriminate between two classes of events. The classes in this analysis are the signal events and the dominant source of background the inclusive $b\bar{b}$ events. Starting from a set (n_{var}) of variables (x_i), an iterative method called training computes the weights (c_i) appearing in front of each variable. The combined variable can be written as:

$$FI = c_0 + \sum_{i=1}^{n_{var}} c_i \cdot x_{var} \quad (7.4)$$

The Fisher discriminant only uses the possible *linear* correlations between the variables. It is easy, fast and produces signal and background distributions which are easily parameterizable. The impact of each variable in the

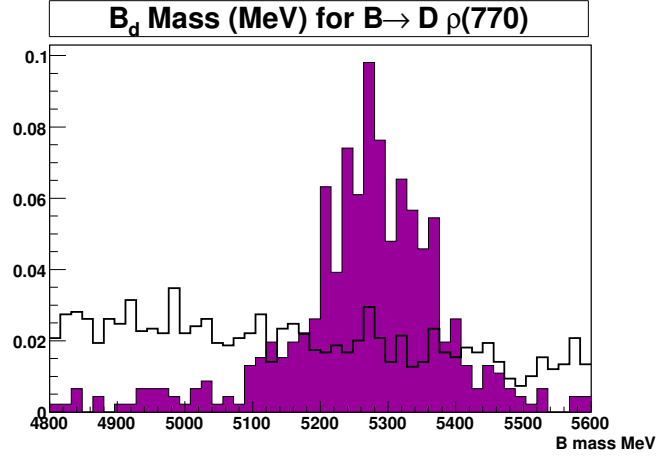


Figure 7.7: B_d reconstructed mass from preselected signal and background samples in $B_d \rightarrow D\rho(770)$, the plain histogram represents the signal events and the white histogram represents the background events. The two distributions are arbitrary normalized to unity.

Variables	Cut
$\pi^0 P_t$	> 500 MeV
$\pi^0 P$	> 1 GeV
πP_t	> 500 MeV
πP	> 1 GeV
$\rho(770)$ Mass window	300 MeV
D_s Mass window	15 MeV
B_s Mass window	500 MeV
B_s Prim. Vertex χ^2	< 10
B_s IPs	< 6
B_s Flight Dist. Sign.	> 3
$B_s \cos \theta_B$	> 0.9999
$\epsilon(\text{Signal})$	$(1.78 \pm 0.44) \times 10^{-2}$
$\epsilon(\text{Background})$	$(0.73 \pm 2.2) \times 10^{-4}$

Table 7.8: Preselection cuts for $B_s \rightarrow D_s^- \rho^+$.

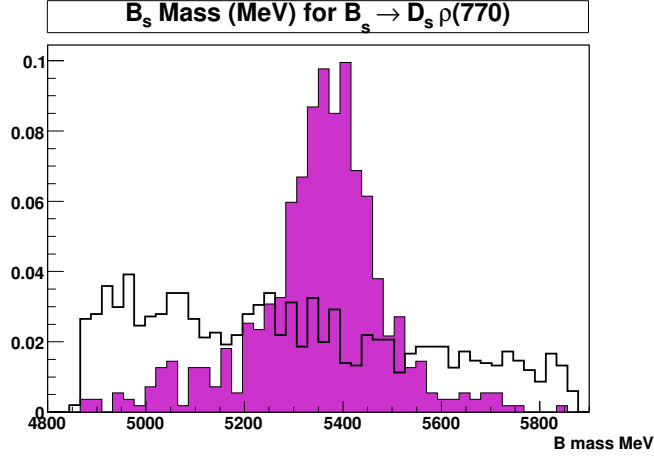


Figure 7.8: B_s reconstructed mass from preselected signal and background samples in $B_s \rightarrow D_s^- \rho(770)^+$, the plain histogram represents the signal events and the white histogram represents the background events. The two distributions are arbitrary normalized to unity.

Variables	Cut
$\pi^0 P_t$	$> 0.5 \text{ GeV}$
$\pi^0 P$	$> 0.750 \text{ GeV}$
$K P_t$	$> 0.3 \text{ GeV}$
$K P$	$> 0.5 \text{ GeV}$
$K^*(892) \text{ Mass window}$	150 MeV
$D_s \text{ Mass window}$	15 MeV
$B_s \text{ Mass window}$	500 MeV
$B_s \text{ Prim. Vertex } \chi^2$	< 10
$B_s \text{ IPs}$	< 6
$B_s \text{ Flight. Dist. Sign.}$	> 3
$B_s \cos \theta_B$	> 0.9999
$\epsilon \text{ (Signal)}$	$(1.4 \pm 0.4) \times 10^{-2}$
$\epsilon \text{ (Background)}$	$(0.28 \pm 3.54) \times 10^{-4}$

Table 7.9: Preselection cuts for $B_s \rightarrow D_s^- K(892)^+$.

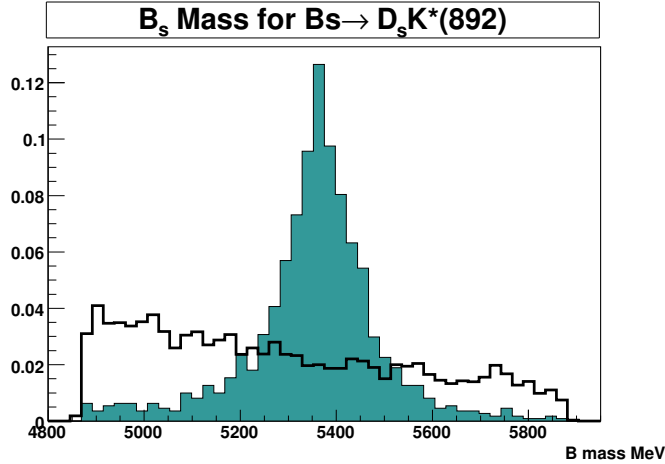


Figure 7.9: B_s reconstructed mass from preselected signal and background samples in $B_s \rightarrow D_s^- K^{*+}(892)$, the plain histogram represents the signal events and the white histogram the background events. The two distributions are arbitrary normalized to unity.

Fisher is directly visible, since it is expressed by the value of its coefficient c_i . The constants c_i are chosen to maximize the separation between the signal and the inclusive $b\bar{b}$ events. The constant c_0 and the overall scale sign do not affect the separation, but are simply chosen so that the average distribution of the sample is zero, $\langle FI \rangle = 0$ and the signal has a value higher than the background one: $\langle FI_{signal} \rangle > \langle FI_{background} \rangle$. For this analysis, several multivariate methods have been tested (Neural Network for example), Since the Fisher discriminant method has performances, similar to other ones and the simplest one, we will use it in the following, using the TMVA package [60].

Overtraining To avoid the overtraining we split the signal and background in a training sample and a test sample of the same size. Overtraining occurs in a multivariate analysis when they are too few degrees of freedom for example the parameters of the classifier are adjusted on too few data. Practically overtraining will be seen as a training giving the best achievable results in the training sample, but poor results on an independent sample.

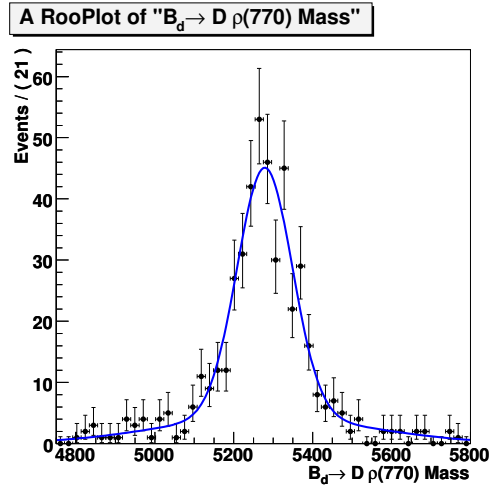


Figure 7.10: B_d invariant mass for signal events for the $B_d \rightarrow D^- \rho(770)^+$ decay channel.

7.5 $B^0 \rightarrow D^- \rho(770)^+$ selection

We describe in this section the extraction of the signal events, $B_d \rightarrow D^- \rho(770)^+$, using a Fisher discriminant method. When this analysis was done, the preselection for $B_d \rightarrow D^- \rho(770)^+$ was not included in the stripping phase. Hence the processed background events correspond to "unstripped" inclusive $b\bar{b}$ background events (for data storage reasons, these samples do contain the minimal information needed, for example they do not contain the Monte Carlo Truth information). The invariant B_d mass shown in Figure: 7.10 is fitted with a double Gaussian (see the definition in Table: 7.6). We obtain, $m = (5278.1 \pm 4.4)$ MeV, $f = (58.9 \pm 5.2)\%$ MeV, $\sigma_1 = (69.7 \pm 5.3)$ MeV and $\sigma_2 = (261.9 \pm 4.3)$ MeV. In the preselection the cut on the mass window of the reconstructed B_d is 500 MeV. Due to the limited amount of Monte Carlo sample background, we use this large cut to increase the amount of selected $b\bar{b}$ events. Nevertheless, for the final annual yields computation, we count of the signal and background events in the B_d signal box which is equal to 300 MeV.

Double counting Among preselected signal and background events samples, some contain more than one candidates. For example, we observe two B_d per event sharing the same tracks (from the D^- and the $\rho(770)^+$) but

not the same π^0 . Therefore, at the very end of the selection, we select the candidate which has the lowest value of a variable called DC based on the D^\pm and π^0 mass:

$$DC = |(m_{D^\pm} - m_{D_{PDG}^\pm})| + |(m_{\pi^0} - m_{\pi_{PDG}^0})| \quad (7.5)$$

Where, m_{D^\pm} and m_{π^0} are the D^\pm and π^0 reconstructed masses of the candidate, while are $m_{D_{PDG}^\pm}$ and $m_{\pi_{PDG}^0}$ the nominal D^\pm and π^0 masses taken from the Particle Data Group [59]. Finally, if more than one candidate remain per event, we choose one candidate completely randomly.

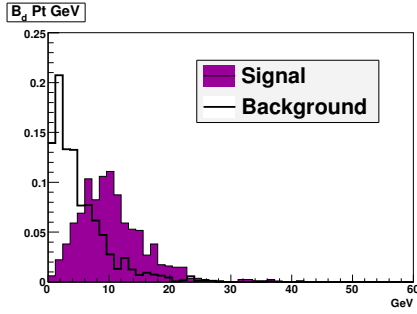
7.5.1 Fisher coefficients computation

The variables used in the Fisher discriminant method are the following:

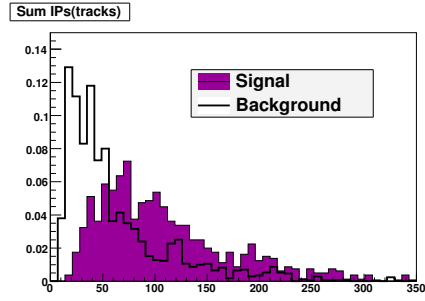
- $P_t(B_d)$, the B_d transverse momentum (see Figure: 7.11(a));
- $\cos(\theta_b)$, cosine of the pointing angle (see definition in SubSection: 7.4 and see Figure: 7.11(c));
- $M(\rho(770))$, the $\rho(770)^+$ invariant mass (see Figure: 7.11(e));
- $|\cos \theta_\rho^*|$, is the cosine of the helicity angle of the vector resonance $\rho(770)^0$. It is defined as the angle between one of the daughters and the flight direction of the resonance axis in its rest frame. For signal events, the helicity is expected to follow the a $|\cos \theta_\rho^*|^2$ distribution while it is flat for the background events (see Figure: 7.11(d))².
- \sum_{tracks} IPs, the sum of the impact parameter significance of the charged tracks (pion from the $\rho(770)^+$, the two pions and the kaon from the D^- (see Figure: 7.11(b)).
- $P_t(\pi^0)$, the transverse π^0 momentum. (see Figure: 7.11(f)).

They are combined using a Fisher discriminant method, in a single variable. The combined variable is a linear combination of the discriminant variables.

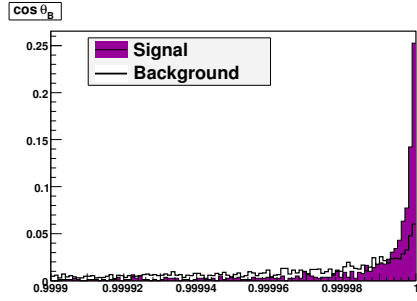
²The resonance $\rho(770)$ is a vector with a spin 1, while the daughter particles: π^+ , π^0 are pseudoscalars with a spin 0. Since the $\rho(770)$ is a vector there are three states: -1, 0, 1. Due to the conservation of the angular momentum, only one fully longitudinal amplitude is accessible. The corresponding Wigner matrix elements is : $d_{0,0}^1 = \cos \theta^*$. The angular probability density function is proportional to $|\cos^2 \theta|$. This angular property is also true for the decays: $K(892)^{*\pm} \rightarrow K^+ \pi^0$, $\phi(1020) \rightarrow K^+ K^-$ and $K(892)^{*0} \rightarrow K^+ \pi^-$.



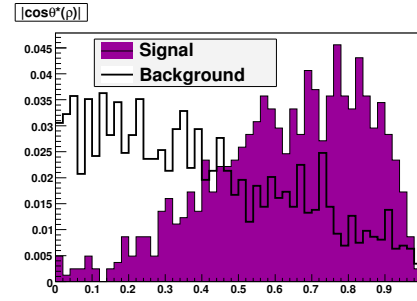
(a) B_d transverse momentum



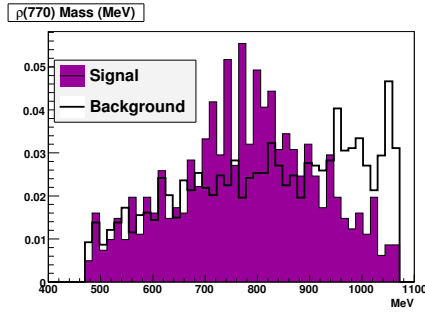
(b) $\sum_{\text{tracks}} \text{IPs}$



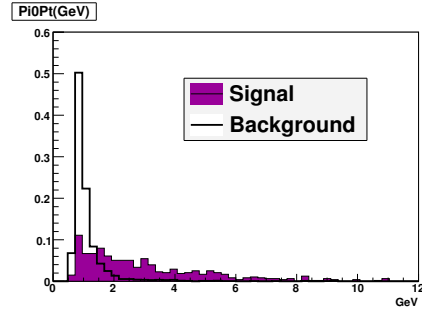
(c) $\cos(\theta_b)$



(d) Absolute value of the cosine of the $\rho(770)^+$ helicity angle



(e) $\rho(770)^+$ invariant mass



(f) π^0 transverse momentum

Figure 7.11: Variables related to the $B_d \rightarrow D^- \rho(770)^+$ decay channel, all distributions are normalized to unity.

Variables	Fisher Coef.
$\cos \theta_B$	+0.035
$Pt(B_d)$	+0.212
$Pt(\pi^0)$	+0.896
$M(\rho(770)^+)$	-0.078
$\sum_{\text{tracks}} \text{IPs}$	+0.326
$ \cos \theta_{\rho(770)^+}^* $	+0.035

Table 7.10: The Fisher coefficient of the variables used in the Fisher discriminant method for $B_d \rightarrow D^- \rho(770)^+$. The π^0 transverse momentum is the most discriminating variable.

The coefficients c_i defined in Equation: 7.4 appearing in front of each variable represents the weight of each variable see Table: 7.10. A variable with a high discriminating power will contribute more in the combined variable, in this analysis this is the case for the π^0 transverse momentum.

7.5.2 $\frac{S}{\sqrt{S+B}}$ optimization

Once we built this new variable, using the whole signal and background samples (see the distributions of Figure: 7.12), a single cut is optimized to maximize the ratio $\frac{S}{\sqrt{S+B}}$. It is the statistical significance comparing the number of signal events S to the total number of events $S+B$. Figure: 7.13 shows the variation of the statistical significance as a function of the cut applied on the combined variable. Both signal and background events are normalized to an integrated luminosity of 2 fb^{-1} . The maximum of $\frac{S}{\sqrt{S+B}}$ is obtained for $F=0.024$.

7.5.3 Signal and background estimation

Both combined variables shown in Figure: 7.12 are fitted with a bifurcated Gaussian. N_i is defined as the fraction of events above the optimized cut as following:

$$N_i = \frac{\int_{F_{\text{FisherCut}}}^{F_{\text{Max}}} BG_i(F) dF}{\int_{F_{\text{Min}}}^{F_{\text{Max}}} BG_i(F) dF}, \text{ where: } i = \text{signal or background.} \quad (7.6)$$

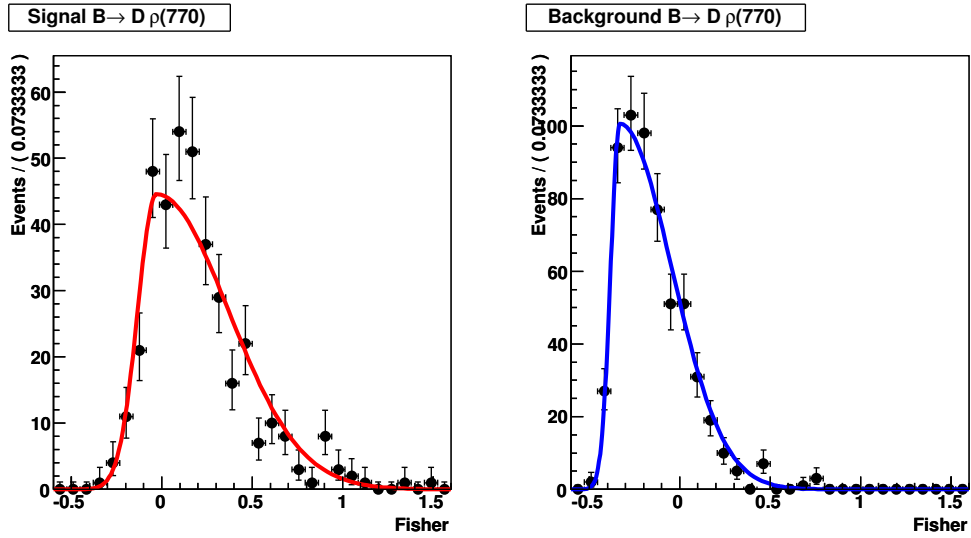


Figure 7.12: Fisher distribution for signal events (left) background events (right).

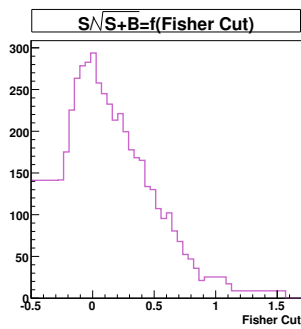


Figure 7.13: $\frac{S}{\sqrt{S+B}}$ as a function of the cut in the combined variable, obtained by means of a Fisher discriminant method for $B_d \rightarrow D^- \rho(770)^+$.

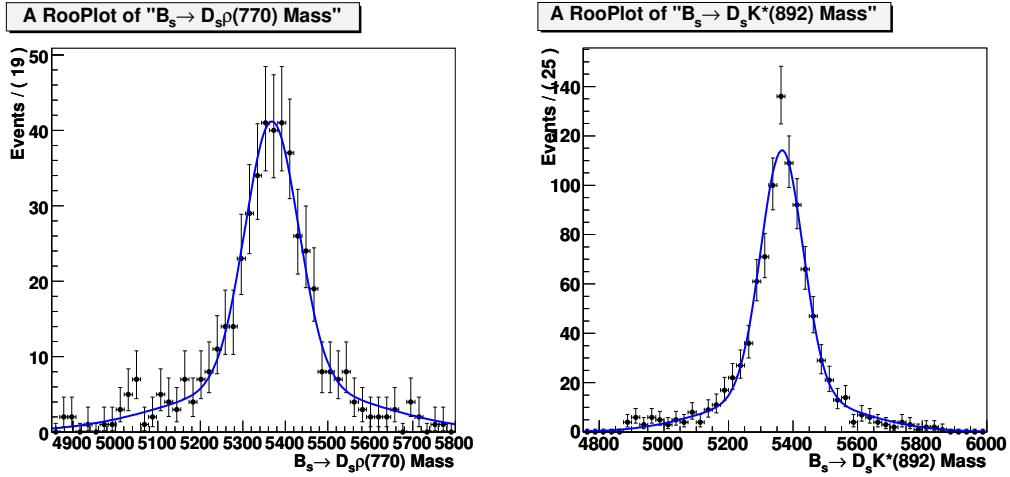


Figure 7.14: B_s invariant mass for signal events in $B_s^0 \rightarrow D_s^- \rho(770)^+$ (left), and for signal events in $B_s^0 \rightarrow D_s^- K^{*+}(892)$.

The fitted number of signal and background events are extrapolated to a 2 fb^{-1} luminosity. Finally, as shown in Table: 7.11, one could expect at LHCb $\sim 450 \text{ k}$ $B_d \rightarrow D^- \rho(770)^+$ signal events for 2 fb^{-1} (before trigger). As can

	Signal	Background	B/S
Best $S/\sqrt{S+B}$	450 k	725 k	1.6

Table 7.11: Annual yield for 2 fb^{-1} for $B_d \rightarrow D^- \rho(770)^+$

be seen in Table: 7.11 the size of the signal sample is very large and a much higher S/B could be obtained while keeping a visible $B_d \rightarrow D^- \rho(770)^+$ mass peak. From the same table, one can conclude that this decay mode should be one of the first hadronic channels with a π^0 observed at LHCb.

7.6 $B_s^0 \rightarrow D_s^- \rho(770)^+$ and $B_s^0 \rightarrow D_s^- K^{*+}(892)$ selection

The channels $B_s^0 \rightarrow D_s^- \rho(770)^+$ and $B_s^0 \rightarrow D_s^- K^{*+}(892)$ are very similar. They differ by the nature of the bachelor hadron (pion or kaon) coming from the vector resonances, ($\rho(770)^+$ or $K^{*+}(892)$), and the natural widths of these resonances (150 MeV and 50 MeV respectively [59]). The invariant mass distributions of the B_s mesons for the two channels of interest are fitted

with a double Gaussian (see the definition in Table: 7.6). The corresponding fitted variables are:

- for $B_s^0 \rightarrow D_s^- \rho(770)^+$: $m = (5368.4 \pm 4.5)$ MeV, $f = (61.2 \pm 6.2)\%$, $\sigma_1 = (62.7 \pm 5.3)$ MeV and $\sigma_2 = (227.9 \pm 28.8)$ MeV,
- for $B_s^0 \rightarrow D_s^- K^{*+}(892)$: $m = (5365.3 \pm 3.0)$ MeV, $f = (58.9 \pm 5.2)\%$, $\sigma_1 = (65.7 \pm 4.1)$ MeV and $\sigma_2 = (270.9 \pm 15.3)$ MeV.

Double candidates At the very end of both selection, multiple candidates are removed, using the same approach as in $B_d \rightarrow D^- \rho(770)^+$ selection. We first reduce the multiple candidates, choosing the one with the smallest parameter DC defined as:

$$DC = |(m_{D_s^\pm} - m_{D_s^\pm P_{DG}}) + (m_{\pi^0} - m_{\pi^0 P_{DG}})| \quad (7.7)$$

where, $m_{D_s^\pm}$ and m_{π^0} are the D_s^\pm and π^0 reconstructed masses of the candidate, while $m_{D_s^\pm P_{DG}}$ and $m_{\pi^0 P_{DG}}$ the nominal D_s^\pm and π^0 masses taken from the Particle Data Group [59]. If in a given event some multiple candidates remain, choose one candidate randomly. We have shown in SubSection: 7.3.1 that according to their kinematics the π^0 s can be reconstructed as resolved or merged. As the preselected signal and background samples are large enough for both $B_s^0 \rightarrow D_s^- \rho(770)^+$ and $B_s^0 \rightarrow D_s^- K^{*+}(892)$, we will build by means of a Fisher discriminant two variables, one for each type of π^0

7.6.1 Fisher coefficients computation

The following variables are combined using a Fisher discriminant method for both channels:

- $P_t(B_s)$, the transverse B_s momentum (see Figure: 7.15(a) and Figure: 7.16(a));
- $\cos(\theta_b)$, cosine of the pointing angle (see Figure: 7.15(e) and Figure: 7.17(b));
- The vector resonance invariant mass, see the $\rho(770)^+$ mass distribution in Figure: 7.18(a) and the $K^{*+}(892)$ mass distribution in Figure: 7.20(a);

- $|\cos \theta_{Vec}^*|$, absolute value of the cosine of the helicity angle of the vector resonance, see Figure 7.18(b) and 7.20(b);
- \sum_{tracks} IPs, the sum of the impact parameter significance of the charged tracks, ie the bachelor hadron from the vector resonance, the pion and the two kaons from the D_s (see the distributions in Figure: 7.15(d), Figure: 7.17(a));
- $Pt(\pi^0)$, the transverse π^0 momentum, see distributions in Figure: 7.19(b) and Figure: 7.21(a).

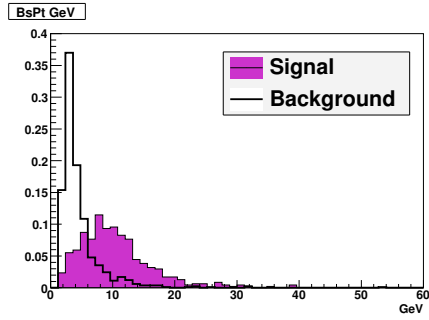
For the $B_s^0 \rightarrow D_s^- K^{*+}$ (892) selection, we add the kaon PID ($\Delta \ln \mathcal{L}_{K\pi}$) shown in Figure: 7.16(b) to the list of discriminating variables previously mentioned. We give for both channels in tables: 7.12, 7.13, the Fisher coefficients computed for each type of π^0 s.

Variables	Fisher Coef.(resolved π^0 s)	Fisher Coef.(merged π^0 s)
$\cos \theta_B$	+0.220	+0.540
$Pt(B_s)$	+0.329	-0.561
$Pt(\pi^0)$	+0.508	-0.062
$M(\rho(770)^0)$	-0.158	+0.110
\sum_{tracks} IPs	+0.505	+0.108
$ \cos \theta_{\rho(770)^+}^* $	+0.088	+0.359

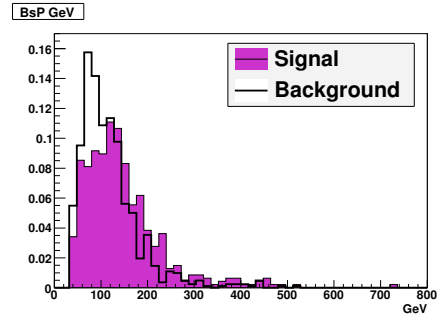
Table 7.12: The Fisher coefficients of the variables using in the Fisher discriminant method for $B_s \rightarrow D_s^- \rho(770)^+$. For events with a resolved π^0 the most discriminating variable is the π^0 transverse momentum, for events with a merged π^0 the most discriminating variable is $P_t(B_s)$.

7.6.2 $\frac{S}{\sqrt{S+B}}$ optimization

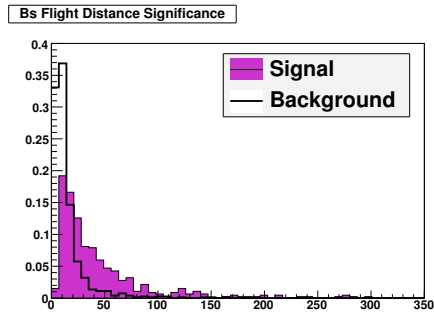
The combined variable obtained for each type of neutral pion and for both $B_s \rightarrow D_s^- \rho(770)^+$, $B_s \rightarrow D_s^- K^{*+}$ (892) are shown in Figures: 7.22, 7.23, 7.24, 7.25. We adopt the same optimization strategy as for the $B \rightarrow D^- \rho(770)^+$ channel. We optimize a single cut on the combined variable in each case to maximize the statistical significance ($\frac{S}{\sqrt{S+B}}$). All the combined variables are fitted with a bifurcated Gaussian. The number of signal and background are computed using Equation: 7.6. The evolution of $\frac{S}{\sqrt{S+B}}$ as a function of the cut on the



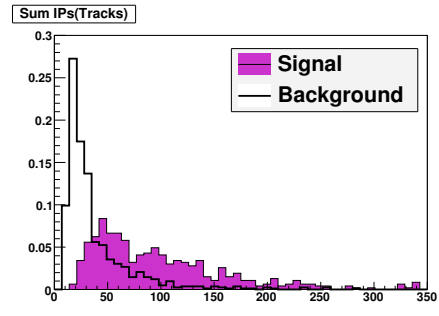
(a) B_s transverse momentum (MeV/c)



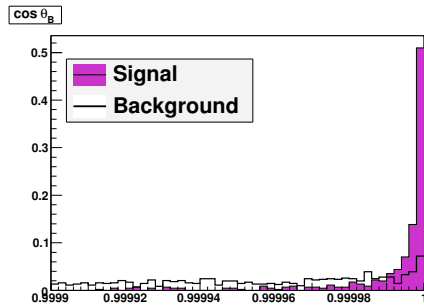
(b) B_s momentum (MeV/c)



(c) B_s flight distance significance

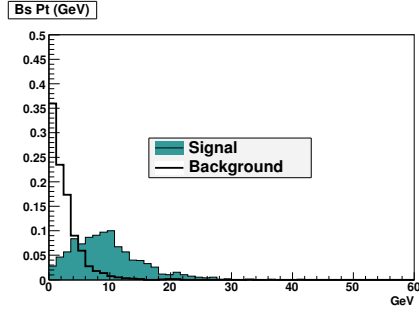


(d) $\sum_{IP_{tracks}}$

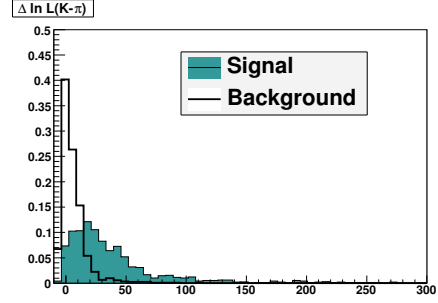


(e) $\cos(\theta_b)$

Figure 7.15: Variables for $B_s \rightarrow D_s^- \rho(770)^+$, all distributions are normalized to unity.

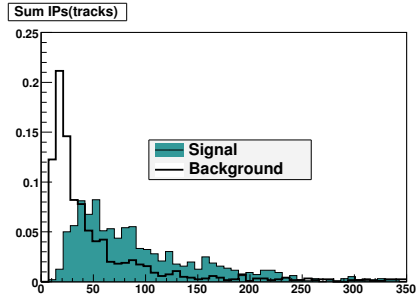


(a) B_s transverse momentum

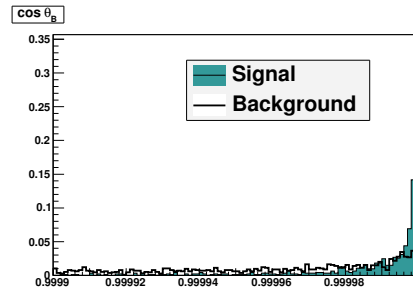


(b) $\Delta \ln \mathcal{L}_{K\pi}$

Figure 7.16: Variables for $B_s \rightarrow D_s^- K^{*+}$ (892), all distributions are normalized to unity.

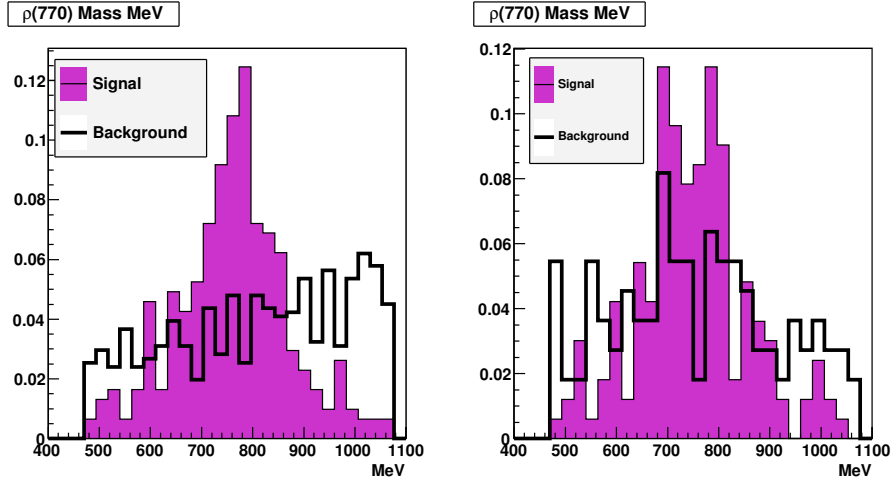


(a) $\sum IP_{tracks}$

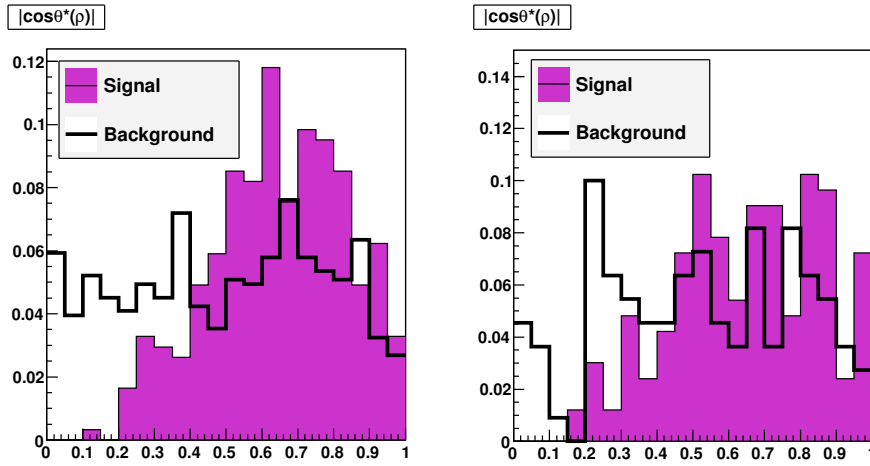


(b) $\cos(\theta_b)$

Figure 7.17: Variables for $B_s \rightarrow D_s^- K^{*+}$ (892), all distributions are normalized to unity.

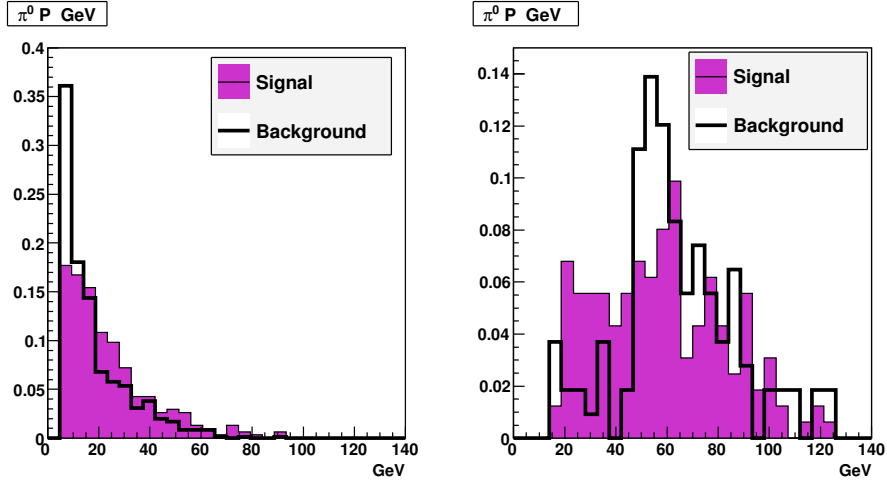


(a) $\rho(770)^+$ invariant mass with a resolved π^0 in the final state (left) and merged $\rho(770)^+$ invariant mass in the final state (right)

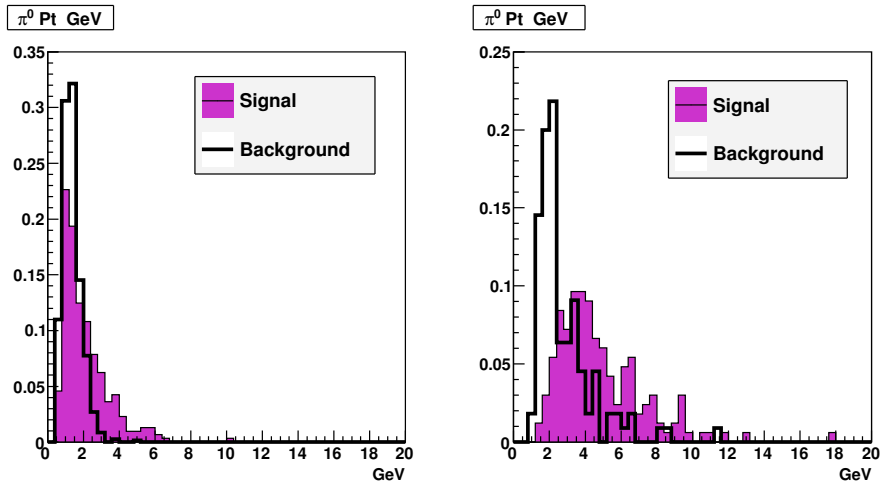


(b) Absolute value of the cosine of the $\rho(770)^+$ helicity angle with a resolved π^0 in the final state (left) and merged π^0 in the final state (right)

Figure 7.18: Variables for $B_s \rightarrow D_s^- \rho(770)^+$, all distributions are normalized to unity.

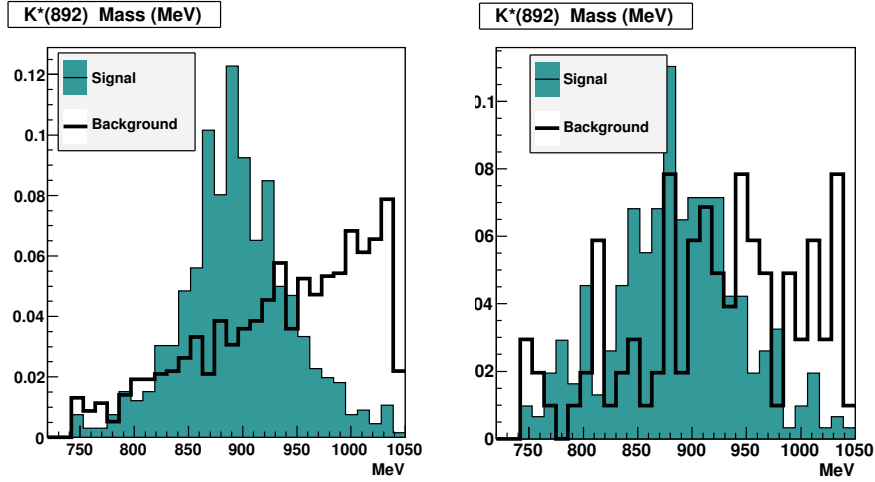


(a) π^0 momentum with a resolved π^0 in the final state (left) and merged π^0 in the final state (right)

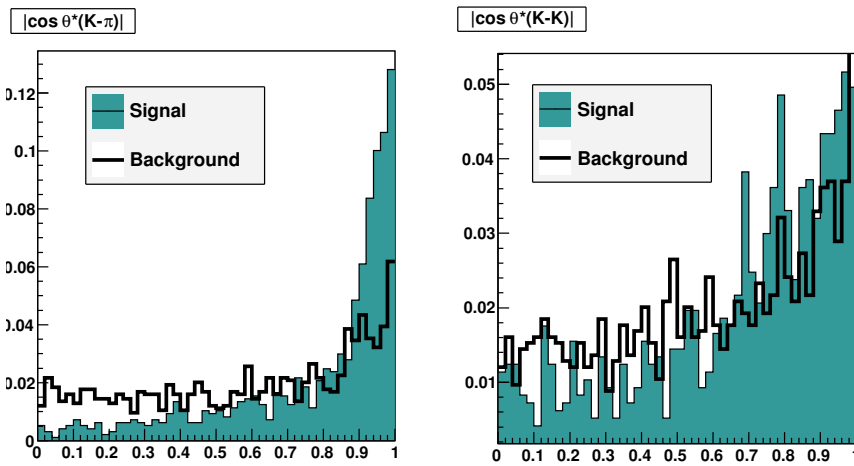


(b) π^0 transverse momentum with a resolved π^0 in the final state (left) and merged π^0 in the final state (right)

Figure 7.19: Variables for $B_s \rightarrow D_s^- \rho(770)^+$, all distributions are normalized to unity



(a) $K^{*+}(892)$ invariant mass with a resolved π^0 in the final state (left) and merged invariant mass $K^{*+}(892)$ in the final state (right)



(b) Absolute value of the cosine of the $K^{*+}(892)$ helicity angle with a resolved π^0 in the final state (left) and merged π^0 in the final state (right)

Figure 7.20: Variables for $B_s \rightarrow D_s^- K^{*+}(892)$, all distributions are normalized to unity

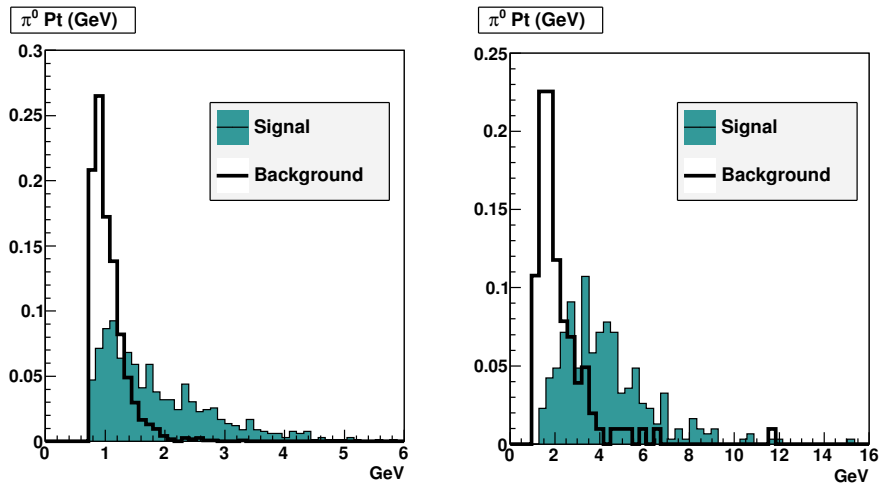
Variables	Fisher Coef.(resolved π^0 s)	Fisher Coef.(merged π^0 s)
$\cos \theta_B$	-0.009	+0.368
$Pt(B_s)$	+0.410	+0.806
$Pt(\pi^0)$	+0.270	-0.137
$M(K^{*+}(892))$	-0.025	-0.172
$\sum_{\text{tracks}} \text{IPs}$	+0.109	+0.283
$ \cos \theta_{K^{*+}(892)}^* $	+0.0024	+0.338
$(\Delta \ln \mathcal{L}_{K\pi})$	+0.431	+0.454

Table 7.13: The Fisher coefficients of the variables using in the Fisher discriminant method for $B_s \rightarrow D_s^- K^{*+}(892)$. For events with a resolved π^0 the most discriminating variable is the kaon PID, for events with a merged π^0 the most discriminating variable is $Pt(B_s)$.

combined variable is shown in Figures: 7.26, 7.27. For $B_s \rightarrow D_s^- \rho(770)^+$, $\frac{S}{\sqrt{S+B}}$ is maximized for 0.08 and 0.09 for the samples with a resolved π^0 and a merged π^0 respectively. While $B_s \rightarrow D_s^- K^{*+}(892)$, $\frac{S}{\sqrt{S+B}}$ is maximized for 0.5 and 0.6 for the samples with a resolved π^0 and a merged π^0 respectively.

7.6.3 Exploring the D_s^- properties

The kinematics of a three body decay can be described using two variables. In a Dalitz plot the axes of the plot are the squared root of the invariant masses of two pairs of the decay products. In the case of D_s particle decaying into $KK\pi$, the Dalitz plot uses the invariant mass KK in the y axis and the invariant mass $K\pi$. If the decay does not involve a resonant structure, then the distribution of the Dalitz plot is uniform. The D_s decays through the resonant modes $D_s \rightarrow (\phi(1020) \rightarrow KK)\pi$ and $D_s \rightarrow (K^*(892) \rightarrow K\pi)K$. We observe for D_s signal events in the right distribution of Figure: 7.28 a non uniform distribution due to the contributions of the resonances $\phi(1020)$ and $K^{*0}(892)$. The Dalitz plot in the left plot of Figure: 7.28 obtained for fake D_s candidates the distribution is flat. The top distributions of Figure: 7.29(a) show the m_{KK} and $m_{K\pi}$ invariant masses. For the m_{KK} distribution the peak highlighted with vertical arrows correspond to the $\phi(1020)$ resonance. Similarly, the peak in the $m_{K\pi}$ distribution, the highlighted peak with vertical arrows correspond to the $K^{*0}(892)$ resonance. To evaluate a mass cut on this resonances, both distributions are fitted with a non relativistic Breit-Wigner (see distributions of Figure: 7.30):



(a) π^0 transverse momentum with a resolved π^0 in the final state (left) and merged π^0 in the final state (right)

Figure 7.21: Variables for $B_s \rightarrow K^{*+}(892)$, all distributions are normalized to unity.

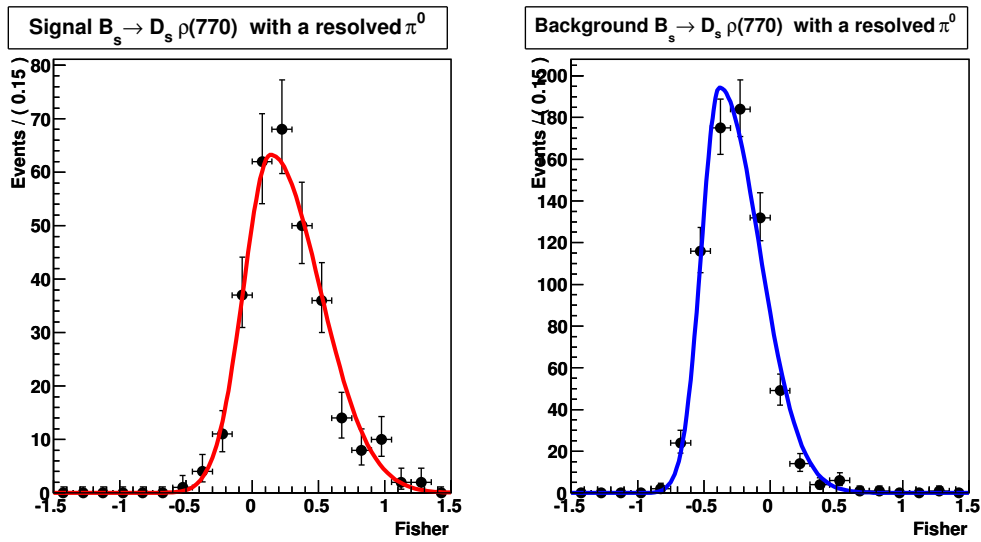


Figure 7.22: Combined variable obtained with a Fisher discriminant method with a resolved π^0 in the final state for signal events (left) and background events (right) for $B_s \rightarrow D_s^- \rho(770)^+$

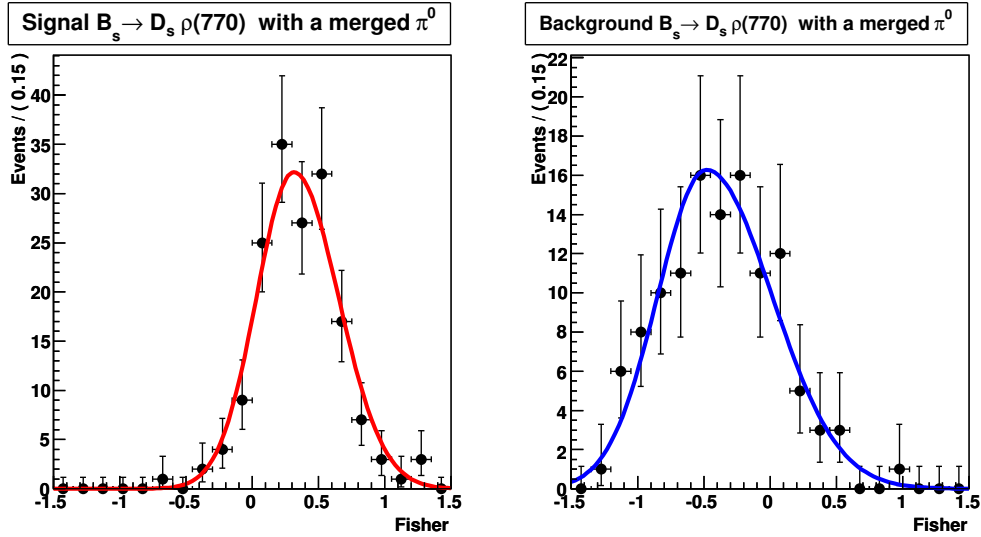


Figure 7.23: Combined variable obtained with a Fisher discriminant method with a merged π^0 in the final state for signal events (left) and background events (right) for $B_s \rightarrow D_s^- \rho(770)^+$

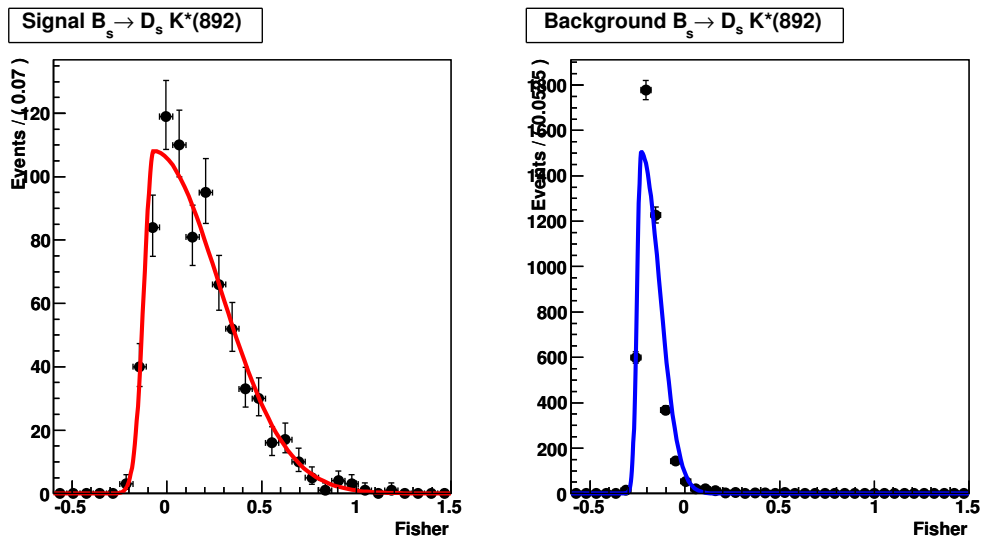


Figure 7.24: Combined variable obtained with a Fisher discriminant method with a resolved π^0 in the final state for signal events (left) and background events (right) for $B_s \rightarrow D_s^- K^{*+}(892)$

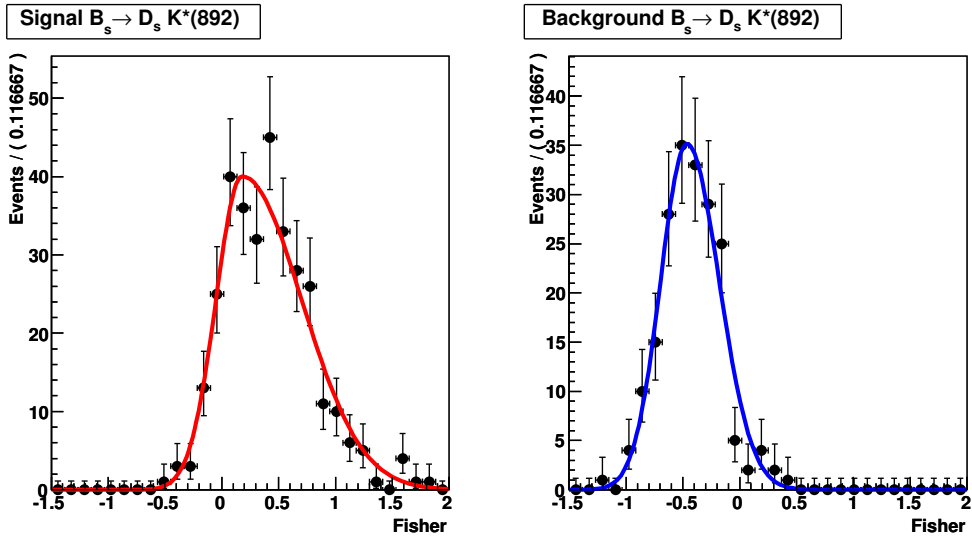


Figure 7.25: Combined variable obtained with a Fisher discriminant method with a merged π^0 in the final state for signal events (left) and background events (right) for $B_s \rightarrow D_s^- K^{*+}(892)$

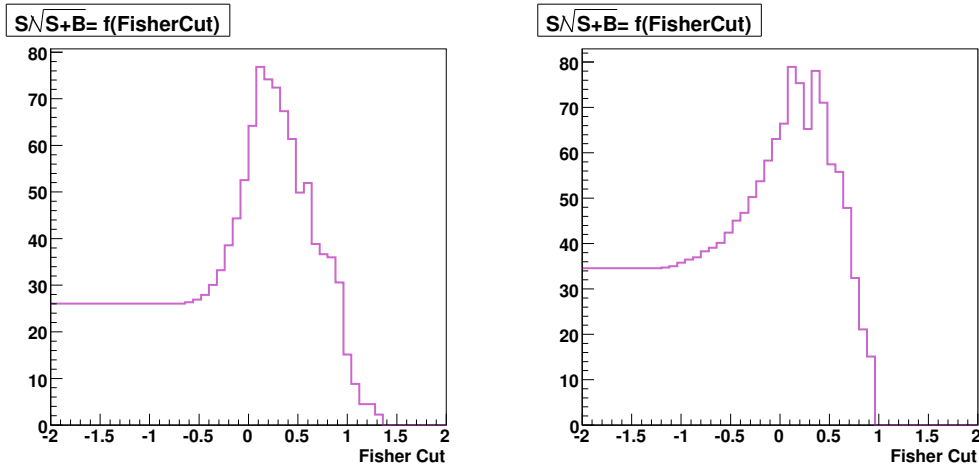


Figure 7.26: Evolution of the statistical significance $\frac{S}{\sqrt{S+B}}$ as a function of the cut on the combined variable obtained with a Fisher discriminant method for $B_s \rightarrow D_s^- \rho(770)^+$, for events containing a resolved π^0 (left) or a merged π^0 (right) in the final state.

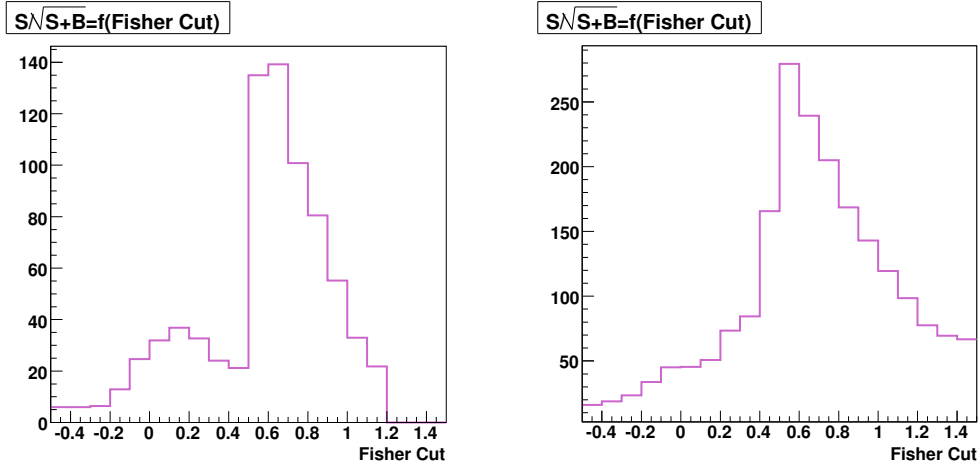


Figure 7.27: Evolution of the statistical significance $\frac{S}{\sqrt{S+B}}$ as a function of the cut on the combined variable obtained with a Fisher discriminant method for $B_s \rightarrow D_s^- K^{*+}$, for events containing a resolved π^0 (left) or a merged π^0 (right) in the final state.

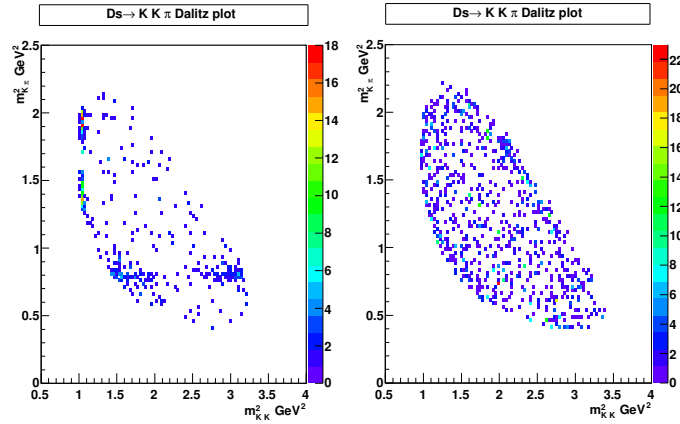


Figure 7.28: D_s Dalitz plot for true D_s candidates(left figure) from the signal sample $B_s \rightarrow D_s^- \rho(770)^+$. D_s Dalitz plot for D_s candidates(right figure) from the $b\bar{b}$ background sample, from the $B_s \rightarrow D_s^- \rho(770)^+$ channel.

- $m_{\phi(1020)} = 1019.8 \pm 0.2 \text{ MeV}/c^2$ and $\Gamma_{\phi(1020)} = 4.7 \pm 0.5 \text{ MeV}/c^2$;
- $m_{K^{*0}(892)} = 895.3 \pm 1.6 \text{ MeV}/c^2$ and $\Gamma_{K^{*0}(892)} = 50.8 \pm 6.2 \text{ MeV}/c^2$.

The resonances $\phi(1020)$ and $K^{*0}(892)$ are spin 1 particles decaying into two pseudo-scalars, thus they benefit from the same angular decay distribution property as for the $\rho(770)$ (see Figure: 7.29(b)).

Using the D_s properties we introduce two sets of cuts to increase the background rejection. For both channels of interest ($B_s \rightarrow D_s^- \rho(770)^+$ and $B_s \rightarrow D_s^- K^{*+}(892)$) we require, $|M(\phi(1020) - 1020)| < 15 \text{ MeV}$ or $|M(K^*(892) - 892)| < 50 \text{ MeV}$ and $|\cos\theta_\phi^*| > 0.4$ or $|\cos\theta_{K^*0}^*| > 0.4$. Due to the limited amount of Monte Carlo data, we can not apply these cut before building the combined variable obtained by means of the Fisher discriminant method. $\sum_{\text{tracks}} \text{IPs}$, is the variable used in the Fisher discriminant which might be the most correlated with the D_s daughters variables. The distributions shown in Figures: 7.31, 7.32 show the variation of the invariant masses $m_{K\pi}$ and m_{KK} as a function of $\sum_{\text{tracks}} \text{IPs}$, and $\cos(\theta^*)$. The corresponding linear correlation factors are listed in the tables: 7.14 and 7.15. In all the cases the correlations are smaller than 7%, therefore it is possible to apply the cuts on the D_s daughters after building the combined variable.

	$m(KK)$	$m(K\pi)$	$\cos \theta_{KK}^*$	$\cos\theta_{K\pi}^*$
Signal $\sum_{\text{tracks}} \text{IPs}$	-1.49 %	2.51 %	-5.14%	-7.03%
Background $\sum_{\text{tracks}} \text{IPs}$	4.67 %	4.05 %	-4.23%	-6.91%

Table 7.14: Linear correlation factors between the sum of the impact parameter significances of the charged tracks and the D_s daughters mass and helicity for the $B_s \rightarrow D_s^- \rho(770)^+$ channel

	$m(KK)$	$m(K\pi)$	$\cos \theta_{KK}^*$	$\cos\theta_{K\pi}^*$
Signal $\sum_{\text{tracks}} \text{IPs}$	6.24 %	-5.35 %	5.56%	-2.28%
Background $\sum_{\text{tracks}} \text{IPs}$	-1.68 %	1.39 %	-0.76%	-6.10%

Table 7.15: Linear correlation factors between the sum of the impact parameter significances of the charged tracks and the D_s daughters mass and helicity for the $B_s \rightarrow D_s^- K^{*+}(892)$ channel

7.6.4 Signal and background estimation for $B_s \rightarrow D_s^- \rho(770)^+$

After optimizing a cut on the combined variable obtained by means of a Fisher discriminant and adding the D_s daughter cuts, we give in Table: 7.16 the number of signal $B_s \rightarrow D_s^- \rho(770)^+$ and $b\bar{b}$ background events expected at LHCb for an integrated luminosity of 2 fb^{-1} , in a $\pm 300 \text{ MeV}$ B_s mass window.

	Signal	Background	B/S
Best $S/\sqrt{S+B}$	72 k	133 k	1.84

Table 7.16: Annual yield for 2 fb^{-1} for $B_s \rightarrow D_s^- \rho(770)^+$ using a multi-variate analysis

Comparison of the performances of the multi-variate analysis with a cut based selection A preliminary study of the decay channel $B_s \rightarrow D_s^- \rho(770)^+$ was done using the previous Monte Carlo Data Challenge (DC04) [64]. To be able to compare the performances of this selection with the multi-variate analysis presented in this thesis, we apply exactly the same cut based selection (see Table: 7.17) on the new Monte Carlo (DC06). The variables

Variables	Cuts
$\sum_{tracks} \text{IPs}$	> 35
B_s Flight dist.sign.	> 5
$ \cos\theta_{\rho(770)}^* $	> 0.4
$P_t(B_s)$	$> 5 \text{ GeV}/c$
$P(B_s)$	$> 60 \text{ GeV}/c$
$P_t(\pi^0)$	$> 1.25 \text{ GeV}/c$
$P(\pi^0)$	$> 10 \text{ GeV}/c$

Table 7.17: Selection cuts for the $B_s \rightarrow D_s^- \rho(770)^+$ decay channel

which are not included in the Fisher discriminant and used in the cut based selection are:

- $P(B_s)$, momentum of the B_s , see Figure: 7.15(b).
- $P(\pi^0)$, the transverse of the $P(\pi^0)$, see Figure: 7.15(b).
- The B_s flight distance significance, see Figure: 7.15(c).

Even if with the cut based method the signal yield given in Table: 7.18 is slightly larger (+% 8), the high B/S value clearly shows the power of the Fisher discriminant technique.

	Signal	Background	B/S
Best $S/\sqrt{S+B}$	79 k	322 k	4.08

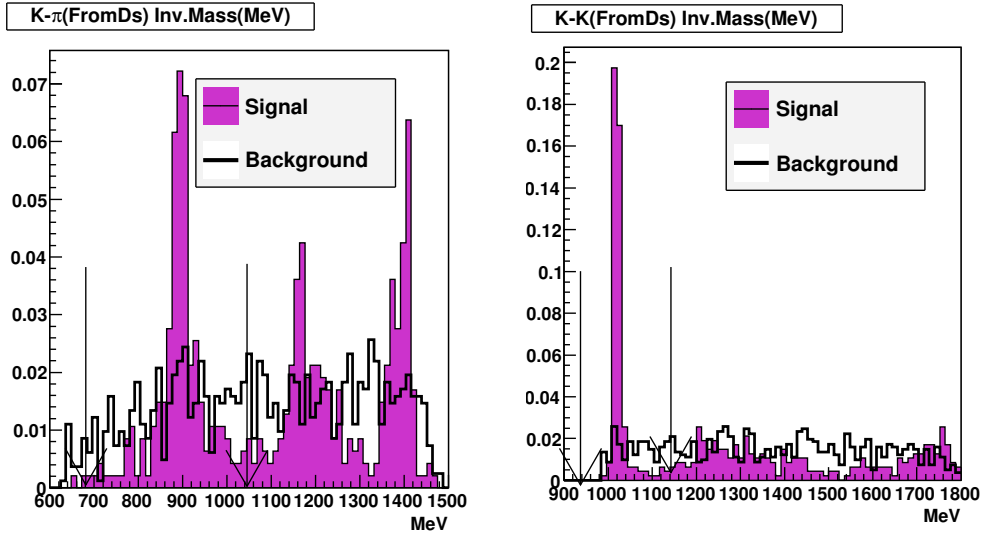
Table 7.18: Annual yield for 2 fb^{-1} for $B_s \rightarrow D_s^- \rho(770)^+$ using a cut based selection

7.6.5 Signal and background estimation for $B_s \rightarrow D_s^- K^{*+}(892)$

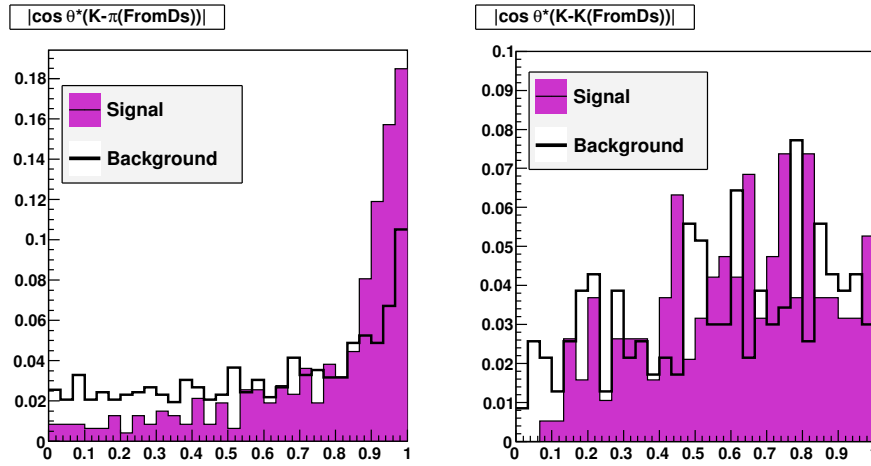
After the final selection, no $B_s \rightarrow D_s^- K^{*+}(892)$ background events remain in the Monte Carlo sample. At a nominal luminosity, 19 million inclusive $b\bar{b}$ events correspond to only 3 minutes and 10 seconds of data taking at LHCb. We use the 90% confidence levels(CL)[ν_1, ν_2] for the mean of a Poisson distribution variable given by the number of selected background events. The method Feldman-Cousins [65] for the construction of confidence intervals is used. The 90% CL for B/S from inclusive $b\bar{b}$ events for $B_s \rightarrow D_s^- K^{*+}(892)$ in 2 fb^{-1} in a 300 MeV mass window is :

$$\frac{B^{\bar{b}b}}{S} < 6,$$

for 1300 selected signal events.



(a) Invariant mass of the $K - \pi$ system (left), invariant mass of the $K - K$ system (right) for the $B_s \rightarrow D_s^- \rho(770)^+$ channel



(b) Absolute value of the cosine of helicity of the $K - \pi$ system (left), absolute value of the cosine of the helicity of the $K - K$ (top right) for the $B_s \rightarrow D_s^- \rho(770)^+$ channel

Figure 7.29: D_s daughters related variables for the $B_s \rightarrow D_s^- \rho(770)^+$ decay channel.

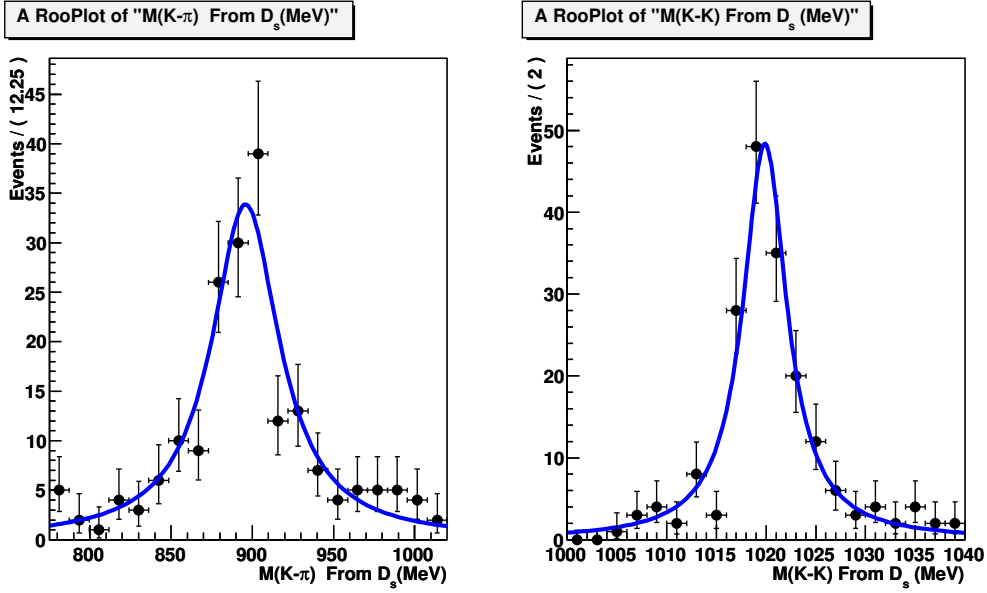


Figure 7.30: $K^{*0}(892)$ invariant mass(left) distribution, $\phi(1020)$ invariant mass, from the signal sample $B_s \rightarrow D_s^- \rho(770)^+$. All distributions are normalized to unity.

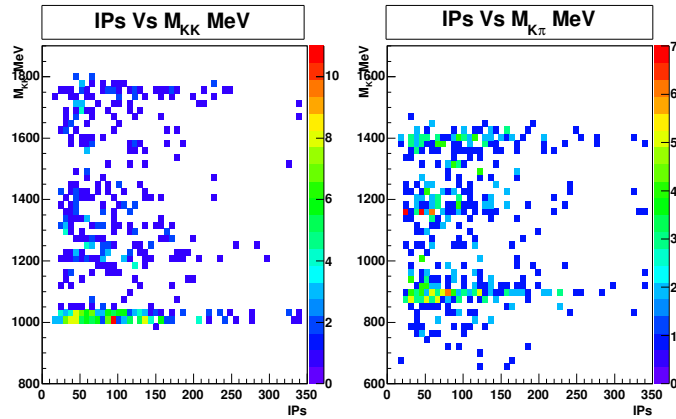


Figure 7.31: Correlation between the sum of the impact parameter significances of the charged tracks in the event and the KK invariant mass (left) or with the $K\pi$ invariant mass (right).

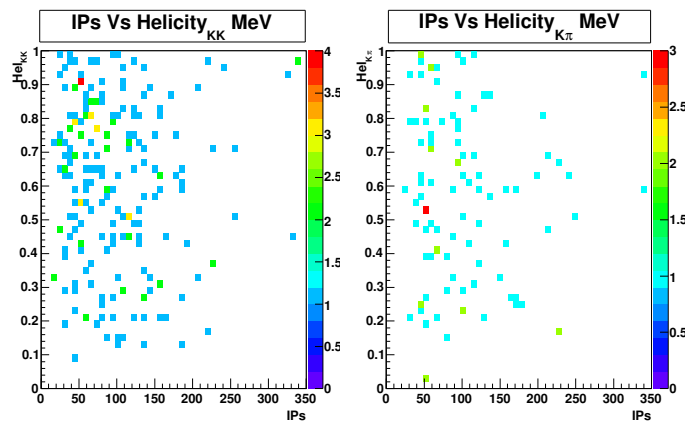


Figure 7.32: Correlation between the sum of the impact parameter significances of the charged tracks in event and the helicity of the KK system (left) or with the helicity of the $K\pi$ system (right).

7.7 Conclusion

A multivariate analysis was performed to select the $B \rightarrow D^- \rho(770)^+$, $B_s \rightarrow D_s^- \rho(770)^+$ and $B_s \rightarrow D_s^- K^{*+}(892)$ decay channels. All these channels involve the reconstruction of a neutral pion in the final state. When we were not limited by the amount of Monte Carlo inclusive $b\bar{b}$ samples, we have separated the π^0 s categories, to maximize the discriminating power of the combined variables. The expected yields before trigger in 2 fb^{-1} of data taking at LHCb is 450×10^3 events for $B \rightarrow D^- \rho(770)^+$, 71×10^3 events for $B_s \rightarrow D_s^- \rho(770)^+$ and 1.3×10^3 events for $B_s \rightarrow D_s^- K^{*+}(892)$. The background estimates are completely dominated by the size of the available Monte Carlo samples. The B/S fraction is found to be equal to 1.6 for $B \rightarrow D^- \rho(770)^+$, 1.8 for $B_s \rightarrow D_s^- \rho(770)^+$. For the $B_s \rightarrow D_s^- K^{*+}(892)$ channel, since no background events remain after the selection, only an upper limit was obtained: $B/S < 6$. A cut based selection for the decay modes $B_{d,s} \rightarrow D_{d,s}(\pi, K)$ has been designed in a unified approach using DC06 [70]. The expected signal yield after the selection in 2 fb^{-1} data is 2.7×10^6 for $B_d \rightarrow D\pi$, 3.7×10^5 for $B_s \rightarrow D_s\pi$, and 3.1×10^4 for $B_s \rightarrow D_s K$. Although the modes $B \rightarrow D^- \rho(770)^+$, $B_s \rightarrow D_s^- \rho(770)^+$ have larger visible branching ratios (the visible branching ratios for $B_s \rightarrow D_s K$ and $B_s \rightarrow D_s^- K^{*+}(892)$ are the same), the obtained signal yields for the $B_{d,s} \rightarrow D_{d,s}(\pi, K)$ decay modes are larger. This signal yield loss can be explained by two facts. One has to take account that, about only $\sim 40\%$ of the π^0 s can be reconstructed in the calorimeter. Also, due to the presence of a neutral pion in the final state and the natural width of the resonances in the decay the combinatorial background is more important and thus the selection has to be tighter to keep the background at a reasonable level.

7.8 What can we do with 200 pb^{-1} of data

The optimization of the multi-variate selection was done for the equivalent of 2 fb^{-1} of data taking. During the first year of the LHC running, one could expect to collect about 200 pb^{-1} . We extrapolate the obtained yields to this integrated luminosity before applying the Level-0 trigger. For the channel $B \rightarrow D^- \rho(770)^+$ we expect about 45×10^3 signal events. While for the channels $B_s \rightarrow D_s \rho(770)^+$ and $B_s \rightarrow D_s^- K^{*+}(892)$ we obtain respectively

7100 and 310 events. As argued in the theory chapter, the initial interest for these modes is provided by their sensitivity to the weak phase γ and the frequency of the oscillations in the the neutral B_s system, Δm_s . All these measurements require a time dependent analyses. Therefore a good knowledge of both of the proper time acceptance and the tagging performances is needed. With these channels, obtaining a competitive measurement of the observables γ or Δm_s will be difficult. Nevertheless, one could explore the high yield of the $B \rightarrow D^- \rho(770)^+$ channel. This decay mode is expected to be one the first observed hadronic channels with a neutral pion in the final state at LHCb. The selected $B \rightarrow D^- \rho(770)^+$ events will allow us to check the performances of both the π^0 offline and online (HLT) reconstructions.

Conclusion

The work presented in this thesis has two main parts: the development of a method to perform the time alignment of the electromagnetic and hadronic calorimeters and the study of hadronic decays with a neutral pion in the final state. LHCb will start taking data in autumn 2009. It is of particular importance to achieve as soon as possible the best possible time alignment. In fact, the time alignment procedure contains several components: the internal time alignment of each sub-detectors, the relative time alignment between them, and the overall LHCb alignment with respect to the LHC clock. We have developed a method to convert measurable quantities, the asymmetries, into a measurement of the time shift. We have simulated in the electromagnetic calorimeter a very simple case of high energy electrons coming from the primary vertex and pointing to a cell of the ECAL. With this sample, we have shown that the time information provided by the integrated signal of the photo-multiplier is well handled. At this stage we have found that the best achievable sensitivity to any source of time misalignment is obtained when sampling the signal around its mid-height. Using a realistic simulation (minimum bias events) we were able to find the necessary conditions to perform the time alignment. We have demonstrated that we need at least 58 k minimum bias events without the magnetic field to internally align the ECAL and the HCAL with a precision of 0.5 ns. Over a million of cosmic events were analyzed in this thesis. Besides being extremely useful to test the calorimeter noise, the Level-0 system and the DAQ, these events allowed us to test *insitu* our asymmetry based method. We developed tools to reconstruct cosmic events in the calorimeter. With these data, we have checked the internal time alignment of the ECAL and the HCAL, 0.3 ns and 0.6 ns respectively. Various corrections were applied to have a good relative time alignment between these two subdetectors. Nevertheless the time information in the calorimeter appeared to be slightly biased. After testing different

hypotheses to isolate this bias, we have found that it can be due to the shape of the integrated signal used in the simulation which might be different *in situ*. A detailed Monte Carlo study, was done to find the best way and the running conditions to measure this shape. The very few synchronized events delivered by the LHC were useful to check the time alignment between the hadronic calorimeter and the LHC clock. The strategy which will be adopted is the following. This preparatory work has allowed to define a possible time alignment strategy for the LHC start-up. For the ECAL and HCAL (using for example the SPD multiplicity trigger or the muon trigger), we will shift the sampling time around the mid-height and collect enough data to precisely time align these two subdetectors in the Time Alignment Event mode. Afterward, we will shift back to the nominal conditions after correction. At this point, similarly to cosmics events runs, the ECAL and the HCAL, will be used as a reference to the other subdetectors. For the ECAL, an other dedicated run will be required to scan the shape of the integrated signal. Once this shape will be obtained, it will be included in the Monte Carlo simulations.

The second part of this thesis was dedicated to the analysis of the hadronic decay modes $B \rightarrow D^- \rho(770)^+$, $B_s \rightarrow D_s^- \rho(770)^+$ and $B_s \rightarrow D_s^- K^{*+}(892)$. The un-measured branching ratios estimates are shown in the theoretical overview chapter. These channels share common topologies, for the three of them we reconstruct a neutral pion coming from a vector resonance. The aim of this study was to check the π^0 reconstruction performance and to estimate the yields for these modes in the equivalent of 2fb^{-1} of data taking. For this purpose we have designed a preselection and a multivariate selection. We have explored the differences in the kinematics of the two types of π^0 s when ever possible. The multi-variate selection was optimized to maximize the statistical significance of each mode, with respect to the $b\bar{b}$ background. Even in 200 pb^{-1} the obtained yield for the decay channel $B \rightarrow D^- \rho(770)^+$ is high enough to be able to use these events for the offline and the online reconstruction tuning.

Résumé

Cette thèse a été effectuée sur l'expérience LHCb, située sur le collisionneur proton-proton LHC au CERN. Sa première partie porte sur l'alignement en temps des calorimètres. Nous décrivons une méthode basée sur une asymétrie permettant d'assurer l'alignement en temps des calorimètres électromagnétique (ECAL) et hadronique (HCAL). Nous montrons qu'avec des faisceaux de 450 GeV, et en l'absence du champ magnétique, il faut 55 000 événements minimum bias pour aligner en temps 84% des cellules du ECAL et 96 % des cellules du HCAL avec une précision de 0.5 ns. Lors de la mise en service des sous-détecteurs, nous avons analysé plus d'un million d'événements cosmiques, et vérifié que l'alignement interne est meilleur que 1 ns dans le ECAL et le HCAL. D'autre part nous avons aligné en temps le ECAL et le HCAL et obtenu une précision de l'ordre de 2 ns. Grâce aux gerbes hadroniques produites par le faisceau du LHC le 10 septembre 2008, nous avons montré que l'alignement global du HCAL avec l'horloge du LHC est de l'ordre de 0.8 ns.

La seconde partie de cette thèse porte sur la reconstruction des canaux $B_d \rightarrow D^- \rho(770)^+$, $B_s \rightarrow D_s^- \rho(770)^+$ et $B_s \rightarrow D_s^- K^{*+}(892)$. Une méthode multivariable a été utilisée pour sélectionner les événements de signal et minimiser le bruit de fond $b\bar{b}$. Avec une année nominale de prise de données à LHCb, on attend 450 000 événements $B_d \rightarrow D^- \rho(770)^+$, 71 000 événements $B_s \rightarrow D_s^- \rho(770)^+$ et 1300 événements $B_s \rightarrow D_s^- K^{*+}(892)$ avec des rapports signal sur bruit variant entre 1.6 et 6.

Mots clefs : *LHC, LHCb, Calorimètre, Alignement en temps, Mésons beaux, Muons cosmiques.*

Abstract

This thesis has been performed in the framework of the LHCb experiment installed on the LHC proton-proton collider at CERN. First, we have developed an asymmetry-based method to time align both the electromagnetic (ECAL) and hadronic (HCAL) calorimeters. We have shown that with 450 GeV beams and without the magnetic field 55 000 minimum bias events are necessary to time align, with a precision of 0.5 ns, 84 % of the ECAL cells and 96 % of the HCAL cells. During the commissioning we have analyzed over a million cosmic events and checked that the internal time alignment of the ECAL and HCAL is better than 1 ns. We have adjusted the relative time alignment between the ECAL and the HCAL to 2 ns. On 10th of September 2008, the LHC delivered one hour of beam. The interaction between a collimator located upstream of LHCb and the beam leads to the production of hadronic showers, detected in the HCAL. We have shown that the global time alignment of the HCAL and the LHC clocks is about 0.8 ns. We have studied the $B_d \rightarrow D^- \rho(770)^+$, $B_s \rightarrow D_s^- \rho(770)^+$ et $B_s \rightarrow D_s^- K^{*+}(892)$ decay modes. All three modes have a neutral pion in the final state. We developed a method that selects signal events and minimizes the $b\bar{b}$ background. With a nominal year of data, we expect 450 000 events for the $B_d \rightarrow D^- \rho(770)^+$ mode, 71 000 events for the $B_s \rightarrow D_s^- \rho(770)^+$ mode and 1300 events for the $B_s \rightarrow D_s^- K^{*+}(892)$ mode, with a background over signal fraction varying between 1.6 and 6.

Key words: *LHC, LHCb, Calorimeter, Time alignment, Beauty mesons, Cosmic muons.*

Bibliography

- [1] E. Noether. Invariant Variations probleme *Nachr. d. König. Gesselsch. d. Wiss. zu Göttingen*, pages 235 – 257, 1918.
- [2] J. H. Christenson, J. W. Cronin, V. L. Fitch and R. Turlay, *Phys.Rev.Lett* **13** (1964) 138.
- [3] Averages of b -hadrons and c hadrons Properties at the End of 2007. arXiv:0808.1297v3 [hep-ex].
- [4] J. Wess, “*The Cpt Theorem And Its Significance For Fundamental Physics*,” *Nucl. Phys. Proc. Suppl.* **8** (1989) 461.
- [5] F.Abe et al.(CDF Collab.), *Phys.Rev.Lett* **81**,2432(1998); F.Abe et al. (CDF Collab),*Phys.Rev.* **D58**,112004(1998).
- [6] T.Inami and C.S.Lim, *Prog.Theor.Phys.* **65** (1981) 297; *ibid.* **65** (1981) 1772.
- [7] S. Weinberg, “*Mixing Angle In Renormalizable Theories Of Weak And Electromagnetic Interactions*,” *Phys. Rev. D* **5** (1972) 1962.
- [8] N. Cabibbo, “*Unitary Symmetry And Leptonic Decays*,” *Phys. Rev. Lett.* **10** (1963) 531; M. Kobayashi and T. Maskawa, “*CP Violation In The Renormalizable Theory Of Weak Interaction*,” *Prog. Theor. Phys.* **49** (1973) 652.
- [9] A.J. Buras, M. Jasmin and P.H. Weisz, *Nucl. Phys.* **B347** (1990) 491.
- [10] T. T. E. Group et al. [CDF Collaboration], arXiv:0803.1683 [hep-ex].
- [11] S. Herrlich and U. Nierste, *Nucl. Phys.* **B419** (1994) 192.
- [12] CKMfitter <http://ckmfitter.in2p3.fr>

- [13] L. L. Chan and W. L. Keung, Phys.Rev Lett.53 (1984) 1802.
- [14] L. Wolfenstein, Phys.Rev.Lett.51 (1983) 1945.
- [15] A. J. Buras, M. E. Lautenbacher and G. Ostermaier, Phys. Rev. D **50** (1994) 3433.
- [16] G. Buchalla, A. J. Buras and M. E. Lautenbacher, “ *Weak Decays Beyond Leading Logarithms,*” Rev. Mod. Phys. **68** (1996) 1125
- [17] The analog Readout of the LHCb Vertex Detector and Study of the Measurement of B_s Oscillations- Jeremie Borel Juin 2008
- [18] Observation of the $B_s - \bar{B}_s$ Oscillations. CDF Collaboration. arXiv:060904v[hep-ex] .
- [19] J.Ellis. Physics beyond the Standard Model. arXiv:0902.0357 [hep-ph]
- [20] M. Bona et al., The UTfit Collaboration <http://www.utfit.org/>.
- [21] F.Polci Time dependent Dalitz analysis of the $B_0 \rightarrow D^- K^0 \pi^+$ decays for the measurement of the $2\beta + \gamma$ with the BaBar detector.
- [22] M.Baak Measurement of CKM-angle gamma with Charmed B^0 Mesons Decay. SLAC-R-858.
- [23] R.Fleisher New strategies to Obtain Insights into CP Violation Through $B_s \rightarrow D_s K, D_s^* K, \dots$ and $B_d \rightarrow D\pi, D^*\pi, \dots$ Decays. hep-ph/-304027.
- [24] V.V Gligorov, G.Wilkinson. Strategies for measuring γ from the decay channels $B_d \rightarrow D\pi$ and $B_s \rightarrow D_s K$ at LHCb. LHCb-2008-035.
- [25] Y.Keum, H.Li and A.I Sanda. Penguin Enhancement and $B \rightarrow K\pi$ decays in perturbative QCD. arXiv:0004173v1[hep-ph] .
- [26] Robert Fleischer. Flavor Physics and CP Violation: Expecting the LHC, arXiv:0802.2982v1.
- [27] Les Houches, Session LXVIII. Probing the standard Model of particle interactions Part I.
- [28] M.Neubert and B.Stech, *Ads. Ser.Direc High Phys* 15 (1998) 294.

- [29] J. D. Bjorken, “ *Topics in B Physics*,” Nucl. Phys. Proc. Suppl. **11** (1989) 325.
- [30] Exclusive Hadronic B Decays to Charm and Charmonium Final States, CLEO collaboration, hep-ph/9403295
- [31] Measurement of the ratio of the branching fraction $Br(B_s \rightarrow D_s\pi)/Br(B^0 \rightarrow D\pi)$; CDF collaboration, CDF note 7862
- [32] First observation of $B_s \rightarrow D_s K$. CDF note 8850.
- [33] Exclusive Hadronic B Decays to Charm and Charmonium Final States, CLEO collaboration, hep-ph/94032
- [34] P.Nason and al. Bottom production. G.Altarelli and M.L Mangano, editors, Proceedings of the 1999 Workshop on Standard Model Physics at the LHC, volume CERN -2000-004. hep-ph/0003142.
- [35] T.Nakada and O.Schneider. LHCb Trigger. Proceedings of the 4th International Workshop on B physics and CP violation, 2001 Japan. IPHE 2001.
95.
- [36] P.Ball, G.Jones, R.Zwicky Published in Phys.Rev.D75:054004,2007.
- [37] CERN document server. <http://weblib.cern.ch>
- [38] TDR, LHCb Reoptimized Detector Design and Performance, CERN/LHCC 2003-030.
- [39] TDR, LHCb RICH, CERN/LHCC/2000-0037.
- [40] TDR, the LHCb Trigger system, CERN/LHCC 2003-31.
- [41] TDR, LHb magnet CERN/LHCC/2000-007.
- [42] TDR, the LHCb Velo, CERN/LHCC 2001-011.
- [43] TDR, The the LHCb Outer Tracker, CERN/LHCC/2001-024.
- [44] TDR, The the LHCb Inner Tracker, CERN/LHCC/2002-029.
- [45] TDR, the LHCb muon system, CERN/LHCC 2001-010.

- [46] TDR, LHCb computing, CERN/LHCC 2005-019.
- [47] TDR, LHCb online system, CERN/LHCC 2005-019.
- [48] LHCb computing web page, <http://lhcb-comp.web.cern.ch/lhcb-comp/>
- [49] TDR, LHCb Calorimeters, CERN/LHCC/2000-0036.
- [50] L.Garrido et al, *Results of tagger photon test beams for the scintillator pad detector*, Note LHCb-2000-032.
- [51] SN.Filippov et al. Experimental performance of PS/SPD prototypes. Note LHCb-2000-031.
- [52] Patrick Robbe, talk given at Calor 2004 - Perugia, Italy.
- [53] Jones <http://www.particle.cz/conferences/c2cr2005/talks/Jones.pdf>
- [54] Travnicek <http://www.particle.cz/conferences/c2cr2005/talks/Travnicek.pdf>
- [55] J.Lefrancois, CW and noise measurement, LHC Calorimeter Commissioning meeting. CERN, 04-11-2008. Jacques
- [56] Hernando,J; Rodrigues, E. Tracking Event Model CERN-LHCb-2007-007
- [57] Y.Amhis,"Cosmics time scan", LHCb Calorimeter Commissioning meeting. CERN, 28-07-2008.
- [58] Photon and neutral reconstruction-LHCb-Note-2007-046.
- [59] Particle Data Group 2006
- [60] Toolkit for MultiVariate Analysis User Guide.
- [61] Pythia <http://home.thep.lu.se/~torbjorn/Pythia.html>
- [62] EvtGen <http://www.slac.stanford.edu/~lange/EvtGen/>
- [63] Geant4 <http://wwwasd.web.cern.ch/wwwasd/geant4/geant4.html>
- [64] O.Deschamps, S.Monteil "First look at $B_s \rightarrow D_s \rho(770)$ ". LHCb-Proper Time and Mixing Working group, CERN, 01-19-2006.

- [65] Feldman-Cousins- A Unified approach to the Classical Statistical Analysis of Small Signals.
- [66] G.Raven, "Selection of $B_s \rightarrow J/\psi\phi$ " and $B^+ \rightarrow J/\psi K^+$.CERN-LHCb-2003-118, 2003
- [67] M.Needham "Performance of the LHCb Track Reconstruction Software". CERN-LHCb-2008-001, 2007
- [68] Vertex Fitters at LHCb "<https://twiki.cern.ch/twiki/bin/view/LHCb/VertexFitters>"
- [69] Parameters of DC06 Monte Carlo productions <https://twiki.cern.ch/twiki/bin/view/LHCb/SettingsDc06>
- [70] V. Gligorov Reconstruction of the decay modes $B \rightarrow D\pi$, $B_s \rightarrow D_s\pi$, and $B_s \rightarrow D_s K$ at LHCb. CERN-LHCb-2009-003.

Remerciements, Sahitou

Je tiens à remercier Guy Wormser d'avoir accepté de présider mon jury de thèse. Je remercie aussi Marie-Noëlle Minard et Isabelle Wingerter-Seez d'avoir accepté d'être mes rapporteurs. En particulier Marie-Noëlle qui a suivi mon travail au sein du groupe calorimètre. Merci également à Olivier Pène et Fabian Zomer d'avoir accepté de faire partie de mon jury de thèse.

Jacques Lefrançois, je ne sais pas par où commencer... Merci d'avoir été patient avec moi pendant que je cherchais mes "trompes". Merci de m'avoir accordé tellement de temps de discussion. Ce fut un véritable plaisir de travailler à tes côtés, je ne serai jamais assez reconnaissante. Marie-Hélène Schune, la première fois que je t'ai rencontré c'était il y a huit maintenant. Merci de m'avoir accepté pour faire le stage de licence, merci de m'avoir encouragé à continuer et surtout merci d'avoir encadré cette thèse. J'ai appris un Zillion de choses avec toi, et j'espère sincèrement que cela va continuer l'année prochaine (l'année du démarrage du LHC !) même si je suis chez les Suisses.

Benoît, se prononce Be-No-I-T, je m'incline devant toi, peut-être que c'est parce qu'on a partagé le bureau quand j'étais en 3^{ème} année mais tu parles plus que moi! Aurélien, alias 'O mon thésard' t'as intérêt à vite mesurer γ ! Enfin, t'as du temps encore, mais s'il te plait, juste pour me faire plaisir, fais le avant les anglais. Il me semble que c'est un argument scientifique objectif et rationnel tout à fait valable. Patrick Roudeau, merci d'avoir honoré une de mes slides en l'accrochant sur ton mur légendaire. Un grand merci à toute l'équipe LHCb, Patrick Robbe, Ioana Vidau, Olivier Callot, Frédéric Machefert, Sergey Barsuk, Bernard Jean-Marie, Bernard d'Almagne, Jibo, Wenbin et Victor. Merci pour votre aide et vos encouragements.

Patrick Koppenburg, promis la prochaine fois j'utilise la mailing list davinci@cern.ch si j'ai un problème, merci pour ton aide, et pour tes conseils. A Huge thank you Gloria Corti, it was really great to learn about LHCb for the very first time with you. Vanya, thanks for your help with everything, you were always very patient and kind to me thank you! Olivier Deschamps, merci pour tout... je n'aurai jamais pu faire ce que j'ai fait dans cette thèse sans ton aide! Longue vie à **CaloCosmic-**

TrackTool. Sincèrement un million de fois merci! Patrick Robbe, tu me donnes 5 ans et on joue la première sonate de Brahms pour Violoncelle et Piano! Aussi merci pour ton aide avec Gauss! Stéphane Monteil, merci pour ton aide avec $D_s\rho(770)$ et pour ton traité de : "Comment se changer les idées à l'Aviation ou l'élégance au Bowling de Meyrin". Sébastien Descotes-Genon merci pour la théorie. Laurent Serin, merci pour tous tes bons conseils! Niko, thanks for the 'Marylin', for Schubert and Mozart and the morning hot chocolates at CERN. A huge thanks to the National Scot Grid Army, Andrew, Greig and Stuart, you guys saved my not so wee Monte Carlo productions and my mental health. Stephane Poss, ou Stephaaaaaaaaaaane, mon ultime compagnon de galère dans le soft de LHCb! Je sais, je sais, j'ai encore oublié de faire **source setup.csh**, promis je vais plus oublier. Yo Tristan! thanks for our wordless coffees at R1 man, muscle man. Michelle, your timing with the candies was triple ace, my office is now yours in building 208. Vava, my dear ghetto friend, the keeper of the Monte Carlo truth at LHCb, thanks for being the best coach one could think of, thanks for reminding every single bloody time that one should say "If I were" instead of "If I was", I think this summarizes everything I have to say.

Blandine ma copine de Violoncelle, merci d'avoir vérifié si je mangeais bien 5 fruits et légumes par jour, promis la prochaine fois je serai en rythme et en 4 ème pour les duos d'*Offenbach*. Merci à *Johann Sebastian Bach*, *Jaqueline du Pre* et **System of Down**, cette thèse n'aurait pas été la même sans vous.

Oh! my darling Clément, merci d'avoir sauvé mes genoux a Moriond et pour le bain de mer a Lisbonne. Justine, merci pour Björk et pour les concerts à la guinguette pirate! Francesco, "Prima la musica" c'est pas parce que tu es un CR2 hyper cool (rouler les "r") ou que tu fais *Higgs* $\rightarrow \gamma\gamma$ (appuyer sur les "m" de gamma) maintenant, que tu sera pas pour toujours *mio piccolo*. Andreas, merci pour mon premier cours de guitare, merci pour Tool et Battle of Mice, I promise, I shall not push you down the stairs. Dimitris le DJ officiel de ces trois dernières années, promis je serai plus artiste l'année prochaine. Marcel, je te rappelle que tu dois toujours mettre tes mains dans le ketchup. Le joueur de tambour, les dragons, les galériens, le poisson rose et l'avion et tous les autres te disent merci. João (il faut attraper la crève ou simplement se boucher le nez pour bien dire son nom, il est portugais c'est pas de sa faute) quand même, même quand on a été les fantômes du 208, tu diras ce que veux mais on a bien rigolé! Violina, le désert d'Algérie nous attend... On est loin l'une de l'autre, mais ça c'est juste pour le moment!

Le prince D'Avout D'aerstaedt, Le Duc en tongues, Le jouer d'échecs, mon ami de toujours, what can I say?? It's "The agony of choice". Khaled, Nadjib, ya mhaynenkoum, je vous jure (à dire forcément avec l'accent Kabyle), ici ça n'a rien avoir les TPs de physique du Nouveau bâtiment De Descartes. Lilia, Sarah, mes copines de Descartes, on se voit bientôt à la petite auberge ! Aichouche! Aichouche... si je dis "jaune "+ " nous " tu dis ? voilà, ça résume tout! y'a

que toi qui peut comprendre ça , et c'est pas because tu es ma meilleure amie depuis...bah! longtemps!

Les Amhis fous, Jamil, Nassima, Yann et Louiza, mais vraiment fous de Sucy-En-Brie. Vous m'avez ouvert les portes de votre maison quand je suis arrivée à Paris...même si vous appelle pas souvent je n'oublierai jamais ce que vous avez fait pour moi. Ma tante Fatiha de Kouba, qui continue à dire aux gens à Alger que sa nièce est en train de construire une fusée et qu'elle va aller dans l'espace. Yeyes, ma grand-mere revolutionnaire et oui tu es la seule grand mère dans l'univers qui pendant les 9 ans ou j'ai mangé chez toi tous les jours à 11 h 26 fut capable de faire les meilleurs poivrons rouges au monde, et les pulls en laine les plus doux qui soient. Mais, surtout de m'expliquer avec passion, ce qu'est un Alexandrin ou le théorème de Pytagore. Mey, Ney, mes soeurs, mes anges, je suis la seule à savoir que derrière vos sourires se cachent les pires diables de l'humanité... On va continuer à rire (de manière très discrète évidemment...) comme on l'a toujours fait et à se moquer de la terre entière, même quand on aura un million d'années et une dent chacune. Papa, merci de m'avoir appris à nager, à sauter des rochers, à faire de l'apnée, à chasser les clous, à serrer les dents quand les méduses m'ont piquées, et surtout merci de m'avoir montrer comment chanter de plus en plus fort l'ouverture de *Carmen* quand les vagues devenaient de plus en plus grandes. Maman, tu es la personne la plus douce de l'univers, sans ton amour je n'aurai jamais survécue, encore moins sans tes 15 millions de coups de téléphone. Merci pour tout petite mère.

Mon grand-père, Didis, j'avais encore tellement d'histoires à te raconter... Heureusement qu'on s'est bien amusé dans le jardin d'Hydra à jouer aux chasseurs d'abricots et aux apprentis sorciers qui transforment les pétales blancs des jasmins en bleu nuit.